Imperial College London

Models of X-rays and Electron Beams from Laser Wakefield Accelerators

Adam James Hughes

Thesis submitted in partial fulfilment of the requirements for the degree of Doctor of Philosophy in Physics of Imperial College London and for the Diploma of Imperial College London

Wednesday 22nd May 2024

Department of Physics
Imperial College London
Prince Consort Road
London, United Kingdom
SW7 2BZ

Declaration of Authorship

The material presented in this thesis was produced by the author, unless otherwise stated, cited or acknowledged in the text.

Supervisor: Prof. Zulfikar Najmudin

The copyright of this thesis rests with the author. Unless otherwise indicated, its contents are licensed under a Creative Commons Attribution-Non Commercial-No Derivatives 4.0 International Licence (CC BY-NC-ND). Under this licence, you may copy and redistribute the material in any medium or format on the condition that; you credit the author, do not use it for commercial purposes and do not distribute modified versions of the work. When reusing or sharing this work, ensure you make the licence terms clear to others by naming the licence and linking to the licence text. Please seek permission from the copyright holder for uses of this work that are not included in this licence or permitted under UK Copyright Law.

Abstract

This thesis focuses on electron and radiation beams produced in laser wakefield accelerators (LWFAs). The first part presents two radiation computation codes (RCCs) built to model x-ray beams from LWFAs. One RCC models the temporal intensity profile and photon fluence spectrum at different positions. The other RCC models the angular energy density distributions. Six experiments were modelled. The modelled radiation beams have a duration between 40 and 100 fs, a peak spectral fluence of 3×10^2 to 7×10^4 photons/mrad^2/0.1% bandwidth (BW) and a peak brightness of 2×10^{21} to 6×10^{22} photons/s/mrad^2/mm^2/0.1% BW. The modelled angular energy density distributions are compared with experimental results and discussed.

The second part considers simulating an LWFA for future light source applications. A machine learning algorithm was used to optimise the peak energy and total charge from simulated LWFAs driven by a 30 mJ, 7.5 fs laser. In optimising the peak energy, the algorithm primarily adjusted the plasma density, plasma length, laser focal position and plasma density up-ramp length. The optimised electron beams had a local maximum in their spectra at 125 MeV. Optimising the total charge, the algorithm adjusted the plasma density, up-ramp length, laser focal position and spectral phase coefficients. The optimised electron beams had a total charge of 200 pC above 10 MeV.

Finally, an experiment was performed using a 44 mJ, 12 fs laser pulse to drive LWFAs at a 10 Hz repetition rate. The first electron beams produced with this system are reported, with energies of up to 60 MeV and a total detected charge between 2.0 and 3.5 fC above 10 MeV. In scans of the plasma density and focal position, electron beams with the highest energy and charge were produced at plasma densities of 4.5×10^{19} cm^{-3} when focusing the laser at least 0.2 mm into the plasma.

Contents

Declaration of Authorship **2**

Abstract **4**

List of Figures **8**

List of Tables **12**

List of Symbols **12**

Acknowledgements **17**

1 Introduction **18**
1.1 Synchrotron Light Sources 19
1.2 Laser Wakefield Acceleration 22
1.3 Thesis Outline 28

2 Theoretical Background **30**
2.1 Lagrangian Mechanics 30
2.2 Single Charged Particle in an Electromagnetic Wave 31
2.3 Electromagnetic Waves in Plasma 34
2.4 Laser Pulse Evolution in Plasma 37
2.5 Laser-Driven Plasma Waves 42
2.6 The Bubble Regime 45
2.7 Injection of Electrons into the Wakefield 47
2.8 Electron Acceleration in the Bubble Regime 53
2.9 Limits of Electron Acceleration 54
2.10 Betatron Oscillations 56
2.11 Synchrotron Radiation 60
2.12 Synchrotron Radiation from LWFAs 68

3 Radiation Simulation Methods **77**
3.1 Particle-in-Cell Simulations 77

3.2 Model Setup . . . 78
3.3 Temporal Intensity Profile . . . 79
3.4 Spectral Intensity Profile . . . 82
3.5 Angular Energy Density Distribution . . . 83
3.6 Temporal Resolution . . . 83
3.7 Temporal Coherence of Radiation from a Single Macroparticle . . . 88

4 Modelled X-ray Beams from LWFAs 90
4.1 Simulated LWFAs . . . 90
4.2 Modelled Temporal Intensity Profiles . . . 91
4.3 Modelled Photon Fluence Spectra . . . 101
4.4 Modelled Angular Energy Density Distributions . . . 113
4.5 Summary . . . 123

5 Bayesian Optimisation of PIC Simulations for eSYLOS 125
5.1 Laser Focusing . . . 125
5.2 Bayesian Optimisation (BO) of FBPIC Simulations . . . 126
5.3 Results of Optimisations . . . 132
5.4 Summary . . . 146

6 Electron Beams from LWFAs Driven by the SEA Laser at eSYLOS 148
6.1 Experimental Setup and Methods . . . 148
6.2 Experimental Results . . . 159
6.3 Summary . . . 166

7 Conclusions 168
7.1 Modelled X-ray Beams from LWFAs . . . 168
7.2 Bayesian Optimisation of PIC Simulations of eSYLOS . . . 171
7.3 Electron Beams from LWFAs Driven by the SEA Laser at eSYLOS . . . 172

Bibliography 175

A General Definitions and Equations 200
A.1 Normalised Parameters . . . 200
A.2 Maxwell's Equations . . . 200
A.3 Electromagnetic Potentials . . . 201
A.4 Poisson's Equation . . . 201
A.5 Continuity Equation . . . 202

B Single Charged Particle Interactions with Electromagnetic Waves 203
B.1 Lagrangian of a Relativistic Charged Particle in an Electromagnetic Potential . . . 203
B.2 Ponderomotive Force . . . 205
B.3 Charged Particle in an Electromagnetic Plane Wave . . . 206

C Laser-Plasma Interactions 212
C.1 Electromagnetic Wave Equation in Plasma . . . 212
C.2 Dispersion Relation for an Electromagnetic Wave in Plasma . . . 212
C.3 Plasma Frequency . . . 214
C.4 Nonlinear Refractive Index of a Plasma . . . 215
C.5 Photon Acceleration . . . 216
C.6 Self-Focusing of a Laser Pulse in Plasma . . . 218
C.7 Linear Plasma Waves . . . 221
C.8 Electron Density in a Plasma Wave . . . 224

D Electron-Wakefield Interactions 225
D.1 Electron Acceleration in the Bubble Regime . . . 225
D.2 Transverse Scalar Potential in the Bubble Regime . . . 227
D.3 Betatron Oscillations at Constant Energy . . . 227
D.4 Electron Trajectories in the Bubble Regime . . . 228

E Synchrotron Radiation Properties 233
E.1 Angular Intensity Distribution of Radiated Synchrotron Radiation . . . 233
E.2 Angular Energy Density Distribution in an LWFA . . . 238
E.3 Inverse Doppler Shifting Factor . . . 244
E.4 Duration of a Synchrotron Radiation Flash . . . 244

List of Figures

Figure 1 Electron beam in an insertion device 20
Figure 2 Plasma wave in the bubble regime 24
Figure 3 Process of emission of x-ray beam in an LWFA 25

Figure 4 Electron trajectory in an electromagnetic plane wave 33
Figure 5 Laser Pulse Compression in Plasma 38
Figure 6 Photon Acceleration in a Laser Pulse in Plasma 39
Figure 7 Schematic of self-focusing of a laser pulse in plasma 40
Figure 8 One-dimensional plasma wave solutions driven by laser pulses with different normalised potentials 44
Figure 9 PIC simulation of the bubble regime 46
Figure 10 Comparison of self-injection thresholds for laser potential 49
Figure 11 Phases in one-dimensional plasma waves for ionisation and trapping of electrons from a high Z gas in ionisation injection 51
Figure 12 Required phase in the wakefield, peak normalised potential and pulse length for successful trapping of an electron in the wakefield via ionisation injection. 52
Figure 13 Transverse electric field in the bubble regime 56
Figure 14 Theoretical electron trajectories of ultrarelativistic electrons in the bubble regime following constant and parabolic energy progressions 58
Figure 15 Transverse momentum component of electron following parabolic energy progression 60
Figure 16 Position vectors for calculating the electromagnetic fields of synchrotron radiation 61
Figure 17 Setup of Cartesian and angular coordinates in deriving the angular intensity distribution of synchrotron radiation 64
Figure 18 angular intensity distribution of synchrotron radiation from an electron following a circular trajectory 65
Figure 19 Range of angles over which synchrotron radiation from an electron following a circular trajectory reaches a stationary observer 66
Figure 20 Angular energy density spectra from electrons in a storage ring 68

Figure 21 Angles of divergence of the electron trajectory and instantaneous synchrotron radiation cone 69
Figure 22 2D overview of power emitted at each angle of divergence and angular energy distribution produced by an electron following a sinusoidal trajectory 70
Figure 23 Numerical and analytical energy density distributions of radiation beams produced by an electron following a sinusoidal trajectory . 72
Figure 24 Three-dimensional angular energy density distributions in the plane of oscillation of electrons following sinusoidal trajectories 72
Figure 25 Electric fields against time and energy density spectra for oscillating electrons with different K-parameters 74
Figure 26 On-axis energy density spectra produced by electrons with different Lorentz factors in an LWFA with a plasma density of 2×10^{18} cm^{-3}. All electrons considered in this plot have a betatron oscillation amplitude of 2 µm. 76

Figure 27 Schematic of setup in radiation computation code 79
Figure 28 Schematic of the retarded-observed time problem 79
Figure 29 Overview of process of locating, interpolating and summing the electric field arrays from particle tracking data at an observation point . 81
Figure 30 Comparison of interpolations in the retarded time and the time of observation 84
Figure 31 Schematic of problem interpolating trajectories from PIC simulation directly 85
Figure 32 Interpolation of Liénard-Wiechert field against time 88
Figure 33 Total electric field produced by temporally incoherent electrons oscillating with $K = 10$ 89

Figure 34 $N(\xi)$ and $N(\xi)\gamma_{peak}^4(\xi)$ profiles of Rousse (2004) and Wood (2018) and their electron density maps 92
Figure 35 Modelled temporal intensity profiles of x-ray beams from low power LWFAs and energy progression of electrons in LWFA 94
Figure 36 Modelled temporal intensity profiles of x-ray beams from high power LWFAs and energy progression of electrons in LWFA 96
Figure 37 Tracked electron trajectories and energy of Rousse (2004) and Wenz (2015) 99
Figure 38 Tracked electron trajectories and energy of Wood (2018) and Bloom (2020) 100
Figure 39 Tracked electron trajectories and energy of EPAC 100
Figure 40 Modelled on-axis photon fluence spectra 102

Figure 41 Histograms of Lorentz factor and critical energy at turning points of electron trajectories . . . 103
Figure 42 Estimated on-axis spectral fluence from properties of simulated electron trajectories . . . 104
Figure 43 Detection curves for x-ray beams for low laser power LWFAs . . 105
Figure 44 Expected detected on-axis spectral fluence from low power LWFAs 106
Figure 45 Expected detected on-axis spectral fluence from high power LWFAs . . . 107
Figure 46 Input laser power against modelled and experimental peak spectral fluence . . . 109
Figure 47 Peak brightness against input laser power . . . 110
Figure 48 Modelled spectral fluence at different divergence angles . . . 112
Figure 49 Modelled angular energy density distributions of x-ray beams from LWFAs . . . 114
Figure 50 X-ray beam divergence against photon energy . . . 116
Figure 51 Time-averaged electron spectrum of each LWFA . . . 118
Figure 52 Slices of angular energy density distributions produced by RCC compared with mathematical models . . . 119
Figure 53 Conceptual diagram of radiation energy density distributions from electrons in different planes of oscillation . . . 120
Figure 54 Two randomly sampled trajectories of electrons in PIC simulation in three-dimensions . . . 122
Figure 55 Overview of Bayesian optimisation algorithm . . . 128
Figure 56 Example electron spectrum for analysis in machine learning algorithm . . . 131
Figure 57 Output peak energy of electron beam in each simulation in Bayesian optimisation . . . 133
Figure 58 Scatter plots of input parameters in each simulation in peak energy optimisation by the BO algorithm, colour-coded against their output peak energy . . . 134
Figure 59 Side view analysis of the input parameter space in the n_{He}-L_{plasma} plane . . . 135
Figure 60 Maps of Bayesian model of peak energy . . . 136
Figure 61 Laser pulse and wakefield progression in LWFA with different laser's focal positions . . . 137
Figure 62 Progression of laser pulses in LWFAs with different second-order spectral phase coefficients . . . 138

Figure 63 Comparison of electron spectra, electron energy progression and laser normalised potential in initial and optimal simulations for peak energy 139
Figure 64 Scatter plots of input parameters in each simulation in total charge optimisation by the BO algorithm, colour-coded against their output peak energy 140
Figure 65 Modelled total charge against nitrogen dopant concentration and helium gas density 141
Figure 66 Modelled and simulated total charge against laser focus position and length of gas density up-ramp 142
Figure 67 Scans of total simulated electron beam charge against density up-ramp length and laser's focal position 143
Figure 68 Electric field slices of laser pulses at start of plasma and start of self-injection process, with progression of normalised potential and total electron beam charge in LWFA 145
Figure 69 Comparison of initial and optimal simulations in total charge optimisation 146

Figure 70 Basic experimental setup of eSYLOS 149
Figure 71 Drawing of gas cell used in eSYLOS experiment 149
Figure 72 Backing pressure against electron density in gas cell 150
Figure 73 Experimental layout of probe beam across plasma and interferometer 152
Figure 74 Overview of phase shift and density retrieved from the measured interference fringes 153
Figure 75 Focal spot image and lineouts along x and y axes 154
Figure 76 Tracking of electron trajectories in electron spectrometer 155
Figure 77 Calibration of electron spectrometer 156
Figure 78 Example of background subtraction from image of scintillator screen in electron spectrometer 157
Figure 79 Electron spectra in electron density scan 159
Figure 80 Peak electron energy in electron density scans compared with experimental results and scaling law 160
Figure 81 Progression of electron beam spectrum and laser potential in optimal shots in density scan 162
Figure 82 Electron spectra in focal position scan 163
Figure 83 Cutoff energy of electron beam against laser's focal position . . 163
Figure 84 Estimated total charge in measured electron beams 165

List of Tables

Table 4.1 Experimental input parameters of LWFAs whose radiation was modelled 91
Table 4.2 Fitted betatron oscillation amplitudes to modelled temporal intensity profiles and mean amplitudes obtained directly from particle tracking data of PIC simulation 98
Table 4.3 Experimentally measured and RCC-modelled FWHM divergence of energy density distributions of radiation beam from each LWFA. . . . 115

Table 5.1 Input parameters and their scales in the Bayesian optimisation algorithm 127
Table 5.2 Starting values, upper and lower bounds of input parameters in Bayesian optimisation of the peak energy 133
Table 5.3 Starting values, upper and lower bounds of input parameters in Bayesian optimisation of total electron beam charge 139

Table A.1 Normalised Parameters used in Laser-Plasma Calculations . . . 200

List of Symbols

Latin Symbols

$\mathbf{A}$	Electromagnetic vector potential
$\mathbf{a}$	Normalised electromagnetic vector potential (see Appendix A.1)
a_t	Threshold normalised laser potential required to ionise an atom or ion
a_0	Peak normalised potential of electromagnetic wave or laser pulse
$\mathbf{B}$	Magnetic field (flux density) vector
$\mathcal{B}$	Peak brightness of radiation beam
c	Speed of light in vacuum
$\mathbf{E}$	Electric field
E	Photon energy
E_c	Critical photon energy in synchrotron spectrum
E_{dph}	Peak energy reached by electrons at their dephasing length
E_L	Total energy of laser pulse
E_{peak}	Peak energy in electron beam
E_{wb}	Electric field of the wavebreaking limit of a plasma wave
e	Charge of an electron
$\mathbf{F_p}$	Ponderomotive force of electromagnetic wave or laser pulse
$\hbar$	Modified Planck's constant
I	Intensity of electromagnetic wave
I_0	Peak intensity of laser pulse
I_t	Threshold laser intensity to ionise an atom or ion
K	Betatron strength parameter or K-parameter of electrons in an insertion device (refers to either parameter depending on context)
k_p	Wavenumber of plasma wave
L_{bunch}	Electron bunch length
L_{dph}	Dephasing length of electrons accelerated in wakefield
L_{pd}	Depletion length of laser driving plasma wave
L_{plasma}	Length of plasma
l_{down}	Down-ramp length at back of gas density profile
l_{up}	Up-ramp length at front of gas density profile

m_e	Rest mass of an electron
N	Number of particles (electrons or photons)
N_{conc}	Concentration of nitrogen dopant, relative to atomic density of helium, used as accelerator medium in this work
N_{osc}	Number of betatron oscillations performed by electron
$\mathbf{n}$	Unit vector of displacement between electron and observer
n_c	Critical plasma electron density
n_e	Electron density of plasma, also called the plasma density
n_{He}	Atomic helium gas density
$\mathbf{P}$	Normalised momentum of charged particle (see Appendix A.1)
P	Power of electromagnetic wave
$P_{\|\|}$	Power of synchrotron radiation emitted due to acceleration component parallel to electron's direction of travel
$P_{\perp}$	Power of synchrotron radiation emitted due to acceleration component perpendicular to electron's direction of travel
P_c	Critical laser pulse power above which laser pulse self-focuses in plasma
$\mathbf{p}$	Momentum of a charged particle
p_{r0}	Initial transverse momentum of electrons just injected into wakefield
Q_{exp}	Total experimentally measured charge in electron beam
Q_{sim}	Total PIC-simulated charge in electron beam
Q_{tot}	Total electron beam charge
$\mathbf{R}(\mathbf{t_{ret}})$	Trajectory of electron relative to origin of a pre-defined coordinate system
$\mathbf{r}$	Displacement vector of electron relative to an observer
r_0	Initial betatron oscillation amplitude of electron just injected into wakefield
$\mathbf{r_p}$	Position of observer relative to origin of a pre-defined coordinate system
r_β	Betatron oscillation amplitude
r_b	Bubble radius of plasma wave in bubble regime
S	Photon fluence spectrum
S_{exp}	Experimentally measured peak spectral fluence
S_{peak}	Peak spectral photon fluence (for general reference)
S_{sim}	RCC-modelled peak spectral fluence
$T(E)$	Transmission ratio of material, as a function of photon energy
t_{obs}	Time of observation of synchrotron radiation from an electron
t_{ret}	Time of emission of radiation from electron, known as retarded time
Δt_{flash}	Duration of radiation flash according to an observer, produced by electron following a (approximately) circular path
Δt_{obs}	Interval in the time of observation of synchrotron radiation
Δt_{ret}	Interval in the retarded time
$\Delta t_{ret,\,PIC}$	Temporal resolution of particle-in-cell simulation

$\Delta t_{2/\gamma}$	Time taken for electron following circular path to travel through an (approximate) arc length covering the angle $2/\gamma$
U	Energy density of electromagnetic radiation
$U_{tot,\,slice}$	Energy density radiated by a slice in the electron beam
$\mathbf{v}$	Velocity of charged particle
$\dot{\mathbf{v}}$	Acceleration of charged particle
v_{drift}	Drift speed of electron in an electromagnetic wave
v_{ph}	Phase velocity of electromagnetic wave or laser pulse
v_g	Group velocity of electromagnetic wave or laser pulse
W	Total energy radiated
w	$1/e^2$ waist of laser pulse, the radial coordinate where intensity falls to $1/e^2$ of its maximum value in the laser
w_0	$1/e^2$ waist of laser at its focal position
z_{focus}	Longitudinal focal position of laser

Greek Symbols

α	Fraction of laser pulse energy inside FWHM of transverse intensity distribution
$\boldsymbol{\beta}$, β	Relativistic velocity factor, relativistic speed factor (see Appendix A.1)
$\dot{\boldsymbol{\beta}}$, $\dot{\beta}$	Rate of change of velocity factor, rate of change of speed factor
γ	Relativistic Lorentz factor
γ_0	Initial Lorentz factor of electron
γ_{max}	Maximum Lorentz factor reached in electron beam
γ_{peak}	Peak Lorentz factor reached by an electron during acceleration
γ_p	Lorentz factor of plasma wave
ϵ_0	Permittivity of free space
η	Refractive index of plasma
θ_e	Angle of divergence of electron trajectory from central axis of propagation
θ_x, θ_y	Divergence angles from z-axis, along x-axis and y-axis
θ_{max}	Maximum angle of divergence of radiation cone produced by relativistic electron emitting synchrotron radiation
λ_β	Spatial period of betatron oscillations
μ_0	Permeability of free space
ξ	Comoving coordinate of charged particle (electron) with respect to electromagnetic wave or laser pulse
ρ	Radius of curvature of curved electron trajectory
τ	Pulse duration (of laser pulse or x-ray pulse)

τ_{FWHM}	FWHM duration of laser pulse
Φ	Normalised scalar potential (see Appendix A.1)
ϕ	Electromagnetic scalar potential
ϕ_e	Polarisation angle of plane of oscillation of an electron
$\phi^{(2)}$	Second-order spectral phase coefficient of laser pulse
$\phi^{(3)}$	Third-order spectral phase coefficient
$\phi^{(4)}$	Fourth-order spectral phase coefficient
ψ	Phase in plasma wave
Ω	Solid angle in radiation spatial distribution
ω	Frequency of electromagnetic wave or laser
ω_0	Central frequency of laser pulse
ω_β	Betatron oscillation frequency
ω_c	Critical frequency of synchrotron radiation spectrum
ω_p	Plasma frequency
$\omega_{p,rel}$	Relativistically-corrected plasma frequency

Acknowledgements

Over the past four years, there have been a number of people who have made it possible for me to complete this project. First, to my supervisor Zulfikar, I would like to thank you for this opportunity. You were always generous with your time and your guidance was always appreciated. I would also like to thank past and present members of Zulfikar's research group, who have been a source of support at various points throughout this project. To the members of the electrons team, thank you for sharing your knowledge of so many details of my project. To the broader group, thank you all for your advice, your professional and at times emotional support.

I would also like to thank my family. To my wife, Lily, thank you for all of your support, kindness and love as you have lived through this with me. Since we met you have made each day brighter. Андрею, Людмиле и Алине, спасибо за вашу доброту и постоянную поддержку Лили и меня. Finally, to Mum, Dad and Emily, thank you for your constant words of encouragement and optimism, forever giving me confidence to keep going and see it through.

1. Introduction

Fundamental to many physical discoveries since their inception, the capabilities of particle accelerators have grown considerably over the last century. The first purpose-built particle accelerator was the "Cockcroft-Walton" generator constructed in 1930 by J.D. Cockcroft and E.T.S. Walton [1]. They were able to accelerate protons through a potential of 300 kV in vacuum [1]. Since the successful demonstration of the Cockroft-Walton generator, much work has gone into increasing the achievable energies in particle accelerators by increasing the accelerating electric field. Modern particle accelerators use radio-frequency (RF) cavities, which are metallic cavities that can support a number of resonant modes [2]. RF cavities can support electric fields of up to 100 MV/m before they start to undergo electrical breakdown [2]. This is a factor of 10^5 greater than the field strengths that were achieved by Cockcroft and Walton.

The present day applications of particle accelerators are wide-ranging. In this work, we focus on the capabilities of electron accelerators. Perhaps the most famous use of particle accelerators is the generation of "bremsstrahlung," first discovered in the late nineteenth century [3]. These are x-rays produced by the collision of electrons with an anode made of a dense material such as tungsten. The electrons are usually accelerated across a potential difference produced by two electrodes to keV-order energies [3]. The radiation produced by the electrons' deceleration is used in a number of areas, for example imaging in medicine and security. Since then, the use of electron accelerators as sources of electromagnetic radiation, or "light," has expanded hugely. Synchrotron light sources are particle accelerators that take advantage of the emission of radiation by electrons following a curved path. The electron beams in synchrotron light sources are multi-GeV or higher. The electrons produce ultraviolet or x-ray beams that are many orders of magnitude brighter than bremsstrahlung [4]. Their radiation beams are used for probing of many material, biological and biomedical samples using a variety of scattering, spectroscopy and imaging techniques [4].

In addition to their uses as bright light sources, electron accelerators also have many applications in medicine. While x-rays and gamma-rays are used in most cases of radiotherapy, electrons beams with energies up to 25 MeV are useful for treating tu-

mours closer to the surface of the skin [5]. There has recently been a proposal to use electron beams with energies between 50 MeV and 250 MeV to deliver high doses deeper into the body [6]–[8], a concept known as very high electron energy (VHEE) radiotherapy. The advantage of electron beams over proton beams is that they are less sensitive to inhomogeneities in density [7], [8]. The concept of VHEE has been demonstrated in both simulation and experiment. VHEE is also a candidate for FLASH radiotherapy, in which the required doses from the accelerated beam would be delivered at higher dose rates [9]–[11]. Pre-clinical data suggests that FLASH radiotherapy spares normal tissue, causing fewer and milder side effects [11], [12]. Potential accelerator layouts for VHEE-FLASH radiotherapy are being investigated [13]–[15].

1.1 Synchrotron Light Sources

The first generation of synchrotron radiation sources were electron storage rings that were built for high energy particle and nuclear physics experiments [4]. Electrons travel in ring-shaped devices: they are accelerated by RF cavities in straight sections and are deflected by dipole magnets around the ring [2], [4]. The advantage of accelerator rings over linear accelerators is that charged particles can be accelerated over many revolutions to higher energies. When deflected by the dipole magnets, the total radiation power emitted by each electron is proportional to the fourth power of the electrons' energy [16]:

$$P = \frac{1}{6\pi\epsilon_0 c^7}\left(\frac{e}{m_e}\right)^2 \frac{(\gamma m_e c^2)^4}{m_e^2 \rho^2}, \tag{1.1}$$

where $\gamma m_e c^2$ is the total energy of the electron and ρ is the bending radius of the dipole magnets. As the electrons are accelerated, their power loss becomes a greater fraction of their total energy. Because electrons have large charge-to-mass ratio, they experience larger energy losses than other charged particles.

The electron energies reached in first generation synchrotron light sources were under or just over 1 GeV [4], [17], producing radiation beams with a high-flux, high polarisation, high collimation and containing photons with energies up to soft x-rays [4]. Compared to bremsstrahlung, first generation of synchrotron light sources have a peak brightness that is several orders of magnitude greater [18]. The brightness of a radiation source is the rate of photons per solid angle in the radiation beam, per unit area of the electron beam, per unit bandwidth [16]. The brightness value cannot be changed using optical techniques such as focusing the radiation beam [16], [17], [19]. While focusing can decrease the size of the radiation beam, it also increases its divergence, thus decreasing the number of photons per solid angle. In the early

1960s, the increased peak brightness of first generation synchrotron light sources attracted interest from the condensed matter community, who used the radiation beams for x-ray absorption spectroscopy and crystallography experiments [17], [20].

Approval for a second generation of synchrotron light sources dedicated to light emission was granted in the mid-1970s [4], [17]. This included the National Synchrotron Light Source at the Brookhaven National Laboratory, USA, the Synchrotron Radiation Source at Daresbury, UK and other facilities in Germany and Japan [17], [20]. These sources were still electron storage rings, but the electron beams in them were accelerated to energies above 1 GeV. For example, the SRS was a 2 GeV storage ring [17]. This was to produce radiation beams that had a higher brightness and contained higher photon energies [17]. The light beams produced at these facilities had a peak brightness between 10^{13} and 10^{16} photons/s/mm^2/mrad^2/0.1% bandwidth (BW) and consisted of photon energies up to hard x-rays [18], [21]. This allowed for more advanced experimental techniques such as the study of electronic structure of surfaces, x-ray absorption fine structure spectroscopy and crystallography experiments of small, unstable samples [17], [20].

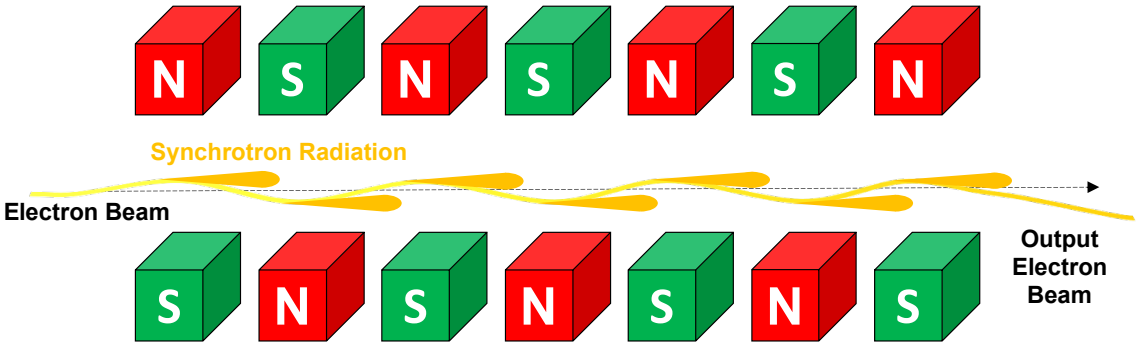


Figure 1: Electron beam oscillating in the periodic magnetic field in an insertion device, emitting synchrotron radiation as it oscillates.

As the demand for increasingly bright synchrotron light sources grew, third generation synchrotron light sources started to be designed and constructed in the 1970s [17], [19], [22]. These devices consist of an array of evenly spaced magnets, usually inserted into the straight sections between the bending magnets in storage rings [17], [19]. For this reason they became known as “insertion devices.” The periodic magnetic field causes the trajectory of an electron beam to oscillate as its passes through the device, as shown in Figure 1. The electrons emit synchrotron radiation as they oscillate, producing a radiation beam propagating in the direction of travel of the electron beam. The first insertion devices were built at the Stanford Synchrotron Radiation Light Source in 1979 [22] and 1981 [23]. However, it was not until 1994 at the European Synchrotron Radiation Facility that one was built whose radiation spectrum

extended up to the photon energies of hard x-rays [24].

Insertion devices can be categorised in two groups: undulators and wigglers. Principally, they are distinguished by the values of their K-parameter, which is a dimensionless parameter proportional to the magnetic field strength of the magnets and the spacing between them. In an undulator, $K \lesssim 1$ and the radiation spectrum is discontinuous, consisting of a number of harmonics with a small bandwidth [2], [25]. The harmonics arise from the constructive interference of the radiation emitted from different periods in the electrons' oscillation [25]. Conversely, in a wiggler, $K \gg 1$ and the radiation spectrum is continuous, like the radiation spectra produced in a dipole bend in a storage ring [2], [25]. For electrons with some energy, the constituent wavelengths of the radiation beam that they produce can be changed by adjusting the magnetic field strength of the magnets [25].

Owing to the increased radiation flux and the reduced area over which the radiation is emitted, insertion devices have a higher peak brightness than earlier synchrotron sources, with values up to 10^{23} photons/s/mm^2/mrad^2/0.1% BW [19]. The improved peak brightness provides an improved spatial resolution and also allows for faster data taking, which is useful for a variety of techniques, including x-ray microscopy, spectroscopy and crystallography [17], [19]. Moreover, the radiation spectrum is tunable by changing the field strength in the magnets [4]. The successful construction of insertion devices opened up the possibility of using their radiation for different areas of research, including atomic and molecular physics, chemistry, surface physics, materials science, microscopy, and life sciences [26].

Fourth generation synchrotron light sources, known as free electron lasers (FELs), were designed to produce radiation beams with even higher peak brightness. FELs comprise an undulator; the radiation spectrum consists of a single harmonic at one wavelength, as explained earlier. Because the electrons oscillate with a small amplitude and travel at nearly the speed of light, the electrons keep up with the synchrotron radiation. The interaction of the electric field of the radiation with the electrons in the bunch produces a train of microbunches that are each separated by a distance equal to the radiation wavelength [27], [28]. Each microbunch effectively becomes a point source, emitting coherent radiation at the same wavelength [29]–[31]. The microbunches continue to oscillate, producing coherent radiation that causes further microbunching while also amplifying the light beam [29]–[31]. The intensity of the radiation from a single microbunch containing N electrons is proportional to N^2 [31].

The output radiation beam from an FEL is high in flux, highly collimated and tem-

porally coherent, producing radiation beams with a peak brightness several orders of magnitude greater than third generation synchrotron light sources. The first x-ray FEL (XFEL) was the Linac Coherent Light Source at the Stanford Linear Accelerator, with a peak brightness of 10^{32} photons/s/mm^2/mrad^2/0.1% BW [32]. Now, XFELs can have a peak brightness up to 10^{35} photons/s/mm^2/mrad^2/0.1% BW [33]. XFELs are used in a variety of fields, including atomic physics, plasma and warm dense matter and condensed matter physics [28], [34]. As they also produce radiation pulses shorter than 100 fs [35], the field of "femtochemistry," probing the molecular dynamics in chemical reactions, has been opened up by these machines [34], [35]. XFELs continue to be built and developed at numerous sites around the world [34].

1.2 Laser Wakefield Acceleration

Laser wakefield accelerators (LWFAs) could be a compact and less expensive alternative to conventional electron accelerators. The basic idea is for an intense, ultrashort laser pulse to drive a wave in a plasma that supports a high electric field that can accelerate electrons, a concept initially proposed by Tajima and Dawson in 1979 [36]. The wakefield supports electric field strengths on the order of 100 GV/m [36], three orders of magnitude greater than the maximum achievable field in RF cavities. At least in principle, an LWFA could accelerate electrons to the same energy as in a conventional accelerator but over one thousandth of the distance. Electrons could be accelerated to GeV-order energies over centimetre scales, rather than in storage rings which are hundreds of metres in circumference.

To drive an LWFA, a laser pulse is focused down to a radius of ~ 10 µm to increase its intensity and also match the scale of the electric field structure that accelerates electrons. The focused laser pulse pushes electrons out of its path. The ions remain stationary as their mass is many times larger. The charge separation between the displaced electrons and stationary ions causes the electrons to move back towards their original positions. As the electrons have some non-zero momentum upon their return, they overshoot and start to oscillate, setting up a wave of electron density, or "plasma wave." The plasma wave has an electric field due to the charge separation, known as the "wakefield." The wakefield can used to accelerate electrons, which can be injected into the wakefield either from the plasma itself or from an external source such as a dopant gas ionised by the laser pulse.

The plasma wave has a characteristic frequency proportional to the square root of the electron number density in the plasma: $\omega_p \propto \sqrt{n_e}$. The front of the pulse pushes electrons forward and the back of the pulse pushes electrons backwards [37]. If the

pulse duration is smaller than or equal to the period of oscillation of the electrons, a resonant excitation of the plasma wave occurs [37]. The forced forward and backward motion of electrons is then synchronised with their natural frequency of oscillation. This produces the largest electron displacements in the plasma wave, and thereby the largest electric field strengths in the wakefield. For example, a plasma with an electron density of 1×10^{19} cm^{-3} has a plasma frequency of 1.78×10^{14} Hz, which corresponds to a period on the order of 10 fs. Hence, a laser pulse with a duration on the order of 10 fs would be required for resonant excitation of the plasma wave.

When the principle of laser wakefield acceleration was first proposed in 1979 [36], laser pulses shorter than 100 fs were not available [37]. As a workaround, a plasma beat-wave accelerator (PBWA) scheme was proposed in 1984 [38]. A PBWA is driven by two laser pulses with different frequencies such that $\omega_1 - \omega_2 = \omega_p$ [38]. The two laser pulses interfere to form a series of "beats" with a duration on the timescale of the period of the plasma wave [38]. A maximum electric field of 1 GV/m was first measured in 1985 [39], and later in 1993 externally injected electrons were accelerated in the PBWA up to 9 MeV, corresponding to an electric field of 0.7 GV/m [40]. The electric field strength was limited to such values because the increase in the relativistic electron mass at larger plasma wave amplitudes produced a decrease in the plasma frequency and shifted the laser beats out of resonance [41].

The limitation of PBWAs was first overcome by self-modulated laser wakefield accelerators (SM-LWFAs), where the plasma wave itself modulates a long laser pulse into smaller pulselets with durations equal to the period of the plasma wave [42], [43]. The first SM-LWFAs were demonstrated experimentally in 1995, accelerating electrons to tens of megaelectronvolts [44], [45]. Electron beams with energies up to 100 MeV were subsequently produced in SM-LWFAs [46]–[49].

By the early 2000s, laser pulses with a duration shorter than 100 fs could be produced and amplified to TW-order power [50]. The main advancement in laser technology that eventually allowed for such laser pulses to be produced was chirped pulse amplification [50]–[53], which was first demonstrated by Strickland and Mourou in 1985 [51]. The timescale of laser pulses shorter than 100 fs is approximately equal to the period of a plasma wave. Laser pulses with TW-order power or higher can be focused to intensities greater than 10^{22} W/m^2. This is sufficient to drive a plasma wave with a large amplitude. In 2004, three groups produced near-monoenergetic electron beams: Mangles *et al.* produced a beam between 50 MeV and 80 MeV with 3% energy spread [54], Faure *et al.* produced a beam of 170 MeV with 24% energy spread [55], and Geddes *et al.* produced ~ 100 pC, low emittance electron beams at ener-

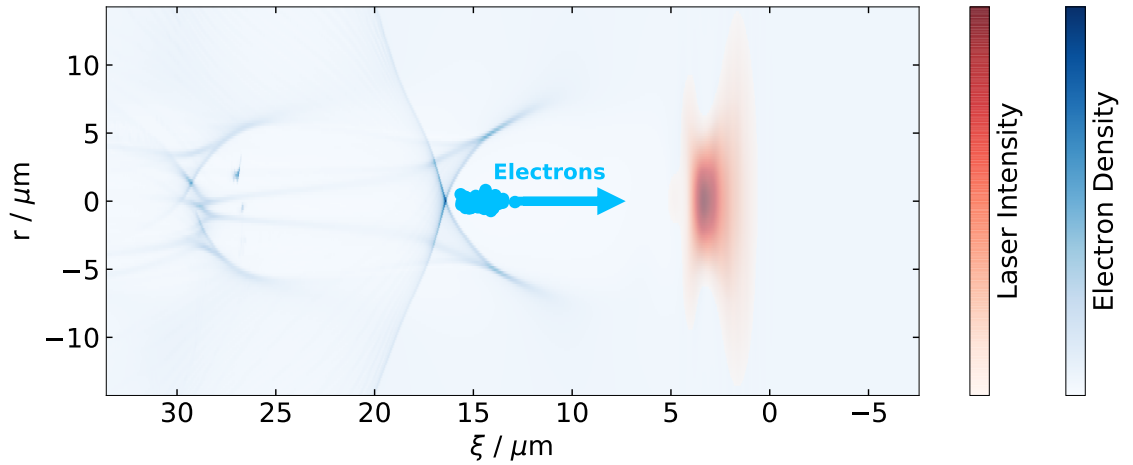


Figure 2: Maps of electron density and laser intensity in a plasma wave in the bubble regime. Electrons are accelerated in the bubble.

gies above 80 MeV with a percent-level energy spread [56]. The obtained energies and acceleration lengths corresponded to acceleration gradients of ~ 100 GeV/m, or electric fields of 100 GV/m. The reduced energy spread was a marked improvement on the continuous, near-100% spread electron spectra produced in SM-LWFAs [54].

Simulations of sub-picosecond, intense laser pulses in plasma performed by Mora and Antonsen in 1996 first demonstrated plasma electron cavitation due to the ponderomotive force of a laser [57]. The so-called "bubble regime" was first studied for the purposes of electron acceleration by Pukhov and Meyer-ter-Vehn in 2002 [58], who performed simulations showing that hundred-megaelectronvolt electron beams with a relatively small energy spread could be produced by focusing joule-level, sub-100 fs laser pulses into plasma. The bubble regime formed the theoretical basis for the acceleration of the aforementioned electron beams in 2004 [54]–[56]. At laser intensities equal to or higher than 2×10^{22} W/m^2, the motion of displaced electrons becomes relativistic and the structure of the plasma wave in the wake of the laser pulse takes the form of a series of "bubbles" of low electron density [58]. In effect, electrons are expelled in the path of the laser pulse, leaving behind a "bubble" devoid of electrons like the one shown in Figure 2. In being expelled by the laser pulse, some of these electrons loop round to the back of the bubble, are trapped and accelerated.

1.2.1 X-ray Beams from LWFAs

In the bubble regime, the wakefield has both a longitudinal and a transverse component. A map of the transverse electric field component of the wakefield is shown in Figure 3. While the longitudinal component accelerates electrons, the transverse component exerts a force on the electrons that moves them towards its central longit-

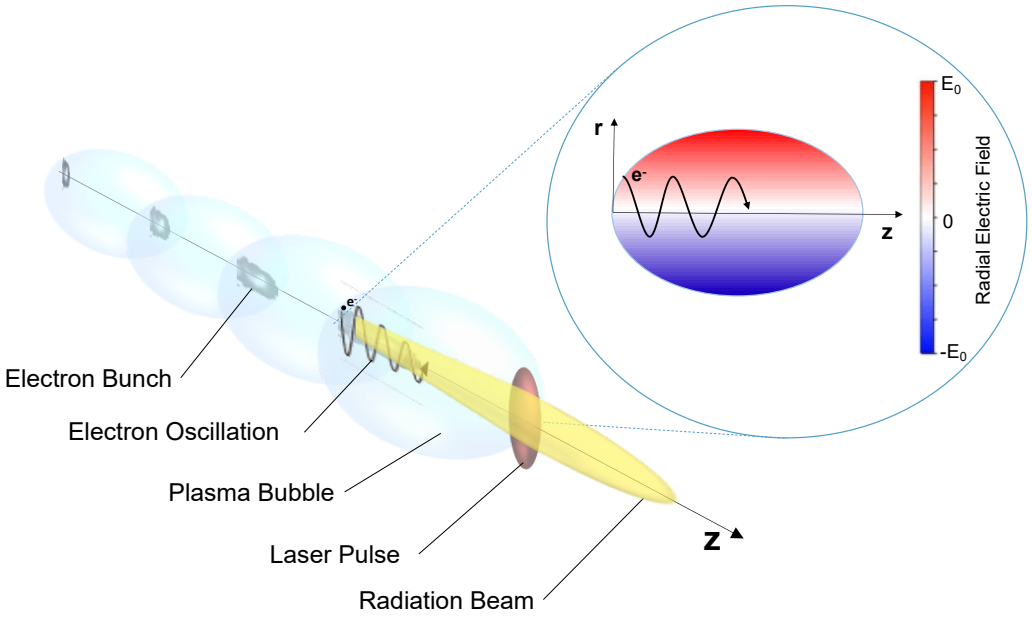


Figure 3: An electron oscillating in the bubble regime in an LWFA and producing a synchrotron radiation beam.

udinal axis, along which the laser pulse and the wakefield propagate. This focusing force is essential for keeping the electrons in the bubble so they can be accelerated over millimetre or centimetre-scale distances. As electrons are often injected slightly off-axis and with some transverse momentum, they overshoot the central axis and begin to oscillate [59]. Similarly to electrons oscillating in an insertion device, the oscillating electrons in the bubble regime emit synchrotron radiation [59]. A radiation beam of this kind was first measured by Rousse *et al.* in 2004 [60]. The radiation had a divergence of 50 mrad and photon energies extending to soft x-rays [60]. The x-ray pulse has a similar ~ 10 fs duration to the electron beam producing it [59]–[63], because the electron beam travels at approximately the same speed as the x-ray beam.

X-ray beams with greater intensity, smaller divergence and higher energy photons have since been produced by LWFAs, due to the availability of lasers with higher power than the 30 TW laser used by Rousse *et al.*. This has enabled electron acceleration to higher energies [59]. The x-ray beams from LWFAs have photon yields of up to 10^{10}, divergences of tens of milliradians and a broadband synchrotron-like spectrum stretching up to hard x-rays and in some cases γ-rays [59], [64]. The amplitudes of oscillation of the electrons producing the radiation are on the micrometre scale [65], [66]. LWFA-based light sources thus have a peak brightness that has been inferred to be in the range of $10^{22} - 10^{23}$ photons/s/mm^2/mrad^2/0.1% BW [59], which is comparable to third generation synchrotron light sources.

For certain applications, the radiation beams from LWFAs are a compact, inexpensive alternative to conventional synchrotron light sources. This micrometre-scale source size and the small x-ray beam divergence have allowed for micrometre-scale biological samples to be imaged using phase contrast imaging [67]–[71]. Tomographies of some of these samples have been made by producing hundreds of phase contrast images at different angles of rotation [70], [71]. The tens of femtosecond duration of these x-ray pulses has also been exploited by imaging ultrafast processes occurring at hundreds of kilometres per second, for example shock waves in high energy density physics [72]. Their broadband spectrum has also been used to perform x-ray absorption spectroscopy [73], [74].

LWFAs thus offer a smaller and less expensive alternative to synchrotron light sources in some areas. X-ray beams are produced in LWFAs over millimetre and centimetre scales, in contrast to conventional wigglers which have lengths of a few metres [19]. A large-scale synchrotron facility costs over £100 million to construct, for example the Diamond light Source in the United Kingdom cost £300 million to build [59], [75]. An LWFA-based light source could cost on the order of £10 million [59].

1.2.2 LWFAs from High Repetition Rate, Few-Cycle Laser Pulses

In the last twenty years, there have been many LWFA experiments using lasers with 10 TW to 1 PW power. These systems deliver laser pulses, and thereby electron beams, with repetition rates lower than 1 Hz (1 pulse per second). The system with the highest repetition rate at these powers is BELLA in Berkeley, USA, with a repetition rate of 1 Hz [76], [77]. Increasing the repetition rates of laser pulses driving LWFAs would be advantageous for a number of reasons [78], [79]. In terms of applications, electron beams delivered at a higher repetition rate would allow for active feedback control to provide more stable electron beams, fast data acquisition, integration and averaging of data over multiple shots to increase signal-to-noise ratio and to potentially generate higher dose rates for radiobiological applications [78], [79].

There have been many experiments where LWFAs have been driven by laser pulses at kHz repetition rates. In the first experiments of this kind, the laser pulse had a duration of tens of femtoseconds and a total energy on the order of 10 mJ, producing a sub-TW power [80]–[85]. The LWFAs driven by these laser pulses produced electron beams with continuous spectra with small peak energies ranging between 100 keV and 3 MeV [80]–[85]. In an experiment by Salehi *et al.* in 2017, the length of the laser pulse was so much longer than the period of the plasma wave at the high plasma

densities they used that electrons were accelerated in a SM-LWFA [83], [86]. However, uses of these kHz electron beams were found in the probing of various materials using electron diffraction [80]–[82].

In the mid to late 2000s, laser systems delivering sub-10 fs duration, multi-TW power pulses at high repetition rates started to be produced [87]–[90]. Laser pulses with such short durations are often referred to as few-cycle, owing to the small number of oscillations in the electromagnetic fields within the short laser pulse duration. With tens of millijoules of total energy giving them multi-TW power, few-cycle laser pulses are capable of driving an LWFA in the bubble regime. The advent of these laser systems was the result of the development of a technique known as optical parametric chirped pulse amplification [87]–[90]. There are now a number of laser systems producing multi-TW few-cycle laser pulses at repetition rates of 10 Hz, with powers ranging up to 20 TW and total energies on the order of 100 mJ [90]–[92].

The first few-cycle laser system used to drive an LWFA was the Light Wave Synthesizer-10, delivering pulses of 50 mJ total energy and 8 fs duration at a repetition rate of 10 Hz. This laser system was used by Schmid *et al.* in 2009 [93]. The LWFA driven by this laser system produced quasi-monoenergetic electron beams with energies up to 25 MeV [93]. Since then, experiments using ~ 10 fs, few-cycle laser systems to drive LWFAs have been sparse. There was one set of experiments using a 60 mJ, 6.6 fs laser pulse, producing electron beams with similar spectra, with peak energies between 20 and 30 MeV [94]. More focus has been placed on the generation of lower energy electron beams with few-mJ, few-cycle laser pulses at kHz repetition rates, which have been more widely available [95]–[98]. Electron beams with energies ranging from 100 keV up to 15 MeV have been produced with these laser systems, ideal for applications such as ultrafast electron diffraction [78], [86], [99]. Single-cycle laser pulses with energies between 1 and 10 mJ have also been used to accelerate electron beams to hundred-keV to MeV-order energies [78], [100], [101].

1.2.3 eSYLOS

The SYLOS laser system at ELI-ALPS, Hungary aims to be one of the first multi-TW, few-cycle systems that operates at a repetition rate of 1 kHz [102]. Currently, the SYLOS laser system is in the second stage of its development, in which the laser system delivers 30 mJ laser pulses with a duration potentially down to 6.6 fs [102]. This laser is known as the SYLOS-2 laser. One of its target applications is the acceleration of electrons in an LWFA at the so-called eSYLOS facility. The first measurement of an electron beam produced by a similar 1 kHz laser system was made recently by

Lazzarini *et al.* at ELI-Beamlines, Czech Republic. 1 pC, 50 MeV electron beams with 25% energy spread were produced in an LWFA driven by a laser pulse with a total energy of 26 mJ and a duration of 15 fs [103]. In simulations of LWFAs driven by similar laser pulses, electron beams reach peak energies of 100 MeV and have total charges of up to 10 pC [104].

The main advantage of using a few-cycle laser pulse is that the conversion efficiency of the laser pulse energy to the total energy in the electron beam is meant to be higher. This is because few-cycle laser pulses have higher power and intensity for a given total energy and also the short laser pulse fits inside the bubble so most of the pulse self-focuses and compresses inside rather than diffracting away at its front [105], [106]. In simulations of LWFAs driven by the SYLOS-3 laser, which is planned to produce 100 mJ, 9 fs FWHM pulses at 1 kHz [107], [108], conversion efficiencies of 27% were obtained [105]. This is a significant improvement on the few-percent conversion efficiencies inferred in previous experiments using laser pulses with joule-level energy and ~ 30 fs duration [105], [109], [110]. Although, more recently, the conversion efficiency of an LWFA driven by a 6 J, 50 fs laser was optimised to 20% [106].

The eSYLOS facility promises to deliver electron beams and radiation beams at kilohertz repetition rates for a variety of applications. Electron beams with tens to hundreds of megaelectronvolt energies can be used for radiation generation. X-ray beams will be produced in LWFAs by the betatron oscillations of the accelerated electrons. X-rays and γ-rays can also be produced when the electrons strike a dense metal target in their path [111]. THz radiation, which covers the infrared and microwave parts of the electromagnetic spectrum, could also be produced either from the laser-plasma interaction or by placing an aluminium foil in the path of the electron beam [111], [112]. The electron beams could also be ideal for VHEE radiotherapy [113]–[115].

1.3 Thesis Outline

The remainder of this thesis is structured as follows. In Chapter 2, we walk through the theoretical background of the generation of laser-driven plasma waves, the acceleration of electrons and the generation of x-ray beams in LWFAs. After this point, the thesis is split into two parts: computation of properties of radiation beams from LWFAs and electron beam optimisation at eSYLOS. The first part is covered in Chapters 3 and 4 and the second part is covered in Chapters 5 and 6.

Radiation computation codes (RCCs) have been built to model the properties of radiation beams produced in simulated LWFAs. In Chapter 3, we describe the com-

putational methods used to model the temporal intensity profiles, the energy density spectra and the angular energy density distributions of the radiation, using electron trajectories and momenta tracked in particle-in-cell (PIC) simulations. In Chapter 4, these radiation computation codes are applied to LWFA-based light source experiments reported in literature, and report on the properties of the modelled radiation.

In the second part of this thesis, electron beams at the eSYLOS facility were optimised in simulations and experiment. In Chapter 5, we first describe the machine learning methods applied to PIC simulations of LWFAs driven by the SYLOS-2 laser and then report the results of optimisations of the peak energy and total charge in the simulated electron beams. In Chapter 6, we describe the experimental methods used to measure and optimise the electron beam properties in LWFAs using the SEA laser, which can deliver 42 mJ, 12 fs pulses at a repetition rate of 10 Hz [102]; this laser system was used due to the unavailability of the SYLOS-2 laser at the time of the experiment. We report on the measured cutoff energies and total charge of the electron beams produced in this experiment, which are the first electron beams generated at the eSYLOS facility.

2. Theoretical Background

In this chapter, we review the relevant theory for the setting up of a wakefield, the acceleration of electrons and the emission of x-ray beams in LWFAs. Most equations of motion for electrons in LWFAs can be derived from the Lagrangian for a relativistic charged particle in an electromagnetic potential. First, a brief overview of the basic principles of Lagrangian mechanics is given. We then move on to describe the dynamics of a laser pulse in plasma and the properties of laser-driven plasma waves. The dynamics of electrons in the wakefield are then described, including their injection, acceleration and oscillation in the wakefield. Finally, we investigate the properties of the radiation beams produced by electrons performing betatron oscillations.

2.1 Lagrangian Mechanics

Lagrangian mechanics will be used to derive many of the equations of motions of electrons in LWFAs. It is beneficial to review the fundamental equations for deriving equations of motion in Lagrangian mechanics. The states of the system being considered are described by a quantity called the Lagrangian, whose integral in time represents the action on the system [116]. The Lagrangian is effectively the function that minimises the action [116]. From the Lagrangian describing the motion of a particle in any arbitrary system, its equations of motion are derived from the Euler-Lagrange set of equations [116]:

$$\frac{d}{dt}\left(\frac{\partial L}{\partial \dot{q}_i}\right) - \frac{\partial L}{\partial q_i} = 0, \tag{2.1}$$

where L is the Lagrangian, i denotes the axis being considered in the chosen coordinate system, q_i is the coordinate of the particle and $\dot{q}_i$ is its time derivative. The derivations of the Euler-Lagrange equation are quite mathematically involved; a derivation is outlined in Goldstein's book, "Classical Mechanics" [116]. The Euler-Lagrange equations show that the rate of change of a generalised momentum, known as the canonical momentum, is equal to some generalised force. The canonical momentum is calculated from the Lagrangian of the system [116]:

$$u_i = \frac{\partial L}{\partial \dot{q}_i}. \tag{2.2}$$

Another useful quantity in Lagrangian mechanics is the Hamiltonian. The Hamiltonian relates to the total energy of the system and is defined in terms of the canonical momentum and the Lagrangian [116]:

$$H = \sum_i u_i \dot{q}_i - L. \tag{2.3}$$

The equations of motion of the particle in the system can also be derived using Hamilton's equations [116]:

$$\dot{q}_i = \frac{\partial H}{\partial p_i}, \tag{2.4}$$

$$\dot{p}_i = -\frac{\partial H}{\partial q_i}, \tag{2.5}$$

where p_i is the kinetic momentum of the particle and $\dot{p}_i$ is its time derivative. While, in an n-dimensional system, the Euler-Lagrange equations produce n second-order differential equations describing the motion of the particle in the system, Hamilton's equations produce $2n$ first-order differential equations.

2.2 Single Charged Particle in an Electromagnetic Wave

The equations of motion for a charged particle in an electromagnetic wave can be derived from the Lagrangian describing a relativistic charged particle in an electromagnetic potential, which will be used to derive a number of different equations of motion for electrons interacting with the laser pulse or its wakefield in plasma. A derivation of this Lagrangian is shown in Appendix B.1 and the result is given by Equation 2.6:

$$L = -\sqrt{1 - \frac{v^2}{c^2}}\, mc^2 + q(\mathbf{v} \cdot \mathbf{A}(t,\, \mathbf{r})) - q\phi(\mathbf{r}), \tag{2.6}$$

where $\mathbf{v}$ is the velocity of the particle, m is its mass, q is its charge, c is the speed of light in vacuum. $\mathbf{A}(t,\, \mathbf{r})$ is a vector electromagnetic potential and $\phi(\mathbf{r})$ is the scalar electromagnetic potential, which depend on time, t, and position, $\mathbf{r}$. In the case of a charged particle interacting with an electromagnetic wave, the potentials are the potentials of the wave, which are oscillating functions of time and space.

2.2.1 Charged Particle in an Electromagnetic Plane Wave

To derive expressions describing the evolution of the laser pulse in the plasma and the formation of plasma waves, it is also important to consider the interaction of a plasma electron with the oscillations in the laser pulse. The interaction of charged particle in a monochromatic electromagnetic plane wave is considered. Two equations of motion

are derived in Appendix B.3 that describe the motion of the particle in the longitudinal direction and the transverse direction:

$$\frac{dr}{d\xi} = a, \tag{2.7}$$

$$\frac{dz}{d\xi} = \frac{a^2}{2}, \tag{2.8}$$

where z is the longitudinal coordinate, r is its transverse coordinate, ξ is a comoving coordinate defined as $\xi = ct - z$ and a is the size of the potential of the electromagnetic wave in normalised units: $a = \frac{qA}{mc}$, which is also defined in Appendix A.1. Another result that comes out of the derivation in Appendix B.3 is $\gamma = 1 + P_z$, with $P_z = \frac{1}{2}a^2$ being the longitudinal momentum of the charged particle in normalised units of $P = \frac{p}{mc^2}$. The relativistic Lorentz factor of the charged particle can thus be related to the normalised potential:

$$\gamma = 1 + \frac{1}{2}a^2. \tag{2.9}$$

This is a useful relation which will be used in later derivations. However, one point that this equation shows is that when $a \gtrsim 1$, the Lorentz factor becomes significantly higher than unity, so the charged particle's motion becomes relativistic.

The normalised vector potential, pointing in the transverse direction, can be written as a function of the comoving coordinate: $a = a(\xi) = a_0 \cos(k\xi)$, where a_0 is the amplitude of the potential and k is the wavenumber. This expression is substituted into Equations 2.7 and 2.8 before integrating with respect to the comoving coordinate, with the initial conditions $z = 0$ and $r = 0$ for $t = 0$. Equations 2.10 and 2.11 are the solutions to the equations of motion of the particle:

$$r = \frac{a_0}{k} \sin(k\xi), \tag{2.10}$$

$$z = \frac{a_0^2}{8k}\Big(2k\xi + \sin(2k\xi)\Big). \tag{2.11}$$

These equations show that the charged particle oscillates in the transverse direction at the same frequency as the electromagnetic wave, and in the longitudinal direction at double this frequency. While the time average of the trigonometric term in Equation 2.11 is zero, the first term shows that the particle has an average motion in the direction of propagation of the plane wave. Differentiating Equation 2.11 with respect to time and taking the time-average produces an expression for the average velocity of the particle, known as the drift velocity:

$$v_{drift} = \frac{c}{\frac{4}{a_0^2} + 1}. \tag{2.12}$$

When $a_0 \gtrsim 1$, the drift velocity becomes relativistic. In a frame of reference moving at this drift velocity along the z-axis, the particle follows a 'figure of eight" motion, which is shown in the left plot of Figure 4. The trajectories of charged particles in three different monochromatic electromagnetic plane waves with $a_0 = 0.5$, 1.0 and 2.0 are shown. In the comoving frame in the left panel of Figure 4, the amplitudes of oscillation in the transverse and longitudinal directions are proportional to the normalised potential and its square, respectively. The trajectory of the particle as viewed in the laboratory frame of reference is shown in the right panel of Figure 4. In this frame, the trajectory has sharp peaks at its turning points.

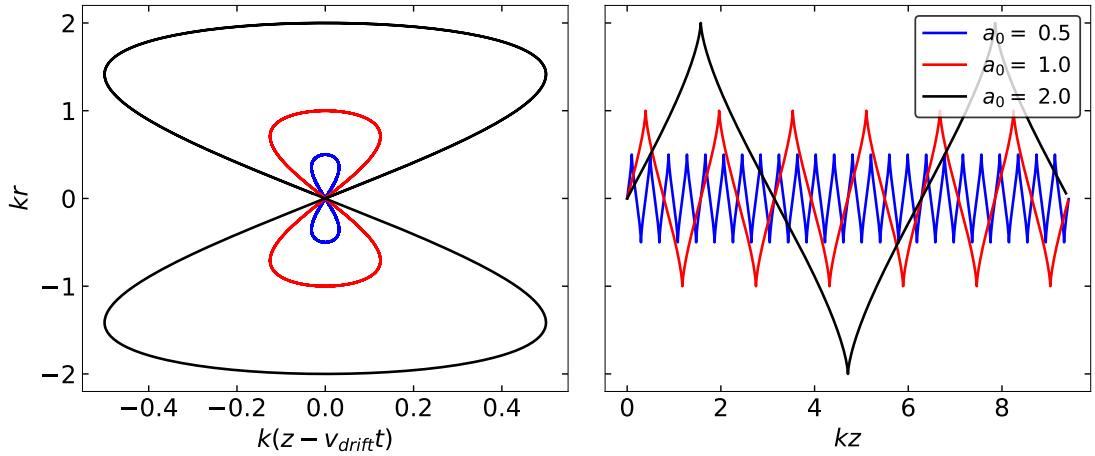


Figure 4: Trajectory of a charged particle in an electromagnetic plane wave as viewed in (left) a frame of reference moving at the drift velocity given by Equation 2.12 and (right) in the laboratory frame.

2.2.2 Ponderomotive Force

The ponderomotive force of a laser pulse repels charged particles away from regions of high intensity. The high-frequency oscillations in the laser pulse potential are neglected. This is of particular importance when the resonant frequency of oscillation of the electrons in a plasma is much smaller than the frequency of the laser pulse. Taking the Lagrangian for a relativistic charged particle in an electromagnetic potential, given by Equation 2.6, an equation of motion for the particle is obtained by applying the Euler-Lagrange equations:

$$\frac{d}{dt}(\mathbf{p} + q\mathbf{A}) = q\nabla(-\phi + \mathbf{v} \cdot \mathbf{A}). \tag{2.13}$$

For simplicity, the quantities in this equation of motion are re-expressed as normalised, dimensionless quantities:

$$\mathbf{P} = \frac{\mathbf{p}}{mc}, \qquad \boldsymbol{\beta} = \frac{\mathbf{v}}{c}, \qquad \Phi = \frac{q\phi}{mc^2}, \qquad \mathbf{a} = \frac{q\mathbf{A}}{mc}. \tag{2.14}$$

These normalised quantities are also defined in Appendix A.1, and are used for the remainder of this section. The equation of motion expressed in terms of these normalised quantities is given by Equation 2.15:

$$\frac{d}{dt}(\mathbf{P} + \mathbf{a}) = c\nabla(-\Phi + \boldsymbol{\beta} \cdot \mathbf{a}). \tag{2.15}$$

The normalised kinetic momentum can be written as the product of the relativistic Lorentz factor and speed factor: $\mathbf{P} = \frac{\gamma \cancel{m} \mathbf{v}}{\cancel{m} c} = \gamma \frac{\mathbf{v}}{c} = \gamma\boldsymbol{\beta}$, where γ is the relativistic Lorentz factor. The normalised canonical momentum is given by $\mathbf{u} = \mathbf{P} + \mathbf{a}$. The equation of motion can be re-expressed in terms of the canonical momentum and the electromagnetic potentials:

$$\frac{d\mathbf{u}}{dt} = -\nabla\Phi + \frac{c}{\gamma}\mathbf{u} \cdot \nabla\mathbf{a} - \frac{c}{\gamma}\nabla\frac{\mathbf{a}^2}{2}. \tag{2.16}$$

This equation of motion describes the general case for a relativistic charged particle in an electromagnetic potential. In the case of an LWFA, the electromagnetic potentials describe a laser pulse and the charged particle is an electron in the plasma. The motion of the ions in the plasma is neglected owing to their significantly larger mass. The ponderomotive force is the time-averaged force on the electron, which is derived in Appendix B.2:

$$\mathbf{F_p} = -\left\langle \frac{c}{\gamma}\nabla\frac{\mathbf{a}^2}{2} \right\rangle, \tag{2.17}$$

where the triangular brackets indicate time-averaged quantities. As $I \propto a^2$, where I is the intensity of the laser, the ponderomotive force pushes charged particles away from regions of high laser intensity. As this equation contains the quantity $\mathbf{a}^2$, the force acts in the same direction for both positively and negatively charged particles.

2.3 Electromagnetic Waves in Plasma

The evolution of a laser pulse in plasma is governed by the wave equation for an electromagnetic wave in plasma. Derived in Appendix C.1, this equation describes the spatial variation and temporal evolution of the fields in the electromagnetic wave:

$$\nabla^2\mathbf{E} = \mu_0\frac{\partial\mathbf{j}}{\partial t} + \frac{1}{c^2}\frac{\partial^2\mathbf{E}}{\partial t^2}, \tag{2.18}$$

where $\mathbf{E}$ is the electric field of the wave and $\mathbf{j}$ is the current density in the plasma. In contrast to the wave equation for an electromagnetic wave in vacuum, Equation 2.18 has an extra term containing the current density, known as the plasma response term. Currents in the plasma are induced by its interaction with the laser pulse, as described in Section 2.2. As will be shown in Section 2.4, this affects the evolution of the structure of the laser pulse.

2.3.1 Dispersion Relation

The dispersion relation for an electromagnetic wave in plasma is derived from its wave equation by considering the electromagnetic wave as a plane wave. This is an approximate description of a laser pulse with $\tau \gg \frac{2\pi}{\omega_0}$ and $w_0 \gg \lambda_0$, where τ is the duration, ω_0 is the angular frequency, w_0 is the transverse width and λ_0 is the wavelength of the wave. The dispersion relation is derived in Appendix C.2. The plasma response term adds an extra term to the dispersion relation for an electromagnetic wave in vacuum:

$$c^2k^2 = \omega^2 - \omega_p^2, \tag{2.19}$$

where k is the wavenumber of the electromagnetic wave, ω is its angular frequency and ω_p is the plasma frequency, which is the natural frequency of oscillation of an electron displaced from a position of equilibrium in plasma. The plasma frequency is given by Equation 2.20:

$$\omega_p = \sqrt{\frac{e^2 n_e}{m_e \epsilon_0}}, \tag{2.20}$$

where n_e is the number density of electrons in the plasma, usually called the "plasma density". This equation is derived in Appendix C.3. When $\omega^2 < \omega_p^2$, the right-hand side of Equation 2.19 becomes negative and as such the wavenumber becomes an imaginary number. The solution to the wave equation becomes $\mathbf{E} \propto \mathbf{E_0} e^{-kz}$. The electric field of the electromagnetic wave decreases exponentially with distance into the plasma. The electromagnetic wave thus does not travel in the plasma. By setting the right-hand side of the dispersion relation to zero and substituting Equation 2.20, a parameter known as the critical plasma density can be derived:

$$n_c = \frac{\omega^2 m_e \epsilon_0}{e^2}. \tag{2.21}$$

This is the maximum electron density for the electromagnetic wave to propagate in the plasma. A plasma with an electron density under this threshold is said to be "underdense", meaning that an electromagnetic wave with some frequency, ω, can propagate through it. It is these plasmas that are of interest for producing LWFAs, since they produce a travelling solution to the wave equation.

The phase velocity and the group velocity of the wave, defined by the relations $v_{ph} = \frac{\omega}{k}$ and $v_g = \frac{\partial \omega}{\partial k}$ respectively, are derived from the dispersion relation:

$$v_{ph} = c\left(1 - \frac{\omega_p^2}{\omega^2}\right)^{-\frac{1}{2}}, \tag{2.22}$$

$$v_g = c\left(1 - \frac{\omega_p^2}{\omega^2}\right)^{\frac{1}{2}}. \tag{2.23}$$

When $\omega \gg \omega_p$, $v_p > c$ but $v_g < c$, so a laser pulse in plasma propagates slower than the speed of light in vacuum.

2.3.2 Refractive Index of Plasma

The refractive index of the plasma is the ratio of the speed of light in vacuum to the phase velocity of the electromagnetic wave:

$$\eta = \sqrt{1 - \frac{\omega_p^2}{\omega^2}}. \tag{2.24}$$

This expression is valid when electrons displaced by the electromagnetic wave in the plasma move at subrelativistic speeds. For relativistic electron motion, the natural frequency of oscillation is modified by their Lorentz factor, due to their relativistic mass increase. This modifies the plasma frequency:

$$\omega_{p,rel} = \sqrt{\frac{n_e e^2}{\langle\gamma\rangle m_e \epsilon_0}}. \tag{2.25}$$

Derived when considering a single charged particle in an electromagnetic wave, Equation 2.9 can be used to relate the Lorentz factor of the electrons to the intensity of the electromagnetic wave. Equation 2.9 is substituted into the expression for the refractive index of the plasma. Expanding that expression in a Taylor series, as performed in Appendix C.4, produces Equation 2.26:

$$\eta \approx 1 - \frac{1}{2}\frac{\omega_p^2}{\omega^2}\left(1 - \frac{a_0^2}{4}\right). \tag{2.26}$$

Because of the Taylor expansion, this equation is only valid for laser pulses with $a_0 \leq 1$, where the electron motion is only weakly relativistic. The refractive index approaches unity as the normalised potential is increased.

2.4 Laser Pulse Evolution in Plasma

As a laser pulse drives a plasma wave in an LWFA, spatial gradients in the plasma density and laser intensity produce gradients in the refractive index of the plasma. As shall be shown, a longitudinal gradient in the refractive index within the laser pulse produces gradients in its phase velocity and group velocity. This causes the laser pulse to compress and its wavefronts to bunch or separate. A transverse gradient in the refractive index produces a gradient in the phase velocity across the wavefronts, causing them to bend and the laser pulse to self-focus in the plasma.

2.4.1 Perturbations to the Refractive Index

The refractive index of the plasma is also altered by perturbations in the electron density or the laser frequency, and as such often has some spatial variation. The expression for the refractive index in a plasma experiencing small perturbations in the electron density and the frequency of the electromagnetic wave is derived in Appendix C.4 and given by Equation 2.27:

$$\eta \approx 1 - \frac{1}{2}\frac{\omega_{p,0}^2}{\omega_0^2}\left(1 + \frac{\delta n_e}{n_{e,0}} - 2\frac{\delta\omega}{\omega_0} - \frac{a_0^2}{4}\right), \tag{2.27}$$

where $\frac{\delta n_e}{n_e} \ll 1$, $\frac{\delta\omega}{\omega} \ll 1$ and $a_0 \leq 1$. This is applicable to situations where the electron density is non-homogeneous and where the electromagnetic wave has a non-homogeneous, non-constant frequency, for example in a plasma disturbed by the ponderomotive force of a laser pulse.

2.4.2 Pulse Compression

A gradient in the refractive index across the length of the laser pulse produces a gradient in its group velocity. Considering two points at different comoving coordinates in the laser pulse, like those shown in Figure 5, the group velocity is different at each of these points. After a small time interval, the laser pulse propagates some distance and the separation of the points changes by a small amount:

$$\Delta L = (v_{g,\,2} - v_{g,\,1})\Delta t, \tag{2.28}$$

where ΔL is the change in separation of the two points over the time interval, Δt, and $v_{g,\,1}$ and $v_{g,\,1}$ are the group velocities at the two points in the laser pulse. The change in the points' separation can be re-expressed in terms of the longitudinal gradient in group velocity: $\Delta L = L\frac{\partial v_g}{\partial z}\Delta t = -L\frac{\partial v_g}{\partial \xi}\Delta t$, where $\xi = ct - z$. Using the relation between the group velocity and refractive index, $v_g = c\eta$, the rate of hange of the

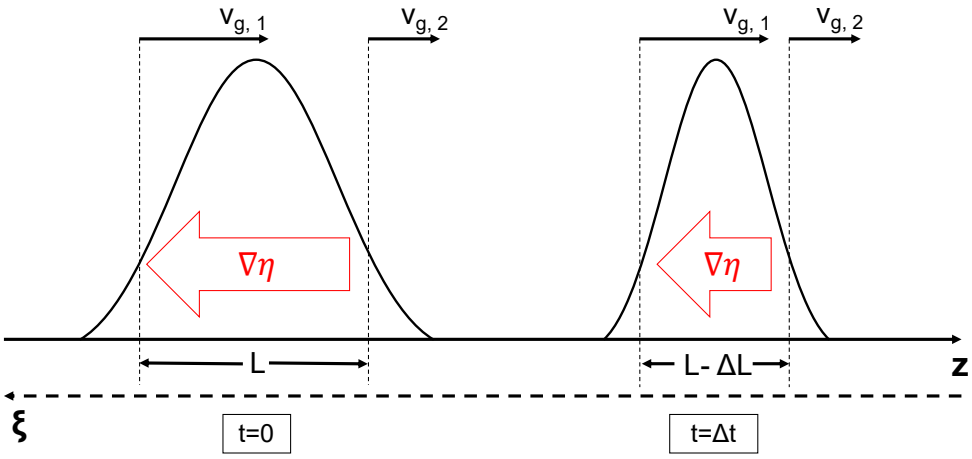


Figure 5: Compression of a laser pulse in plasma due to a positive refractive index gradient with respect to ξ, the comoving coordinate. The red arrow points in the direction of increasing refractive index. The laser pulse is propagating in the positive z-direction, to the right of the page.

pulse length can be expressed in terms of the longitudinal gradient in refractive index. Considering an infinitesimal time interval, $\Delta t \to 0$, the rate of change of separation of the two points can be expressed by a differential equation:

$$\frac{\partial L}{\partial t} = -Lc\frac{\partial \eta}{\partial \xi}. \tag{2.29}$$

Equation 2.29 shows that a positive longitudinal gradient in the refractive index with respect to the comoving coordinate causes the pulse to compress as it travels through the plasma. In Figure 5, there is a positive gradient with respect to the comoving coordinate, where the refractive index increases along the red arrow, from the front to the back of the laser pulse travelling to the right of the page. After a time interval, Δt, the pulse becomes shorter. Conversely, a negative gradient in refractive index would cause the laser pulse to elongate. In an LWFA, the laser pulse compresses as the front of the laser pulse pushes electrons out of its path. In the bulk of the laser pulse behind the front, there is a negative gradient in electron density: $\frac{\partial n_e}{\partial \xi} < 0$ so $\frac{\partial \eta}{\partial \xi} > 0$, causing the laser pulse to compress.

2.4.3 Photon Acceleration

A longitudinal gradient in refractive index that is comoving with the laser pulse causes the phase velocity to change over the length of the laser pulse. Two consecutive wavefronts in the laser pulse are considered, like the two on the left diagram in Figure 6. Their initial separation is equal to the initial wavelength of the laser: $z_1 - z_2 = \lambda_0$, where z_1 and z_2 are the longitudinal positions of the wavefronts and λ_0 is the initial wavelength. A comoving gradient in refractive index between these wavefronts gives

them different phase velocities, which are labelled in Figure 6. After some time interval, the wavefronts move different distances to new longitudinal coordinates.

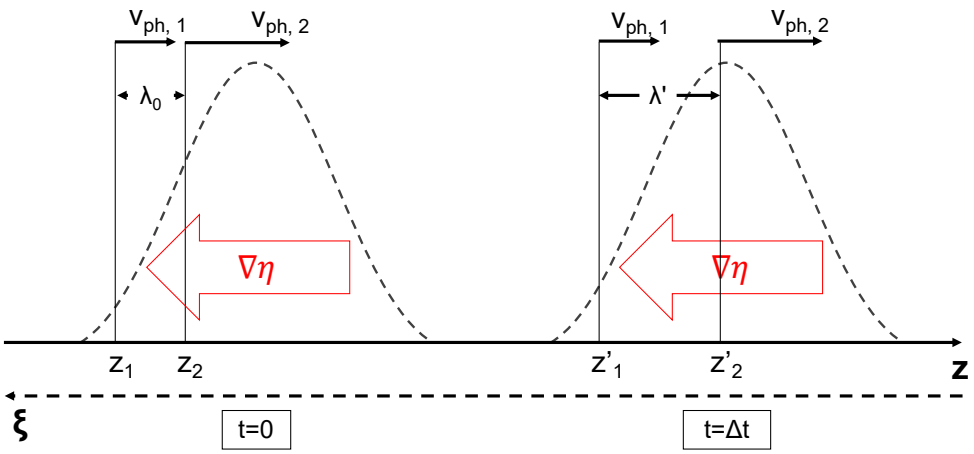


Figure 6: Overview of stretching between wavefronts in a laser pulse due to a positive refractive index gradient with respect to ξ, the comoving coordinate. The laser pulse is propagating in the positive z-direction, to the right of the page.

In Figure 6, there is a positive refractive index gradient in the laser pulse with respect to the comoving coordinate. This means that the phase velocity of the leading wavefront is larger than for the trailing wavefront. The diagram on the right shows that after some time interval, Δt, their separation has increased. The new wavelength, λ', is the distance between the wavefronts' new positions, which is related to the difference in their phase velocities:

$$z_2' - z_1' = \lambda_0 + (v_{ph,2} - v_{ph,1})\Delta t, \tag{2.30}$$

where z_2' and z_1' are the new positions of the wavefronts and $v_{ph,2}$ and $v_{ph,1}$ are their phase velocities. Equation 2.30 demonstrates that a longitudinal gradient in the refractive index of the plasma changes the wavelengths in the laser pulse, depending on the longitudinal position of the wavefronts in the laser pulse. In Appendix C.5, the rate of change of frequency in the laser pulse is related to the comoving gradient in refractive index of the plasma:

$$\frac{1}{\omega}\frac{\partial \omega}{\partial t} = -\frac{c}{\eta^2}\frac{\partial \eta}{\partial \xi}. \tag{2.31}$$

A negative gradient in the refractive index with respect to the comoving coordinate, $\frac{\partial \eta}{\partial \xi} < 0$, causes the frequency of the laser pulse to increase over time. This process is known as photon acceleration, named after the change in energy of laser photons.

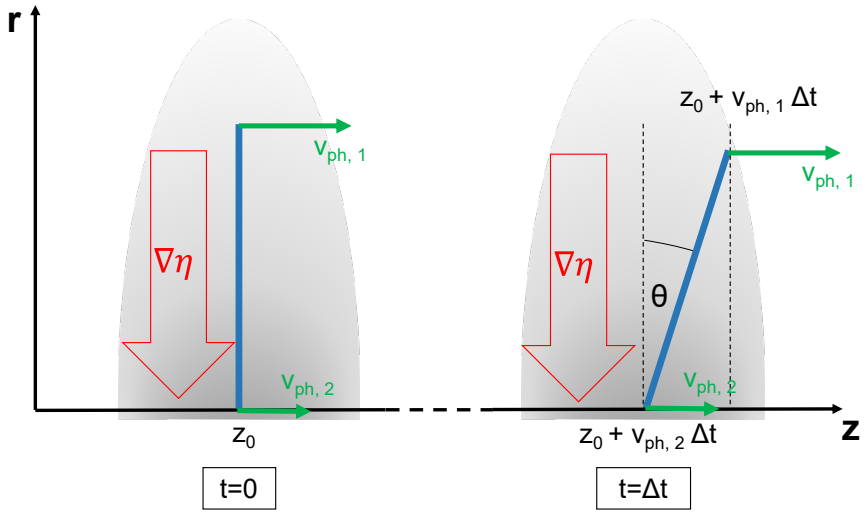


Figure 7: Forward bending of wavefronts in a laser pulse due to a negative transverse gradient in refractive index in the plasma.

2.4.4 Self-Focusing

A gradient in refractive index transverse to the laser's propagation direction produces a gradient in the phase velocity across the pulse. This gradient runs parallel to the surface of a flat wavefront in the laser. Two points on an initially flat wavefront in the laser pulse are considered: one at the centre of the pulse and one at the edge of the pulse. After a short time interval, these points in the same wavefront move different distances in the laser's direction of travel. The angle between a straight line connecting the two points and the transverse axis, shown in Figure 7, is the "bending" angle between the points. For sufficiently short time intervals, the bending angle is small. The small angle approximation can be used to equate the bending angle to the difference in phase velocities between the two points:

$$\tan\theta \approx \theta = (v_{ph,\,1} - v_{ph,\,2})\frac{\Delta t}{w}, \tag{2.32}$$

where θ is the bending angle, $v_{ph,\,1}$ and $v_{ph,\,2}$ are the phase velocities at each of the points in Figure 7 and w is the distance between them. For a sufficiently small laser pulse width and phase velocity difference, the angle can be written in terms of the phase velocity gradient with respect to r. As $\Delta t \to 0$,

$$\frac{\partial\theta}{\partial t} = \frac{\partial v_{ph}}{\partial r}. \tag{2.33}$$

A transverse gradient in the refractive index of the plasma causes the wavefront to bend. As the wavefront bends, the direction of energy propagation gains a radial component. This is because the direction of energy propagation is always perpendicular to the wavefront. When the laser pulse travels faster at its edges than at the

centre, energy is directed towards the central axis in the direction of propagation of the laser pulse. This is the case in Figure 7, where there is a negative transverse gradient in refractive index.

Derived in Appendix C.6, the acceleration in the width of the laser pulse is governed by Equation 2.34:

$$\frac{\partial^2 w}{\partial t^2} = \frac{c^2}{\eta^2}\frac{\partial \eta}{\partial r}. \tag{2.34}$$

The second derivative of the pulse width with respect to time can be seen as an "acceleration" of the pulse width, describing the focusing force of the plasma on the laser pulse. The second derivative of the pulse width with respect to time is hereon referred to as the pulse width acceleration. Recalling Equation 2.26 for the nonlinear refractive index in terms of the normalised potential of the laser pulse, and expanding in a Taylor series up to its first-order term,

$$\frac{\partial^2 w}{\partial t^2} \approx \frac{c^2\omega_p^2}{8\omega^2}\frac{\partial a^2}{\partial r}. \tag{2.35}$$

This equation assumes that perturbations to the plasma density, which affect the refractive index according to Equation 2.27, are negligible. Equation 2.35 shows that negative gradients in the laser intensity produce a negative "acceleration" in the laser pulse width. One example is a Gaussian laser beam, whose intensity falls away from its centre. If the laser starts travelling as a collimated beam in the plasma, it will start to self-focus, increasing its intensity in the process.

Self-Focusing Threshold for a Gaussian Laser Pulse

The pulse width only decreases when the self-focusing is stronger than the natural diffraction of the laser pulse. The condition for this is determined by finding the point where the self-focusing of a laser pulse in plasma is balanced by its natural diffraction after its focal position. This condition is derived in Appendix C.6.1 for a Gaussian laser pulse by equating the pulse width accelerations of each of these effects, which produces the following condition:

$$a_0^2 w_0^2 = \frac{32c^2}{\omega_p^2}, \tag{2.36}$$

where a_0 is the normalised potential of the laser pulse and w_0 is the distance from the beam centre where the laser intensity at its focal point falls to $1/e^2$ of its peak value at its centre, known as the beam waist. Because the quantity $a_0^2 w_0^2$ is proportional to the intensity of the laser pulse multiplied by the area that it covers, we can derive a

threshold power for the laser pulse to self-focus in a plasma [117]:

$$P_c = 17.4 \frac{\omega_0^2}{\omega_p^2} \quad \text{[GW]}, \tag{2.37}$$

where ω_0 is the central frequency in the spectrum of the Gaussian laser pulse. Equation 2.37 is the critical power for self-focusing, above which the laser pulse self-focuses in the plasma. The condition for the laser pulse to self-focus depends on its power rather than intensity. This is because a laser pulse focused to smaller waist sizes and thereby higher intensities will experience a larger focusing force from the plasma, but an equally large defocusing force due to the larger divergence angle of the incoming beam.

2.5 Laser-Driven Plasma Waves

In an LWFA, the ponderomotive force of the laser pulse pushes electrons out of its path. The displaced electrons experience an electrostatic restoring force that causes them to move back towards their initial equilibrium positions. The electrons overshoot and start to oscillate. This produces a wave in electron density, which is the plasma wave. The structure of the plasma wave depends primarily on the intensity profile of the driving laser pulse. It is shown that plasma waves governed by linear wave equations are driven by low-intensity laser pulses and nonlinear plasma waves are driven by high-intensity laser pulses. The solutions to their wave equations are discussed.

The wave equation for a linear plasma wave can be derived by considering perturbations to the electron density, the electrons' velocities and the electric fields when electrons are perturbed by small distances from their equilibrium positions. The derivation is performed in Appendix C.7; the wave equation for a linear plasma wave is given by Equation 2.38:

$$\left(\frac{\partial^2}{\partial \xi^2} + k_p^2\right)\Phi = \frac{k_p^2}{2}a^2, \tag{2.38}$$

where k_p is the wavenumber of the plasma wave. This equation applies when $a_0 \ll 1$, and hence $n_1 \ll n_0$, where n_1 is the perturbed electron density and n_0 is the initial electron density in the plasma. The plasma wave is driven by the potential of the laser pulse. Taking the spatial derivative of this expression produces an expression for the electric field in the plasma wave. The driving term in this equation is proportional to the ponderomotive force of the laser pulse, where $F_p \propto \nabla a^2$ as given by Equation 2.17. Equation 2.38 is in the form of an inhomogeneous Helmholtz equation, which

can be solved with the Green's functions [118], [119]:

$$\Phi = k_p \int_0^{\xi} \sin\left(k_p(\xi - \xi')\right) \frac{a^2}{2}\, d\xi'. \tag{2.39}$$

The scalar potential, the electric field and the electron density perturbation in the plasma wave follow a sinusoidal function of space and time behind the laser pulse.

When electrons are displaced by distances greater than the plasma skin depth, $1/k_p$, layers of electrons in the plasma begin to overlap and the linear plasma wave structure begins to break down. Electron displacements of this size produce electric fields greater than the wave breaking limit, which is the electric field produced by the charge separation of electrons displaced by the skin depth [120]:

$$E_{wb} = \frac{m_e c \omega_p}{e}. \tag{2.40}$$

This equation can be derived using Gauss' law, by integrating the charge density over the plasma skin depth in the plasma. Evaluating the constants and substituting Equation 2.20, Equation 2.40 equates to $E_{wb} = 96\sqrt{n_e\,[\text{cm}^{-3}]}$ GV/m. The electric field at the wave breaking limit depends only on the electron density of the plasma.

Equations for one-dimensional, nonlinear plasma waves have been derived in a number of ways [121]–[124]. The wave equation is a second order, nonlinear, inhomogeneous differential equation [121]–[123]:

$$\frac{\partial^2 \Phi}{\partial \xi^2} = \gamma_p^2 k_p^2 \left(\beta_p \left[1 - \frac{1 + a^2}{\gamma_p^2 (1 + \Phi)^2} \right]^{-\frac{1}{2}} - 1 \right), \tag{2.41}$$

where γ_p is the relativistic Lorentz factor of the plasma wave, β_p is its speed factor and k_p is its wavenumber. The Lorentz factor of the plasma wave relates to its phase velocity, equal to the group velocity of the laser pulse that drives it: $\gamma_p = 1/\sqrt{1 - v_g^2/c^2}$. As $v_g = \eta c$, this parameter can be related to the refractive index of the plasma by $\gamma_p = 1/\sqrt{1 - \eta^2}$. Substituting Equation 2.24 for the refractive index of the plasma,

$$\gamma_p = \frac{\omega_0}{\omega_p}, \tag{2.42}$$

or $\gamma_p = \sqrt{n_c/n_e}$. When the displaced electrons travel at ultrarelativistic speeds, such that $\beta_p \to 1$ and $\gamma_p \gg 1$, a simpler wave equation for a one-dimensional nonlinear plasma wave can be derived [125], [126]:

$$\frac{\partial^2 \Phi}{\partial \xi^2} = \frac{k_p^2}{2} \left(\frac{1 + a^2}{1 + \Phi^2} - 1 \right). \tag{2.43}$$

The assumption made in this derivation is that the laser pulse duration must be greater than the period of the central frequency of the laser pulse [126]: $\tau \gg 2\pi/\omega_0$. Equations 2.41 and 2.43 generally do not have analytical solutions and must be solved numerically [121]–[123], [125], [126].

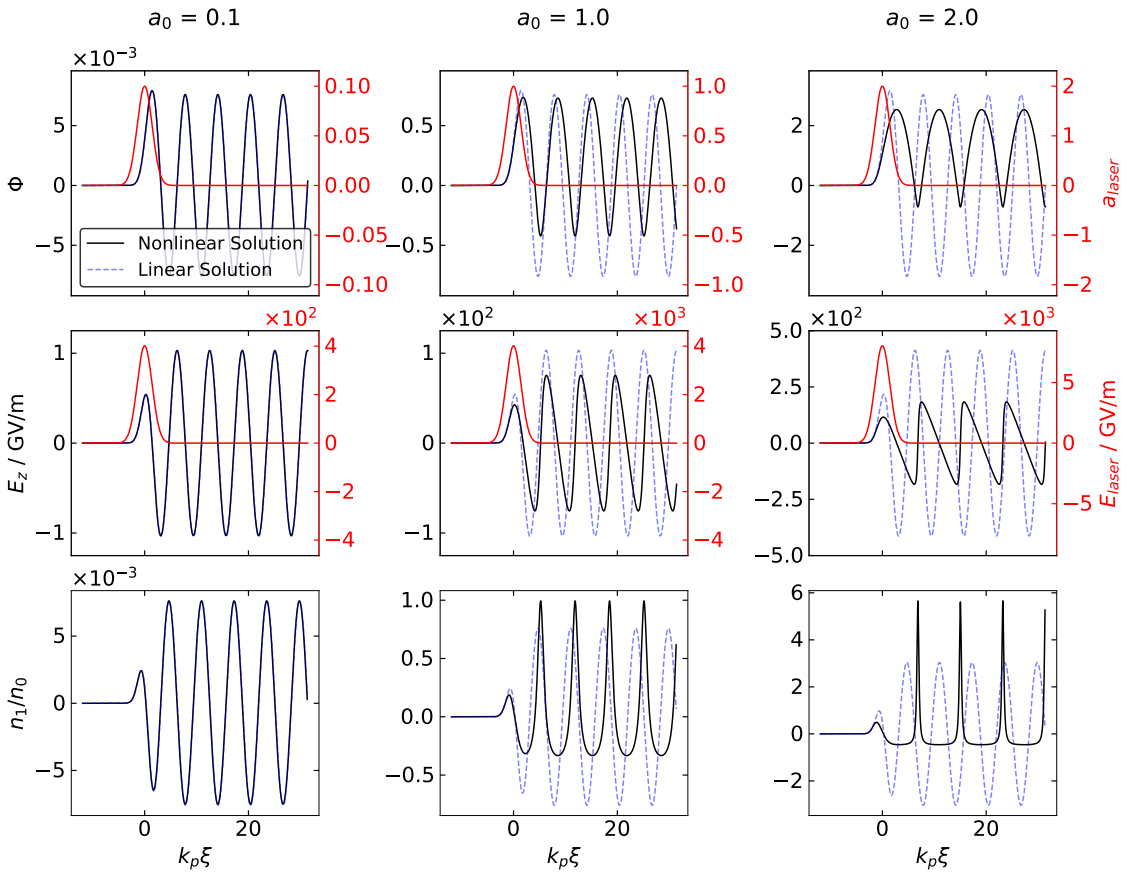


Figure 8: Nonlinear (black) and linear (blue) solutions for the scalar potential (top row), electric field (middle row) and electron density perturbation (bottom row) of a plasma wave driven by Gaussian laser pulses with normalised potentials of 0.1 (left column), 1.0 (middle column) and 2.0 (right column). (Red) Envelopes of the (top row) normalised potential and (middle row) electric field of laser pulses.

Figure 8 shows numerical solutions to Equation 2.41 for different Gaussian laser pulses driving the plasma wave. Each laser pulse has a FWHM duration of 30 fs, which is a typical pulse duration, chosen so that $\tau_{FWHM} < 2\pi c/\omega_p$ for resonant excitation of the plasma wave. Each solution has been computed assuming that $\Phi = 0$ at the front of the laser pulse at $\xi = -2\tau_{FWHM}c$, where τ_{FWHM} is the FWHM duration of the laser pulse. In each column in Figure 8, the driving laser pulse has one of $a_0 = 0.1$, 1.0 or 2.0. The corresponding solution to the linear wave equation, given by Equation 2.38, is also plotted as the dashed blue line in each plot.

As $a_0 \to 1$, the linear solution is no longer sufficient to describe the plasma wave.

The spatial period of the plasma wave becomes longer, as shown in the middle and right columns of Figure 8. As a_0 increases, the potential of the plasma wave becomes more parabolic. The electric field becomes a sawtooth-like function of the comoving coordinate. When $a_0 = 2$, the amplitude of the electric field is greater than the wave breaking limit, which in this case is equal to 140 GV/m for a plasma density of 2×10^{18} cm^{-3}. The amplitudes of the electric fields are on the order of 100 GV/m, three orders of magnitude greater than the electric fields produced in state-of-the-art conventional RF particle accelerators. The electric field increases linearly from the back to the front of each spatial period in the wave. The electron density is sharply peaked at the back of each spatial period, with regions of approximately constant electron density of $n_1/n_0 = c/(c - v_z)$ in between, where n_0 is the initial electron density in the plasma. Derived in Appendix C.8, this places a lower limit on the electron density in the plasma wave of $n_1/n_0 = -1/2$, in any regions where $v_z = -c$.

2.6 The Bubble Regime

The bubble regime refers to three-dimensional nonlinear plasma wave generation driven by a laser pulse with a normalised potential greater than 1 and a duration shorter than $\lambda_p = 2\pi/k_p$. In three dimensions, electrons can be expelled transversely by the laser pulse. The ponderomotive force of the laser pulse is chiefly responsible for the formation of a nonlinear plasma wave, as this force acts over the longest timescale compared to the oscillation of the electromagnetic fields of the laser and the wakefield, proportional to $1/\omega_0$ and $1/\omega_p$ respectively. In the bubble regime, a series of ion cavities, or "bubbles", is produced behind the laser pulse as electrons have been expelled by the ponderomotive force. Behind each ion cavity is a narrow sheath of electrons where the majority of the trajectories of the expelled electrons overlap [127], [128]. The electron density in the sheath is at least an order of magnitude higher than in the cavity.

An analytical description of the highly nonlinear plasma wave structure in the bubble regime was derived by Lu *et al.* in 2006 [127]. The result is a second order, nonlinear differential equation describing the outermost radial coordinate of the ion cavity in terms of the comoving coordinate. The equation contains many terms, but can be simplified for cases when the thickness of the electron sheath is much smaller than the radius of the cavity:

$$r_b \frac{d^2 r_b}{d\xi^2} + 2\left(\frac{dr_b}{d\xi}\right)^2 + 1 = -\frac{d|a|^2}{dr}\frac{1}{\left(1 + \frac{\beta r_b^2}{4}\right)^2}, \tag{2.44}$$

where r_b is the outermost radial coordinate of the cavity, $\beta \approx \ln(1 + \frac{\Delta}{r_b})^2 - 1$ and Δ is the thickness of the electron sheath [127], [128]. The term on the right-hand side of Equation 2.44 is the driving term. Comparing this term to Equation 2.17, the driving term is proportional to the ponderomotive force of the laser pulse. At the back of the ion cavity where $\frac{d|a|^2}{dr} \approx 0$, the driving term vanishes:

$$r_b \frac{d^2 r_b}{d\xi^2} + 2\left(\frac{dr_b}{d\xi}\right)^2 + 1 = 0. \tag{2.45}$$

This equation is very similar to the differential equation describing a sphere. By writing the equation for a sphere as $r_b^2 + \xi^2 = R^2$, where $r_b^2 = x^2 + y^2$ and R is the bubble radius, a similar differential equation to Equation 2.45 is obtained by finding the implicit double derivative. The only difference is that there is no factor of two in the first-order differential's term like there is in Equation 2.45.

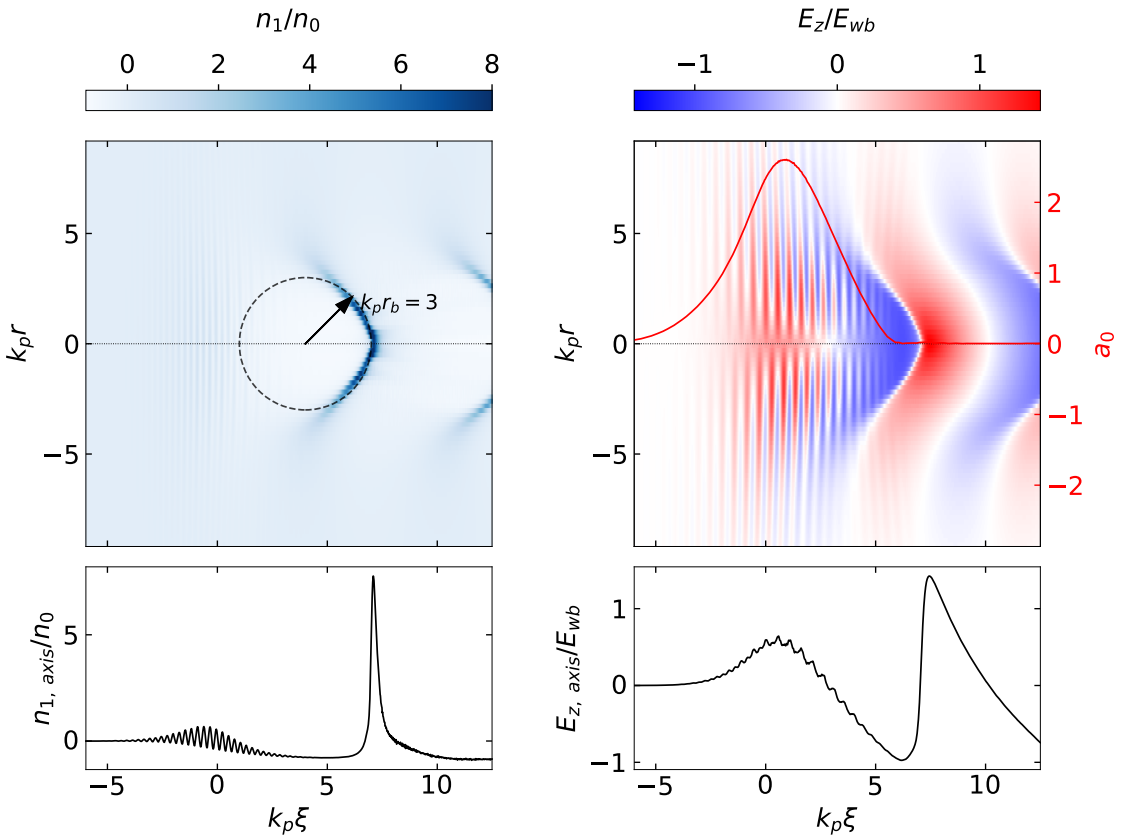


Figure 9: Electron density (left) and longitudinal electric field (right) inside the plasma in the bubble regime simulated using the PIC code, Smilei. Their values along the central longitudinal axis at $k_p r = 0$ are plotted in the bottom panels.

The geometry of the ion cavity in an LWFA can be examined in three-dimensional PIC simulations, an example of which is shown in Figure 9, on the next page. The laser pulse driving the plasma wave has $a_0 = 2.3$, producing a plasma wave in the bubble

regime. The top left plot is a map of the electron density in the plasma. As predicted by Equation 2.45, the ion cavity takes on a spherical shape at its rear. In the top left plot, the black dashed circle fit to the first bubble behind the laser pulse has a radius of $r_b = 3/k_p$. The bubble radius is related to the normalised potential of the laser pulse and the plasma density by a condition for the laser pulse to be guided in the plasma with an almost constant beam waist. This condition can be estimated by balancing the ponderomotive force of the laser pulse with the electric field inside the bubble [127], [129], which produces a proportionality: $k_p r_b \propto \sqrt{a_0}$. A more refined condition was produced by Lu *et al.* in 2007 by comparing the bubble radius with the plasma density and the normalised potential of the laser pulse in PIC simulations [129]. This scaling law contains the same proportionality:

$$k_p r_b = 2\sqrt{a_0}. \tag{2.46}$$

In the example PIC simulation in Figure 9, $k_p r_b = 2\sqrt{2.3} = 3.0$, as shown by the black dashed circle. Along the central axis, the electron density follows the same sharply peaked profile as predicted by Equation 2.41. This can be seen by comparing the bottom left plot of Figure 9 with the bottom right plot of Figure 8. In three dimensions, the sharp peak in electron density is the on-axis density profile of the electron sheath.

The top right plot of Figure 9 is a map of the longitudinal electric field component of the same plasma wave. The normalised potential of the laser pulse along the central longitudinal axis is plotted in red. This map shows that the structure of the ion cavity deviates from a spherical shape at the front where the laser fields and potential are stronger. The longitudinal electric field component along the central longitudinal axis is plotted in the bottom right plot of Figure 9. Similarly to the one-dimensional nonlinear solution shown in the middle right plot of Figure 8, the longitudinal electric field increases linearly from the back to the front of the ion cavity.

2.7 Injection of Electrons into the Wakefield

For an electron to be accelerated in a plasma wave, it must first be trapped in an accelerating phase in the wakefield. While there are a number of possible injection mechanisms, the main mechanisms of interest in this work are self-injection and ionisation injection. Overviews of both of these injection mechanisms are given.

2.7.1 Self-Injection

In the bubble regime, background electrons in the plasma can become trapped in the wakefield. For this to occur, the trajectories of different displaced electrons need

to overlap in some way such that some electrons arrive at the back of the bubble with sufficient longitudinal momentum to keep up with the bubble, which travels with a phase velocity equal to the group velocity of the laser pulse in the plasma. A number of conditions for self-injection to occur have been derived. A trapping condition was first produced by Kostyukov *et al.* in 2004 [130] by numerically integrating Hamilton's equations for an electron in the laser field. This was later supported by Kostyukov and Nerush in 2009, who derived an analytical relation in a similar form [131]:

$$\frac{\gamma_p c}{\omega_p r_b} \lesssim \frac{1}{\sqrt{2}}. \tag{2.47}$$

By taking the bubble radius given by Equation 2.46, the condition can be rewritten in terms of the normalised potential of the laser pulse: $a_0 \gtrsim \gamma_p^2/2$. As noted by Thomas in 2010 [61], this condition requires the normalised potential to be abnormally large at low plasma densities. Thomas derived a less conservative trapping condition by assuming that displaced electrons follow elliptical trajectories [61]. An electron is said to be trapped if the distance that the electron slips back relative to the bubble is smaller than the bubble's radius, producing the following trapping condition [61]:

$$\frac{c\sqrt{\ln\left(2\gamma_p^2\right) - 1}}{\omega_p r_b} \lesssim \frac{1}{\sqrt{2}}. \tag{2.48}$$

Again, substituting Equation 2.46 into this condition produces the trapping condition in terms of the normalised potential of the laser pulse: $a_0 \gtrsim \ln\left(2\gamma_p^2\right) - 1$. In Figure 10, the threshold normalised potentials in the conditions of Kostykov and Thomas are compared at a range of plasma densities. At all densities, Kostukov's condition requires significantly higher normalised potentials than Thomas. At low plasma densities, Kostyukov's condition requires $a_0 \gtrsim 100$, whereas Thomas' condition requires $a_0 \gtrsim 10$. The threshold potentials of the two potentials become comparable as $n_e/n_c \to 0.1$. For example, for $n_e/n_c = 0.1$, Thomas' trapping condition becomes $a_0 \gtrsim 2.0$ and Kostyukov's condition produces $a_0 \gtrsim 4.9$.

Mangles *et al.* in 2012 [132] took Thomas' trapping condition and applied pre-existing scaling laws for the laser pulse properties in plasma. They initially produced a threshold for the energy and duration of a Gaussian laser pulse focused in a plasma with some electron density [132]:

$$\alpha E > \frac{\pi \epsilon_0 m_e^2 c^5}{e^2} \left[\ln\left(\frac{2n_c}{3n_e}\right) - 1 \right]^3 \frac{n_c}{n_e}\, \tau(l), \tag{2.49}$$

where E is the energy of the laser pulse, α is the fraction of the total energy within the FWHM of the Gaussian laser pulse and $\tau(l)$ is the duration of the laser pulse as

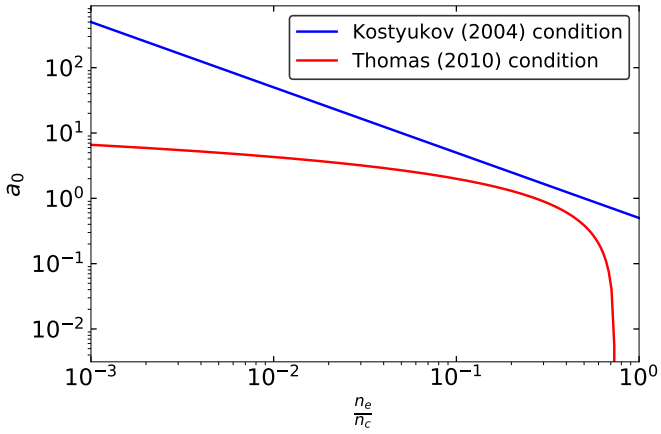


Figure 10: Threshold normalised potentials required by conditions derived by (blue) Kostyukov and (red) Thomas.

a function of the propagation distance in the plasma. For the case where the laser pulse energy depletes completely in the plasma, a trapping condition in terms of the power of the laser pulse was produced [132]:

$$\frac{\alpha P}{P_c} > \frac{1}{16}\left[\ln\left(\frac{2n_c}{3n_e}\right) - 1\right]^3, \tag{2.50}$$

where P_c is the critical power for the laser pulse to self-focus in the plasma, given by Equation 2.37. For a laser pulse with a total energy of 0.7 J and a duration of 40 fs, good agreement was found between the measured threshold electron density and the threshold density given by Equation 2.50. Threshold electron densities between 1×10^{18} cm^{-3} and 3×10^{18} cm^{-3} were found for $\alpha = 0.1$ to 0.4 [132].

It was shown by Kalmykov *et al.* in 2009 [133] that self-injection is also caused by the expansion of the bubble. This theory also explains the idea behind the density down-ramp injection mechanism [134]–[136], as the bubble expands through regions of decreasing electron density. In a frame of reference comoving with the bubble, they considered the change in the Hamiltonian of a displaced electron in the plasma due to an increase in the bubble radius, which was assumed to be linear in time [133], [137]. By relating the change in the Hamiltonian to the rate of bubble expansion, a trapping condition was derived [133], [137]:

$$\Delta H = \epsilon R_{in} \int \frac{\partial H}{\partial R} \frac{d\xi}{v_g - v_z} < -1, \tag{2.51}$$

where ϵ is the bubble expansion rate, R_{in} is the bubble radius at the point of injection, ΔH is the change in the Hamiltonian of the electron in the comoving frame, R is the bubble radius and v_z is the longitudinal velocity of the electron. As normally $v_z > v_g$,

this condition shows that the for self-injection to take place $\epsilon > 0$ and should be above some threshold determined by the dynamics of the electron being considered. The slippage time is another important factor determining whether the electron becomes trapped, which is the duration of the interaction between the electron and the bubble potential, given by $T_{slip} = \int d\xi/(v_g - v_z)$ [133], [137]. While this trapping condition is analytically complex and is analysed by numerically integrating trajectories of electrons displaced by the laser pulse, it was found that a small number of electrons are self-injected when this condition is satisfied [133], [137]. PIC simulations of lasers of 1-2 PW in plasmas with densities on the order of 10^{17} cm^{-3} were used to demonstrate this self-injection during periods of rapid bubble expansion [133], [137], [138].

2.7.2 Ionisation Injection

An alternative injection mechanism that offers some control over the injection threshold is ionisation injection. In ionisation injection, the accelerator medium is a low Z (atomic number) gas such as helium, which the laser pulse ionises as it travels through. The accelerator medium is doped with a low, typically $0.1 - 10$% concentration of high Z gas such as nitrogen [139]–[143]. In regions where the laser intensity is high enough, typically around the centre of the laser pulse, K-shell electrons in the high Z gas are ionised and can be injected in the wakefield [139], [140].

For electrons from the high Z species to become trapped in the wakefield, they must be ionised at a particular phase in the plasma wave. If they are ionised at earlier phases, the ionised electrons acquire a potential that is too large and thus stream back through the wakefield. A trapping condition accounting for these considerations was derived by Chen *et al.* in 2012 [144]. The condition requires that the Hamiltonian of the ionised electron be smaller than the Hamiltonian of some electron following a closed orbit in phase space inside the bubble. Expressed in terms of the properties of the plasma wave and laser pulse,

$$1 - \Phi(\psi_{ion}) \leq \frac{\sqrt{1 + a_\perp^2(\psi_{ion})}}{\gamma_p} - \Phi_{min}, \tag{2.52}$$

where Φ is the potential of the plasma wave, Φ_{min} is the minimum potential, ψ_{ion} is the phase in the wakefield where the electron is released from its molecule, atom or ion and $a_\perp$ is the transverse component of the vector potential of the laser.

However, the phase in the plasma wave at which the above condition is satisfied also needs to coincide with the front half of the laser pulse, where, assuming that the laser pulse intensity peaks at its centre, the laser pulse is most likely to ionise the high

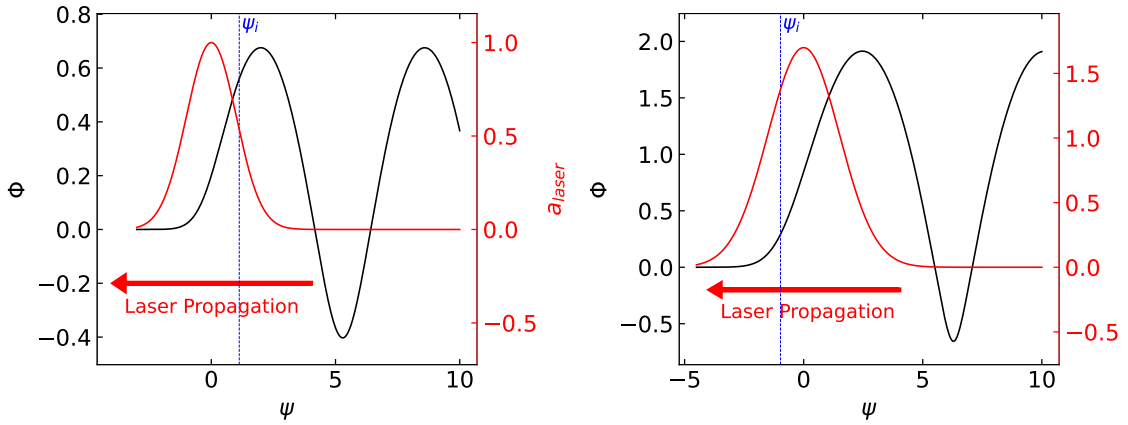


Figure 11: Normalised scalar potential of plasma wave (black) and normalised potential of laser pulse (red) plotted against phase in plasma wave. ψ_i (dashed blue line), the earliest phase satisfying the condition given by Equation 2.52, is marked on these plots for two different cases: (left) when $a_0 = 1.7$, $k_p\sigma_z = 1.5$ and $\psi_i < 0$, and (right) $a_0 = 1.0$, $k_p\sigma_z = 1.0$ and $\psi_i > 0$.

Z atoms. We consider the earliest phase in the plasma wave satisfying the above trapping condition, denoted as ψ_i. If ψ_i coincides with the back of the laser pulse, then electrons would have been ionised by the front of the laser pulse, which lies at even earlier phases that do not satisfy the above trapping condition. They will not be trapped in the wakefield. The left panel of Figure 11 shows one such example, where the laser pulse potential is plotted in red and the potential of the plasma wave is plotted in black against the phase of the plasma wave. ψ_i is plotted as the vertical blue dashed line, which coincides with the back of the laser pulse. By contrast, an example where the earliest phase satisfying Equation 2.52 is shown on the right panel of Figure 11. ψ_i is earlier in the plasma wave and coincides with the front of the laser pulse. In this case, trapping the electrons is possible.

In Figure 11, ψ_i was changed to a more advantageous position by adjusting both the peak potential and the duration of the laser pulse, which are included in the caption of Figure 11. In Figure 12, ψ_i is plotted against the peak potential of the laser pulse for lasers with six different pulse durations. $\psi = 0$ is the phase where the peak of the laser pulse lies, with the front of the laser pulse at $\psi < 0$. Increasing the peak potential of the laser pulse moves ψ_i earlier in the plasma wave, pushing it towards the front of the laser pulse. This is due to the general increase in the right hand side of Equation 2.52, which contains a term containing $a_\perp$ but also the term $-\Phi_{min}$ becomes smaller. ψ_i is pushed to the phases of smaller potentials at the front of the plasma wave. Figures 11 and 12 also show that increasing the length of the laser pulse is also a method of making $\psi_i < 0$. While a longer laser pulse drives the plasma wave out of resonance, and thus at a lower amplitude, the plasma wave is effectively shifted

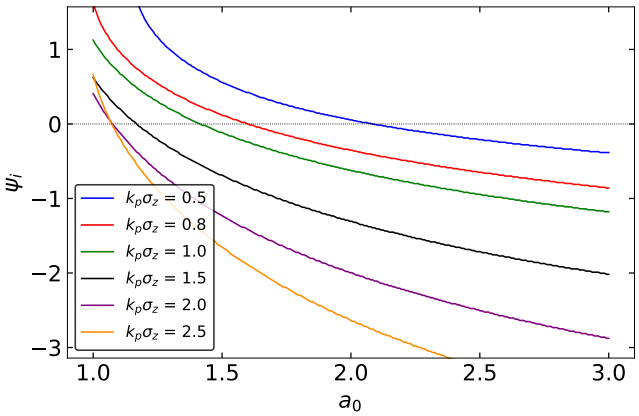


Figure 12: Peak normalised potential of a Gaussian laser pulse against phase required for electrons from a high Z species to be ionised and trapped, plotted for different laser pulse lengths at an electron density of 2×10^{18} cm^{-3}.

in phase, which turns out to be advantageous for trapping K-shell electrons.

Threshold Laser Intensity for Ionisation

Another factor to consider in the ionisation injection mechanism is the intensity of the laser pulse required to release the K-shell electrons in the high Z species. By modelling the potential barrier binding the electron in an ion, atom or a molecule as a Coulomb barrier in one dimension, a threshold intensity to release the electron from a binding potential can be estimated [145]:

$$I_t = \frac{\pi^2 \epsilon_0^3 c}{2e^6} \frac{E_{ion}}{Z^2}, \tag{2.53}$$

where E_{ion} is the ionisation energy of an ion with a charge of $Z-1$. Equating the intensity to the normalised potential of the laser pulse, $a = e\sqrt{\frac{1}{2}c\epsilon_0 I_t}/\omega m_e c$, a threshold potential can be estimated:

$$a_t \approx 0.29\, Z^{-2}\, \lambda\,[\mu\text{m}]\; E_{ion}\,[\text{eV}]. \tag{2.54}$$

As an example, the ionisation energy required to produce N^{7+} is 552 eV [146]. According to Equation 2.54, the laser pulse needs to have $a_0 \geq 2.7$. At laser potentials that are lower but still comparable, the binding potential is lowered and there is some probability of the electron tunnelling through the potential [147], [148].

2.8 Electron Acceleration in the Bubble Regime

Electrons injected into the wakefield are accelerated by the longitudinal electric field component of the wakefield. When electrons are accelerated to $\gamma m_e c^2 \gtrsim 10$ MeV, they are said to be ultrarelativistic and travel at approximately the speed of light. Meanwhile, the wakefield moves in the same direction with a velocity equal to the group velocity of the laser pulse in the plasma. As $v_g < c$, the ultrarelativistic electron advances in phase in the wakefield.

The energy progression of an electron in the bubble regime is derived in Appendix D.1, by calculating the work done by the electric field as the electron advances in phase in the bubble. The variation of the longitudinal electric field along the z-axis can be derived using Gauss' law by assuming that the bubble is a spherical cavity with a constant charge density of $\rho = n_e e$, so $E_z = (e n_e/\epsilon_0)\,\xi$. Assuming that a non-evolving electric field structure in the bubble, an electron injected at the back of the bubble is found to follow a quadratic relation in time:

$$E(t) = \gamma_p m_e c^2 + m_e \omega_p^2 c^2 \bigg(-\frac{1}{4\gamma_p^2} t^2 + \frac{r_b}{c} t \bigg). \tag{2.55}$$

In this model, the electron eventually reaches a maximum energy at the centre of the bubble, where the longitudinal electric field component is zero. The electron then enters a region in the bubble where this electric field component changes direction, decelerating the electron. This process is known as dephasing. The peak energy reached by the electron due to dephasing can be found by locating the vertex of this quadratic function of time: $E_{dph} = \gamma_p m_e c^2 + m_e \omega_p^2 \gamma_p^2 r_b^2$ at $t = 2\gamma_p^2 r_b/c$. Using Equation 2.46 for the radius of the bubble, the maximum energy of the electron due to dephasing can be written in terms of the normalised potential of the laser pulse. Neglecting the initial energy of the electron upon injection,

$$E_{dph} \approx 4\gamma_p^2 m_e c^2 a_0. \tag{2.56}$$

As $\gamma_p^2 = n_c/n_e$, Equation 2.56 shows that decreasing the plasma electron density and increasing the laser intensity increases the peak energy reached by electrons in an LWFA in the bubble regime. That is, assuming that the length of the plasma is sufficient to accommodate the electrons reaching their peak energy and that the laser pulse does not deplete before this occurs. Moreover, Equation 2.56 was derived assuming no evolution in the wakefield structure nor its phase velocity. In the next section, it is shown that the peak energy of the electron is modified by a slowing of the phase velocity of the wakefield due to the evolution of the laser pulse [129].

2.9 Limits of Electron Acceleration

As described in Section 2.8, dephasing is the process of an electron accelerated in the wakefield reaching a phase where $E_z = 0$ in the wakefield and then decelerating, as the electron travels at a greater speed than the phase velocity of the wakefield. The distance in the plasma over which an electron reaches $E_z = 0$ in the wakefield is known as the dephasing length. The phase velocity of the wakefield is given by the group velocity of the laser pulse, given by $v_g = \eta c$. If the electron travels at approximately the speed of light in vacuum,

$$L_{dph} = \frac{\Delta\xi}{1-\eta}, \tag{2.57}$$

where $\Delta\xi$ is the comoving distance between the comoving coordinate where the electron is injected and where $E_z = 0$. It is assumed that the acceleration starts at the position in the wakefield where the longitudinal electric field is most negative, as in the case of self-injection where electrons are injected at the back of the bubble. An electron dephases after traversing half of the spatial period of the plasma wave. In the bubble regime, the electric field follows a sawtooth-like function like the one shown in Figure 9; the electron dephases after traversing the bubble radius, given by Equation 2.46. Approximating $v_g/c = \eta \approx (1 - \frac{1}{2}\omega_p^2/\omega_0^2)$, which applies when $a_0 \lesssim 1$ [129],

$$L_{dph} = \begin{cases} \frac{1}{2}\gamma_p^2\lambda_p, & \text{1D linear} \\ \frac{4}{3}\gamma_p^2 k_p^{-1}\sqrt{a_0}, & \text{3D nonlinear} \end{cases} \tag{2.58}$$

By comparing the dephasing length in the 3D nonlinear case with the location of the vertex of Equation 2.55 at $ct = 2\gamma_p^2 r_b = 4\gamma_p^2 c/\omega_p\sqrt{a_0}$, it an be seen that a factor of $2/3$ has been introduced. This factor was introduced by Lu *et al.* in 2007 [129] and accounts for the slowing of the phase velocity of the wakefield due to etching of the front of the laser pulse as it travels through the plasma. By integrating the wakefield in each case from $z = 0$ to $z = L_{dph}$, in a similar way to the derivation performed in Appendix D.1, the peak energy reached by an electron accelerated in the wakefield can be expressed:

$$E_{dph} = \begin{cases} 2\gamma_p^2 m_e c^2, & \text{1D linear} \\ \frac{2}{3}a_0\gamma_p^2 m_e c^2, & \text{3D nonlinear} \end{cases} \tag{2.59}$$

This is the peak energy reached by electrons provided that the length of the LWFA is longer than the dephasing length. By comparing Equation 2.59 in the 3D nonlinear case to Equation 2.56, the peak energy is decreased by a factor of $1/6$ when considering the slowing of the phase velocity of the wakefield.

Another factor limiting the energy gained by an electron accelerated in the wakefield is the loss of energy of the laser pulse to the plasma wave, often referred to as pump depletion. The pump depletion length is the distance that laser pulse travels in the plasma before its energy is depleted. In a one-dimensional, linear plasma wave, the pump depletion length can be calculated by equating the energy densities of the initial laser pulse and the plasma wave at the pump depletion length. Decker *et al.* in 1996 [149] showed that the laser depletes locally and that the front of the laser pulse is etched at a speed of $v_{etch} = c\omega_p^2/\omega_0^2$. This was verified in two-dimensional PIC simulations [149], and later in three-dimensional PIC simulations by Lu *et al.* in 2007 [129]. In the bubble regime in three dimensions, an expression for the pump depletion length was produced [129]. The results for both the one-dimensional linear case and the three-dimensional nonlinear case are summarised in Equation 2.60 [129], [149]:

$$L_{pd} = \begin{cases} \frac{\gamma_p^2}{a_0^2}\lambda_p, & \text{1D Linear} \\ \gamma_p^2 c\tau_{FWHM}, & \text{3D Nonlinear} \end{cases} \tag{2.60}$$

The ratio of the depletion length and the pump depletion length for the 3D nonlinear case is given by $L_{dph}/L_{pd} = (4/3)\sqrt{a_0}/(k_p c\tau_{FWHM})$. If this ratio is greater than unity, the LWFA is dephasing-limited; otherwise it is depletion-limited. If the length of the laser pulse is $c\tau_{FWHM} \approx k_p^{-1}$, the ratio becomes $L_{dph}/L_{pd} = (4/3)\sqrt{a_0}$. As $a_0 > 1$ in a nonlinear plasma wave, $L_{dph}/L_{pd} > 1$ if this condition is satisfied.

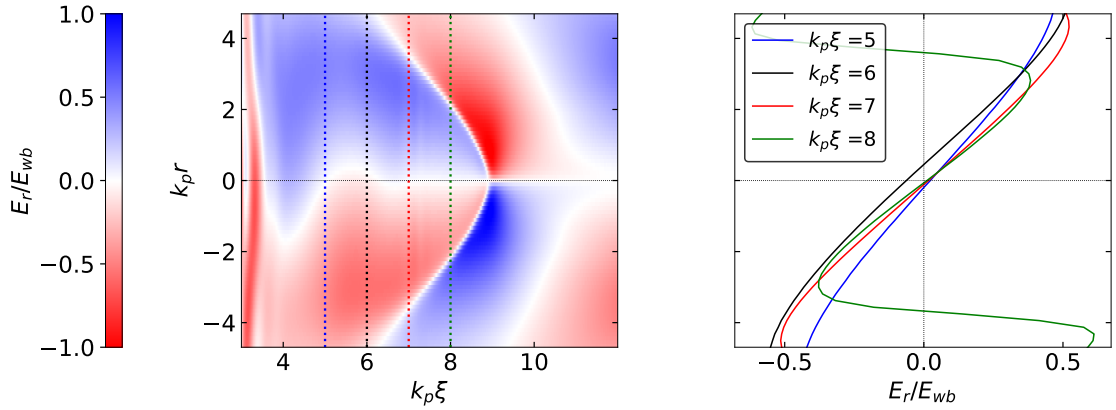


Figure 13: (Left) Map of transverse electric field in the bubble regime. (Right) Along different transverse axes in the map, shown in the left plot, the transverse electric field of the electric field is plotted.

2.10 Betatron Oscillations

In the bubble regime, an injected electron encounters not only a longitudinal electric field but also a transverse component. While the longitudinal component gives the electron a greater total energy, the transverse component produces a focusing force on the electron towards the central longitudinal axis of the bubble. On the left panel of Figure 13, the transverse electric field in a PIC simulation of the bubble regime is mapped, showing that the transverse electric field in the bubble increases in magnitude away from the central longitudinal axis at $r = 0$, where the transverse field is approximately zero. The transverse electric field is plotted along different transverse axes in the bubble in the right panel, which are indicated by the coloured lines on the left. The right panel shows that all along the bubble, the magnitude of the transverse electric field component increases linearly away from the central axis where it is zero.

2.10.1 Electron Trajectory at Constant Energy

An electron with a constant total energy experiences a strong transverse force directed towards the central longitudinal axis in the bubble. An equation of motion of the electron in terms of its transverse coordinate can be derived from the Lagrangian for a relativistic charged particle in an electromagnetic potential, which is outlined in Appendix D.3. The equation of motion describes a particle performing simple harmonic oscillations about the central longitudinal axis in the bubble:

$$\frac{d^2r}{dt^2} = -\frac{\omega_p^2}{2\gamma}r. \tag{2.61}$$

The frequency of the oscillations is called the betatron frequency. In the case of an electron with constant energy, and thereby a constant Lorentz factor, the betatron frequency is constant in a plasma with constant density:

$$\omega_\beta = \frac{\omega_p}{\sqrt{2\gamma}}. \tag{2.62}$$

The solution to the simple harmonic equation of motion is a sinusoidal function of time with some amplitude:

$$r(t) = r_\beta \cos(\omega_\beta t), \tag{2.63}$$

where r_β is the amplitude of oscillation. The transverse component of the velocity factor of the electron is found by differentiating this solution with respect to time and dividing it by the speed of light:

$$\beta_r(t) = -\frac{r_\beta \omega_\beta}{c} \sin(\omega_\beta t). \tag{2.64}$$

As the energy of the electron is constant, and so is its total speed factor, the longitudinal velocity factor must be perturbed by small amounts by the periodically varying transverse velocity. Making the approximation $\beta_z(t) = \sqrt{\beta^2 - \beta_r(t)^2} \approx \beta(1 - \frac{1}{2}\beta_r(t)^2)$,

$$\beta_z(t) = \beta\left(1 - \frac{\omega_\beta^2 r_\beta^2}{4c^2}\right) + \beta\frac{\omega_\beta^2 r_\beta^2}{4c^2} \cos(2\omega_\beta t). \tag{2.65}$$

An expression for the longitudinal coordinate of the oscillating electron is then derived by integrating the longitudinal speed factor component with respect to time:

$$z(t) = \beta\left(1 - \frac{\omega_\beta^2 r_\beta^2}{4c^2}\right)ct + \beta\frac{\omega_\beta r_\beta^2}{8c} \sin(2\omega_\beta t), \tag{2.66}$$

where the constant of integration has been set to zero such that $z = 0$ when $t = 0$. In Equations 2.65 and 2.66, the first term represents the drift motion of the electron as it travels through the plasma. The drift velocity is the average velocity of the electron in the plasma. The second terms are the perturbations in the drift motion due to the transverse oscillations. As $\gamma \to \infty$, $\omega_\beta \to 0$ so the size of these perturbations becomes zero and $\beta_z = 1$. For an ultrarelativistic electron, $\gamma \gg 1$ so $\beta_z \approx 1$ and the size of these perturbations can be neglected. The top panel of Figure 14 shows that the electron follows a sinusoidal trajectory for $\gamma \gg 1$.

2.10.2 Trajectory of an Electron Accelerated in the Bubble

A more realistic electron trajectory in the bubble regime is produced by considering the effect of the longitudinal as well as the transverse electric field component of the

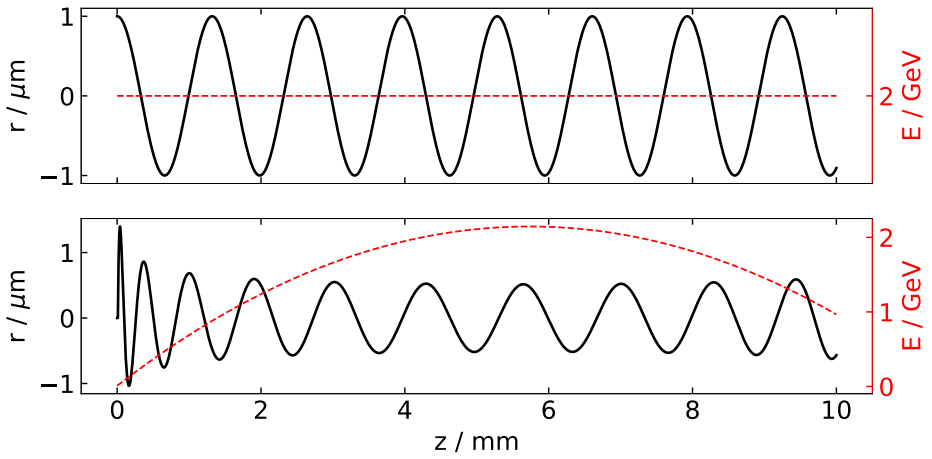


Figure 14: Example trajectories (black) and energy progressions (red dashed) of ultrarelativistic electrons oscillating in the bubble regime, (top) for an electron with constant energy and (bottom) an electron following a parabolic energy progression according to Equation 2.55 and a trajectory following Equation 2.68. Trajectories plotted for typical LWFA parameters of $n_e = 5 \times 10^{18}$ cm^{-3}, $a_0 = 3$ and $r_0 = 2$ µm.

bubble on the electron. While the longitudinal component gives the electron a greater total energy, the transverse component produces a focusing force on the electron towards the central longitudinal axis of the bubble. The Lorentz factor is no longer a constant of the electron's motion. However, as outlined in the derivation in Appendix D.4, if the rate of change of the Lorentz factor of the electron is significantly smaller than the rate of change of the radial speed factor, an approximately simple harmonic equation of motion can be derived for the electron's transverse motion:

$$\frac{d^2r}{dt^2} = \frac{\omega_p^2}{2\gamma(t)}r, \tag{2.67}$$

where the Lorentz factor is a slowly varying function of time. As stated in Appendix D.4, this equation of motion is valid if $\beta_r \frac{d\gamma}{dt} \gg \gamma \frac{d\beta_r}{dt}$. This is true for an ultrarelativistic electron, which has $\gamma \gg 1$ and $\beta_r < 1$; differentiating Equation 2.55 with respect to time, dividing by $m_e c^2$ and setting $t = 0$ shows that the Lorentz factor is accelerated over a minimum timescale of $1/\omega_p^2$, whereas the transverse speed factor oscillates over a timescale of $1/\omega_\beta$. Therefore, as $\gamma \gg \beta_r$ and $1/\omega_\beta \gg 1/\omega_p^2$, the equation of motion is valid for an ultrarelativistic electron.

Because the equation of motion is still of simple harmonic form, the electron is expected to oscillate about the central longitudinal axis of the bubble with a slowly varying frequency: $\Omega_\beta(t) = \omega_p/\sqrt{2\gamma(t)}$. A solution to the equation of motion can be derived by applying the Wentzel-Kramers-Brillouin (WKB) approximation, which is performed

in Appendix D.4. In that derivation, it is shown that the WKB approximation is valid when $\frac{d\Omega_\beta(t)}{dt} \ll \Omega_\beta(t)^2$. Substituting the expression for the slowly varying frequency of oscillation, that condition is satisfied when $\frac{d\gamma}{dt} \ll \omega_p/\sqrt{2\gamma(t)}$. Expressed qualitatively, the Lorentz factor and thereby the frequency of oscillation must be slowly varying compared to the timescale of the oscillations performed by the electron. Originally derived by Kostyukov *et al.* in 2004 [130], the solution to the equation of motion describes an electron oscillating with a slowly varying frequency and amplitude:

$$r(t) = \frac{p_{r0}}{m_e\omega_p}\sqrt{\frac{2}{\gamma_0}}\left(\frac{\gamma_0}{\gamma(t)}\right)^{\frac{1}{4}} \sin\left[\int \Omega_\beta(t)\,dt\right], \tag{2.68}$$

where γ_0 is the initial Lorentz factor of the electron and p_{r0} is its initial transverse momentum when injected into the bubble. In the bottom panel of Figure 14, the trajectory of the electron following this equation is plotted for an electron following the quadratic energy progression given by Equation 2.55, plotted in red. The ultrarelativistic electron travels at approximately the speed of light in the z-direction, and is approximated as $z \approx ct$. The plot shows that the increase in energy of the electron is accompanied by a decrease in oscillation amplitude and an increase in the oscillation wavelength. The amplitude of oscillation follows a function in time, which can be inferred from Equation 2.68:

$$r_\beta(t) = r_0\left(\frac{\gamma_0}{\gamma(t)}\right)^{\frac{1}{4}}, \tag{2.69}$$

where $r_0 = p_{r0}/(m_e\omega_p)\sqrt{2/\gamma_0}$ is the initial amplitude of oscillation.

The solution for the transverse momentum component of the oscillating electron is also derived in Appendix D.4:

$$p_r(t) = p_{r0}\left(\frac{\gamma(t)}{\gamma_0}\right)^{\frac{1}{4}} \cos\left[\int \Omega_\beta(t)\,dt\right]. \tag{2.70}$$

The transverse momentum component of the electron is plotted against its longitudinal coordinate in the top panel of Figure 15, showing the increase in the amplitude of the transverse momentum with the electron's energy. This is due to the increase in the transverse force on the electron, which scales with the Lorentz factor: $F_r = \frac{dp_r}{dt} = \gamma\frac{d^2r}{dt^2}$. By contrast, the amplitude of the betatron oscillations decreases with the Lorentz factor according to Equation 2.69. While this may be somewhat counter-intuitive, it should be remembered that the longitudinal momentum component of the electron is approximately proportional to the Lorentz factor. This means that as the electron's energy increases, its momentum becomes more strongly directed in the longitudinal direction, as $p_r/p_z \propto \gamma^{-\frac{3}{4}}$. The bottom panel of Figure 15 is a plot of

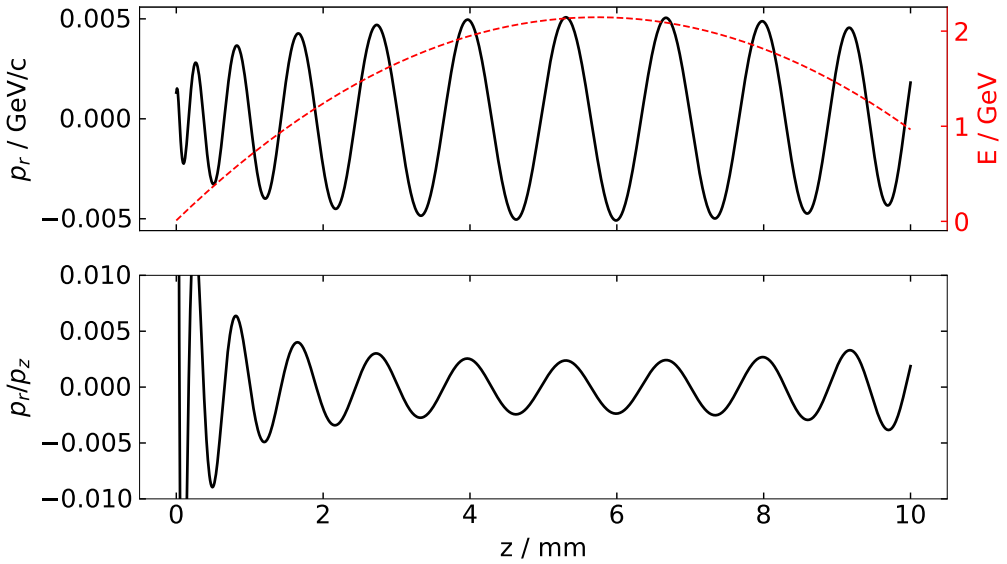


Figure 15: (Top) (Black) Transverse momentum component of electron and (red) energy progression against longitudinal coordinate, where $n_e = 5 \times 10^{18}$ cm^{-3}, $a_0 = 3$ and $r_0 = 2$ µm. (Bottom) Ratio of transverse and longitudinal momentum components of the same electron.

p_r/p_z against the electron's longitudinal coordinate, where it has been assumed that $pz \approx p$. In this plot, $p_r/p_z \sim 10^{-3}$ apart from at the start of the acceleration where $p_r/p_z \sim 10^{-2}$. The amplitude of the oscillations of p_r/p_z, shown in the bottom plot, decreases with increasing electron energy.

2.11 Synchrotron Radiation

A charged particle moving with some non-zero acceleration emits electromagnetic radiation called synchrotron radiation [2]. Synchrotron light sources typically consist of a series of dipole magnets that cause charged particles to follow a curved trajectory, which mean that they undergo some transverse acceleration. In this section, the general properties of synchrotron radiation produced by electrons following curved trajectories are derived and discussed. These properties include the time progression of the electromagnetic fields, the spatial and spectral intensity distributions.

2.11.1 Retarded and Observed Times

The trajectory of the electron describes its position as a function of time. The observer of the synchrotron radiation lies at another position and is stationary with respect to the laboratory frame of reference, as shown in Figure 16. The relative position of the electron with respect to the observer is a function of time, equal to the difference of

these displacement vectors:

$$\mathbf{r}(t) = \mathbf{r_p} - \mathbf{R}(t), \tag{2.71}$$

where $\mathbf{r_p}$ is the position of the observer relative to a pre-defined origin and $\mathbf{R}$ is the trajectory of the electron relative to the same origin. At some point in time, the electron emits radiation in the direction of the observer. The radiation arrives at the observer after some time interval determined by the distance that the radiation has to travel to reach the observer's position. The time when the radiation meets the observer thus depends on this distance:

$$t_{obs} = t_{ret} + \frac{|\mathbf{r}(t_{ret})|}{c}, \tag{2.72}$$

where t_{ret} is the time at which the radiation is emitted, known as the retarded time.

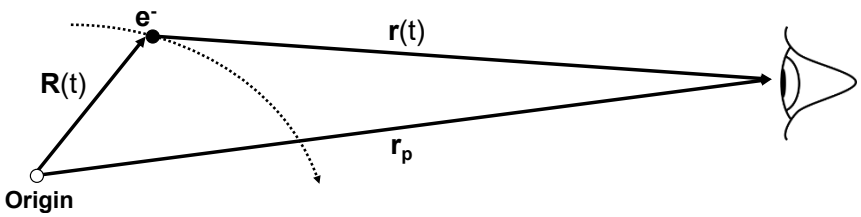


Figure 16: Displacement vectors for an electron following a curved trajectory and an observer of its synchrotron radiation. Their positions are defined with respect to a pre-defined origin.

An observed time interval in the radiation depends on the motion of the electron. To demonstrate this, we consider the following example. An electron moves from one position $\mathbf{R_1}$ at some retarded time $t_{ret,1}$ to $\mathbf{R_2}$ at $t_{ret,2}$. The electron-observer distances at these retarded times are r_1 and r_2. Considering the radiation produced at each of these retarded times, the corresponding times of observation can be calculated using Equation 2.72. The difference between these times of observation is the observed time interval:

$$\Delta t_{obs} = \Delta t_{ret} + \frac{\Delta r}{c}, \tag{2.73}$$

where $\Delta t_{ret} = t_{ret,2} - t_{ret,1}$ and $\Delta r = r_2 - r_1$. If the electron is travelling towards the observer, $\Delta r < 0$, so the observed time interval is shorter than the corresponding retarded time interval. If the electron is travelling away, $\Delta r > 0$ so $\Delta t_{obs} > \Delta t_{ret}$.

Considering an infinitesimal time interval in the retarded time, the corresponding observed time interval becomes

$$dt_{obs} = \left(1 + \frac{1}{c}\frac{d|\mathbf{r}|}{dt_{ret}}\right) dt_{ret}, \tag{2.74}$$

which is derived by differentiating Equation 2.72 with respect to the retarded time.

This expresses the rate of change of the observed time with respect to the retarded time. Substituting Equation 2.71 into Equation 2.74 and differentiating with respect to time produces an alternative expression for Equation 2.74:

$$dt_{obs} = (1 - \mathbf{n} \cdot \boldsymbol{\beta})\, dt_{ret}, \tag{2.75}$$

where $\mathbf{n} = \mathbf{r}/|\mathbf{r}|$ is the unit vector pointing in the direction of the observer from the electron's position and $\boldsymbol{\beta} = \frac{1}{c}\frac{d\mathbf{r}}{dt_{ret}}$ is the velocity factor of the electron.

2.11.2 Liénard-Wiechert Fields

The potentials of the radiation produced by a charged particle being accelerated were derived by Liénard in 1898 [150] and independently by Wiechert in 1901 [151]. From these expressions, the electromagnetic fields of the radiation as functions of time were derived, and are known as the Liénard-Wiechert fields [25]:

$$\mathbf{E}(t_{obs}) = \frac{e}{4\pi\epsilon_0\gamma^2}\left(\frac{\mathbf{n} - \boldsymbol{\beta}}{r^2(1 - \mathbf{n}\cdot\boldsymbol{\beta})^3}\right)_{ret} + \frac{e}{4\pi\epsilon_0 c}\left(\frac{\mathbf{n}\times((\mathbf{n} - \boldsymbol{\beta})\times\dot{\boldsymbol{\beta}})}{r(1 - \mathbf{n}\cdot\boldsymbol{\beta})^3}\right)_{ret}, \tag{2.76}$$

$$\mathbf{B}(t_{obs}) = \frac{e\mu_0}{4\pi}\left(\frac{\mathbf{n}\times\boldsymbol{\beta}\gamma^2}{r^2(1 - \mathbf{n}\cdot\boldsymbol{\beta})^3}\right)_{ret} + \frac{e\mu_0}{4\pi}\left(\frac{\mathbf{n}\times(\mathbf{n}\times((\mathbf{n} - \boldsymbol{\beta})\times\dot{\boldsymbol{\beta}}))}{r(1 - \mathbf{n}\cdot\boldsymbol{\beta})^3}\right)_{ret}. \tag{2.77}$$

where $\dot{\boldsymbol{\beta}}$ is the rate of change of the relativistic speed factor of the particle with respect to the retarded time. Derivations of the Liénard-Wiechert potentials of radiation from accelerating charge and the Liénard-Wiechert fields can be found in Hoffman's book, "The Physics of Synchrotron Radiation" [25]. Comparing the equations for the electromagnetic fields, there is a simple relation between the two fields [25]:

$$\mathbf{B}(t_{obs}) = \frac{1}{c}\mathbf{n}\times\mathbf{E}(t_{obs}). \tag{2.78}$$

All of the parameters describing properties of the particle in Equation 2.76 are functions of time. All of these parameters describe the electron in the retarded time, rather than as measured by the observer.

2.11.3 Angular Intensity Distribution

The first term in Equation 2.76 is the near-field contribution to the electric field of the synchrotron radiation, and the second term is the far-field contribution. At large distances, where $r \gg 1$, the far-field contribution is several orders of magnitude greater than the near-field contribution. If $\gamma \gg 1$, the far-field contribution is also greater by even more orders of magnitude, due to the squared Lorentz factor in the denominator of the near-field term. In most synchrotron light sources, $\gamma \gg 1$ and $r > 1$ m.

Therefore, only the far-field term in the Liénard-Wiechert fields is used to describe the spatial power distribution of the synchrotron radiation.

The angular distribution of the power emitted per solid angle by an electron undergoing some acceleration can be derived from the Poynting vector produced by its Liénard-Wiechert fields. This is performed in Appendix E.1 and the result is given by Equation 2.79:

$$\frac{dP}{d\Omega} = \frac{e^2}{(4\pi)^2\epsilon_0 c}\frac{\left(\mathbf{n}\times((\mathbf{n}-\boldsymbol{\beta})\times\dot{\boldsymbol{\beta}})\right)^2}{(1-\mathbf{n}\cdot\boldsymbol{\beta})^5}. \tag{2.79}$$

This is the angular distribution emitted by the electron in the retarded time, rather than the distribution according to the observer.

Total Radiated Power

The total radiated power by the electron is derived by integrating the power distribution over the entire solid angle covered by the radiation distribution. An expression for the total radiated power is derived in Appendix E.1.1. The result is the relativistically-corrected Larmor formula, also known as the Liénard formula [2]:

$$P = \frac{e^2}{6\pi\epsilon_0 c}\gamma^6\left(\dot{\boldsymbol{\beta}}^2 - (\boldsymbol{\beta}\times\dot{\boldsymbol{\beta}})^2\right). \tag{2.80}$$

This expression for the total radiated power can be broken down into two contributions: one due to an acceleration parallel to the electron's velocity and one due to the acceleration perpendicular to its velocity. When the acceleration and velocity of the electron are parallel, the angle between them is zero, so $|\dot{\boldsymbol{\beta}}\times\boldsymbol{\beta}| = \dot{\beta}\beta\sin 0 = 0$. Then in the relativistically-corrected Larmor formula, $\dot{\boldsymbol{\beta}}^2 - (\boldsymbol{\beta}\times\dot{\boldsymbol{\beta}})^2 = \dot{\boldsymbol{\beta}}^2$, producing an expression for its contribution to the radiated power:

$$P_{||} = \frac{e^2}{6\pi\epsilon_0 c}\gamma^6\dot{\boldsymbol{\beta}}_{||}^2. \tag{2.81}$$

When the velocity and acceleration of the electron are perpendicular, the vector product has its largest magnitude: $|\dot{\boldsymbol{\beta}}\times\boldsymbol{\beta}| = \dot{\beta}\beta\sin 90^\circ = \dot{\beta}\beta$. In the relativistically-corrected Larmor formula, $\dot{\boldsymbol{\beta}}^2 - (\boldsymbol{\beta}\times\dot{\boldsymbol{\beta}})^2 = \dot{\boldsymbol{\beta}}^2(1-\boldsymbol{\beta}^2) = \dot{\boldsymbol{\beta}}^2\gamma^{-2}$. The power contribution due to the acceleration perpendicular to the electron's velocity can also be expressed:

$$P_{\perp} = \frac{e^2}{6\pi\epsilon_0 c}\gamma^4\dot{\boldsymbol{\beta}}_{\perp}^2. \tag{2.82}$$

The forces on the electron producing an acceleration in either direction are given by $m_e\dot{\boldsymbol{\beta}}_{||}c = \gamma^{-3}\frac{d\mathbf{p}_{||}}{dt}$ and $m_e\dot{\boldsymbol{\beta}}_{\perp}c = \gamma^{-1}\frac{d\mathbf{p}_{\perp}}{dt}$. These force components can be substituted

into their corresponding power contributions:

$$P_{\parallel} = \frac{e^2}{6\pi\epsilon_0 c}\frac{1}{m_e^2 c^2}\left(\frac{d\mathbf{p}_{\parallel}}{dt_{ret}}\right)^2, \tag{2.83}$$

$$P_{\perp} = \frac{e^2}{6\pi\epsilon_0 c}\frac{\gamma^2}{m_e^2 c^2}\left(\frac{d\mathbf{p}_{\perp}}{dt_{ret}}\right)^2. \tag{2.84}$$

These equations are of the same form, but Equation 2.84 contains an extra factor of γ^2. A force applied perpendicular to the direction of motion of the electron will lead to the emission of synchrotron radiation that is a factor of γ^2 greater than the radiation produced by an electron accelerated in its direction of travel. For an electron experiencing both a parallel and a perpendicular acceleration, when $\gamma \gg 1$, the power contribution from the parallel acceleration component emitted becomes negligible.

Angular Intensity Distribution from an Electron Following a Circular Trajectory

While many electrons producing synchrotron radiation do not follow circular trajectories, for example electrons oscillating in an insertion device, many electron trajectories over short distances can be approximated by arcs of a circle with some radius of curvature. It is thus instructive to examine the spatial power distribution produced by an electron following a circular trajectory, for which $\frac{dp_{\perp}}{dt} = 0$. The angular intensity distribution, derived in Appendix E.1.2, is given by Equation 2.85:

$$\frac{dP}{d\Omega} = \frac{e^2}{(4\pi)^2\epsilon_0 c}\frac{\dot{\beta}^2}{(1-\beta\cos\theta)^3}\left(1 - \frac{\cos^2\phi\sin^2\theta}{\gamma^2(1-\beta\cos\theta)^2}\right), \tag{2.85}$$

where the angles are defined in Figure 17. This equation expresses the power radiated per unit solid angle, which is proportional to the intensity of the emitted radiation.

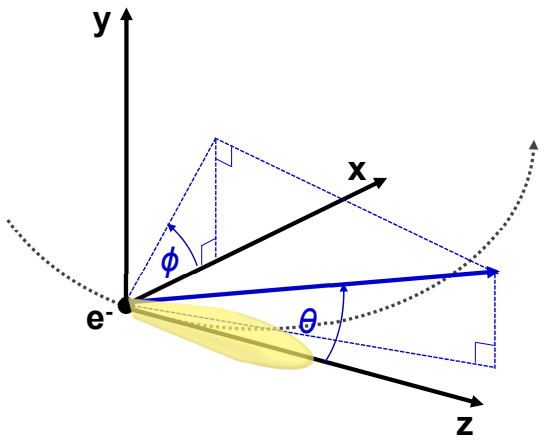


Figure 17: Setup of Cartesian and angular coordinates in deriving the angular intensity distribution of synchrotron radiation from an electron following a circular trajectory.

As predicted by Equation 2.79, as the direction of the electron-observer displacement approaches the direction of the electron's velocity, $\theta \to 0$, the angular intensity distribution approaches its peak value. In the direction perpendicular to the direction of travel of the electron, when $\phi = 90°$, the flux of the radiation falls as $(1 - \beta\cos\theta)^3$ away from the axis of travel of the electron.

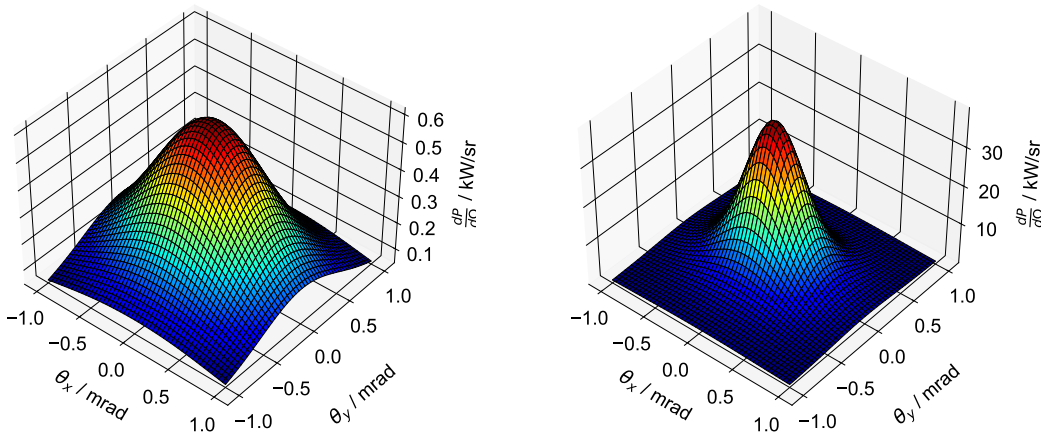


Figure 18: Surface plots of angular intensity distribution of radiation from electrons following a circular trajectory. Each electron has $\beta_z \sim 10^{11}$ s^{-1} with (left) $\gamma = 1000$ and (right) $\gamma = 2000$.

In Figure 18 are two plots of the angular intensity distribution given by Equation 2.85 for two electrons with different Lorentz factors. For a more intuitive visualisation of the angular intensity distribution, the angles θ and ϕ have been transformed to angles of divergence from the z-axis, θ_x and θ_y. In both plots, the angular intensity distribution is concentrated in a cone with an opening angle of $\sim 1/\gamma$ around the axis of travel of the electron. The cone thus gets narrower as the Lorentz factor of the electron is increased. Also, the peak intensity at the centre of the cone increases, which is due to the increase in the power emitted by the electron.

For $\theta \ll 1$, small angle approximations can be applied to the trigonometric functions in Equation 2.85: $\sin\theta \approx \theta$ and $\cos\theta \approx 1 - \frac{1}{2}\theta^2$. For ultrarelativistic electrons, the relativistic speed factor can be approximated as $\beta \approx 1 - \frac{1}{2}\gamma^{-2}$, so the angular intensity distribution can be expressed in the following simplified form:

$$\frac{dP}{d\Omega} = \frac{e^2}{2\pi^2\epsilon_0 c}\frac{\gamma^6\dot{\beta}^2}{(1+\gamma^2\theta^2)^3}\left(1 - \frac{4\gamma^2\theta^2\cos^2\phi}{(1+\gamma^2\theta^2)^2}\right). \tag{2.86}$$

The angular distribution of radiated power varies with the angle approximately as

$(\gamma^{-2} + \theta^2)^{-3}$. Setting $\phi = 0$, Equation 2.86 falls to zero at some maximum angle in the radiation cone:

$$\theta_{max} = \pm\frac{1}{\gamma}. \tag{2.87}$$

The angular flux distribution only falls to zero at this angle only for $\phi = 0$. When $\phi \neq 0$, the flux distribution approaches zero without ever reaching it for increasing angles from the electron's axis of travel.

2.11.4 Angular Energy Density Spectrum Produced by an Electron Following a Circular Trajectory

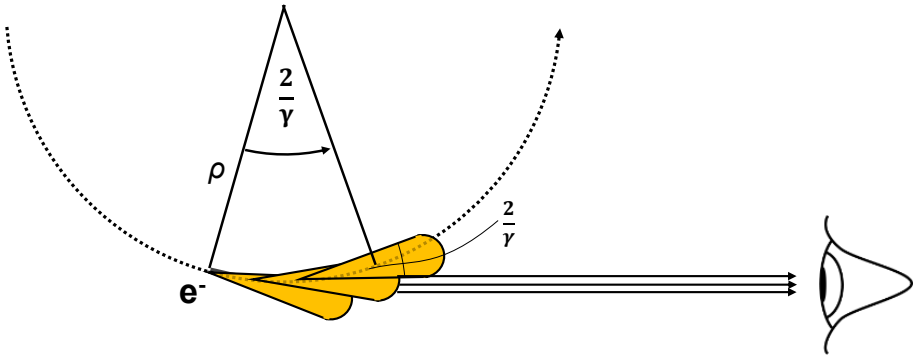


Figure 19: Synchrotron radiation produced by an electron following a circular trajectory reaches a stationary observer when the electron is travelling within an arc with an angle equal to the opening angle of the radiation.

As the trajectory of an oscillating electron can be approximated by a circular arc over short distances, it is instructive to understand the synchrotron radiation spectrum produced by an electron following a circular trajectory. The observed radiation spectrum is continuous and is characterised by a parameter known as the critical frequency, above and below which half of the energy of the radiation is produced [2]. The critical frequency is determined by the duration of the short flash "seen" by the stationary observer as the radiation cone sweeps across the observer like a flashlight moving around its curved trajectory, as shown in Figure 19. The duration of a flash produced by a electron following a circular arc is derived in Appendix E.4:

$$\Delta t_{flash} = \frac{4\rho}{3\gamma^3 c}, \tag{2.88}$$

where ρ is the radius of curvature of the electron's trajectory. Scaling as γ^{-3}, the duration of the radiation pulse is very short, so the spectrum of the radiation is expected to be broad. From the time-bandwidth product, the critical frequency is given by $\omega_c \approx 2/\Delta t_{flash}$, quantifying the frequencies that the spectrum extends to [2]. Substi-

tuting the expression for the radiation flash duration,

$$\omega_c = \frac{3}{2}\frac{\gamma^3 c}{\rho}, \tag{2.89}$$

where ρ is the radius of curvature of the electron trajectory. The corresponding critical photon energy, $E_c = \hbar\omega_c$, can be written:

$$E_c = \frac{3\hbar}{2}\frac{\gamma^3 c}{\rho}. \tag{2.90}$$

A derivation of the angular energy density spectrum of an electron following a uniform circular trajectory can be found in Wiedemann's book, "Particle Accelerator Physics" [2]. Due to the many steps involved in deriving this relation, the derivation is not reviewed here. Its result is given in Equation 2.91 [2]:

$$\frac{d^2W}{d\Omega\, d\omega} = \frac{e^2}{16\pi^3\epsilon_0 c}\gamma^2\left(\frac{\omega}{\omega_c}\right)^2(1+\gamma^2\theta^2)^2\left[K_{2/3}^2(\xi) + \frac{\gamma^2\theta^2 K_{1/3}^2(\xi)}{1+\gamma^2\theta^2}\right], \tag{2.91}$$

where $\xi = \frac{1}{2}\frac{\omega}{\omega_c}(1+\gamma^2\theta^2)^{\frac{3}{2}}$ and $K_{1/3}(\xi)$ and $K_{2/3}(\xi)$ are modified Bessel functions of the second kind. The spectrum in terms of the photon energy can also be expressed:

$$\frac{d^2W}{d\Omega\, dE} = \frac{1}{\hbar}\frac{d^2W}{d\Omega\, d\omega}, \tag{2.92}$$

where E is the photon energy.

On the surface plot in Figure 20, this equation is mapped and the on-axis spectrum is plotted for different values of the Lorentz factor. The electron's total energy is 3 GeV and its trajectory's radius of curvature is 7.15 m, which are the parameters of the storage ring at the Diamond Light Source in the United Kingdom [152], [153]. A significant amount of radiation energy is produced at photon energies up to 100 keV. The surface plot in Figure 20 shows that the radiation beam has a different divergence at each photon energy. The divergence of the radiation beam decreases at increasing photon energies. The peak intensity is observed on-axis, at a frequency just above the critical frequency of the on-axis spectrum.

On the right of Figure 20, the on-axis intensity spectra produced by electrons with a range of Lorentz factors are plotted. The spectra have critical photon energies ranging up to 100 keV, which are shown as the vertical dashed lines. Increasing the Lorentz factor of the electron increases both the peak intensity and the critical photon energy of the spectrum. A higher critical energy means that the spectrum stretches to higher photon energies.

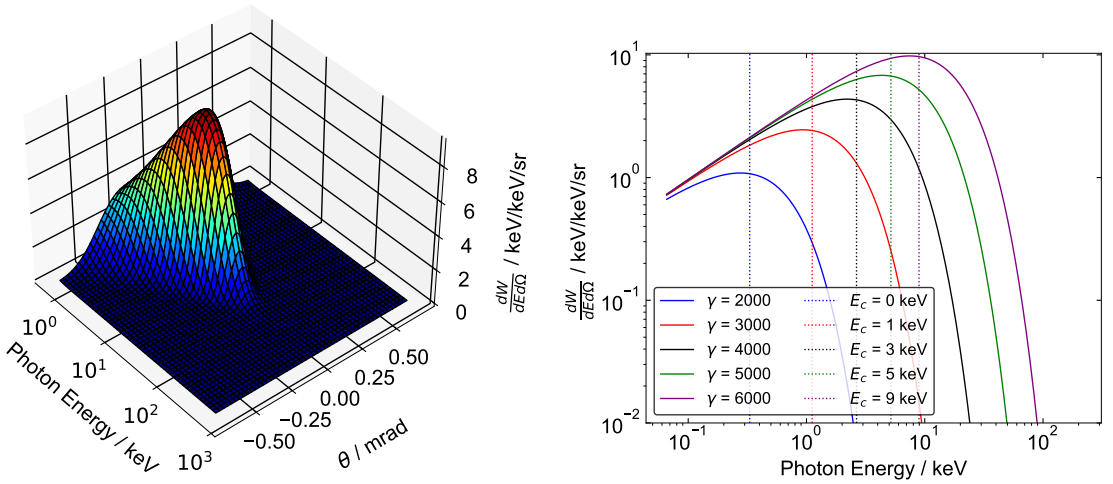


Figure 20: (Left) Surface plot of angular energy density spectrum from an electron in a storage ring with $\gamma = 6000$ and $\rho = 7.15$ m. (Right) On-axis angular energy density spectra produced by storage ring electrons with different Lorentz factors, all with $\rho = 7.15$ m.

2.12 Synchrotron Radiation from LWFAs

It was shown in Section 2.10 that electrons accelerated in the bubble regime in an LWFA perform oscillations about the central longitudinal axis of the bubble. In doing so, these electrons emit a form of synchrotron radiation, often called betatron radiation. The exact form of the angular and spectral intensity profiles of this radiation is generally not well-described analytically, owing to the large, sometimes near-100% energy spreads in the electron beams in LWFAs, causing large variations in the properties of the radiation produced by different electrons in the beam. The basic principles of the radiation emission from a single electron in an LWFA are described here.

2.12.1 Angular Energy Density Distribution

An electron oscillating in an LWFA emits radiation over the range of angles of divergence from the longitudinal axis in its trajectory. The angle of divergence of its trajectory from the z-axis is $\theta_e = \arctan(p_r/p_z)$, which for an ultrarelativistic electron can be approximated using the small angle approximation if $\theta_e \ll 1$: $\theta_e \approx \beta_r/\beta_z \approx \beta_r$, as $\beta_z \approx 1$. Over a few oscillations when the electron is at its highest energies, the trajectory of an electron in an LWFA may be described by a sinusoidal function of time, as was done for an electron with a constant energy performing betatron oscillations. Using Equation 2.64,

$$\theta_e \approx -k_\beta r_\beta \sin(\omega_\beta t), \tag{2.93}$$

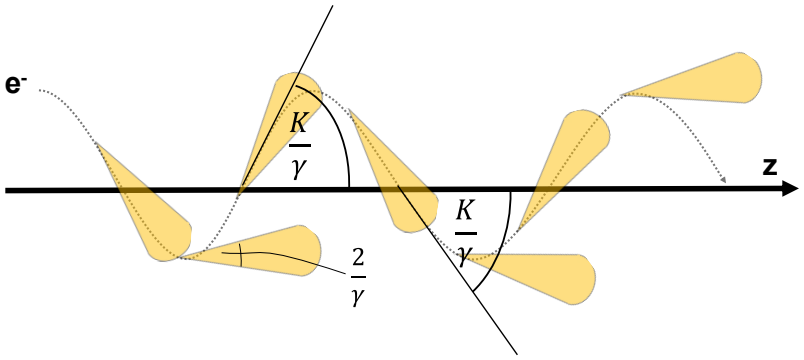


Figure 21: The maximum angles of divergence of the electron trajectory from the z-axis compared with the smaller opening angle of the instantaneous radiation cone emitted at each point along the trajectory.

where k_β is the wavenumber of the betatron oscillations, given by $k_\beta = \omega_\beta / v \approx \omega_\beta / c$. In an insertion device, where the trajectories of an electron can also sometimes be described by a sinusoid, the electron is described in terms of a dimensionless "K-parameter", which describes the strength and the period of the magnetic field produced by the magnets causing the electron beam to oscillate [2]. In an LWFA, we define the betatron strength parameter, which is the product of the betatron oscillation amplitude, the oscillation wavenumber and the Lorentz factor [61], [154]:

$$K = \gamma r_\beta k_\beta. \tag{2.94}$$

Physically, the K-parameter quantifies the amplitude of the oscillation in the transverse momentum of the electron. The betatron strength parameter can be used to quantify the maximum angle of divergence of the electron's trajectory from the z-axis:

$$\theta_e = \frac{K}{\gamma} \sin(\omega_\beta t). \tag{2.95}$$

The maximum angle of divergence in the electron trajectory is thus K/γ and the range of angles covered in the trajectory is $2K/\gamma$. An example trajectory is shown in the schematic in Figure 21, emitting synchrotron radiation at each point. The radiation cone produced at each point has an opening angle of $2/\gamma$, as deduced from Equation 2.87. When $K \gg 1$, $2K/\gamma \gg 2/\gamma$, so the range of divergence angles covered in the electron trajectory is larger than the opening angle of the instantaneous radiation cone, as shown in Figure 21. Hence, the angular energy density distribution of the radiation produced by the oscillating electron is determined primarily by the power radiated by the electron as it travels in each direction within its trajectory, rather than the angular intensity distribution of the instantaneous radiation cone. The oscillation amplitude and wavenumber in an LWFA are typically on the order of 1 µm and 10^7 m^{-1}, respectively, whereas in an insertion device these parameters are generally

on the order of 1 µm and $2\pi \cdot 10^3$ m^{-1} [155]–[157]. Thus, for electrons accelerated to hundred-MeV and GeV-order energies in an LWFA, $K \gg 1$.

By considering the power of the radiation emitted when the electron is travelling at each angle of divergence, an expression for the angular energy density distribution of its radiation beam can be produced. Considering an electron following a sinusoidal trajectory, an expression for the rate of change of transverse momentum of the electron can be produced by differentiating Equation 2.64 with respect to time, which can then be substituted into the expression for the radiated power given by Equation 2.84:

$$P(t_{ret}) = \frac{e^2}{6\pi\epsilon_0 c^3}\gamma^4\omega_\beta^4 r_\beta^2 \cos^2(\omega_\beta t_{ret}). \tag{2.96}$$

The largest contribution to the angular energy density distribution comes from the radiation emission when the electron is at a turning point in its trajectory. This is where its rate of change of transverse momentum is largest, which, according to Equation 2.84, means that the electron radiates at the highest power. The top panel of Figure 22 shows that most of the power emitted by the electron is around its turning points, where the divergence angle of the electron's direction of travel is around zero, as shown in the middle panel Figure 22.

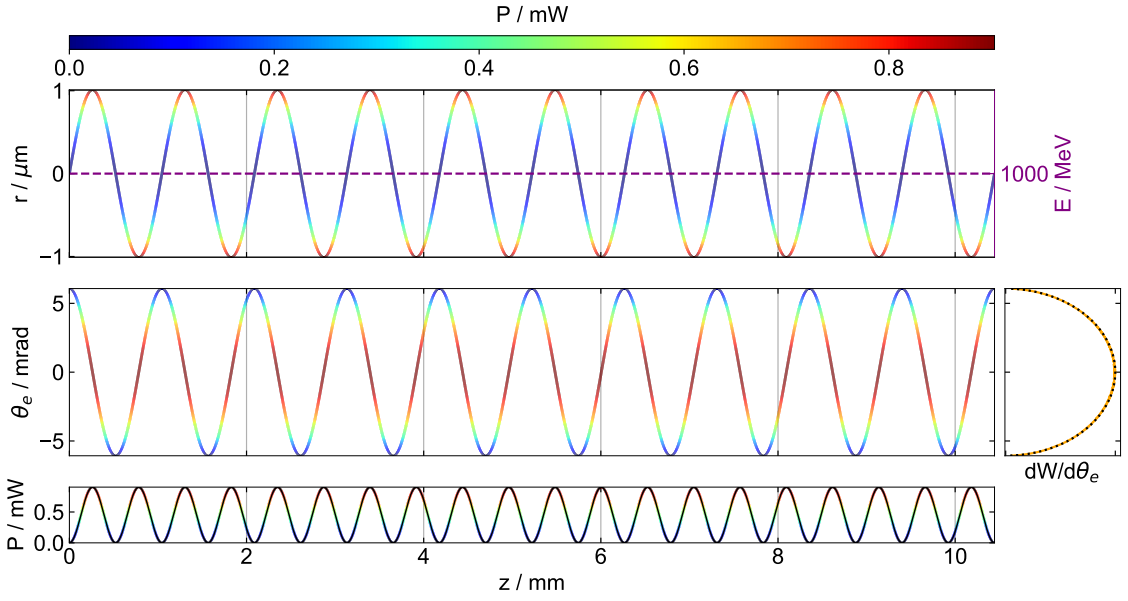


Figure 22: (Top) Sinusoidal electron trajectory. (Middle) Angle between electron's direction of travel and z-axis. (Bottom) Power emitted by electron. All three plots are colour-coded against emitted power. (Right) Histogram of the power per unit angle emitted (orange) compared with two-dimensional model for the angular energy density distribution given by Equation 2.97 (black).

By considering the power emitted by the electron at each angle and the time spent by the electron travelling through each angle, the energy radiated per unit angle is derived in a two-dimensional model in Appendix E.2:

$$\frac{dW}{d\theta_e} = \frac{e^2}{6\pi\epsilon_0 c}\gamma^4\omega_\beta\sqrt{\frac{K^2}{\gamma^2} - \theta_e^2}, \tag{2.97}$$

which is the angular energy line density distribution produced by an electron performing one sinusoidal oscillation. The angular energy distribution is semi-circular along the axis of θ_e. As expected from Equation 2.93, the angular distribution falls to zero at $\theta = \frac{K}{\gamma}$, equal to the maximum angle between the electron's trajectory and the z-axis. Equation 2.97 is plotted as the black dotted line in the left panel of Figure 22. It is compared with the power emitted by the electron at each angle integrated into bins with small angular ranges. This is the orange line in the plot, which is also a semi-circular distribution. There is good agreement between Equation 2.97 and that numerically calculated distribution.

The above two-dimensional model only produces an energy per unit angle of the radiation. In three dimensions, an expression can be derived for the energy per unit solid angle radiated by the electron, which is a quantity that is more easily measured in experiment. The derivation is outlined in the second part of Appendix E.2, but is less intuitive than the two-dimensional case. The following expression describes the energy radiated per unit solid angle of the radiation beam produced by the electron having performed a single oscillation:

$$\frac{d^2W}{d\theta_y\, d\theta_e} = \frac{e^2}{16\pi\epsilon_0 c}\gamma^5\omega_\beta\sqrt{\frac{K^2}{\gamma^2} - \theta_e^2}\left[\frac{1}{(1+\gamma^2\theta_y^2)^{\frac{5}{2}}}\left(3 - \frac{5}{4(1+\gamma^2\theta_y^2)}\right)\right]. \tag{2.98}$$

where θ_y is the angle of divergence in the plane perpendicular to the plane of oscillation; the electron oscillates in the x-z plane. The energy density distribution is a semi-circular function of θ_e, falling to zero at a divergence angle of K/γ. In the direction perpendicular to the plane of oscillation, the intensity of the radiation beam from the electron should still fall rapidly at divergence angles larger than $1/\gamma$.

The energy density distribution described by Equation 2.98 is compared with a numerical model in Figure 23. In the numerical model, the Liénard-Wiechert fields are calculated at a grid of observation points spanning the solid angle covered in Figure 23, from which the intensity is calculated and then integrated over the time of observation. The main difference between the numerical and analytical models is that the analytical model seems to be slightly broader in the y-direction. This is due to the

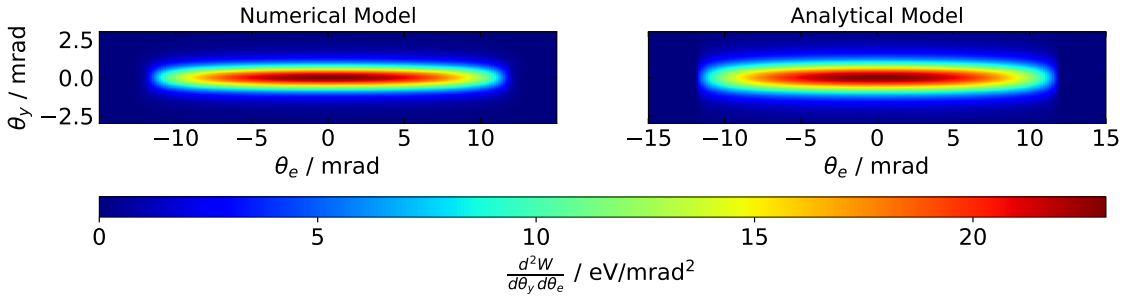


Figure 23: Numerical and analytical energy density distributions of radiation beams produced by an electron following a sinusoidal trajectory, with $K = 10$, $\gamma = 1000$ and in a plasma with $n_e = 4 \times 10^{18}$ cm^{-3}.

approximations made in producing Equation 2.86 from Equation 2.85 for the angular intensity distribution of the instantaneous radiation cone. The other difference is that in the analytical model, there is no value for the distribution when $\theta_e > K/\gamma$. In Figure 23, the distribution has been set to zero when $\theta_e > K/\gamma$.

In the plane of oscillation of the electron, when $\theta_y = 0$,

$$\frac{d^2W}{d\theta_e\, d\theta_y} = \frac{7e^2}{64\pi\epsilon_0 c}\gamma^5\omega_\beta\sqrt{\frac{K^2}{\gamma^2} - \theta_e^2}. \tag{2.99}$$

Equation 2.99 is of a similar form to Equation 2.97, but contains an extra factor of γ and a slightly different constant at the front of the equation, which account for the non-zero divergence of the instantaneous radiation cone in the direction perpendicular to the plane of oscillation. In the two dimensional case, it is effectively assumed that all

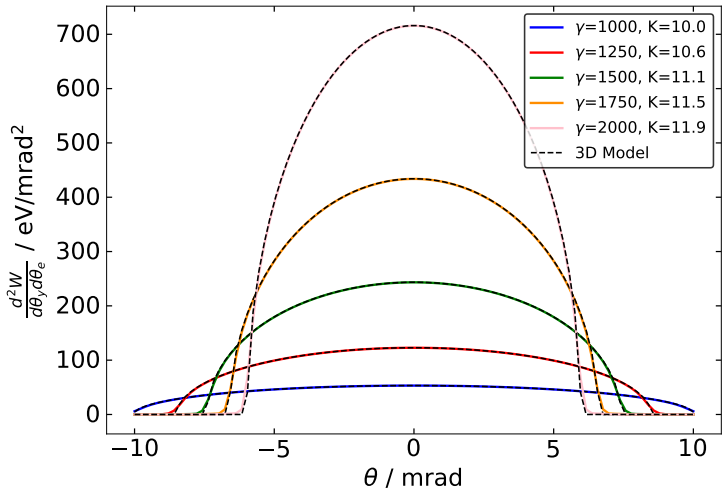


Figure 24: Comparison of numerical and analytical models for energy density of a radiation beam in the plane of oscillation of electrons following a sinusoidal trajectories. The plasma has an electron density of $n_e = 4 \times 10^{24}$ cm^{-3}.

of the radiation power in the cone is contained in the plane of oscillation.

The analytical energy density distribution described by Equation 2.99 is compared with the numerically calculated distribution in Figure 24. The distributions are produced by an electron following the sinusoidal trajectories with different Lorentz factors and K-parameters. The numerical method is the same as used to produce the numerical distribution in Figure 23; the observation points are in an arc in the plane of oscillation of the electron. There is clearly good agreement between the analytical and numerical distributions.

2.12.2 Energy Density Spectrum

Before investigating the spectral characteristics of the radiation produced by an oscillating electron in an LWFA, it is helpful to understand temporal profile of the radiation. The temporal electric field profile is best understood in terms of the K-parameter of the electron. Plotted on the left column of Figure 25 are the Liénard-Wiechert fields at an on-axis point of observation produced by electrons with different K-parameters, each with $\gamma = 500$ and in a plasma with $n_e = 4 \times 10^{18}$ cm^{-3}. When $K \ll 1$, some part of the radiation cone is always pointing along the axis. This produces the quasi-sinusoidal temporal profile at the top of Figure 25. When $K \geq 1$, $K/\gamma > 1/\gamma$; there are parts of the electron's trajectory when the radiation cone is not directed towards the observer. The electron radiates toward the observer in short flashes, interspersed with regions of zero electric field, as shown in the middle profile in Figure 25. When $K \gg 1$, these flashes become shorter because $K/\gamma \gg 1/\gamma$, as the proportion of the electron trajectory where the radiation cone points towards the observer is smaller.

In the right column of Figure 25, the energy density spectrum calculated from each Liénard-Wiechert field is plotted. These spectra were calculated from the fast-Fourier transform of the Liénard-Wiechert fields. The spectrum of the radiation when $K < 1$ consists of one main peak that is three orders of magnitude in energy density greater than at other photon energies, as shown in the top spectrum in Figure 25. When $K = 1$, the spectrum consists of a series of harmonics with comparable energy density at higher photon energies. Comparing the top and the middle panels, the first harmonic is at a similar photon energy as in the case of $K < 1$.

When $K \gg 1$, many harmonics are produced at high photon energies, with a higher energy density than the fundamental. In the bottom spectrum in Figure 25, the spectrum starts to look continuous at photon energies above 1 keV. The spectrum also looks like the energy density spectrum produced by an electron following a circular

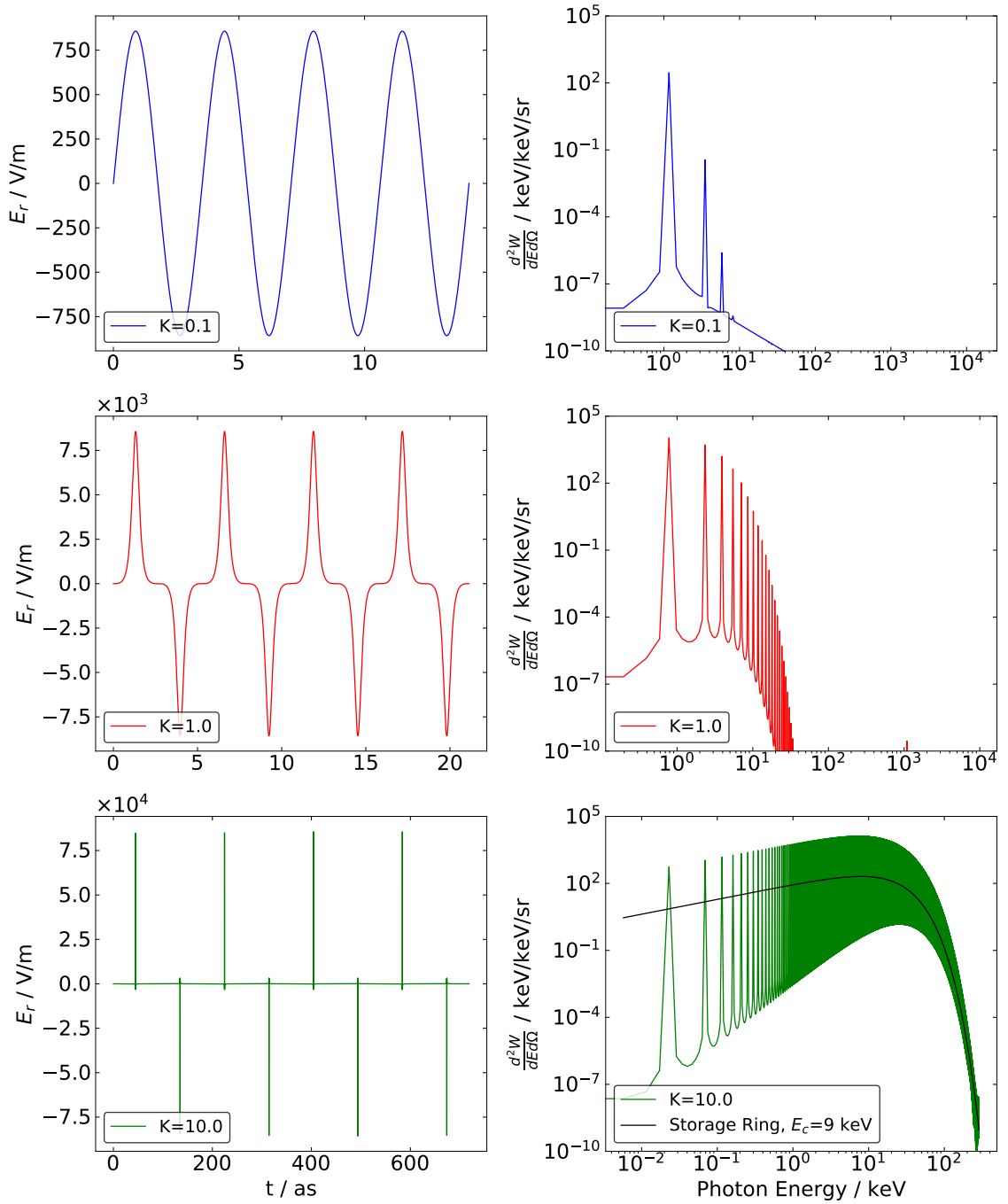


Figure 25: (Left) Transverse electric field component against time of observation. (Right) Energy density spectrum at an on-axis observation point for an electrons with different K-parameters following sinusoidal trajectories.

trajectory, which was introduced in Section 2.11.4. This was described by Equation 2.91, plotted as the black line in the bottom spectrum in Figure 25. For a critical photon energy of 9 keV, there is good agreement between Equation 2.91 and the numerical spectrum. This suggests that the trajectory of the oscillating electron with $K \gg 1$ can be modelled by a circular arc at the points where the radiation cone points towards the observation point. A circular arc could be fitted to the electron trajectory using the formula for the radius of curvature of a function [158]:

$$\rho(z) = \left| \frac{\left(1 + \left(\frac{dr}{dz}\right)^2\right)^{\frac{3}{2}}}{\frac{d^2r}{dz^2}} \right|. \tag{2.100}$$

Using Equation 2.93 for the direction of travel of the electron and the approximation $z \approx ct$, the radius of curvature can be written as a function of this parameter:

$$\rho(\theta_e) = \left| \frac{(1 + \theta_e^2)^{\frac{3}{2}}}{k_\beta \sqrt{\frac{K^2}{\gamma^2} - \theta_e^2}} \right|. \tag{2.101}$$

For an on-axis observation point like the one used in Figure 25, $\theta_e = 0$ so the radius of curvature becomes $\rho = 1/k_\beta^2 r_\beta$. This describes the radius of curvature of the sinusoidal trajectory at its turning points, where the electron emits radiation on-axis. In the case of $K = 10$ in Figure 25, $\gamma = 500$, $k_\beta = 1.2 \times 10^4$ m^{-1} and $r_\beta = 1.7$ µm, producing a radius of curvature of 4.2 mm. Substituting this into Equation 2.90 produces a critical energy of 9 keV, which is also the critical energy producing the best fit in the bottom spectrum of Figure 25.

The energy density spectrum of the radiation produced by an electron oscillating in an LWFA can thus be described by the spectrum produced by an electron following a circular trajectory. Figure 26 shows the on-axis synchrotron spectra produced by electrons with different Lorentz factors that are typically reached in LWFAs. A typical oscillation amplitude of 2 µm was chosen. In these parameter regimes, the critical energies are between 10 and 100 keV, which are comparable to those reached in the storage ring of the Diamond Light Source, analysed earlier. The spectral energy densities reached are not as high as those reached in the storage ring plotted in Figure 20, which is due to the smaller Lorentz factors of the electrons in the LWFA.

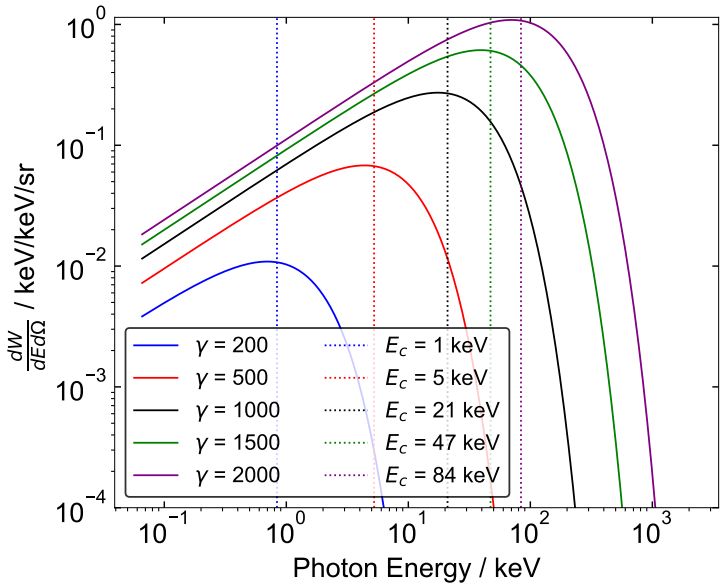


Figure 26: On-axis energy density spectra produced by electrons with different Lorentz factors in an LWFA with a plasma density of 2×10^{18} cm^{-3}. All electrons considered in this plot have a betatron oscillation amplitude of 2 µm.

3. Radiation Simulation Methods

The synchrotron radiation from an LWFA was modelled by simulating the particle trajectories and momenta of particles in a PIC simulation and then calculating the Liénard-Wiechert fields at different positions on a user-defined grid. The intensity and energy density of the radiation can then be calculated. The first radiation computation code (RCC) computes the temporal and spectral intensity profiles at each point in the grid. The second RCC computes the angular energy density distribution of the x-ray beam, which is run at a higher spatial resolution than the first. The computation procedures of both RCCs are described here.

3.1 Particle-in-Cell Simulations

The PIC code "Smilei" was used to simulate an LWFA and track the trajectories and momenta of electrons accelerated in the wakefield. A detailed description of the workings of this PIC code is given by Derouillat *et al.* [159]. A brief overview is given here. The spatial domain of the plasma is set up as a grid of small cells. Each cell contains a number of macroparticles, each of which represent some number of electrons, determined by the initial electron density of the plasma and the pre-defined number of macroparticles per cell.

The initial number density, mean velocity and temperature of the electrons are prescribed by the user [159]. For simulating an LWFA, whose plasma is formed from a cold, ionised gas, the number density should mimic the gas density profile. The PIC simulation loads the macroparticles with statistical weights such that the plasma has this number density. They are distributed uniformly in each grid cell [159], and are initialised to have zero momentum and zero mean velocity. The laser pulse is loaded at its initial position outside the plasma.

The motion of the particles is simulated using the Maxwell-Vlasov system of equations in a series of discrete time-steps. Each grid cell has some charge and current density, determined by the number of constituent macroparticles and their motion in the cell. In

each time-step, the charge and current densities in each grid cell are calculated, from which the electromagnetic fields are calculated using Maxwell's equations. Then, the motion of the macroparticles due to these fields are calculated from the Lorentz force due to those fields [159].

3.1.1 PIC Simulations for Modelling X-rays from LWFAs

In this work, the LWFAs were simulated using Smilei in a cylindrical geometry with azimuthal mode decomposition, which decreased the computational load and computation time. As shown by Lifschitz *et al.* in 2009 [160], the scalar and vector fields can be decomposed into a Fourier series containing a number of azimuthal modes. The electromagnetic fields in each mode are solved using Ampère's law and Faraday's law in Fourier space [160], which has some advantages in the simulation of LWFAs. This method removes certain numerical dispersion effects that can result in the slowdown of electromagnetic waves in plasma [161], and counteracts the numerical emittance growth of ultrarelativistic electron beams [162].

To model the synchrotron radiation from PIC simulations from an LWFA, the trajectories and momenta of accelerated electrons are required to calculate their Liénard-Wiechert fields. To obtain the particle trajectories and momenta, the PIC simulation is run with a particle tracking diagnostic. So that only electrons accelerated in the wakefield are considered, to save computation time, a filter is applied to this diagnostic such that electrons with an energy above some threshold are tracked. This threshold is set to a minimum of 10 MeV. When electron beams are accelerated to GeV-order energies the threshold is set higher at 200 MeV. It is assumed that the radiation produced by electrons at lower energies is negligible, as implied by Equation 2.99.

3.2 Model Setup

The synchrotron radiation properties are computed at the positions of different points on a user-defined grid, as shown in Figure 27. The grid is centred on the longitudinal axis along which the centre of the laser pulse, the wakefield, the electron beam and the radiation beam propagate. In these RCCs, this axis is set to be the z-axis. The accelerated electrons in the LWFA thus oscillate in the planes perpendicular to the z-axis. In the first RCC computing the temporal and spectral properties of the radiation, the grid typically consists of 9×9 observation points. Computing the temporal and spectral intensity profiles requires more computational steps that involve processing large arrays that can have over 10^6 elements. As such, in the second RCC computing the spatial energy density distribution, the grid typically consists of 32×32 points.

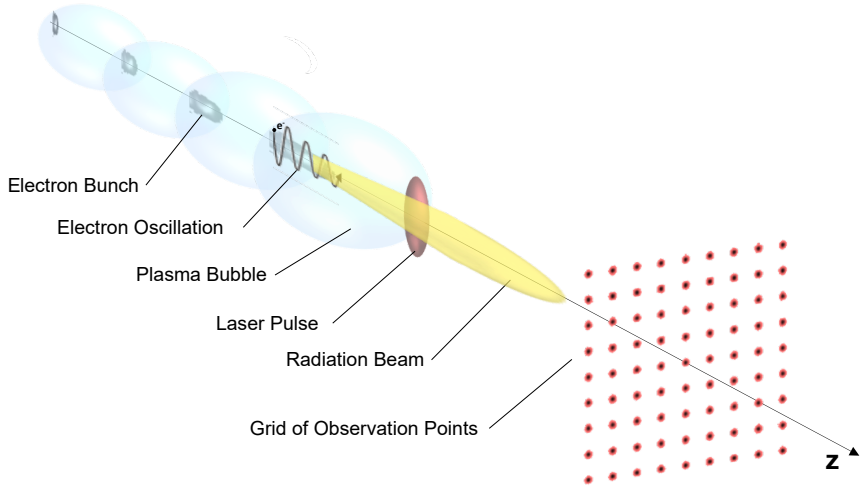


Figure 27: Setup of observation radiation computation model, consisting of a grid of observation points centred on the longitudinal axis.

3.3 Temporal Intensity Profile

The temporal intensity profile is the radiation property that is most computationally challenging and expensive to model. Most of the effort in the first RCC is put into counteracting the "retarded-observed time problem," which arises when calculating the Liénard-Wiechert fields from the trajectories and momenta of tracked particles in the PIC simulation. Considering two particles accelerating at the same time-step in the PIC simulation and emitting synchrotron radiation, corresponding to the retarded time, two different distances from a stationary observer (one observation point), the times of observation of the radiation that they produce are given by Equation 2.72:

$$t_{obs,\,1} = t_{ret} + \frac{r_1}{c}, \tag{3.1}$$

$$t_{obs,\,2} = t_{ret} + \frac{r_2}{c}. \tag{3.2}$$

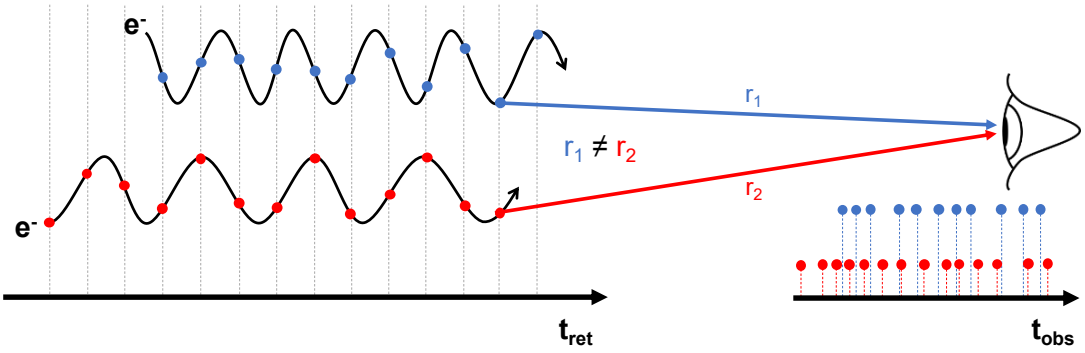


Figure 28: Schematic of the retarded-observed time problem considering two electrons whose data points correspond to the same array of retarded times.

r_1 and r_2 are the distances of the respective electrons from the observer, as shown in Figure 28. In this conceptual diagram, $r_1 \neq r_2$, so $t_{obs,\,1}$ and $t_{obs,\,2}$ are different. The radiation emitted by the first electron is observed at a different time to the radiation from the second electron.

In the particle tracking diagnostic of the PIC simulation, the trajectory of every particle is recorded at the same set of times. In terms of radiation emission, this is a set of retarded times, as the electrons emit the radiation at these times. When calculating the Liénard-Wiechert field produced by an electron at these retarded times, the results correspond to a sequence of times of observation, calculated using Equation 2.72. Considering another electron following a different trajectory, its Liénard-Wiechert field array corresponds to a different sequence of times of observation. To calculate the total electric field, the arrays of these two Liénard-Wiechert fields can only be added together if the arrays correspond to the same sequence of times of observation. This is highly unlikely because their trajectories, and thereby their distance to the observer at each retarded time, are different.

3.3.1 Workaround to the Retarded-Observed Time Problem

For the arrays representing the Liénard-Wiechert fields of the radiation from different electrons to be superposed at some position of observation, their elements need to correspond to the same sequence of times of observation. Each Liénard-Wiechert field array computed needs to be transformed onto the same sequence of times of observation. Thus, an array of times of observation is defined with a constant, user-defined difference between its elements, represented by the axis in Figure 29. The resolution of this axis is chosen based on the discussion in Section 3.6. The starting and ending times on the axis are the minimum and maximum times of observation from all of the tracked electrons, calculated from their positions in the first and final time step of the PIC simulation. Alongside this sequence of times, an array of the same length is defined for each component of the total electric field, initially set with zeros as all of its values.

In Figure 29, a single electric field component computed from a single electron at a single observation point is considered. The electron's Liénard-Wiechert field is calculated using Equation 2.76, repeated here:

$$\mathbf{E}(t_{obs}) = \frac{e}{4\pi\epsilon_0\gamma^2}\left(\frac{\mathbf{n}-\boldsymbol{\beta}}{r^2(1-\mathbf{n}\cdot\boldsymbol{\beta})^3}\right)_{ret} + \frac{e}{4\pi\epsilon_0 c}\left(\frac{\mathbf{n}\times((\mathbf{n}-\boldsymbol{\beta})\times\dot{\boldsymbol{\beta}})}{r(1-\mathbf{n}\cdot\boldsymbol{\beta})^3}\right)_{ret}. \tag{3.3}$$

The calculation is performed by taking the arrays representing the trajectory and mo-

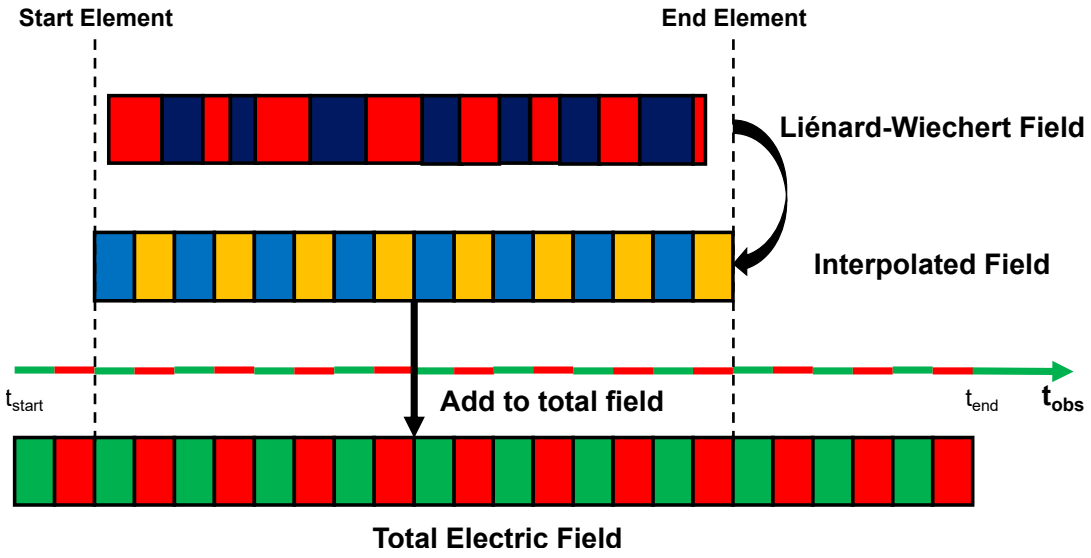


Figure 29: Overview of transformation of the Liénard-Wiechert field onto a temporal axis, defined by an array of times increasing linearly. The output electric field is added to an array for the total observed electric field, defined on the same temporal axis.

mentum progression of the electron in the plasma, which produces an array of electric field values corresponding to some array of times of observation dependent on the electron's trajectory. This set of times of observation is calculated from Equation 2.72; an array of times of observation is produced. The times of this array's first and last elements are used to locate the corresponding starting and ending elements on the pre-defined temporal axis. The top array in Figure 29 is the initially calculated Liénard-Wiechert field array located on the pre-defined temporal axis. However, this array's elements do not align exactly with the pre-defined temporal axis and have different temporal separations. A linear interpolation is then performed on the initial Liénard-Wiechert field array, producing an array of interpolated electric field values shown as the second array in Figure 29. The interpolated array lines up with the elements of the pre-defined temporal axis. This interpolated electric field array can then be added to the pre-defined total electric field array between the starting and ending elements.

The above procedure of calculating the Liénard-Wiechert field array, interpolating that array and then adding the interpolated array to the total electric field array is repeated for each particle, one by one. It should be remembered that each particle is a macroparticle from the PIC simulation, representing a many electrons. Once all of the particles have been processed, the total electric field array is the electric field of the radiation pulse produced by all of the electrons represented by those particles.

3.3.2 Intensity Calculation

The instantaneous radiation intensity is given by the magnitude of the Poynting vector of the electromagnetic fields [163]:

$$I = |\mathbf{S}| = \frac{1}{\mu_0}|\mathbf{E} \times \mathbf{B}|. \tag{3.4}$$

Using the identities $\mathbf{B} = \mathbf{n} \times \mathbf{E}/c$ and $1/\mu_0 = c^2\epsilon_0$, the intensity can be written in terms of the electric field magnitude only:

$$I = c\epsilon_0|\mathbf{E}||\mathbf{E}||\cancelto{1}{\mathbf{n}}|\cancelto{1}{\sin 90^\circ}\cancelto{1}{\sin 90^\circ} = c\epsilon_0|\mathbf{E}|^2. \tag{3.5}$$

This spares the RCC the steps of calculating the magnetic field and performing the vector product of the Poynting vector. The intensity of the radiation pulse is calculated using just the total electric field array:

$$I(t_{obs}) = c\epsilon_0\big(|E_x(t_{obs})|^2 + |E_y(t_{obs})|^2 + |E_z(t_{obs})|^2\big). \tag{3.6}$$

3.4 Spectral Intensity Profile

The intensity spectrum is calculated from the temporal profile of the total electric field, obtained via the procedure described in the previous section. At one observation point at a time, the fast-Fourier transform of each electric field component is taken. Then, the intensity spectrum is calculated similarly to the temporal intensity profile:

$$I(\omega) = c\epsilon_0\big(|E_x(\omega)|^2 + |E_y(\omega)|^2 + |E_z(\omega)|^2\big). \tag{3.7}$$

To calculate the energy density spectrum, the intensity spectrum is multiplied by the duration of the x-ray pulse: $U(\omega) = \tau I(\omega)$. The pulse duration is calculated by dividing the total energy density of the temporal intensity profile by the numerically calculated mean intensity:

$$\tau = \frac{\int_0^\infty I(t_{obs})\, dt_{obs}}{\langle I(t_{obs})\rangle}. \tag{3.8}$$

The energy density spectrum can be used to calculate the spectral brightness of the x-ray beam, which is the commonly reported quantity from experimental measurements of x-ray beams from LWFAs [59], [60], [65], [67], [70]–[72], [164]. The spectral brightness is written in units of photons/s/mrad^2/mm^2/0.1% BW. First, the photon fluence spectrum is calculated by dividing the energy density spectrum by the photon energy, $N(\omega) = U(\omega)/\hbar\omega$, and then integrating the spectrum into bins of 0.1% bandwidth. Then, the peak spectral brightness is calculated by dividing the peak on-axis

spectral fluence by the area of the electron beam and the duration of the x-ray pulse:

$$\mathcal{B} = \frac{1}{\pi r_\beta^2 \, \tau} \left(\frac{d^2 N}{d\Omega dE} \right). \tag{3.9}$$

As the peak spectral brightness is produced on-axis, the source size is determined by the average oscillation amplitude of the electrons.

3.5 Angular Energy Density Distribution

The angular energy density distribution of the radiation beam is computed using fewer computational steps than for the temporal and spectral intensity profiles. Each particle is still processed individually; each particle's Liénard-Wiechert field is calculated using its trajectory and momentum in Equation 2.76. The temporal intensity profile of this field is then computed using Equation 3.6, which is then integrated over the time of observation to produce an energy density:

$$U(t_{obs}) = \int_0^\infty I(t_{obs}) \, dt_{obs}. \tag{3.10}$$

Because the radiation beam is temporally incoherent, which is explained in Section 3.7, the total energy density of the radiation beam can be calculated by adding the energy density of the individual waves from the electrons. This energy density is then added to a pre-defined energy density array, whose values are initially set to zero.

3.6 Temporal Resolution

It was shown in Section 2.12.2 that an oscillating electron with $K \gg 1$ produces a Liénard-Wiechert field that consists of a series of flashes, emitted when the electron is travelling in the direction towards the point where the radiation is observed. The angular range over which some part of the radiation cone is directed towards the observer is well-approximated by $2/\gamma$. By approximating the trajectory of the electron as a circular arc and assuming that the electron travels at the speed of light in vacuum, the time taken for the electron to travel through an angle of $2/\gamma$ can be expressed:

$$\Delta t_{2/\gamma} = \frac{2\rho}{\gamma c}, \tag{3.11}$$

where ρ is the radius of curvature of the electron's trajectory, which can be calculated using Equation 2.101. As a typical example in an LWFA driven by a 10 TW-class laser, an electron in a plasma with $n_e = 1 \times 10^{19}$ cm^{-3} oscillating with $r_\beta = 5$ µm and $\gamma = 600$ produces $\Delta t_{2/\gamma} = 7$ fs. For a 100 TW-class laser, an electron in a plasma

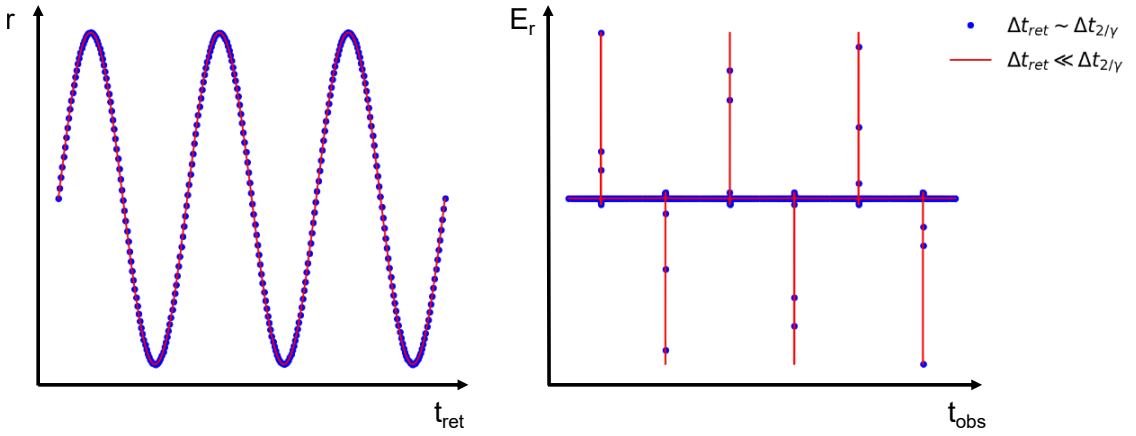


Figure 30: Data points produced from a particle trajectory with $\Delta t_{ret} \approx \Delta t_{2/\gamma}$ and interpolated functions for (left) the particle trajectory against retarded time and (right) the Liénard-Wiechert field against time of observation.

with $n_e = 2 \times 10^{18}$ cm^{-3} oscillating with $r_\beta = 5$ µm and $\gamma = 1500$ this becomes $\Delta t_{2/\gamma} = 30$ fs.

For the flashes in the Liénard-Wiechert field to be resolved, the condition $\Delta t_{ret} < \Delta t_{2/\gamma}$ must be satisfied, where Δt_{ret} is the retarded time interval between successive data points in the particle trajectories must be smaller than this retarded time interval. However, having a PIC simulation record the particle trajectories and momenta after every short time interval of $\Delta t_{2/\gamma}$ can consume a lot of memory and time. Instead, the PIC simulation records the electrons' positions and momenta at around $\Delta t_{ret,\,PIC} \sim \Delta t_{2/\gamma}$, and a higher temporal resolution is obtained in the RCC by performing a quadratic interpolation of the particle trajectories and momenta at a resolution of $\Delta t_{ret} < \Delta t_{2/\gamma}$.

In Figure 30, we consider the example of an electron following a sinusoidal trajectory, travelling with constant energy. On the left plot, the pre-interpolated data points for the particle trajectory are plotted as the blue points. The temporal resolution of these data points is $\Delta t_{ret,\,PIC} \sim \Delta t_{2/\gamma}$. The blue points on the right plot show the calculated Liénard-Wiechert field if it was calculated from the pre-interpolated data points in the particle trajectory. The flashes made up of blue points should all have the same amplitude, but as their temporal resolution is too low the peaks of the flashes are often missed. The red curve on the left plot is the electron trajectory that has been interpolated at $\Delta t_{ret} < \Delta t_{2/\gamma}$. Calculating the Liénard-Wiechert field from this trajectory produces the field given by the red curve on the right plot. All of the flashes in the Liénard-Wiechert field are then resolved.

3.6.1 Interpolation Procedure of Trajectories and Momenta

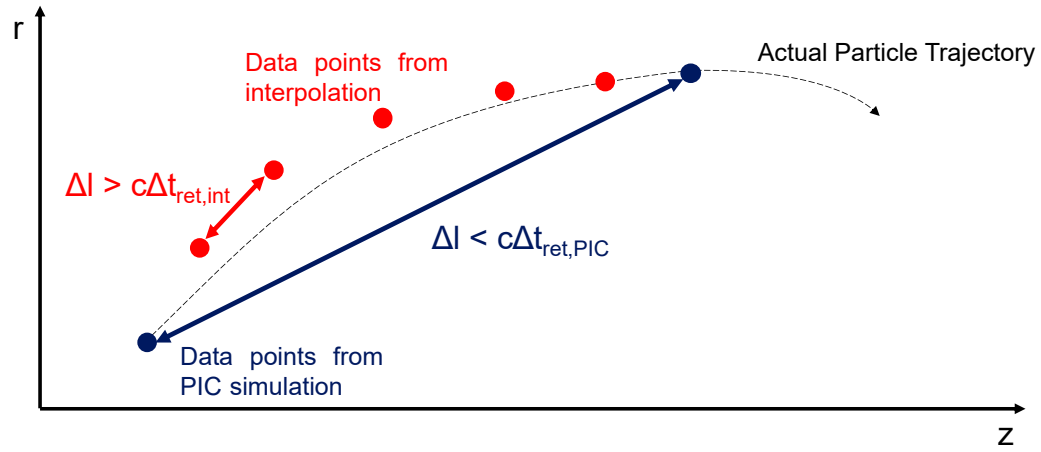


Figure 31: Schematic of problem interpolating trajectories from PIC simulation directly.

Sometimes, interpolating the trajectories of electrons directly can produce trajectories whose data points are separated by a distance of $\Delta l > c\Delta t_{ret}$. For this to occur, the electron would have to travel faster than the speed of light in vacuum, which is obviously unphysical. The interpolated trajectory can differ slightly from the actual trajectory followed by the electron, as shown in Figure 31. In this schematic, the red points are the data points of the interpolated trajectory, which has a slightly larger curvature than the actual trajectory. The distance between some of these points is $\Delta l > c\Delta t_{ret}$. The reason for this is because an interpolation sees the trajectory simply as a mathematical function. The interpolation is not constrained by any physical laws and is not "aware" of the electromagnetic forces experienced by an electron as it passes through the plasma.

The interpolation of each particle trajectory needs to be performed in such a way to satisfy the following condition:

$$\sqrt{(\Delta x)^2 + (\Delta y)^2 + (\Delta z)^2} < c\Delta t_{ret}, \tag{3.12}$$

where Δx, Δy and Δz are the components of the displacement between consecutive interpolated electron positions at t_{ret} and $t_{ret} + \Delta t_{ret}$. Instead of interpolating the trajectories directly, the components of the momentum of the electron are interpolated, from which the velocity components are calculated:

$$\mathbf{v}(t_{ret}) = \frac{\mathbf{p}(t_{ret})}{\gamma(t_{ret}) m_e}, \tag{3.13}$$

where $\gamma(t_{ret}) = \sqrt{p(t_{ret})^2 + m_e^2 c^4}/m_e c^2$. This produces a velocity of the electron that is physical. The trajectory of the electron can then be computed by numerically

integrating its velocity from its initial position at injection:

$$\mathbf{R} = \mathbf{R_0} + \int_0^{t_{ret}} \mathbf{v}(t_{ret})\, dt_{ret}, \tag{3.14}$$

where $\mathbf{R_0}$ is the initial position of the electron. The acceleration of the electron is calculated numerically as the time derivative of the velocity:

$$\dot{\mathbf{v}} = \frac{d\mathbf{v}}{dt_{ret}} \tag{3.15}$$

The interpolated trajectory, velocity, acceleration and Lorentz factor of the electron are then used to calculate the Liénard-Wiechert fields produced by the electron.

3.6.2 Temporal Resolution of Liénard-Wiechert Fields

Equation 2.75 showed that a short interval in the retarded time corresponds to some observed time interval in its radiation. When the electron is travelling towards the observation point, the retarded time interval is shortened by the factor $(1 - \mathbf{n} \cdot \boldsymbol{\beta})$. A result of this temporal shortening is that the Liénard-Wiechert field, calculated from the interpolated electron trajectory and momentum in the retarded time, has its temporal resolution shortened by the same factor:

$$\Delta t_{obs} = (1 - \mathbf{n} \cdot \boldsymbol{\beta})\, \Delta t_{ret}. \tag{3.16}$$

As the electron travels towards an observation point so $\mathbf{n} \cdot \boldsymbol{\beta} = n\beta \cos 0 = \beta$, the retarded time interval is shortened by the factor $(1-\beta)$, which approximates to $1/2\gamma^2$, as derived in Appendix E.3. This is the strongest possible temporal shortening factor for an electron with some Lorentz factor, γ. The temporal resolution of the observed Liénard-Wiechert field can also be approximated using the electron's Lorentz factor:

$$\Delta t_{obs} \approx \frac{\Delta t_{ret}}{2\gamma^2}. \tag{3.17}$$

Equation 3.11 for the retarded time interval can be substituted into Equation 3.17. As $\Delta t_{ret} \ll \Delta t_{2/\gamma}$,

$$\Delta t_{obs} \ll \frac{\rho}{\gamma^3 c}. \tag{3.18}$$

The duration of each radiation flash according to the observer also takes this form, which is derived in Appendix E.4:

$$\Delta t_{flash} = \frac{4\rho}{3\gamma^3 c}. \tag{3.19}$$

The ratio of Δt_{obs} and Δt_{flash} shows that the interval between the observed times of the data points in the Liénard-Wiechert field is much smaller than the duration of the radiation of the radiation flash:

$$\frac{\Delta t_{obs}}{\Delta t_{flash}} \ll 0.75. \tag{3.20}$$

This means that so long as $\Delta t_{ret} < \Delta t_{2/\gamma}$, there are enough data points inside each radiation flash to temporally resolve them. In practice, the energies of the electrons change over time in the LWFA, so Δt_{ret} needs to be shorter than the shortest value of $\Delta t_{2/\gamma}$, which occurs when the electrons reach their peak energy.

3.6.3 Interpolation of the Liénard-Wiechert Fields for the Temporal Intensity Profile

In Figure 32, the Liénard-Wiechert field has been calculated from a single sinusoidal electron trajectory with $K = 10$, which is a typical betatron strength parameter seen in PIC simulations of LWFAs. In the top plot, the time difference between neighbouring data points in that Liénard-Wiechert field is plotted. The top plot shows that even when the energy of the electron is constant, the sampling time changes. This is because the time shortening factor $(1 - \mathbf{n} \cdot \boldsymbol{\beta})$ changes as the direction of travel of the electron changes. The factor is smallest when the electron is at the turning points in its trajectory, as $\mathbf{n} \cdot \boldsymbol{\beta} = n\beta \cos 0 = \beta$, which is its largest possible value. In the bottom panel of Figure 32, the Liénard-Wiechert field is plotted, showing that the minimum in the time shortening factor coincides with when the electron produces the flashes in the Liénard-Wiechert field. Plotted in red is the Liénard-Wiechert field at the times of observation calculated from $t_{obs} = t_{ret} + r/c$. Plotted in black is the interpolated Liénard-Wiechert field. The interpolation does not change the form of the Liénard-Wiechert field; it only applies a transformation to the elements in the array.

It should be stressed that the interpolation of the Liénard fields is **not** to increase the temporal resolution, but to align the electric field data points onto the same temporal axis. If a user wants to resolve higher frequencies in the radiation, the retarded time interval in the interpolation of the electron trajectories and momenta should be increased. Generally, the electron trajectories and momenta are interpolated to a temporal resolution of $\Delta t_{ret} = 0.1$ fs. With electrons reaching energies of hundreds or thousands of megaelectronvolts, this allows frequencies of at least 10^{20} Hz (~ 100 keV photon energies) to be resolved.

In practice, a temporal resolution at which to perform the electric field interpolation

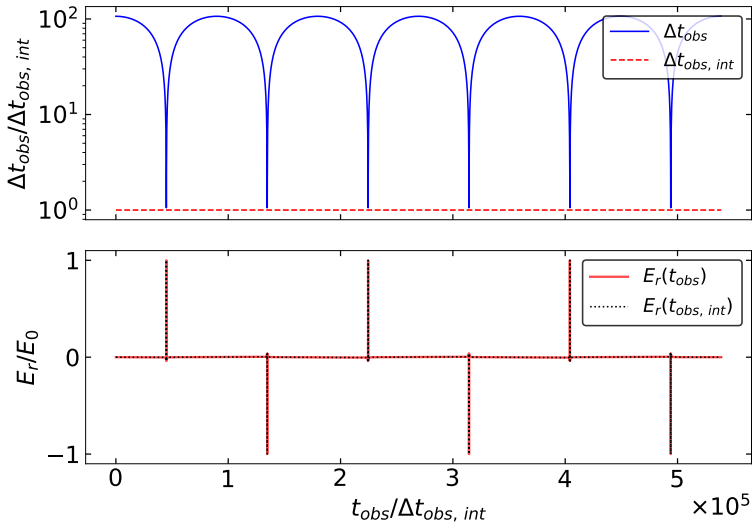


Figure 32: (Top) Difference in time between successive data points in the calculated Liénard-Wiechert field as a fraction of the time interval at which the field is interpolated. (Bottom) Plots of the calculated Liénard-Wiechert field and times of observation, compared with the interpolated field along the pre-defined temporal axis.

is not as straightforward to choose as in Figure 32, owing to the significant spread in the energy and K-parameter of electrons in the accelerated beam. Generally, $\Delta t_{obs,\,i} = \Delta t_{ret}/2\gamma_{max}^2$ is used, where γ_{max} is the Lorentz factor of the electrons with the highest energy in the beam, when at the highest energies in their acceleration. Then, the shortest radiation flashes produced by the electrons with the highest energies should be resolved.

3.7 Temporal Coherence of Radiation from a Single Macroparticle

As explained in Section 3.1, the particles in a PIC simulation are macroparticles that each represent a number of electrons in the plasma. The number of electrons that a macroparticle represents is often referred to as the statistical weight of the macroparticle. In PIC simulations with cells with longitudinal and transverse dimensions of 18.75×187.50 nm, which is the resolution used in the PIC simulations in this work, the macroparticles have weights on the order of 10^5. These 10^5 electrons follow the same trajectory and momentum progression, and crucially produce identical Liénard-Wiechert fields. In effect, their Liénard-Wiechert fields are exactly in phase with each other and interfere totally constructively. The intensity of the radiation would scale as $I \propto N^2$, where N is the statistical weight of the macroparticle [31]. In this case, the electric fields would add linearly and the total field would look like the one plotted in

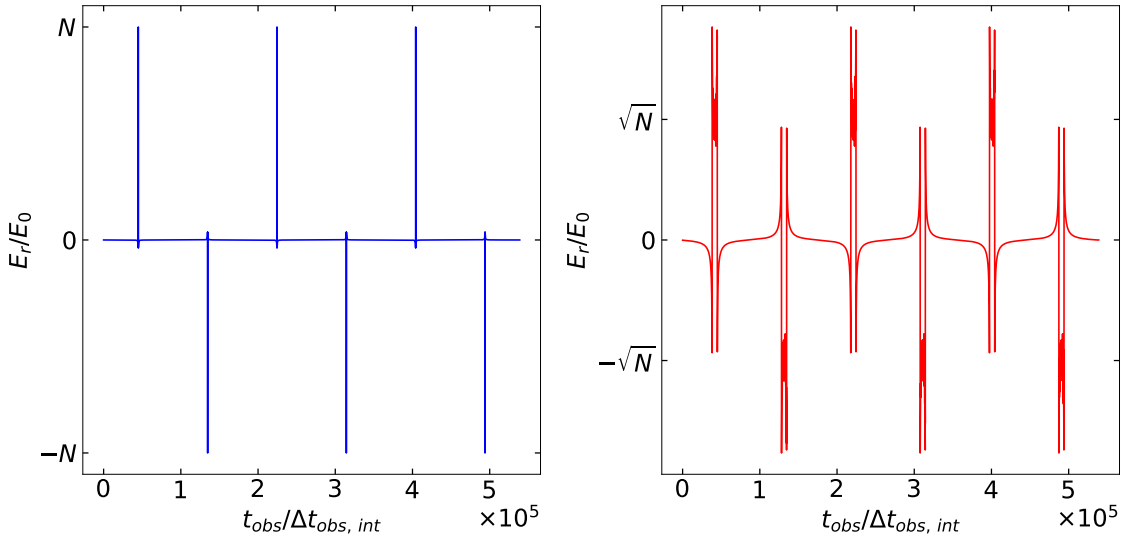


Figure 33: (Left) Normalised electric field produced by 10^5 coherently oscillating electrons, each producing an identical Liénard-Wiechert field with an amplitude of E_0. (Right) Normalised total electric field produced by $N = 10^5$ electrons with uniformly distributed random starting positions within a 1 nm range.

the left panel of Figure 33, where each electron produces a Liénard-Wiechert field with an amplitude of E_0. The amplitude of the total electric field is NE_0.

For an electron beam with a typical total charge of ~ 100 pC and dimensions of $\sim 10 \times 1 \times 1$ µm, assuming an approximately constant charge density, the average distance between electrons can be calculated to be on the order of 1 nm. As this is longer than the wavelength of the radiation that they produce, the electric fields add according to $\sqrt{N}$ and the intensity scales as $I \propto N$, like the radiation from a temporally incoherent source [31], [165]. In the right panel of Figure 33, the total electric field from the superposition of the Liénard-Wiechert fields of $N = 10^5$ electrons has been calculated; each electron has been given a uniformly random starting position within a 1 nm range. The plotted total electric field shows that the amplitude of the total electric field increases proportionally with $\sqrt{N}$. Hence, the macroparticles are not a realistic representation of the the electrons producing the radiation. In the RCC, the charge of the macroparticle is taken as $q = \sqrt{N}e$.

4. Modelled X-ray Beams from LWFAs

In this chapter, we report on the output temporal, spectral and angular intensity profiles produced by the radiation computation codes (RCCs) described in the previous chapter, which have been applied to six different LWFA light sources. In Section 4.2, the modelled temporal intensity profiles produced by the first RCC are reported and analysed. In Section 4.3, we report on the photon fluence spectra produced by the first RCC. Section 4.3 investigates the properties of the intensity spectra modelled by the first RCC, both on-axis and off-axis. Finally, Section 4.4 reports on the output angular energy density distributions of the second RCC.

4.1 Simulated LWFAs

The x-ray beams of six different LWFAs were modelled by performing a PIC simulation of the LWFA and then running the RCCs on the tracked particles. For each LWFA, a PIC simulation was run with a longitudinal, radial and temporal resolution of 18.75 nm, 187.50 nm and 0.06 fs. The electron beam properties were found to converge around these resolutions. The physical input parameters in these experiments are presented in Table 4.1. From this point onward, the experiment labels in this table will be used to refer to whatever LWFA being modelled. In the cases of Rousse (2004), Kneip (2010) and Wenz (2015), listed above the dashed line in Table 4.1, the laser pulses were sub-100 TW and were focused into millimetre-long plasmas with electron densities of 10^{19} cm^{-3}. In the cases of Wood (2018) and Bloom (2020), laser pulses with ~ 100 TW powers were focused into centimetre-long plasmas with densities around 10^{18} cm^{-3}. Finally, the Extreme Photonics Applications Centre (EPAC) is an upcoming facility at the Rutherford Appleton Laboratory in the United Kingdom [166]; a possible LWFA setup was simulated. A 1 PW laser [167] is focused into a plasma with an electron density of 10^{18} cm^{-3} and a length of 40 mm.

Table 4.1: Experimental input parameters of LWFAs whose radiation was modelled

Experiment Label	E / J	τ / fs	P / TW	a_0	w_0 / µm	n_e / cm^{-3}	L_{plasma} / mm
Rousse (2004) [60]	1.0	30	33	1.2	18.0	1.1×10^{19}	3
Kneip (2010) [65]	2.3	32	72	4.7	9.5	8.0×10^{18}	5
Wenz (2015) [70]	1.6	28	57	2.2	18.7	1.1×10^{19}	6
Wood (2018) [72]	10.5	50	210	3.3	16.1	2.5×10^{18}	10
Bloom (2020) [164]	12.0	55	210	3.0	18.7	3.8×10^{18}	10
EPAC	30.0	30	1000	1.7	54.0	1.3×10^{18}	40

4.2 Modelled Temporal Intensity Profiles

We first consider the temporal profile of x-ray beams from LWFAs, which have not yet been fully characterised. In experiment, this is difficult due to the ultrashort pulse duration of the radiation. A temporally resolved measurement would require very sophisticated pump-probe techniques. So far, attempts to model the temporal intensity profile of these radiation beams have been sparse. One attempt by Horný *et al.* in 2017 [168] used numerical methods similar to those described in Section 3.3. The femtosecond duration of the radiation pulses was demonstrated, but their code was only applied to PIC simulations of short LWFAs up to 2 mm in length [168]. The first RCC in this work models temporal intensity profiles of the radiation from electron beams accelerated to higher energies in larger LWFAs. The radiation is also modelled at different points of observation, not just on-axis, allowing for the angular variation of the temporal intensity profiles to be studied.

Before reporting on the temporal intensity profiles produced by the first RCC, an expression is derived for the on-axis intensity of the radiation. This model is compared with the on-axis temporal profiles produced by the RCC. It is shown that these profiles help describe the acceleration of different electron bunches within the beam. The temporal profiles at different points of observation, lying at different divergence angles, are also shown and analysed.

4.2.1 Approximate On-Axis Temporal Intensity Profile

An approximate expression for the on-axis temporal intensity profile is now derived. The electron beam is split into short ~ 1 µm length slices across its length, such that each slice has a different longitudinal coordinate. It is assumed that in each slice, the electrons' energy progression and amplitude of oscillation is the same. It is also assumed that the radiation intensity is dominated by the radiation emitted when the electrons are at the peak energy in their acceleration. Equation 2.99 expresses the energy density of the radiation emitted by a single oscillating electron. By substituting

$K = \gamma k_\beta r_\beta$ into this equation and using Equation 2.62, then setting $\theta_e = 0$, the energy density radiated on-axis by a single electron can be expressed. The total energy density radiated by a slice in the electron beam is approximated by multiplying this expression by the number of electrons in the slice:

$$U_{tot,\,slice} = \frac{7Ne^2}{128\pi\epsilon_0 c^2}\omega_p^2 r_\beta \gamma_{peak}^4, \tag{4.1}$$

where N is the number of electrons in the slice. Dividing the total energy density radiated in the slice by the effective duration of the slice, $\Delta t = \Delta\xi/c$, produces an average radiation intensity for the slice:

$$I = \frac{U_{tot,slice}}{\Delta\xi}c, \tag{4.2}$$

where $\Delta\xi$ is the length of the slice. The on-axis intensity radiated by electrons as a function of their position in the beam is proportional to $N(\xi)\gamma_{peak}^4(\xi)$. The $N(\xi)\gamma_{peak}^4(\xi)$ profile is effectively a predicted intensity profile of the radiation pulse.

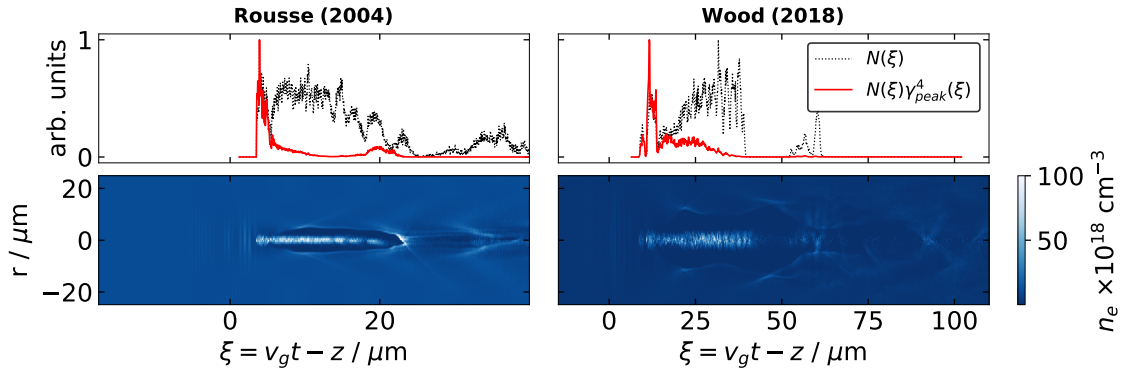


Figure 34: (Top) Longitudinal profiles of the total electrons and total $N(\xi)\gamma_{peak}^4(\xi)$ at the end of each plasma, in arbitrary units. (Bottom) Map of electron density at the same positions in the plasma. The laser pulse is propagating to the left of the page.

The profiles of $N(\xi)$ and $N(\xi)\gamma_{peak}^4(\xi)$ at the end of the plasma are plotted in Figure 34, for the examples of Rousse (2004) and Wood (2018). The electron beams at the end of the plasma are used because all electrons producing radiation have been injected and accelerated by that point. In the top panels, the red lines are the predicted intensity profiles calculated using Equation 4.2 and the black dotted lines are the longitudinal electron number distribution in the electron beam. In the bottom panels are maps of the electron density in the plasma, showing the electron beam in the plasma wave. In all plots, the laser pulse is propagating to the left of the page.

In the PIC simulation of the low power case of Rousse (2004), the $N(\xi)$ profile is

roughly constant in the first 10 µm of the electron beam. However, the $N(\xi)\gamma^4_{peak}(\xi)$ profile peaks in the first 3 µm. It is these electrons that must be accelerated to the highest energies. In the bottom panel of Rousse (2004), the electrons at the front of the electron beam almost reach the front of the bubble at $\xi = 3$ µm by the end of the plasma. The bubble and the electron beam are elongated due to the merging of the two electron bunches in the first and second bubbles behind the laser pulse, once the electrons in the second bubble have traversed the bubble's length. Consequently, the expected x-ray profile in the top panel of Rousse (2004) is one continuous pulse.

Conversely, in the high power case of Wood (2018), the $N(\xi)\gamma^4_{peak}(\xi)$ profile in the top panel consists of two short peaks at the front, followed by a long period of low values between $\xi = 15$ µm and 35 µm. The difference in structure of the expected profile of Wood (2018) to Rousse (2004) is principally due to the difference in the LWFAs' self-injection processes. The two peaks at the front of the $N(\xi)\gamma^4_{peak}(\xi)$ profile align with two electron bunches at the front of the electron beam in the bottom panel. Therefore, electrons in the second bunch at $\xi = 10$ µm are expected to produce the highest x-ray intensities. These leading electron bunches are accelerated to the highest energies in the beam. The predicted intensity is higher for the second bunch because its $N(\xi)$ peak is higher than for the first bunch.

4.2.2 Modelled Temporal Intensity Profiles

The $N(t_{obs})\gamma^4_{peak}(t_{obs})$ profiles at the end of the plasma are now compared with the on-axis temporal intensity profiles modelled by the RCC. The comoving coordinate in the electron beam has been transformed into a time of observation in the x-ray beam by $t_{obs} = (\xi - \xi_0)/c$, where ξ_0 is the comoving coordinate of the front of the electron beam. The $N(t_{obs})\gamma^4_{peak}(t_{obs})$ profile is the part of Equation 4.2 that varies with the temporal coordinate in the electron beam; the profile is converted to an intensity by multiplying by the constants in Equation 4.2. The peak value of the $N(t_{obs})\gamma^4_{peak}(t_{obs})$ profile is scaled to the peak value of the RCC-modelled on-axis temporal intensity profile by adjusting r_β, which is a parameter in Equation 4.2. The values of r_β used are reported and discussed in Section 4.2.3. Here we discuss the form of the temporal intensity profiles, which can be understood from the longitudinal energy and charge distributions in the electron beam.

The left columns of Figure 35 and later Figure 36 demonstrate that the $N(t_{obs})\gamma^4_{peak}(t_{obs})$ profiles are in general a good approximation for the temporal intensity profile. The main discrepancies between the $N(t_{obs})\gamma^4_{peak}(t_{obs})$ and RCC-modelled profiles, for example at the start of the x-ray pulses of Kneip (2010) and Wenz (2015) in the first

10 fs, arise from differences in the oscillation amplitudes between different electron bunches. In a "real" LWFA, the amplitude of oscillation is not constant along the electron beam, which is assumed in the scaling of the $N(t_{obs})\gamma^4_{peak}(t_{obs})$ profile. In the examples just mentioned, the oscillation amplitudes at the front of the electron beam are smaller than in the main part of the beam that produces the highest intensities.

Low Laser Power Cases: Rousse (2004), Kneip (2010) and Wenz (2015)

The RCC-modelled temporal intensity profiles and the $N(t_{obs})\gamma^4_{peak}(t_{obs})$ of Rousse (2004), Kneip (2010) and Wenz (2015), the "low" laser power cases, are plotted in the left column of Figure 35. The coloured lines are the temporal profiles at different observation points lying at different angles of divergence from the z-axis. These observations points lied on a 9×9 grid spanning the expected divergence of the x-ray beam, taken from the literature reporting their experimental measurements or estimates. The lines' transparency increases at increasing divergence angles. The black dotted line is the predicted temporal profile given by the $N(t_{obs})\gamma^4_{peak}(t_{obs})$ profile of the electron beam at the end of the plasma, scaled according to Equation 4.2.

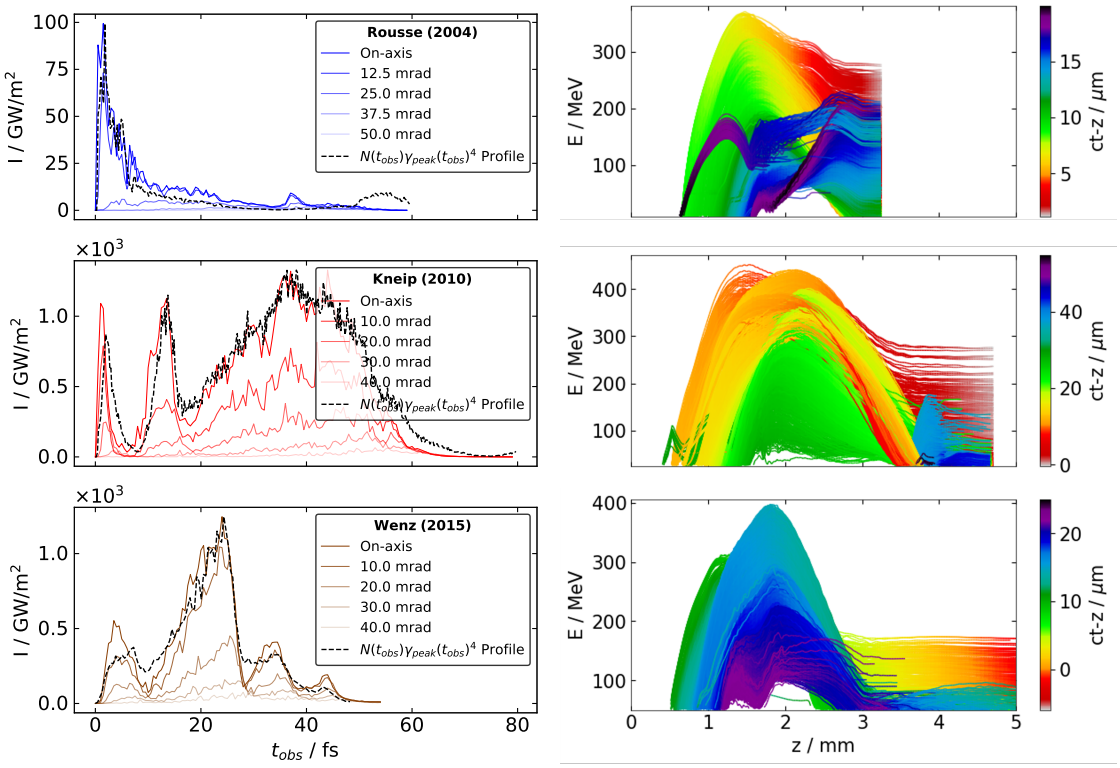


Figure 35: (Left) Modelled temporal intensity profiles of Rousse (2004), Kneip (2010) and Wenz (2015) from (black) $N(t_{obs})\gamma^4_{peak}(t_{obs})$ profile and (coloured) RCC at different angles of divergence from the z-axis. (Right) Energy progression of electrons in each case, colour-coded against their distance behind the laser pulse in the plasma.

For each case in Figure 35, the RCC-modelled on-axis temporal intensity profile can now be compared withe its prediction from the $N(t_{obs})\gamma^4_{peak}(t_{obs})$ profile. The highest on-axis x-ray intensities in the temporal intensity profile of Rousse (2004) are produced at the front of the x-ray pulse. In the case of Rousse (2004), the peak intensities are produced by the front of the electron beam, as predicted by the $N(t_{obs})\gamma^4_{peak}(t_{obs})$ profile. The intensity falls gradually from 90 GW/m^2 towards zero by 60 fs. By contrast, the modelled x-ray pulses of Kneip (2010) and Wenz (2015) consist of multiple peaks. This multi-peak structure has never been measured nor modelled, to the best of our knowledge. The on-axis temporal profile of Kneip (2010) in Figure 35 consists of three peaks of comparable intensity. The three peaks are produced by three electron bunches accelerated to similar energies, with similar numbers of electrons per unit length. The third peak has the highest intensity of 2.0×10^3 GW/m^2 and also the longest duration of 50 fs. The modelled intensity profile of Wenz (2015) is similar, consisting of four short peaks. The second peak is the longest and most intense. This peak reaches an intensity of 1.2×10^3 GW/m^2 and has a duration of 20 fs.

The differences in the form of the three intensity profiles in Figure 35 are the result of differences in the injection and energy progression of electrons accelerated in each LWFA. In the case of Rousse (2004), there is a high-energy electron bunch at the front of the beam accelerated to energies up to 350 MeV by 1.5 mm in the plasma, as shown in the right column of Figure 35. Electrons behind this bunch are accelerated to a maximum of 200 MeV, causing the decrease in the modelled x-ray intensity from front to back. The electron bunch has a length of $L_{bunch} = 18$ µm, corresponding to a duration of $L_{bunch}/c = 60$ fs, matching the duration of the modelled x-ray pulse. In the PIC simulation of Kneip (2010), the increased laser energy allows for multiple injection events. There are three electron bunches injected in the ranges of 0.6 mm to 0.9 mm, 0.8 mm to 1.1 mm and 0.9 mm to 1.6 mm in the plasma. The first bunch is accelerated up to 450 MeV, the second to 420 MeV and the third to 400 MeV. As all three bunches are accelerated to similar peak energies, they produce x-ray peaks with similar intensity. 9×10^9 electrons are accelerated in the third electron bunch behind the laser pulse, producing the longest x-ray peak, which contains the majority of the electrons in the simulated beam containing 1.1×10^{10} electrons. In the case of Wenz (2015), on the right column of Figure 35, electrons in the first bunch only reach 300 MeV. Electrons in the second bunch reach energies up to 400 MeV, and later bunches reach progressively smaller peak energies of 200 MeV and 150 MeV.

High Laser Power Cases: Wood (2018), Bloom (2020) and EPAC

The RCC-modelled temporal intensity profiles of the high laser power cases of Wood (2018), Bloom (2020) and EPAC are shown in Figure 36. The temporal intensity profile of Wood (2018) consists of three peaks. The second peak reaches the highest on-axis intensity of 6.0×10^3 GW/m^2, whereas the first peak only reaches a maximum of 1.8×10^3 GW/m^2. A third 80 fs, 1.9×10^3 GW/m^2 peak is produced by a longer electron bunch, most likely accelerated to lower energies than the first two. The temporal intensity profile of Bloom (2020) consists of just one main peak with a high maximum intensity of 1.7×10^4 GW/m^2. The intensity reached in this peak is three times the highest intensity reached in the case of Wood (2018). The on-axis temporal intensity profile of EPAC consists of two peaks. The first has a duration of 10 fs and the second 40 fs. The intensities reached in this intensity profile are up to an order of magnitude greater than in the cases of Wood (2018) and Bloom (2020). This is because the first and second electron bunches producing these peaks are accelerated to energies that are twice as high, as will be shown.

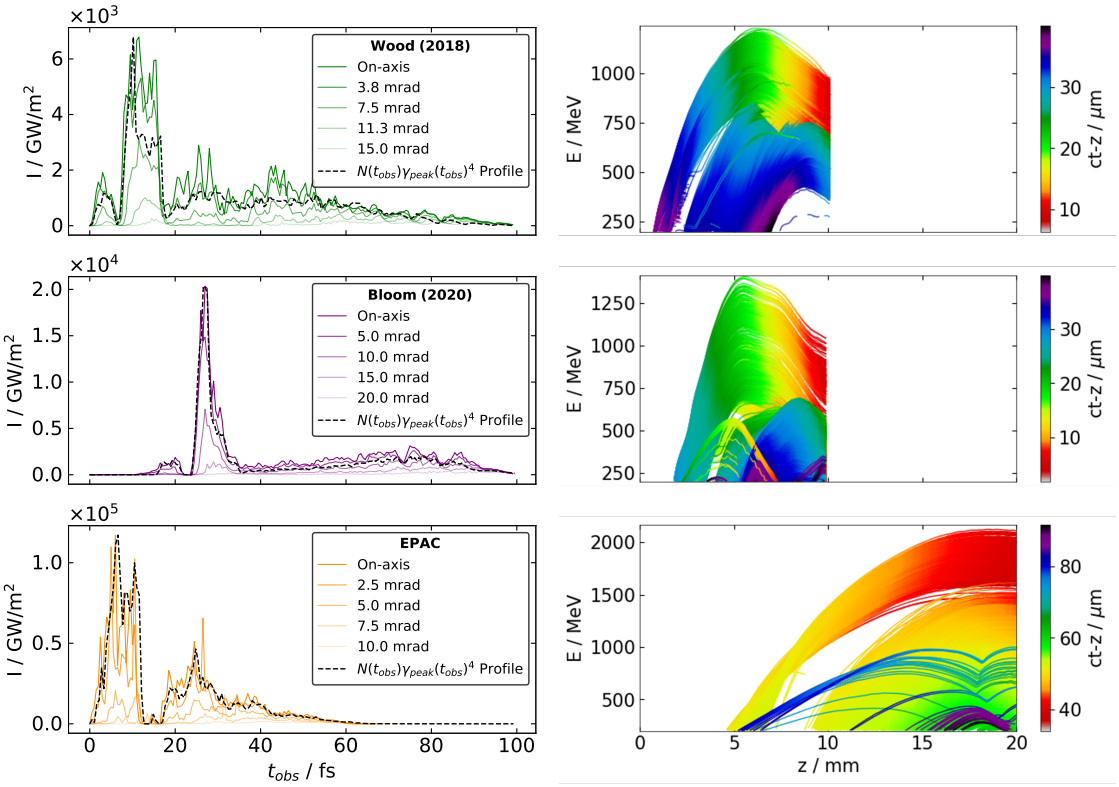


Figure 36: (Left) Modelled temporal intensity profiles of Wood (2018), Bloom (2020) and EPAC from (black) $N(t_{obs})\gamma^4_{peak}(t_{obs})$ profile and (coloured) RCC at different angles of divergence from the z-axis. (Right) Energy progression of electrons in each case, colour-coded against their distance behind the laser pulse in the plasma.

In general, the x-ray intensities produced in the high power cases are at least an order of magnitude greater than in the cases of Rousse (2004), Kneip (2010) and Wenz (2015) because the electrons reach GeV-order energies rather than a few-hundred megaelectronvolts. In the case of Wood (2018), the first two electron bunches producing the first two x-ray peaks are accelerated to peak energies of 1.2 GeV, 6 mm into the plasma, as shown in the right column of Figure 36. In the temporal intensity profile of Wood (2018), the second peak has a much higher intensity because the second electron bunch has twice the number of electrons as the first. A small number of electrons are continually injected into the wakefield behind the second bunch. These electrons are accelerated to a range of energies up to 800 MeV. Similarly, in the electron energy progression plot of Bloom (2020), electrons in one bunch are accelerated to a wide range of energies up to 1.3 GeV by 6 mm in the plasma, followed by a small number of electrons accelerated to lower energies.

The difference in peak x-ray intensities produced in the cases of Wood (2018) and Bloom (2020) is mainly due to the difference in the number of electrons in their electron bunches, as they are accelerated to similar energies of 1.3 GeV and 1.2 GeV. The slice in the electron beam producing the highest x-ray intensities has an electron density of 8×10^8 electrons/μm, versus 5×10^8 electrons/μm in the PIC simulation of Wood (2018). The scaling of Equation 4.2 predicts that the maximum intensity of Bloom (2020) should be greater than that of Wood (2018) by a factor of $(8 \times 10^8/5 \times 10^8) \times (1.3/1.2)^4 \approx 3$, which agrees with the modelled peak intensities.

In the PIC simulation of EPAC, the first and second electron bunches are accelerated to higher energies of 2.4 GeV and 1.5 GeV, respectively. The electron bunches reach their dephasing limits 20 mm into the plasma. In Figure 36, the electron energy progression has only been plotted up to 20 mm to make the energy progression of electrons in the shorter LWFAs of Wood (2018) and Bloom (2020) more visible. The electrons decelerate in the remaining length of the 40 mm plasma.

4.2.3 Scaling the $N(t_{obs})\ \gamma_{peak}(t_{obs})^4$ Profiles

As mentioned in Section 4.2.2, the peak value of the $N(t_{obs})\gamma^4_{peak}(t_{obs})$ profile is scaled to the maximum value in the RCC-modelled on-axis temporal intensity profile by adjusting the parameter r_β in Equation 4.2. The values of r_β used in the fits, denoted by $r_{\beta,\,fit}$, are included in Table 4.2. Also included in Table 4.2 is the mean oscillation amplitude calculated from the tracked particle trajectories in each PIC simulation, $r_{\beta,\,PIC}$. In each case, the two values for the oscillation amplitude are roughly the same, with the exceptions of the values for Wood (2018) and Bloom (2020). In this

case, there is a short, prominent spike in the $N(t_{obs})\gamma^4_{peak}(t_{obs})$ profile that is fit to the peak of the on-axis temporal intensity profile using $r_{\beta,\,fit}$. This spike is about double the height of the next highest peak in the $N(t_{obs})\gamma^4_{peak}(t_{obs})$ profile. Fitting that second peak to the temporal intensity profile produces $r_{\beta,\,fit} = 1.6$ µm, which is closer to the value of $r_{\beta,\,PIC}$ for Wood (2018). In the case of Bloom (2020), the discrepancy is put down to the abundance of low-energy electrons oscillating with larger amplitudes of oscillation than in the bunch producing the high-intensity x-ray peak in the temporal intensity profile. This is now discussed in detail in this section.

Table 4.2: Betatron oscillation amplitudes used to scale Equation 4.2 to RCC-modelled intensity, compared with mean amplitude from PIC simulation.

Experiment Label	$\mathbf{r_{\beta,\,fit}}$ / **µm**	$\mathbf{r_{\beta,\,PIC}}$ / **µm**
Rousse (2004) [60]	0.7	1.0
Kneip (2010) [65]	2.2	1.7
Wenz (2015) [70]	2.0	1.7
Wood (2018) [72]	0.8	1.9
Bloom (2020) [164]	1.1	1.9
EPAC	4.0	3.7

One drawback of using $r_{\beta,fit}$ as a scaling parameter of the intensity profile is that it assumes that the amplitude of oscillation of electrons in different bunches is the same. In the cases of Rousse (2004), Kneip (2010) and Wenz (2015), the amplitude of oscillation in the electron bunches producing lower intensity x-ray peaks is larger than in the electron bunch producing the highest intensity x-rays. This is partly due to the scaling of the amplitude of oscillation with the Lorentz factor, $r_\beta \propto \gamma^{-1/4}$ as in Equation 2.69, but also the initial amplitude of oscillation of these electron bunches is larger. This arises from the dynamics of their injection. As the $N(t_{obs})\gamma^4_{peak}(t_{obs})$ profile has been scaled with a smaller oscillation amplitude than the parameter describing the later bunches, it underestimates the intensity of the radiation in later x-ray peaks produced by these bunches.

Two examples where there are electron bunches with distinctly different amplitudes are those of Rousse (2004) and Wenz (2015). In Figure 37, a side-view of their PIC simulations' electron trajectories are plotted and colour-coded against their energy progression. In the case of Rousse (2004), the first electron bunch accelerated to 400 MeV contains electrons oscillating with a range of amplitudes up to 2 µm. Electrons in the second bunch, accelerated to energies of up to 200 MeV, have oscillation amplitudes up to 4 µm. This larger amplitude of oscillation means that in the trailing part of the x-ray pulse, the $N(t_{obs})\gamma^4_{peak}(t_{obs})$ underestimates the RCC-modelled in-

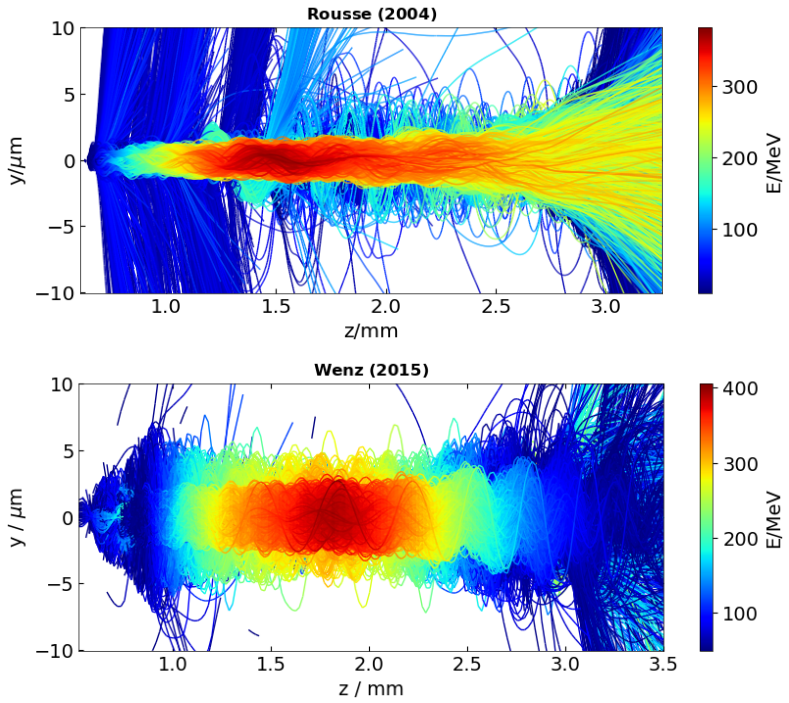


Figure 37: Sample of 25000 tracked electron trajectories colour-coded against the electrons' energy progression in PIC simulation of Rousse (2004) and Wenz (2015).

tensity. In the case of Wenz (2015), the electron bunch accelerated to 400 MeV is the narrow band with amplitudes up to 3 µm in its plot in Figure 37. The electrons accelerated to lower energies are in the wider 5 µm band. This electron bunch produces the first peak in the x-ray pulse of Wenz (2015), which was underestimated by the $N(t_{obs})\gamma^4_{peak}(t_{obs})$ profile.

In the cases of Wood (2018) and Bloom (2020), the main x-ray peaks are followed by long periods of low-intensity x-rays. These are produced by electrons behind the main electron bunch, accelerated to lower energies. In both cases in Figure 38, the main electron bunches are surrounded by a "mess" of electrons, injected throughout the plasma. These electrons oscillate with a wide range of oscillation amplitudes that are generally larger than in the main electron bunches. These electrons produce long periods of low x-ray intensity in the modelled temporal profiles, which were underestimated by the $N(t_{obs})\gamma^4_{peak}(t_{obs})$ profiles.

In the case of EPAC, both $r_{\beta,\,fit}$ and $r_{\beta,\,PIC}$ are notably larger than in the other cases. The simulated electron trajectories of EPAC are plotted and colour-coded against their energies in Figure 39. Indeed, electrons appear to oscillate with an amplitude of multiple micrometres, reaching over 5 µm by 30 mm in the plasma, at which point the electrons have comparably high energies to their dephasing limit reached around $z = 20$ mm. Moreover, the amplitude of oscillation grows as electrons travel across

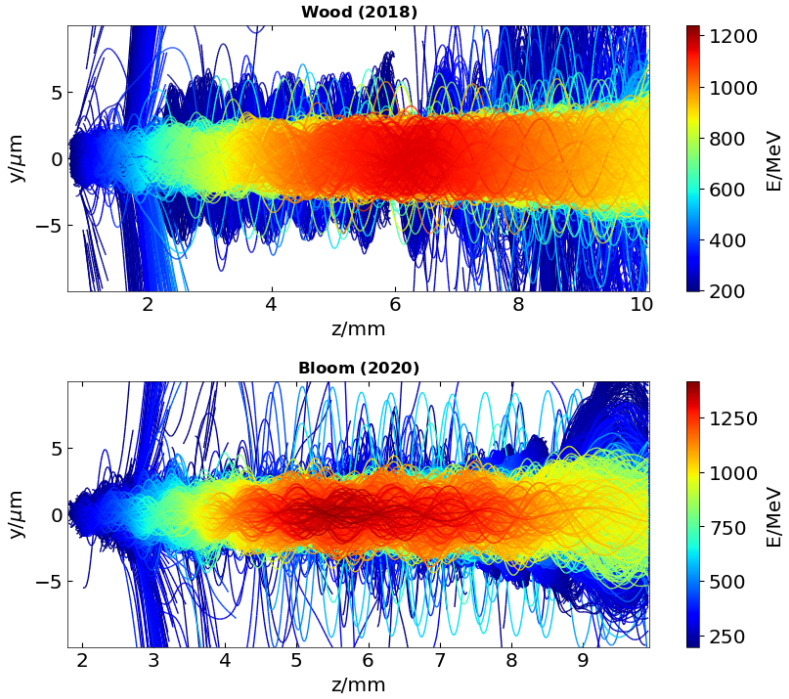


Figure 38: Sample of 25000 tracked electron trajectories colour-coded against the electrons' energy progression in PIC simulation of Wood (2018) and Bloom (2020).

the plasma. This seems to violate the scaling law given by Equation 2.69 [130], which states that the amplitude is inversely proportional to the quarter power of an electron's energy. Upon initial analysis of the electric fields in this PIC simulation, the growth in amplitude is due to the weakening of the wakefield as the laser pulse loses energy in the plasma, which is put down to the weak self-focusing and compression of the laser pulse in the low density plasma.

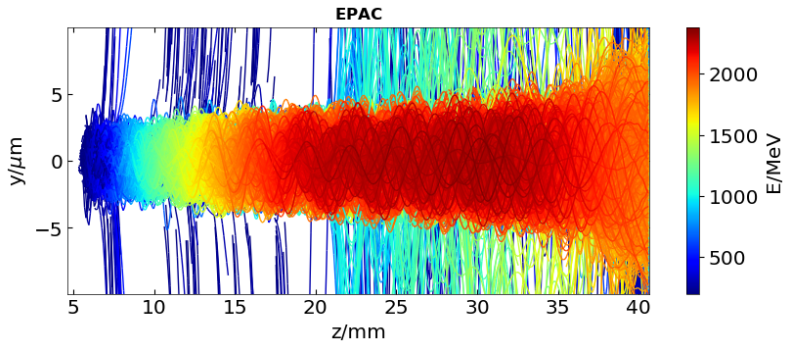


Figure 39: Tracked electron trajectories colour-coded against the electrons' energy progression in PIC simulation of EPAC.

4.3 Modelled Photon Fluence Spectra

A full spectral characterisation of synchrotron radiation from LWFAs has also not yet been achieved. For a full experimental spectral characterisation over the broad bandwidth of the radiation spectrum, some sort of large bandwidth detector or many high photon energy filters would be required. In the absence of such measurements, there have been some attempts over the last fifteen years to model the on-axis spectral profiles, using either analytical equations for the on-axis radiation intensity or similar numerical methods to those described in Chapter 3 [168]–[171]. While these methods have been used to demonstrate the keV-order photon energies and broadband nature of the spectrum, they have only been applied to short LWFAs or small numbers of electrons following near-sinusoidal trajectories. Our first RCC also models the spectral intensity profiles of the radiation from electron beams accelerated to higher energies in larger LWFAs. The radiation is also modelled at different points of observation, not just on-axis.

In this section, we report on the photon fluence spectra produced by the first RCC. We start by plotting the modelled on-axis spectra and comparing them with analytical and semi-analytical models. Accounting for the transmission of the materials between the LWFA and the detector and the quantum efficiency of the detector, the on-axis spectra are then transformed into the spectra that would have been detected in the experiments. The constituent photon energies and the peak fluences of these spectra are compared with the reported values of each experiment. Finally, the photon fluence spectra at off-axis observation points are plotted. The variation of the spectrum with the angle of divergence from the z-axis is discussed.

4.3.1 Modelled On-Axis Spectral Fluence

The photon fluence spectrum, or spectral fluence, is the number of photons received per unit solid angle, integrated into bins with a bandwidth of 0.1% of their central photon energy or frequency. The on-axis spectral fluence of the x-ray beam from each LWFA is plotted in Figure 40. An analytical spectrum derived by Thomas in 2010 is fitted to each RCC-modelled spectrum. This expression was derived by summing the circular orbit spectra that would be produced by an electron at each of the turning points of its trajectory, following the parabolic energy progression given by Equation 2.68 and the trajectory given by Equation 2.55 [61]:

$$\frac{d^2W}{dE\,d\Omega} = \frac{3e^2}{2\pi^3\epsilon_0 c}\gamma_{peak}^2\,\mathcal{A}\left(\frac{E}{E_{c,\,max}}\right), \tag{4.3}$$

where $E_{c,max}$ is the critical energy of the circular orbit spectrum produced by the electron at its peak energy, and

$$\mathcal{A}(x) = x^2 \int_{-1}^{1} \frac{1}{(1-\mu^2)^{\frac{3}{2}}} K_{\frac{2}{3}}^2 \left(\frac{x}{(1-\mu^2)^{\frac{7}{4}}} \right) d\mu. \tag{4.4}$$

This equation thus accounts for the radiation produced over the entire acceleration and deceleration of the electron. These spectra have been normalised to the total energy density in the RCC-modelled spectrum. The best fits of the maximum critical energy, taken as the value that minimised the mean χ^2-parameter, are included in the legends of Figure 40.

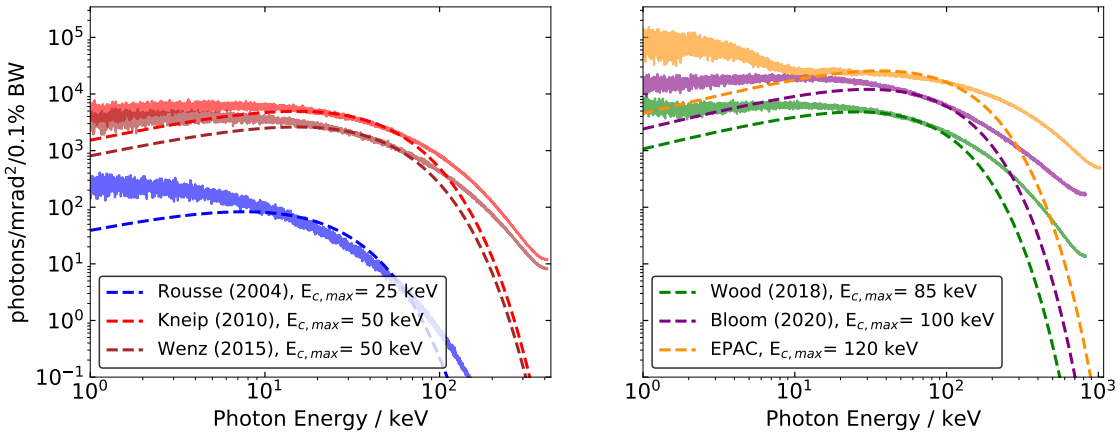


Figure 40: On-axis photon fluence spectra of low laser power cases (left) and high power cases (right), fitted with theoretical spectrum derived by Thomas in 2010 [61].

As expected, the spectra produced by electron beams accelerated to higher energies have a higher peak fluence and stretch to higher photon energies. The spectrum of Rousse (2004) has the smallest peak fluence and stretches to the smallest photon energies. The spectrum reaches 100 keV with a fluence of 10^{-3} of its peak. In the cases of Kneip (2010) and Wenz (2015), whose electron beams are accelerated to similar energies of around 400 MeV, the spectrum stretches to multiple 100 keV before dropping to 10^{-3} of their peak fluence. The peak spectral fluence of these two radiation beams are also similar. In the cases of Wood (2018) and Bloom (2020), where the electron beams are accelerated to energies around 1 GeV, the peak spectral fluence is an order of magnitude higher. The spectra stretch up to photon energies of around 1 MeV. In the case of EPAC, the peak photon fluence is an order of magnitude higher and the spectrum stretches into MeV-order photon energies.

In all six cases in Figure 40, the RCC-modelled on-axis spectra are broader than the spectra produced by Equation 4.3. This is due to the large spread in energy of electrons in the accelerated beams. At a turning point of an electron's trajectory, the

spectrum of the radiation produced at that point is assumed to be a single-energy synchrotron spectrum of the same form as produced by an electron following a circular orbit. The critical energy of that spectrum can be expressed if Equations 2.62 and 2.101 are substituted into Equation 2.90:

$$E_c = \frac{3\hbar}{4c}\omega_p^2 r_\beta \gamma^3. \tag{4.5}$$

Due to the near-100% ranges in the electrons' energies and oscillation amplitudes, there is a large spread in the critical energies of the individual spectra produced by each single electron in the electron beam, at the turning points of their trajectories. In Figure 41 are two examples of two-dimensional histograms of the electrons' Lorentz factors at their turning points against the predicted critical energy of the spectra that they produce at these turning points. The predicted critical energies in the example of Bloom (2020) are generally an order of magnitude higher than the example of Kneip (2010), due to the higher energies to which electrons are accelerated in that LWFA. The critical energies span an order of magnitude at almost all Lorentz factors in both cases. This variation is due to the near-100% spread in the oscillation amplitudes of the electrons at any energy.

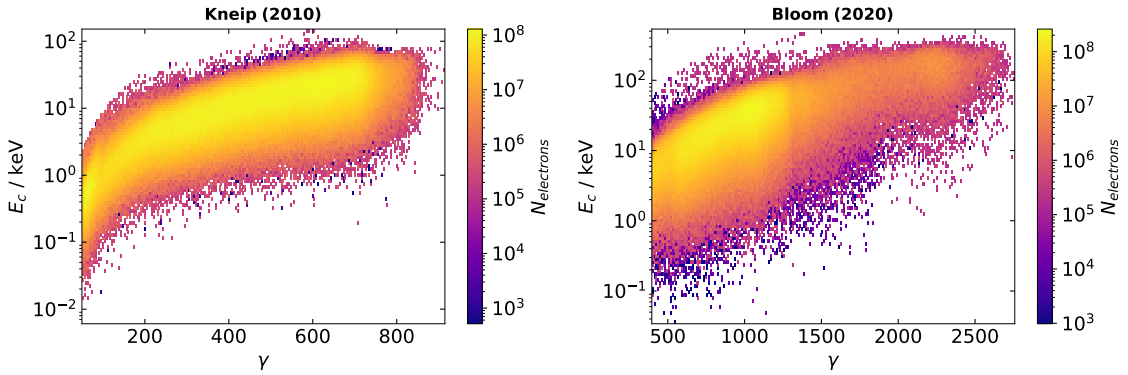


Figure 41: Example two-dimensional histograms of electrons' Lorentz factors and the critical energy of the circular orbit spectra that they would produce, at each turning point in their trajectories.

If each electron contributes a circular orbit spectrum at each turning point in its trajectory, the total spectrum is the sum of all of the spectra produced by all of the electrons. As the critical energies in each of the individual electrons' circular orbit spectra are so wide-ranging, the total spectrum is broad. A total photon fluence spectrum has been estimated by integrating a circular orbit spectrum over the distributions in Figure 41:

$$\left(\frac{d^2W}{dE\ d\Omega}\right)_{tot} = \int_{\gamma_{min}}^{\gamma_{max}} \int_{E_{c,\,min}}^{E_{c,\,max}} N(\gamma,\, E_c) \cdot \frac{d^2W}{dE\ d\Omega}(\gamma, E_c)\ dE_c\, d\gamma, \tag{4.6}$$

where $N(\gamma,\, E_c)$ is the two dimensional distribution like the ones in Figure 41 and $\frac{d^2W}{dE\, d\Omega}$ is the circular orbit spectrum given by Equation 2.91. This integral is evaluated numerically and the resultant photon fluence spectra are plotted in Figure 42 as the dashed lines, which are compared with the RCC-modelled on-axis photon fluence spectrum. The estimated spectra replicate the broad nature of the RCC-modelled spectra and have a peak fluence that is within an order of magnitude of the RCC-modelled value. Particularly, in the low energy part of each spectrum, the predicted and RCC-modelled fluence are similar. The best fits between the spectra from Equation 4.6 and from the RCC come in the cases of Kneip (2010) and Wenz (2015), where there is good agreement at almost all photon energies in the spectra. In the cases of Rousse (2004) and the three spectra in the right plot, the spectral fluence is overestimated at higher photon energies. We put this down to intricacies in the electron trajectories, for example changes in the betatron oscillation frequency due to the evolution of the wakefield.

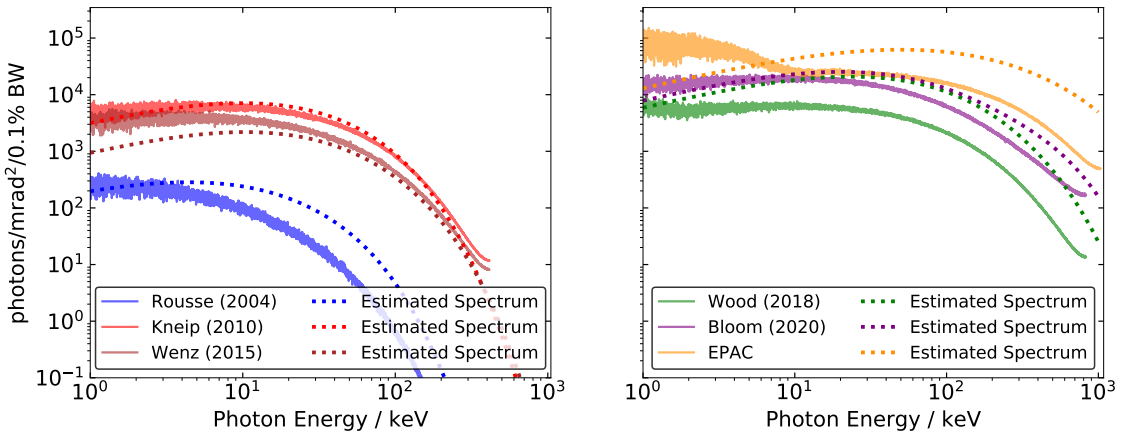


Figure 42: On-axis spectral fluence estimated assuming each electron contributes a circular orbit spectrum at each turning point in its trajectory, compared with modelled spectrum produced by the RCC.

4.3.2 "Detected" Energy Spectrum

To understand what the RCC-modelled spectra would look like if they were measured in their respective experiments, we will now attempt to transform them into "detected" spectra using information about their experimental setups. In experiments, the x-ray beam often has to pass through a variety of materials before reaching the detector. The most common example of this is a sheet or foil of aluminium placed behind the LWFA to block excess laser light that has passed through the plasma. The spectrum of the x-ray beam leaving the LWFA is modified by the total transmission of the materials

between the LWFA and the detector:

$$\left(\frac{d^2N}{dE\ d\Omega}\right)_{trans} = T_{mat}(E)\cdot(1-T_{det}(E)), \tag{4.7}$$

where T_{mat} is the total transmission of the materials. When there are multiple materials, the total transmission is the product of the transmissions of all of the materials. The transmission is an exponential function of the material thickness [172]:

$$T = \frac{I}{I_0} = \exp\big(-\mu(E)d\big), \tag{4.8}$$

where $\mu(E)$ is the x-ray absorption coefficient as a function of photon energy and d is the material thickness. The absorption coefficient as a function of photon energy is taken from the databases available at the National Institute for Standards and Technology (NIST) [173]. The detected photon spectrum is obtained by multiplying the transmitted spectrum by the quantum efficiency of the detector, which is taken as the absorption coefficient of its scintillator screen, $1-T_{det}$, where T_{det} is the transmission of the scintillator screen. The constructed experimental spectrum can thus be expressed in terms of the spectrum produced by the RCC:

$$\left(\frac{d^2N}{dE\ d\Omega}\right)_{exp} = \left(\frac{d^2N}{dE\ d\Omega}\right)_{RCC}\cdot T_{mat}(E)\cdot(1-T_{det}(E)). \tag{4.9}$$

The overall fraction of photons leaving the LWFA that actually make a signal on the detector are plotted as the solid red lines in Figure 43, for each of the low laser power experiments. The plots show that there is only a small bandwidth between 10 keV and 50 keV over which the detected spectrum is similar to the spectrum of the original x-ray beam leaving the LWFA.

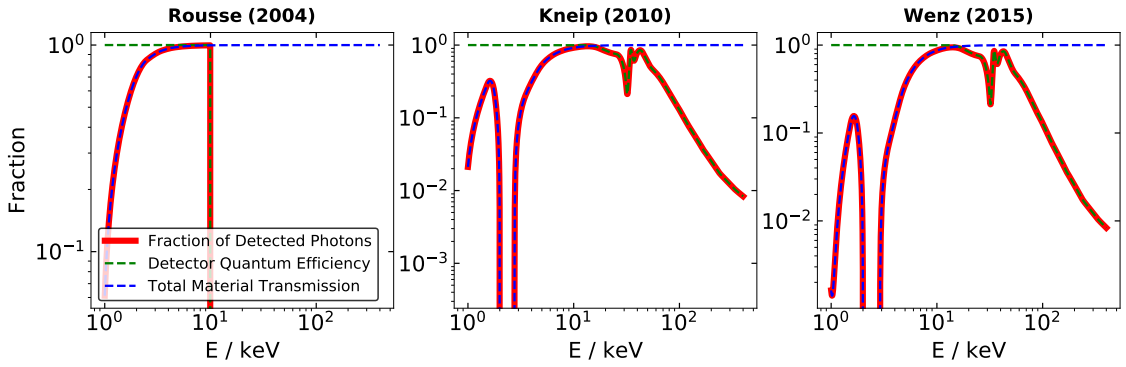


Figure 43: Fraction of detected intensity due to transmission of materials between the plasma and the x-ray detector and the detector's quantum efficiency.

The total transmission of the materials between the LWFA and the detector is plotted against photon energy by the blue dashed lines in Figure 43. In the experiment of Rousse (2004), there was a 25 µm-thick beryllium filter to block photons with energies below 0.8 keV [60]. In the absence of any reported materials, in the case of Kneip (2010), an aluminium foil with a thickness of 12 µm was assumed to have been placed behind the LWFA, as in the experiment of Wood (2018) performed by the same research group at the same laser facility [65], [72]. Finally, in the case of Wenz (2015), there was a 20 µm-thick aluminium foil placed between the LWFA and the x-ray CCD camera [70]. The materials attenuate low energy photons with energies below 10 keV. Above photon energies of 10 keV in the case of Rousse and 20 keV in the cases of Kneip (2010) and Wenz (2015), the transmission is almost unity so virtually all photons pass through the materials.

The quantum efficiency of the detector is plotted as the green dashed line in Figure 43, for each of the low laser power experiments. In the cases of Kneip (2010) and Wenz (2015), the scintillator is taken to be a 150 µm-thick caesium iodide sheet, as in the case of Wood (2018) [72]. In the case of Rousse (2004), there is an upper limit of 10 keV on the photon energies that could be detected with their detector [60], so the detection efficiency was set to zero above 10 keV. At photon energies below 10 keV, the detection efficiency was assumed to be approximately unity, as in the other two cases in Figure 43. The green dashed lines show that the detectors are less sensitive to photons with energies above 50 keV, which is because high energy photons can pass through the detector without being attenuated.

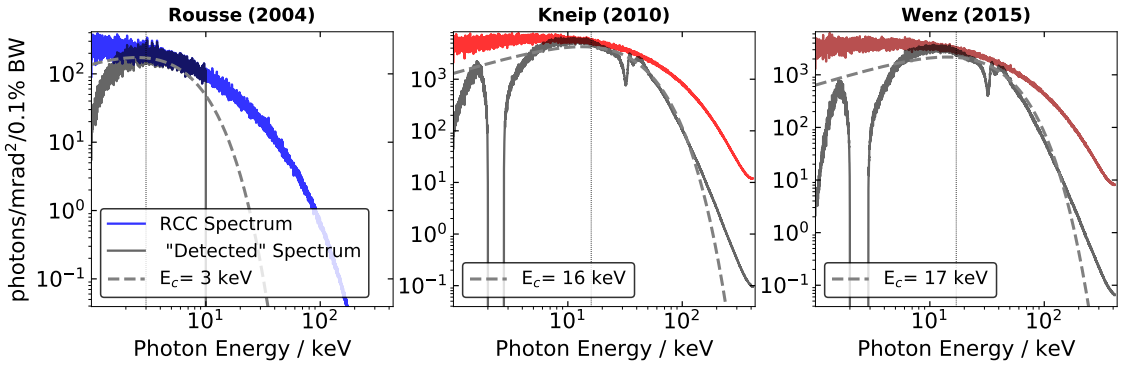


Figure 44: (Coloured) On-axis spectra fluence modelled by RCC and (black) expected on-axis spectral fluence that would have been detected, accounting for the x-ray transmission through materials between the LWFA and the detector and the detector efficiency. (Grey dashed) Circular orbit spectrum fitted to detected spectrum.

In Figure 44, the “detected” photon fluence spectra have been calculated from Equation 4.9 and are plotted in black, with the original spectra produced by the RCC plotted

in their usual colour. The black spectra have a dramatically smaller bandwidth than the spectrum of the original x-ray beam leaving the LWFA, which stretches across bandwidths on the order of 100 keV. In the case of Rousse (2004), the detected spectral flux at photon energies between 3 and 10 keV is almost the same as in the original spectrum. In the cases of Kneip (2010) and Wenz (2015), the "detected" and original spectra are comparable between 10 and 50 keV. Over these small bandwidths, $T_{mat}(E)\,(1 - T_{det}(E)) \approx 1$.

Over the small ~ 10 keV bandwidths over which the spectrum of the radiation beam spectra were experimentally measured, the energy density spectrum has been assumed to take the form of a circular orbit spectrum [174]. In many experiments, the measured radiation spectrum has been fitted with a circular orbit spectrum [65], [67], [70]–[72], [164]. In Figure 44, analytical circular orbit spectra given by Equation 2.91 have been fitted to the "detected" spectra and are plotted as the grey dashed lines. Values for the critical photon energy producing the best fits to the black spectra were obtained by minimising the quantity $\Sigma_i(S_{ana,i}(E) - S_{det,i}(E))^2$, where $S_{ana}(E)$ is the analytical spectrum and $S_{det}(E)$ is the "detected" spectrum. The critical energy values producing the best fits are included in their respective legends in Figure 44. In the cases of Kneip (2010) and Wenz (2015), the best-fit critical energies are consistent with the values deduced from the experimental results [65], [70]. In the case of Rousse (2004), a synchrotron spectrum was not fitted to the experimental spectrum data [60], probably due to the small bandwidth over which x-rays were detected.

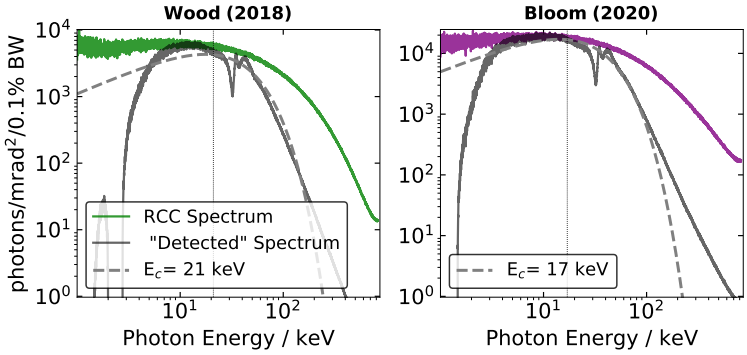


Figure 45: (Coloured) On-axis spectral fluence modelled by RCC and (black) expected on-axis spectral fluence that would have been detected, accounting for the x-ray transmission through materials between the LWFA and the detector and the detector efficiency. (Grey dashed) Circular orbit spectrum fitted to detected spectrum.

In Figure 45, circular orbit spectra have been fitted to the "detected" spectra of Wood (2018) and Bloom (2020) using the same method as before. The critical energies of the circular orbit spectra are included in the legends of the respective plots and

are consistent with the values deduced in their experiments [72], [164]. It should be noted that the exact value of the so-called critical energy of the detected spectrum is determined by the absorption efficiency of the x-ray detector, which is a function of photon energy. Changing the detector or the materials in front of it would change the critical energy of the measured spectrum. Also, in these experiments, the spectra at 100 keV-order photon energies, which form a large part of the modelled spectra, were not measured and were ignored.

4.3.3 Peak Spectral Fluence

The peak spectral fluence is the peak fluence in the on-axis spectrum, which is where the intensity of the x-ray beam is highest. In the top panel of Figure 46, the modelled peak spectral fluences are compared with their corresponding experimental values, which were inferred from the reported peak spectral brightness in each experiment. This is with the exception of EPAC, which, as of yet, has no attributed experimental values as it is still being built [175]. The modelled and experimental peak spectral fluence are also compared to an analytical scaling law for the peak spectral brightness derived by Kneip *et al.* in 2012 [62], which has been modified to relate the peak spectral fluence to the input laser power:

$$S_{peak}\left(\frac{\text{photons}}{\text{s mrad}^2\ \ 0.1\%\ \text{BW}}\right) = 2.7\times10^{19}\ \times\left(\frac{\lambda_0}{0.8\ \mu\text{m}}\right)\times \left(\frac{P}{100\ \text{TW}}\right)^{\frac{2}{3}}\left(\frac{n_c}{n_e}\right)^{\frac{19}{12}}\times 2\sqrt{a_0}\frac{\omega_p}{c}\times\left(\frac{\pi a_0 c^2\omega_0^{\frac{3}{2}}\omega_p^{\frac{1}{2}}}{1\ \text{mm}}\right)^2, \tag{4.10}$$

where P is the input laser power. The last factor in this equation gives the source size [62]. The second to last factor is the length of the electron beam, assumed to span the bubble radius, which gives the x-ray pulse duration [62]. Equation 4.10 is a rough scaling that ignores the nonlinear evolution of the wakefield [61], [62].

Both the experimental and modelled peak fluence are within an order of magnitude of the scaling laws at the laser power of the LWFA, with the exception of EPAC whose modelled result lies much lower. This is primarily due to the small amount of charge in its simulated electron beam. In the bottom panel of Figure 46, the red points plotted are the ratio of the ratios of the simulated and experimental total charges of the electron beams that leave the plasma, Q_{sim} and Q_{exp} respectively. The values are the total charge above a threshold energy set in the experiment, which was also set in the simulation; for example, in the case of Wood (2018), the threshold was set at

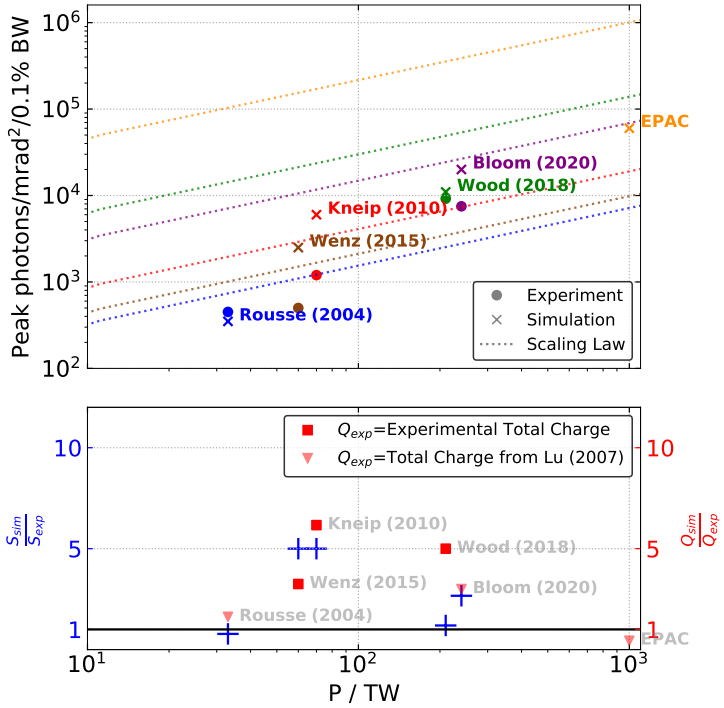


Figure 46: (Top) Input laser power against RCC-modelled and experimental peak spectral fluence, compared with modified scaling law given by Equation 4.10 [62]. (Bottom) Ratio of RCC-modelled and experimentally measured peak spectral fluence (blue) and ratio of the simulated and measured total electron beam charge (red).

200 MeV. In cases where a total charge measurement was not made, an estimate of the total charge was made using a scaling law relating the laser power to the total charge [129]. In the case of EPAC, the total charge in the simulated electron beam is about half of that expected from the scaling law. It should also be noted that the scaling law was derived with 100 TW laser pulses in mind [62] and not necessarily the 1 PW laser power of EPAC.

In the top panel of Figure 46, the points for the RCC-modelled peak fluence are a few times higher than the points of the measured values. As the simulated electron beams seem to have similar peak fluences in their spectra to the values measured, as suggested in the previous section, the most likely reason for this is the increased number of electrons in the simulated electron beams than measured or expected from a scaling law, with the exception of EPAC as just described. PIC simulations have a tendency to overestimate the amount of self-injected charge in the electron beam [176]–[178]. In the bottom panel of Figure 46, the ratio of the modelled, S_{sim} and the experimental peak fluence, S_{exp} is plotted in blue. They are compared with the ratio of the simulated and measured charge of the electron beam. The ratios given by the blue and red points are similar in the cases of Rousse (2004), Kneip (2010), Wenz (2015) and Bloom (2020). Rousse (2004) has the best agreement between its

experimental and modelled results because both the peak fluence and the total charge ratios are around unity. In the cases of Kneip (2010), Wenz (2015) and Bloom (2020), the modelled peak fluence is several times the measured peak fluence. Similarly, the simulated total charge is several times the measured of predicted total charge. The two ratios for each case in the bottom plot are indeed close to each other. An outlier to the matching of S_{sim}/S_{exp} and Q_{sim}/Q_{exp} is the data of Wood (2018). In this case, the modelled and measured peak fluence are in good agreement, despite there being five times the charge in the simulated electron beam than was measured.

Peak Brightness

To place these modelled LWFAs in the context of other synchrotron light sources and compare them with other LWFA-based light sources, the peak spectral brightness has been calculated. In the experiments modelled in this work, the peak brightness has been calculated by dividing the peak spectral fluence by the duration of the x-ray pulse and the source size of the electron beam:

$$\mathcal{B} = \frac{S_{peak}}{\pi r_\beta^2 \tau}, \tag{4.11}$$

where S is the peak spectral fluence and τ is the duration of the x-ray pulse. As the peak spectral fluence is produced on-axis, the source size is taken as the full cross sectional-area of the electron beam, with the amplitude of oscillation of the electrons as its radius. In these experiments, the source size was determined using a number of different methods, and the pulse duration was usually assumed to be equal to the duration of the laser pulse [60], [65], [70], [72], [164]. From our modelled temporal intensity profiles, however, we have values for the x-ray pulse duration and also the amplitude of oscillation from Section 4.2.

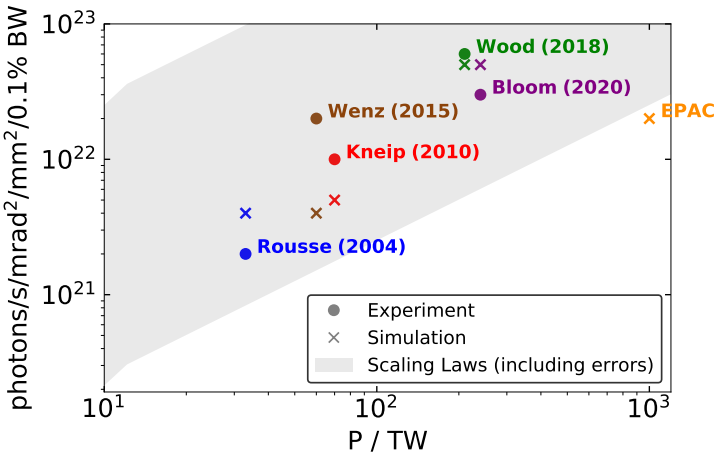


Figure 47: Peak brightness against input laser power.

The peak brightness calculated in the experiments and in the models are plotted in Figure 47 against the power of the input laser pulse. The plot shows the general trend of the peak brightness increasing with the power of the input laser pulse. The calculated peak brightness values are also compared to the scaling law given in Equation 4.10, divided by the pulse duration and the source size. In Section 4.2.2, we obtained more precise values for the x-ray pulse duration, which were used in this scaling law instead of assuming that the duration is equal to that of an electron beam spanning the bubble length [66]. We also find that the source size predicted in the scaling law is around an order of magnitude smaller than the source size obtained in the PIC simulations, which causes the scaling law to overestimate both the experimental and the simulated peak brightness. The source size obtained in the PIC simulations was used instead in the scaling law. Accounting for the uncertainties in the oscillation amplitudes, typically around 0.5 µm, produces a range of values at each input laser power. The scaling laws for all of the modelled experiments have been morphed together into the grey region in Figure 47 for neatness.

In Figure 47, both the experimental and simulated values for the peak brightness lie within the grey region covering the predictions of the adapted scaling law. There is only one outlier, which is the simulated peak brightness of EPAC, which is smaller than the prediction of the scaling law and also the values obtained for Wood (2018) and Bloom (2020). However, the laser power of EPAC is four to five times higher than the laser used in these two experiments; a higher peak brightness would be expected according to existing scaling laws like the one used here [62]. The small peak brightness from the modelling of EPAC is due to two factors. First, the simulated peak spectral fluence is small as the amount of charge injected into the wakefield in the PIC simulation was smaller than expected. Second, the electrons in the PIC simulation had large amplitudes of oscillation, meaning a large source size.

The experimental and the modelled values are within an order of magnitude. This is probably the best agreement that one can hope for with regards to spectral brightness, owing to the difficulty of measuring the source size and the duration of the x-ray pulse in experiment. The largest discrepancy is in the case of Wenz (2015), where the simulated value is almost an order of magnitude smaller than the experimental. This is because the pulse duration used in the experimental calculation was 5 fs, deduced from numerical studies [70]. In the modelled temporal intensity profile in this work, the pulse duration is 55 fs. The modelled pulse durations of Rousse (2004) and Kneip (2010), 60 fs and 80 fs, are also longer than the 30 fs pulse duration assumed at the time of the experiments [60], [65].

4.3.4 Angular Variation of Spectral Photon Fluence

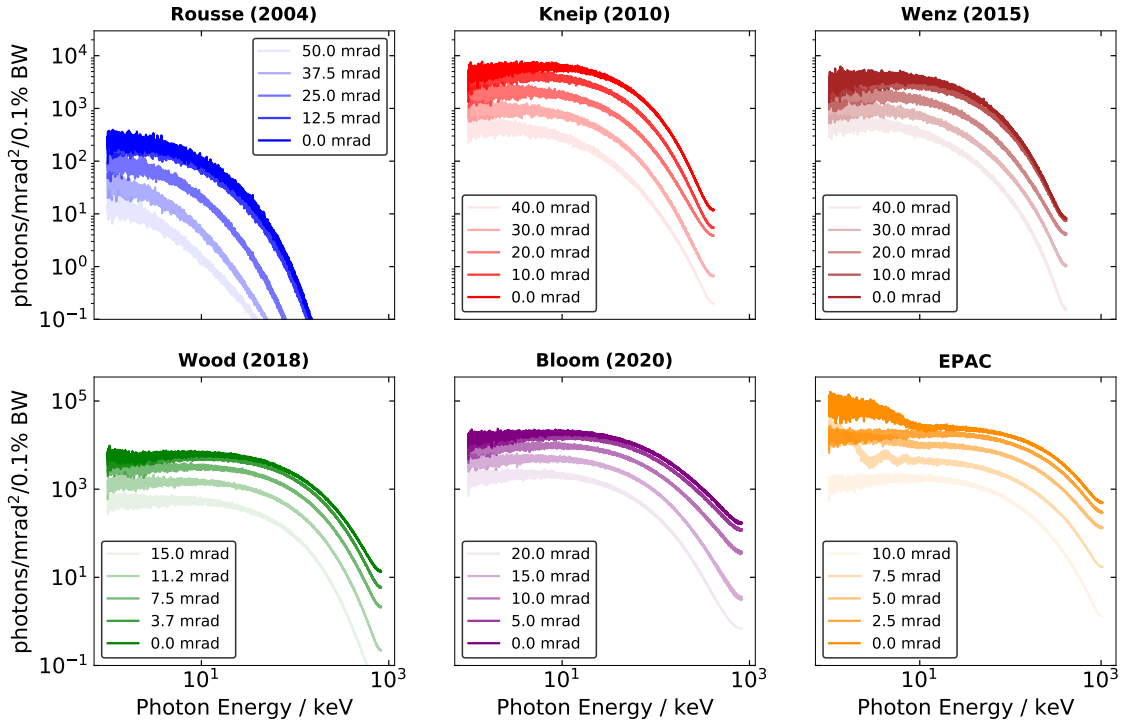


Figure 48: Spectral fluence at different points of observation produced by the RCC. Each point of observation lies at a different angle of divergence from the z-axis.

Another advantage of the RCC presented in this work is that it can model the spectrum of the radiation at different positions on a detector screen in a single run. This capability can be used to improve our understanding of the angular dependence of the spectrum. As a preliminary study, in Figure 48, the spectral fluence is plotted at different points of observation lying at different angles of divergence from the z-axis. The transparency of the plotted lines increases with increasing angle of divergence.

Modelling the spectral fluence of the radiation beams at different angles of divergence has shown that a quantitative, analytical understanding of the angular variation of the spectra is difficult to come by and requires further study. The RCC at least provides a qualitative understanding. In each plot, the peak spectral fluence decreases with increasing angle of divergence. Proportionally, the spectral fluence decreases by more at higher photon energies. Looking at the examples of Kneip (2010) and Bloom (2020), at photon energies over 100 keV, the spectral fluence decreases by two orders of magnitude over the angle between the observation points on-axis and at the edge of the beam. At photon energies on the order of 1 keV, the decrease is around one order of magnitude. The other plots show a similar behaviour. The high energy photons are produced by electrons at the highest energies, which also produce radiation beams with a smaller divergence, as implied by Equation 2.93.

The angular variation of the spectrum is determined by three complex and interplaying factors. The first is the angular dependence of the critical energy of the spectrum produced by an oscillating electron, which is due to the change in the radius of curvature of the trajectory of an electron as it moves towards and away from a turning point, changing its direction of travel as it moves. An expression for the radius of curvature against angle of divergence was derived in Chapter 2 and is given by Equation 2.101. The second factor is the variation of the intensity of the radiation cone produced in different directions as the electron travels along its trajectory. The final factor is the overlapping of the energy density distributions of the radiation beams produced by electrons oscillating in different planes, and thereby the addition of their spectra. The overlapping of the angular energy density distributions in different planes is discussed in more detail later in this chapter.

4.4 Modelled Angular Energy Density Distributions

While numerous measurements of the angular energy density distributions of x-ray beams from LWFAs have been made, there is little quantitative understanding of their scaling with the energies and oscillation amplitudes of the constituent electrons in the accelerated beam. Measurements of the angular distribution are made by placing an x-ray camera in front of the x-ray beam [60], [65], [70], [72], from which the K-parameter of the electrons has often been deduced using $\theta_{max} = K/\gamma$. In reality, the x-ray beam is produced by many electrons with a wide variety of energies and K-parameters. In this section, we report on the outputs of the second RCC, which models the angular energy density distribution of the radiation beam. The divergence of the modelled x-ray beams are reported and discussed. The output distributions are then compared with mathematical models predicting the angular energy density distributions from the energies of the electrons in the accelerated beam. This is to gain insight into the electron beam properties that produce the angular energy density distribution of the radiation beam.

4.4.1 Modelled Angular Energy Density Distributions

Maps of the normalised angular energy density distributions produced by the second RCC are shown in Figure 49. The distributions are normalised in order to compare the divergences of the x-ray beams rather than their energy densities, which differ by orders of magnitude as shown later. As expected, the angular energy density distributions peak on-axis, where $\theta_x = 0$ and $\theta_y = 0$. However, the shapes of the distributions vary from case to case. For example, in the case of Kneip (2010), the x-ray beam

is more sharply peaked at its centre and the energy density falls away quickly from its peak value. In the cases of Rousse (2004) and Wenz (2015), the angular distribution is flat at its centre, before falling away at divergence angles larger than 10 mrad.

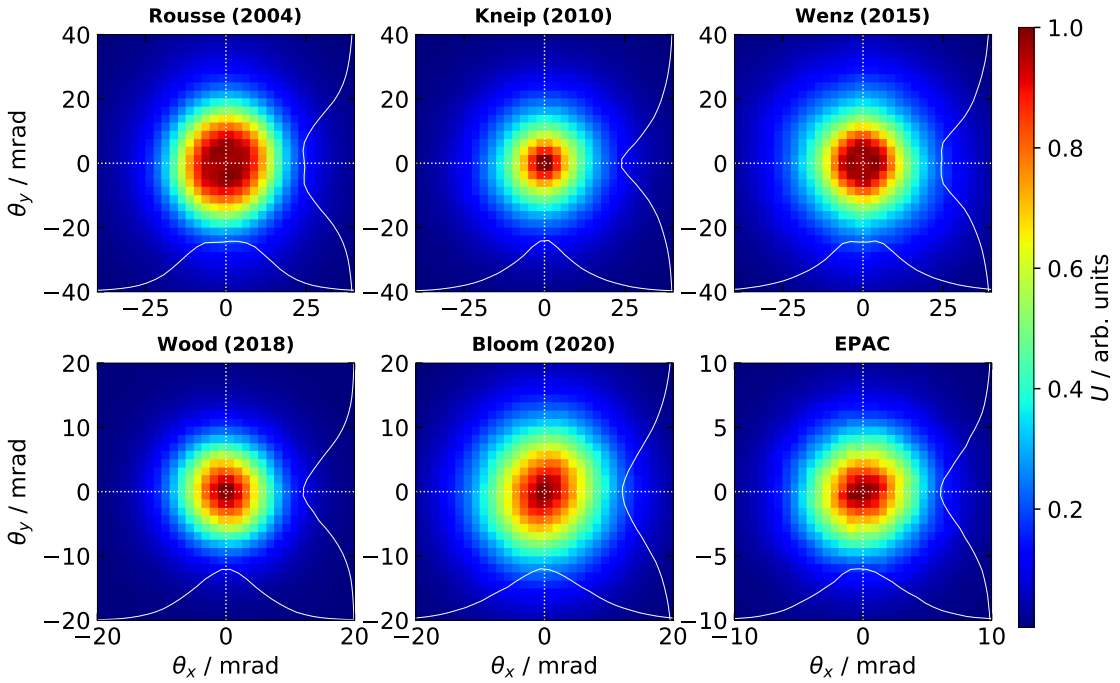


Figure 49: Map of modelled angular energy density distributions of x-ray beams from LWFAs. (White lines) Line-out of energy density along central vertical and central horizontal axes in map.

Comparing the divergence ranges in the top and bottom rows of Figure 49, the divergence of the x-ray beams in the top row are larger. These beams are produced in the LWFAs driven by sub-100 TW lasers. The larger divergence of these x-ray beams is because electrons are only accelerated to energies of up to 400 MeV, as opposed to the GeV-order energies reached in the high laser power cases, whose angular energy density distributions are shown on the bottom row of Figure 49. These angular distributions point towards some scaling of the x-ray beam divergence with the constituent energies of the electron beam, which should be expected considering Equation 2.99. This is discussed in Section 4.4.3.

4.4.2 Modelled X-ray Beam Divergence

The FWHM divergence of each modelled x-ray beam was calculated along the axes of $\theta_x = 0$ and $\theta_y = 0$, and is included in Table 4.3. The experimentally measured x-ray beam divergence is also included where available. The best agreement between the experimental and modelled values is found in the case of Rousse (2004), where the

divergence of the x-ray beam modelled by the RCC falls within the uncertainty of the experimental result. In the cases of Kneip (2010) and Wenz (2015), the divergences of the modelled x-ray beams are significantly larger than the experimental values. These experimental values are surprisingly small considering that the electrons in these experiments were accelerated to 400 MeV. As a rough calculation, substituting these small divergences into the relation $\theta_{e,max} = K/\gamma$, deduced from Equation 2.93, produces $K \approx 1$ and $r_\beta \sim 0.1$ µm for the oscillating electrons. This oscillation amplitude is not consistent with the values obtained in Section 4.2.3; moreover, source size measurements of 2 µm and 3 µm were reported in these experiments [65], [70].

Table 4.3: Experimentally measured and RCC-modelled FWHM divergence of energy density distributions of radiation beam from each LWFA.

Experiment	**Experimental Divergence**		**RCC-Modelled Divergence**	
	$\Delta\theta_x$ / **mrad**	$\Delta\theta_y$ / **mrad**	$\Delta\theta_x$ / **mrad**	$\Delta\theta_y$ / **mrad**
Rousse (2004) [60]	50 ± 20	50 ± 20	31	33
Kneip (2010) [65]	4	13	20	20
Wenz (2015) [70]	6.0 ± 1.1	6.0 ± 1.1	26	28
Wood (2018) [72]	8.9 ± 0.7	20 ± 2	12	12
Bloom (2020) [164]	n/a	n/a	14	17
EPAC	n/a	n/a	7	7

As explained in Section 4.3.2, the fraction of detected photons in experiment varies with the photon energy. The measured angular energy density distributions are distributions of the detected photons, whereas the modelled distributions are integrated over all photon energies. To better understand this, the FWHM divergence of the x-ray beam was calculated at different photon energies using the first RCC, which contains the spectral information of the x-ray beam at different observation points but with a lower spatial resolution. The modelled energy density spectrum was taken at each observation point along the y-axis. At each photon energy, an angular energy density distribution was constructed by taking the energy density at each observation point and then interpolating the energy density against the divergence angle. The FWHM divergence of this angular energy density distribution was then determined. The FWHM divergence at each photon energy in the modelled spectrum was determined by constructing an angular distribution at each photon energy.

Plotted in Figure 50 are the modelled FWHM divergences of the x-ray beams at each photon energy. The shaded regions represent the uncertainty on the calculated FWHM divergence, which were calculated from the variance in the RCC-modelled energy density spectrum: $\Delta\theta = |\frac{\partial\theta_{FWHM}}{\partial U}|\,\Delta U$, where U is the energy density and θ_{FWHM} is the FWHM divergence at a given photon energy. In general, it is found that the di-

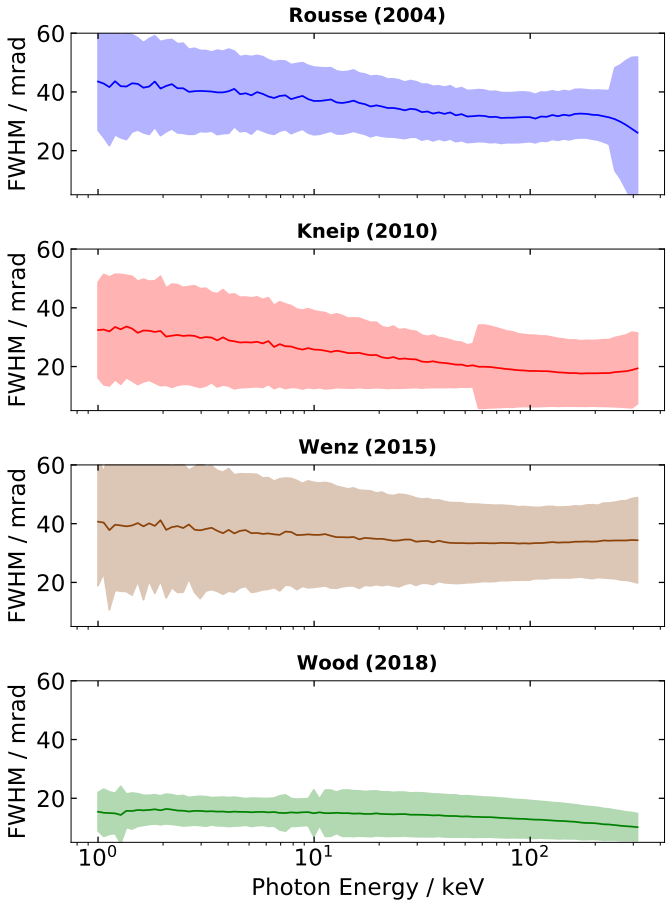


Figure 50: Modelled FWHM x-ray beam divergence against photon energy in different cases. The shaded regions are the errors on the divergence.

vergence of the x-ray beam decreases at larger photon energies. However, in the cases of Kneip (2010) and Wenz (2015), at all photon energies, the modelled FWHM divergences in Figure 50 are closer to the outputs of the second RCC rather than the experimental results.

In the cases of Kneip (2010), Wenz (2015) and Wood (2018), the experimentally measured angular distributions are also more elliptical than the modelled distributions. For the RCC-modelled beam, the divergence values in Table 4.3 are similar along the x-axis and y-axis, suggesting that the RCC-modelled x-ray beam has a high degree of circular symmetry. This implies that the amplitude of oscillation of electrons in the beam does not really change depending on their plane of oscillation. This circular symmetry is because the PIC simulation is performed in a cylindrical coordinate system using azimuthal mode decomposition, with two or three azimuthal modes. To simulate elliptical lasers and electron beams, the PIC simulations would need to be run with more azimuthal modes. However, this would increase the computation time and memory load of the simulation. For example, in the case of Wood (2018), the

experimental focal spot size of the laser was actually $(24 \pm 5) \times (15 \pm 1)$ µm [72]. In the PIC simulation, the mean of these values, 19 µm, was used as the laser's focus size. In this case, the FWHM divergence of the modelled energy density distribution has a circular symmetry and lies between the experimental values for the FWHM divergence along the x-axis and the y-axis.

4.4.3 Scaling of the Angular Energy Density Distributions

Broadly speaking, electron beams that reach higher energies produce x-ray beams with a smaller divergence. This is principally down to the range of angles covered by electrons' trajectories, scaling as K/γ. An analytical relation for the angular energy density distribution of the x-ray beam produced by a single electron following a sinusoidal trajectory was derived in Chapter 2, which takes the form of a semi-circular function of angle in the plane of oscillation of the electron and depends strongly on the electron's energy, but also its K-parameter. Using Equations 2.62 and 2.69, the K-parameter of an electron in an LWFA can also be scaled with just its energy:

$$K = B\gamma^{\frac{1}{4}}, \tag{4.12}$$

where $B = r_0\omega_p\gamma_0^{1/4}/\sqrt{2}c$. This allows Equation 2.98 to be expressed with the Lorentz factor, or the energy of the electron, as its only variable:

$$\frac{d^2W}{d\theta_y\, d\theta_e} = \frac{e^2}{16\sqrt{2}\pi\epsilon_0 c}\omega_p\gamma^{\frac{9}{2}}\sqrt{\frac{B^2}{\gamma^{\frac{3}{2}}} - \theta_e^2}\left[\frac{1}{(1+\gamma^2\theta_y^2)^{\frac{5}{2}}}\left(3 - \frac{5}{4(1+\gamma^2\theta_y^2)}\right)\right]. \tag{4.13}$$

In a "real" LWFA, the electron beam comprises a wide range of energies at any given time, due to the range of times and positions at which they are injected into the wakefield. The energy progression of these electrons also varies. The angular energy density distribution of the radiation beam is produced over the entire acceleration of the electrons. In any calculation or prediction of the angular energy density distribution, the range of energies covered by the electrons over the entire acceleration of the beam should be accounted for, as done by the second RCC. In the remainder of this section, the scaling of the angular energy density distribution with the electron beam spectrum integrated over the entire acceleration is described and discussed.

Time-Integrated Electron Spectra

The total angular energy density distribution of the radiation beam is the time-integrated distribution produced over the entire duration of the electrons' acceleration. It is thus the time-integrated or time-averaged energy spectrum of the electron beam that determines the angular energy density distribution. The time-averaged electron spec-

trum in a PIC simulation is calculated from the particle tracking data by summing histograms of the electron beam's constituent energies in each time-step, summing them and dividing by the number of time-steps. This could be achieved experimentally by averaging the measured spectra of the electron beams leaving plasmas with different lengths, which can be changed when using variable length gas cells.

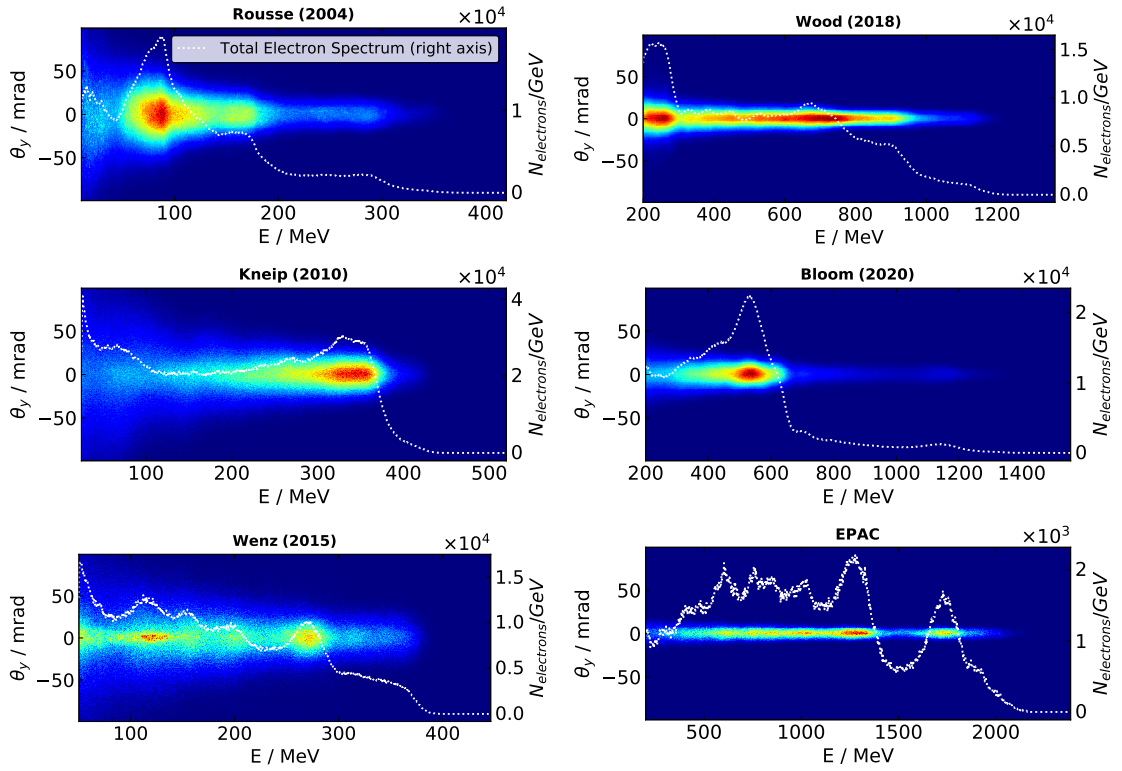


Figure 51: Time-averaged electron spectrum of each LWFA: number of electrons per megaelectronvolt per milliradian (map) and total number of electrons per megaelectronvolt (white dotted line).

The time-averaged electron spectra calculated from each PIC simulation are presented in Figure 51. The colour map represents the number of electrons per unit energy per unit y-divergence, which show the divergence of the electrons decreasing with increasing electron energy. In the case of Rousse (2004) the divergence angles span over 100 mrad. By contrast, the electrons in the case of EPAC span only 10 mrad. As a rough sanity check of the angular distributions produced by the RCC, the range of divergence angles spanned by each electron beam are similar to the angles spanned by their modelled x-ray beam. The numbers of electrons per unit energy, integrated over all divergence angles of the electrons, are represented by the white dotted lines.

Integrating over the Time-Averaged Electron Spectra

It could be assumed that each electron in the beam produces an angular energy density distribution given by Equation 2.98. The addition of the angular distributions from electrons oscillating in different planes is first ignored for convenience. Then, the total angular distribution produced by the electron beam is produced by integrating the product of Equation 2.98 and the time-averaged electron spectrum over the energies of the spectrum:

$$\left(\frac{d^2W}{d\theta_x d\theta_y}\right)_{tot} = \int_{E_{min}}^{E_{max}} \frac{d^2W}{d\theta_x d\theta_y} \cdot N(E) \cdot N_{osc}(E)\, dE, \tag{4.14}$$

where $N(E)$ is the time-averaged electron spectrum and $N_{osc}(E)$ is the number of oscillations performed by an electron in the plasma with some constant energy: $N_{osc}(E) = \frac{L_{plasma}}{2\pi\,\omega_\beta(E)^{-1}}$, with the betatron frequency given by Equation 2.62.

The integral in Equation 4.14 was evaluated numerically. In Figure 52, slices of the energy density profile along the axis $\theta_y = 0$ are shown for each modelled x-ray beam. The central slice of the RCC-modelled angular energy density distribution is shown in black and the distribution from the numerical integration of Equation 4.14 is plotted as the red dashed line. The width and the height of the angular distribution produced by the evaluated integral was changed by adjusting the parameter r_0, as both the height and width of the distribution are proportional to this parameter. r_0 has been adjus-

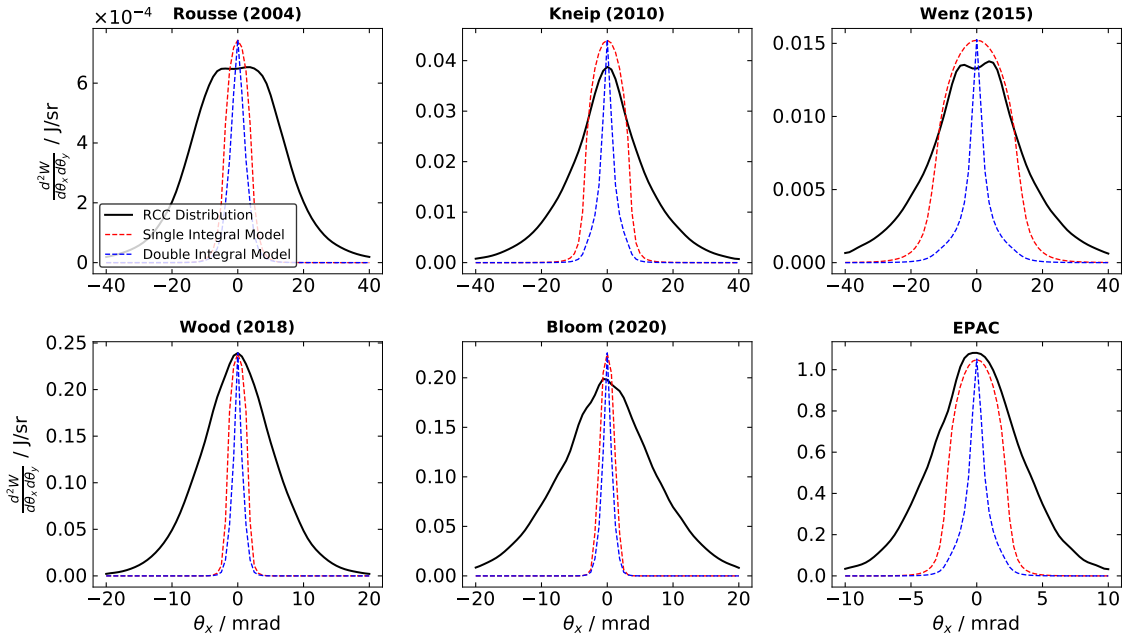


Figure 52: (Black) Slice along $\theta_y = 0$ of angular energy density distribution produced by RCC, (red dashed) distribution produced by Equation 4.14 and (blue dashed) distribution produced by Equation 4.16.

ted such that the peaks of the black and red lines are roughly equal. For example, $r_0 = 2$ µm in the case of Kneip (2010) and $r_0 = 1$ µm in the case of Bloom (2020). It seems that r_0 needs to be scaled down to match the peak intensities, to the point where it is sometimes smaller that the source sizes estimated earlier.

In Figure 52, the shape of the red angular distribution from the evaluated integral is very different from those of the black distributions from the RCC. The RCC-modelled angular distributions are more concave, falling away from their peak value at the centre of the beam faster than the more Gaussian-like angular distributions of the evaluated integral. Also, adjusting r_0 does not change the general shape of the distribution. This indicates that modelling the angular energy density distribution of the radiation beam by considering electrons oscillating in a single plane is inaccurate.

Angular Energy Density Distribution from Electrons Oscillating in Different Planes

The most likely reason for the difference in shape between the black and red distributions in Figure 52 is that the oscillation of electrons in different planes cannot be ignored. The angular energy density distributions produced by electrons oscillating in different planes overlap and sum together, which is neglected in the single integral model described above. Two conceptual energy density maps are shown in Figure 53: on the left is the energy density distribution produced by electrons oscillating in just the x-z plane; on the right is a map of the energy density distribution of electrons oscillating in six different planes. It should be noted that the peak energy density in the right plot is higher than in the first and the colour-maps are in arbitrary units.

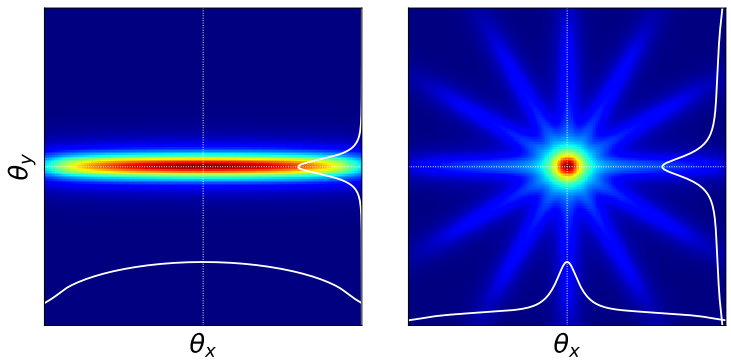


Figure 53: Conceptual diagram to show the effect of adding energy density distributions produced by electrons oscillating in different planes. (Left) angular energy density distribution produced by electrons oscillating in a single plane. (Right) Angular energy density distribution produced by electrons oscillating in a six different planes. (White lines) Line-outs of distributions along axes of $\theta_x = 0$ and $\theta_y = 0$.

While in reality the oscillation of electrons is not constrained to just six planes, the right panel in Figure 53 shows that the total energy density distribution becomes much more prominent around the centre where the individual distributions overlap more. This explains why the distributions produced by Equation 4.14 and the RCC in Figure 52 produce comparable peak values on-axis, as this is where the energy density distributions of all of the electrons oscillating in different planes intersect and add together. The line-outs on the right panel show the general form of the energy density distribution becoming more similar to those of the RCC-modelled angular energy density distributions. The scaling of the divergence of distributions like this will now be discussed.

The summation of different energy density distributions in different planes is now considered. The angle of the plane of oscillation of an electron is defined, ϕ_e, which is the angle of the plane from the x-axis. This is effectively a polarisation angle in the radiation beam. In the simplest case of a circularly symmetric electron beam, there is no ϕ_e-dependence of the oscillation amplitude nor the energy of electrons. The time-averaged electron spectrum can be converted quite simply into a distribution of the number of electrons per polarisation angle through $N(E)/\pi$. The energy density distribution per polarisation angle is then calculated similarly to the numerical integration performed in the previous section:

$$\frac{d^3W}{d\theta_x\, d\theta_y\, d\phi_e} = \int_{E_{min}}^{E_{max}} \frac{d^2W}{d\theta_x d\theta_y} \cdot \frac{N(E)}{\pi} \cdot N_{osc}(E)\; dE. \tag{4.15}$$

This is an adaptation of Equation 4.14, considering the angular distribution produced by electrons oscillating in a single plane. The adaptation is the factor of π for a cylindrically symmetric beam. The total angular energy density distribution of the radiation beam is found by integrating this equation over all polarisation angles:

$$\left(\frac{d^2W}{d\theta_x\, d\theta_y}\right)_{tot} = \int_0^{\pi} \int_{E_{min}}^{E_{max}} \frac{d^2W}{d\theta_x d\theta_y} \cdot \frac{N(E)}{\pi} \cdot N_{osc}(E)\; dE\; d\phi_e. \tag{4.16}$$

This integral is also evaluated numerically. The resulting distributions are also plotted in Figure 52 as the blue dashed lines. The shapes of these distributions are more akin to those produced by the RCC, but their divergence is much smaller. For the distributions given by Equation 4.16, adjusting the parameter r_0 does not change the width of the distribution significantly, apart from around its edges where the energy density is much lower. The distributions are dominated by the region of the central spike because this is where the angular distributions from electrons oscillating in different planes overlap. The size of this region scales strongly with the energy of the electrons in the accelerated beam, because it is determined by the width of the angu-

lar distributions from the individual electrons. The angular distribution of an electron following a sinusoidal trajectory, given by Equation 2.98, has a width of around $1/\gamma$. At low electron energies, this width is larger so there is a larger region over which the individual angular distributions overlap. At high energies, the overlap region is small.

4.4.4 Simulated Electron Trajectories in Three Dimensions

The spatial energy density distribution of the x-ray beam seems to be determined by a combination of the distributions described by Equations 4.14 and 4.16. The divergence of the x-ray beam modelled by the RCC is much closer to that of the distribution described by Equation 4.14, which does not account for the addition of the energy density spectra from electrons oscillating in different planes. When this is accounted for in Equation 4.16, the general shape of the angular distribution is more like that of the RCC, but with a much smaller divergence. Another issue is that to match the peaks of the distributions produced by Equations 4.14 and 4.16 to the RCC-modelled distribution, the parameter r_0 had to be set to values smaller than the source sizes calculated earlier in Table 4.2. This suggests that the peak energy density at the centre of the distribution is actually smaller than these models expect.

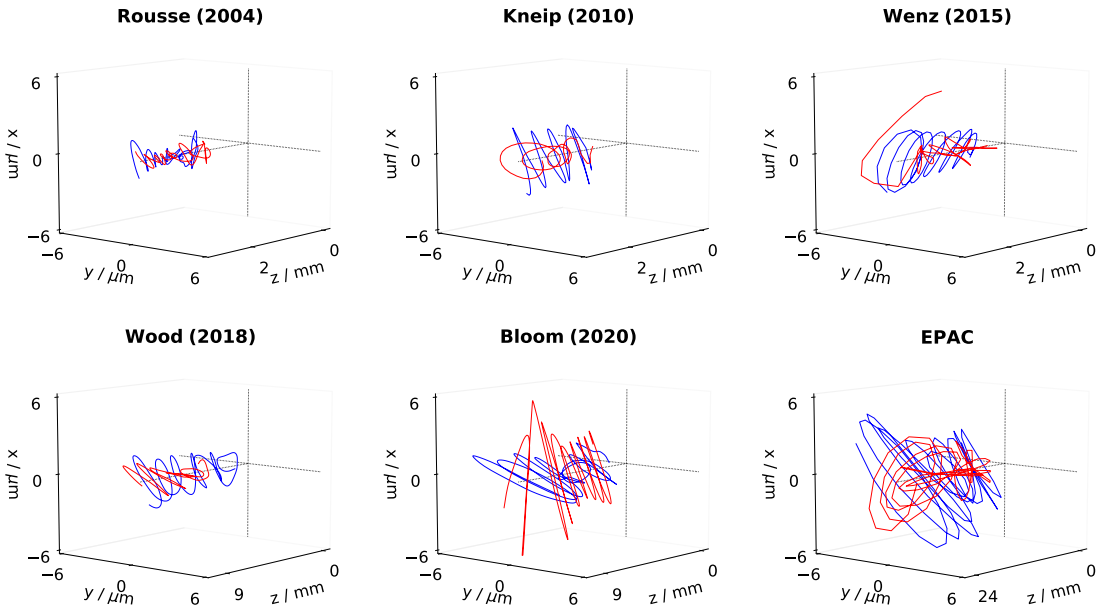


Figure 54: Two randomly sampled electron trajectories from each PIC simulation, plotted in three dimensions.

In the three-dimensional plots in Figure 54 are two randomly sampled electron trajectories from each PIC simulation. Some electrons do indeed oscillate quasi-sinusoidally in a single plane as assumed, but many trajectories also seem to rotate around the

central longitudinal axis. Many electrons in these plots follow elliptical spirals, for example the trajectory in red in the plot of Wenz (2015). This could be due to space charge effects in the electron beam, magnetic field effects [179] or some electrons could have an azimuthal momentum component when injected into the wakefield. The energy density distribution produced by an electron following such a trajectory is an ellipsoidal ring, as observed and calculated by Phuoc *et al.* in 2006 [180]. This perhaps explains why the divergence of the RCC-modelled angular distributions is larger than produced by Equation 4.16, as not all of the angular distributions from individual electrons overlap on-axis.

The trajectories shown in Figure 54 show that analytically or semi-analytically modelling the angular energy density distributions from the electron beam properties is more complicated than assumed in Equations 4.14 and 4.16. Not only does the ellipticity of the trajectories change from particle to particle, but so does the angle of the major axis of the ellipses in the x-y plane. At least, this is further motivation for the building and use of the RCC, which can process such complicated particle trajectories. Analytical or semi-analytical angular distributions could potentially be derived using an equation for the angular distribution produced by an electron following an elliptical trajectory. However, the distribution of the electron trajectories' ellipticity, the distribution of their oscillation amplitudes and the overlapping and adding together of their individual angular distributions would need to be carefully considered.

4.5 Summary

Two RCCs have been built to model the temporal intensity profile, photon fluence spectra and angular energy density distributions of x-ray beams produced by PIC-simulated electron beams from LWFAs. The first RCC models the temporal intensity profile and the photon fluence spectra of the x-ray beam at different observation points in a single run. The second RCC models the angular energy density distribution. The calculation procedure of these RCCs was outlined in Chapter 3.

The RCC-modelled temporal intensity profiles have a duration on the order of 10 fs that depends on the length of the electron beam and the injection dynamics in the LWFA. Many modelled x-ray beams had a multi-pulse structure, produced by the different electron bunches accelerated in the LWFA. The intensity profile was shown to be closely linked to the energy distribution of these bunches, following a profile given by Equation 4.2, proportional to the $N(t_{obs})\gamma^4_{peak}(t_{obs})$ profile of the electron beam at the end of the plasma. The peak value of Equation 4.2 was matched to the peak RCC-modelled intensity by adjusting the parameter r_β. Similar values to the mean r_β

of the accelerated electrons in the PIC simulation produced the best fits.

The first RCC also produced on-axis photon fluence spectra with ~ 100 keV and ~ 1 MeV bandwidths, which are significantly larger than the ~ 10 keV bandwidths over which the x-ray spectra have been measured [174]. The broadness of the spectra is due to the near 100% spread in the electrons' energies and oscillation amplitudes. The large bandwidth and peak photon fluence of the spectra was supported by predicted spectra, calculated by adding the assumed circular orbit spectra produced by the electrons at the turning points in their trajectories. We then constructed the spectra that would be detected in the experiments modelled, by taking the RCC-modelled spectral and multiplying them by the transmission factors of the materials in front of the detector and the quantum efficiency of the detector. Circular orbit spectra were fitted to these "detected" spectra, which had critical energies consistent with those obtained in experimental analysis [65], [70], [72], [164].

For each LWFA modelled, the peak spectral fluence produced by the RCC was within an order of magnitude of its experimentally measured value. The peak fluence produced by the RCC was often a number of times higher due to the increased charge in the electron beam compared to experiment, which is put down to the tendency of PIC simulations to overestimate the amount of self-injected charge [176]–[178]. Armed with values for the x-ray pulse duration and the source size, the modelled LWFA light sources were calculated to have a peak brightness between 2×10^{21} and 6×10^{22} photons/s/mrad^2/mm^2/0.1% BW.

The angular energy density distributions produced by the second RCC were compared with predicted angular distributions derived using Equation 4.13. This equation describes the angular distribution produced by a single sinusoidally oscillating electron and relates it to the electron energy. The first predicted angular distribution of the radiation beam was derived by integrating Equation 4.13 and the time-averaged electron spectrum over the energy range of the spectrum. The second predicted angular distribution spread the first predicted angular distribution over an angle of π, accounting for the overlapping of the distributions from electrons oscillating in different planes. The first predicted angular distributions had divergences closer to those of the RCC-modelled distribution, but a different shape. The second had a similar form, but with a much smaller divergence. Three-dimensional plots of example electron trajectories in PIC simulations showed that some electrons in the beam follow elliptical spirals, rather than performing oscillations in a single plane, as was assumed in both predicted angular distributions.

5. Bayesian Optimisation of PIC Simulations for eSYLOS

The SYLOS laser system is planned to deliver few-cycle pulses with energies of up to 100 mJ at a repetition rate of 1 kHz. At the time that this work was done, the laser was expected to be in the second stage of its development, SYLOS-2. The SYLOS-2 laser is planned to deliver 30 mJ laser pulses, 8 fs in duration at a repetition rate of 1 kHz [102]. The 4 TW power of this laser is an order of magnitude lower than the lowest laser power used in the simulations in Chapter 4. As will be shown, the SYLOS-2 laser could drive LWFAs producing electron beams with energies up to ~ 100 MeV at the eSYLOS facility, producing x-ray beams with a lower intensity. This could be compensated for by using a higher repetition rate, like the 1 kHz SYLOS system, which would increase the average flux and average brightness of the radiation produced. The resulting x-ray beam would be pulsed at a high repetition rate, which would be useful for many applications [111].

As eSYLOS is a new facility, the first step in producing x-ray beams with high brightness is to generate and optimise the electron beams. As a preemptive study, a Bayesian optimisation (BO) algorithm has been used to optimise the input parameters in successive PIC simulations of LWFAs driven by a laser pulse like SYLOS-2. In this chapter, we start by describing the methods used to calculate the width and intensity of the laser focus that is used in the PIC simulations. An overview and discussion of the computational methods used in this algorithm is then given. Then, we report and discuss two separate optimisations by the BO algorithm: the peak energy and total charge of the output electron beams.

5.1 Laser Focusing

At eSYLOS, the laser pulse is focused into the gas using an $f/9$ parabolic mirror [107]. The transverse spatial profile of the laser beam at its focal point is known as the focal spot. In this design of the eSYLOS facility, the radius of the focal spot has

been calculated analytically to be $w_0 = 2.58\lambda_0/\pi \times (f/\#) = 6.6$ µm [107], which is the radius of the beam where the intensity falls to $1/e^2$ of its peak value, often referred to as a beam waist. The planned total energy and FWHM duration of the SYLOS-2 laser are 30 mJ and 7.5 fs [102], from which the intensity of the focused laser pulse can be calculated. The intensity distribution of the focused laser beam is assumed to be Gaussian along the radial and temporal axes of the laser:

$$I(r,t) = I_0 \exp\left(-\frac{2r^2}{w_0^2}\right) \exp\left(-\frac{2t^2}{\tau^2}\right), \tag{5.1}$$

where I_0 is the peak intensity of the laser pulse at its centre and τ the temporal coordinate at which the intensity falls to I_0/e^2. In this coordinate system, $I = I_0$ at $t = 0$ and $r = 0$. The total energy of the laser pulse is found by integrating this expression over all space and time. The peak intensity of the laser pulse can then be written in terms of the total laser energy:

$$I_0 = \frac{4\sqrt{\ln 2}\, E_L}{\tau_{FWHM}\ \pi^{\frac{3}{2}}\ {w_0}^2}, \tag{5.2}$$

where E_L is the total energy and $\tau_{FWHM} = \sqrt{2\ln 2}\,\tau$ is the FWHM duration of the laser pulse. This equation can be simplified to a more easy-to-use expression:

$$I_0 \approx \frac{1.88\, E_L}{\tau_{FWHM}\ \pi {w_0}^2}, \tag{5.3}$$

The peak normalised potential of the focused laser pulse, often referred to as just the normalised potential, can be calculated from the peak intensity:

$$a_0 = 0.855\, \lambda_0\, [\text{µm}] \sqrt{I_0\ [10^{18}\ \text{W/cm}^2]}. \tag{5.4}$$

Using the above parameters for the SYLOS-2 laser, when at its full energy and transform-limited duration, Equation 5.2 produces a peak intensity of 4.3×10^{18} W/cm^2, corresponding to a normalised potential of 1.6.

5.2 Bayesian Optimisation (BO) of FBPIC Simulations

Machine learning algorithms are a useful way of exploring the parameter space as well as optimising properties of the electron beams accelerated in LWFAs [181]–[184]. A BO algorithm has been built to select the input parameters in successive PIC simulations of the SYLOS-2 laser focused in plasma, to optimise user specified electron beam properties. The PIC code, FBPIC, was used because its run-script is written in the programming language, Python and can be easily integrated into the BO algorithm

Table 5.1: Input parameters and their scales in the Bayesian optimisation algorithm

Parameter	Symbol	Scale
Helium Gas Density	n_{He}	Logarithmic
Nitrogen Dopant Concentration	N_{conc}	Logarithmic
Plasma Length	L_{plasma}	Linear
Laser Focal z-position	z_{focus}	Linear
Density Up-Ramp Length	l_{up}	Linear
Density Down-Ramp Length	l_{down}	Linear
Second-Order Spectra Phase	$\phi^{(2)}$	Linear
Third-Order Spectra Phase	$\phi^{(3)}$	Linear
Fourth-Order Spectra Phase	$\phi^{(4)}$	Linear

which is also written in Python. FBPIC works in a similar way to Smilei when run in a cylindrical coordinate system using azimuthal mode decomposition, described in Section 3.1 [159], [185].

5.2.1 FBPIC Simulations

In every simulation, the input laser pulse had a Gaussian spatial and temporal intensity profile, a total energy of 30 mJ and a transform-limited FWHM duration of 8 fs, which were chosen to mimic a pulse from the SYLOS-2 laser. The laser pulse is focused to a focal spot waist of 6.6 µm, which is the waist that is obtained when the laser is focused using an $f/9$ focusing optic like in the experimental setup [107]. The laser pulse was focused into a neutral helium gas doped with a small, variable concentration of nitrogen. This is one of multiple input parameters that could be varied by the BO algorithm to optimise the output electron beam, which are included in Table 5.1. To cover the order of magnitude ranges in the ranges of available values of the helium gas density and nitrogen concentration, the base-10 logarithm of their values are used in the fitted model in the BO algorithm.

In a PIC simulation, the entire plasma is not simulated throughout the entire simulation, but instead the LWFA is simulated in a small box encompassing the laser pulse and the part of plasma wave where electrons are accelerated. This box moves at the group velocity of the laser pulse in plasma, given by Equation 2.23, which reduces the computational load of the simulation. However, as the laser and plasma parameters are changed in each simulation run by the BO algorithm, the simulation box dimensions need to be set at the start of each simulation. The box width is set to accommodate the entire width of the defocused laser at the start of the simulation, before it has reached its focal position: $w_{box} = 6w(z_0)$, where w is the $1/e^2$ waist of the laser pulse and z_0 its initial position in the simulation, which is before the laser reaches its target focal position. The box length is set to accommodate the entire

length of the laser pulse plus the bubble length: $L_{box} = 3c\tau_{FWHM} + 2r_b$, where τ_{FWHM} is the FWHM duration of the laser pulse. The bubble length is estimated as Equation 2.46 multiplied by two. The FWHM duration of the laser pulse is estimated by multiplying its transform-limited FWHM duration, $\tau_{FWHM,0}$, by a stretch factor, which is dependent on its second-order spectral phase coefficient: $\tau_{FWHM} = s\tau_{FWHM,0}$, where $s = \sqrt{1 + 16(\ln 2)^2(\phi^{(2)})^2/\tau^2_{FWHM,0}}$ [186].

In this work, all simulations were run with three azimuthal modes and 1, 2 and 4 particles per cell along the longitudinal, transverse and azimuthal axes. The cell dimensions were different for each electron beam property being optimised, which are discussed in the results of their optimisation in Section 5.3. Particles accelerated to longitudinal momenta above 10 MeV/c were tracked. This energy threshold was chosen to reduce the computational load of the simulation, as electrons with lower energies are generally not trapped in the wakefield.

5.2.2 Algorithm Structure

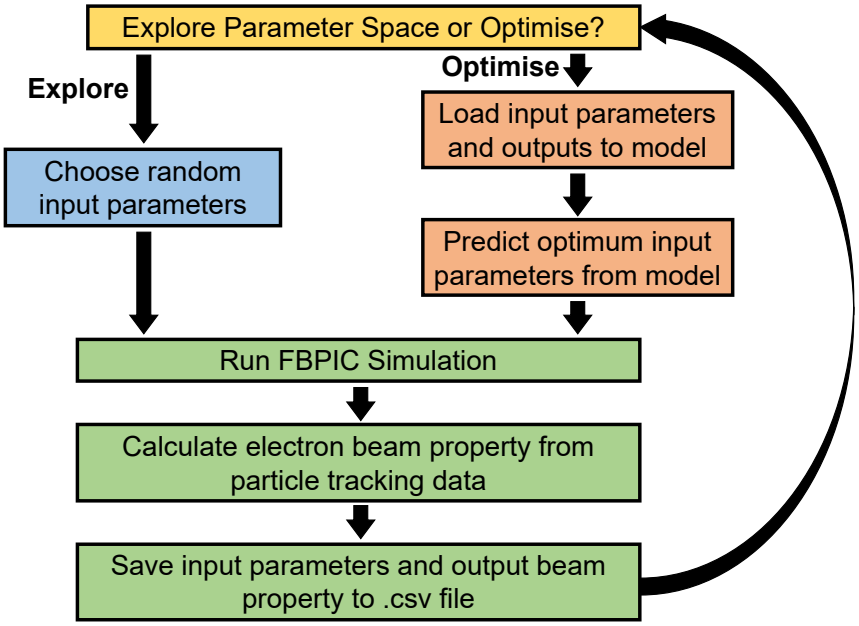


Figure 55: Overview of structure of Bayesian optimisation algorithm

An overview of the BO algorithm structure is given in the flowchart in Figure 55. The algorithm repeats this procedure for a pre-defined number of epochs, or until the user stops it. The “explore” and “optimise” branches in Figure 55 are the two possible methods that the algorithm may choose input parameters for the PIC simulation of each epoch, which are described in the following sections. Once the input parameters have been selected, the FBPIC simulation is run. The details of how each electron

beam property is calculated from the particle tracking data is discussed in Section 5.3. Once calculated, the output electron beam property and the input parameters are saved in a .csv file for training the BO model in future epochs.

5.2.3 "Explore" Branch

The starting input parameters used in the first simulation are a "best guess" expected to produce strong values for the electron beam property of interest, based principally on the scaling laws in Chapter 2. The starting input parameters in each optimisation are included and explained in the results section. The result of this initial simulation will be improved in subsequent simulation through BO. The parameter ranges available for exploration are pre-defined by an upper and a lower bound for each input parameter, included and explained in the results section. In the second and third simulations, the upper and then the lower bounds are used as the input parameters. This ensures that the entire range of the parameter space is explored.

For the next n epochs, where n is set by the user, typically in the range $10 \leq n \leq 40$, the BO algorithm does not try to optimise the electron beam property but simply explores the parameter space. The BO algorithm follows the "explore" branch in Figure 55, where a random value of each input parameter is used in the simulation. This random value is taken from a normal distribution centred on the input parameter's starting value, with a standard deviation (STD) such that $2\sigma = x_{upper} - x_{start}$, where x_{start} and x_{upper} are the upper and lower bounds of the input parameter.

5.2.4 "Optimise" Branch

If the epoch number is greater than a user-defined number and does not satisfy any user-defined conditions, the BO algorithm then follows the "optimise" branch in Figure 55. The input parameters for the next simulation are chosen using BO. A model is fitted to the parameter space using Gaussian process regression (GPR). The theory behind GPR is quite mathematically involved and beyond the scope of this work, but there are a number of resources available if this is of interest, including a book by Rasmussen and Williams, "Gaussian Processes for Machine Learning", written in 2005 [187]. From the GPR-fitted model, a so-called acquisition function is constructed, which quantifies the expected improvement in the output electron beam property at each point in the parameter space. The input parameters are then taken from the coordinates of the peak of the acquisition function. In each epoch, new input parameters for the next simulation are chosen through this procedure, which is repeated until the output electron beam property has converged over a number of epochs.

In this algorithm, the Python classes used to load data to the machine learning model and select the input parameters in the simulations were the same ones as used by Shalloo *et al.* in 2020 [181], which were developed by Stephen Dann. The classes use the scikit-learn package to perform the GPR, which can automatically tune the hyperparameters of the model using a maximum log-marginal likelihood method [188], within pre-specified ranges. The hyperparameters include the length scale and the variance of the model, which determine the closeness of the fitting and its sensitivity to stochastic noise. The mathematical meaning of these hyperparameters and the method of their optimisation is outlined in detail on the scikit-learn webpages [188] among other resources [187].

GPR Model

The GPR model is effectively a probability distribution of all possible functions describing the parameter space. The most probable model is described by a mean function giving the expectation value of the electron beam property in the parameter space. A covariance function describes both the uncertainty on each mean value and the correlation between different parameters. In this algorithm, the covariance function is a Gaussian radial basis function added to a white noise function. A white noise function is included as a correction to the often underestimated statistical error on the electron beam property being modelled. The error is estimated from the noise in the electron spectrum data in each simulation, as described in Section 5.2.5, but it is difficult to predict statistical error due to numerical factors such as the resolution of the simulation. A separate model is fit to the error estimates of the simulations using GPR; the mean function of this model for the errors is used as the variance in the radial basis function for the output electron beam property. While this variance varies at different points in the parameter space, the white noise function provides a global estimate for the noise in the data.

Acquisition Function

In this algorithm, the acquisition function of choice is the expected improvement in the fitted model. This is defined as the expectation value of the difference between a new model if sampled at each point and the maximum of the current fitted model:

$$A(\mathbf{x}) = E(f(\mathbf{x}) - \max(f(\mathbf{x_{opt}})), \tag{5.5}$$

where $\mathbf{x}$ is an arbitrary position vector in the parameter space, $\mathbf{x_{opt}}$ is the position vector of the maximum in the model and $f(\mathbf{x})$ is the mean function of the model in the parameter space. The input parameters of the simulation are taken from the point

in the parameter space where this function is maximised: $\mathbf{x_{new}} = \text{argmax}(A(\mathbf{x}))$. Equation 5.5 is evaluated at 100 different randomly generated position vectors, before selecting the vector that produces the highest value.

5.2.5 Analysis of Particle Tracking Data

In calculating the peak energy and the total charge of the output electron beam, the electron spectrum in the final time-step of the simulation is calculated from the particle tracking data. At this time in the simulation, the electron beam has left the plasma so it is no longer subject to the electromagnetic fields in the plasma. In some simulations, this can be a noisy function like the example "raw" spectrum in Figure 56. A smoothed electron spectrum is obtained through a kernel regression fit, which is the black line. The electron beam property is calculated from this fitted function. The noise level of the electron spectrum is calculated as the RMS difference between the raw and smoothed spectra.

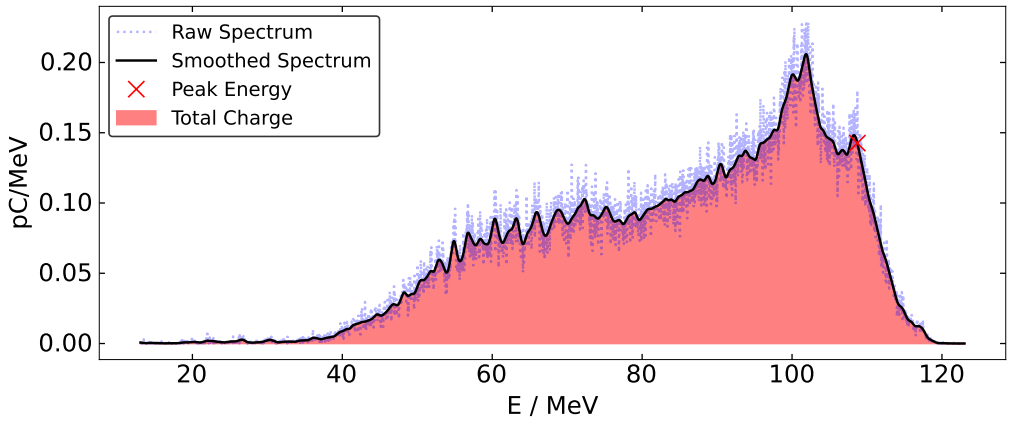


Figure 56: Example raw and smoothed electron spectra from analysis of particle tracking data, with calculated peak energy and total charge

Peak Energy

In the optimisations in this work, the peak energy was not taken as the maximum electron energy in the spectrum, but the highest energy in the spectrum where a local maximum lies. A constraint was placed on this energy: this local maximum must have a height of at least 10% of the spectrum's maximum height. The peak energy was calculated in this way to ensure that a significant portion of the beam is accelerated to comparable energies rather than a small fraction of the total electrons. For example, the spectrum in Figure 56 is dominated by electrons at high energies. This is advantageous for x-ray beam generation.

The statistical error on any energy in the spectrum is calculated from the noise in the electron spectrum at the peak energy:

$$\Delta E = \frac{\partial E}{\partial N} \Delta N, \tag{5.6}$$

where $\frac{\partial E}{\partial N}$ is the gradient of the inverse function of the spectrum, with respect to the number of electrons per unit energy. ΔN is the noise level in the spectrum. To find the error on the peak energy, this equation is evaluated at the peak energy.

Total Charge

The total charge of the electron beam is the area under the curve of the electron spectrum, as shown by the shaded red region in Figure 56. This is calculated by numerically integrating the smoothed electron spectrum over its entire bandwidth. The error on this total charge is the quadrature sum of the errors in each bin, multiplied by the energy range of each bin.

5.3 Results of Optimisations

Two different electron beam properties, the peak energy and the total charge, were optimised in two separate runs of the BO algorithm. In this section, commentaries of both optimisations are given and the effects of the key parameters changed in each optimisation are analysed.

In the optimisation of the peak energy, a cell size of $\Delta z = 0.04$ µm and $\Delta r = 0.30$ µm were used in the PIC simulations, with 1, 2 and 4 particles per cell in the longitudinal, transverse and azimuthal directions. In the optimisation of the total charge, a cell size of $\Delta z = 0.02$ µm and $\Delta r = 0.25$ µm was used. This higher spatial resolution was required due to the highly nonlinear self-injection process being optimised.

5.3.1 Optimising Peak Energy

The input parameters used in the first simulation of the peak energy optimisation are included in Table 5.2. In the first simulation, an n_{He} of 10^{19} cm^{-3} was used, which lies comfortably above the threshold density of 6×10^{18} cm^{-3} for the laser pulse to self-focus, according to Equation 2.37. A small N_{conc} was chosen similar to other experiments using ionisation injection as the injection mechanism [141], [143], [189]–[191]. Such a small concentration would not alter the plasma density significantly. l_{up} was set to 0.1 mm and z_{focus} was set to 0.2 mm in the plasma. l_{up} and z_{focus} were set at these values so that the first electrons are injected after the start of the gas density

Table 5.2: Starting values, upper and lower bounds of input parameters in Bayesian optimisation of the peak energy

Parameter	Unit	Starting Value	Lower Bound	Upper Bound
n_{He}	$\log_{10}$ [cm^{-3}]	19.0	18.0	20.0
N_{conc}	$\log_{10}$ [%]	-0.5	-2.0	1.0
L_{plasma}	mm	0.6	0.2	1.2
z_{focus}	mm	0.20	0.00	0.40
l_{up}	mm	0.10	0.01	0.50
l_{down}	mm	0.10	0.01	0.50
$\phi^{(2)}$	fs^2	0	-50	50
$\phi^{(3)}$	fs^3	0	-500	500
$\phi^{(4)}$	fs^4	0	-5000	5000

plateau, where the accelerating field should be stronger than at the lower densities in the up-ramp itself. The length of the plasma, L_{plasma}, was set such that the end of the plasma coincided with where the electrons reach their dephasing limit, calculated from Equation 2.58 for the dephasing length. Finally, the spectral phase coefficients of the laser pulse were all set to zero for the shortest, highest intensity laser pulse with a Gaussian shape focused into the plasma.

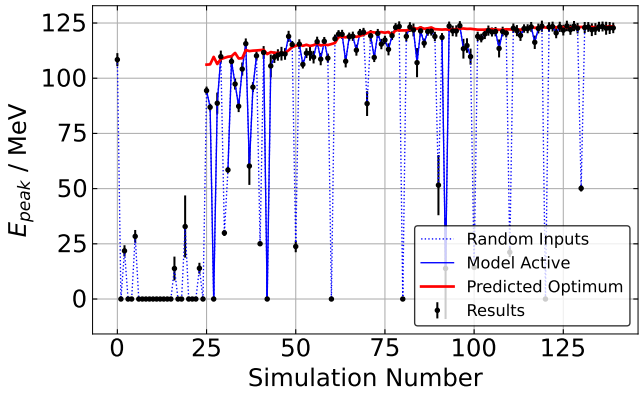


Figure 57: Output peak energy of electron beam against simulation number.

In the first simulation, an electron beam with a peak energy of 109 MeV was produced. This is the first data point in Figure 57, after which a succession of electron beams with smaller peak energies were produced while the parameter space was being explored. In simulations 3 to 25, the input parameters were random values from normal distributions, with means equal to the starting values and STDs of half the difference between the upper and lower bounds in Table 5.2. The dashed blue lines in Figure 57 indicate simulations when random input parameters were chosen like this. The solid blue lines indicate that the BO algorithm was trying to optimise the peak electron beam energy. After 25 simulations, every tenth simulation had its input

parameters chosen randomly to check that the BO algorithm was not just exploiting a local maximum in the parameter space. The input parameters were optimised for the peak electron beam energy in simulations 26 to 155. In Figure 57, after 100 simulations, the data points for the output peak energy converge on 125 MeV, as well as the optimal value predicted by the algorithm shown by the red line.

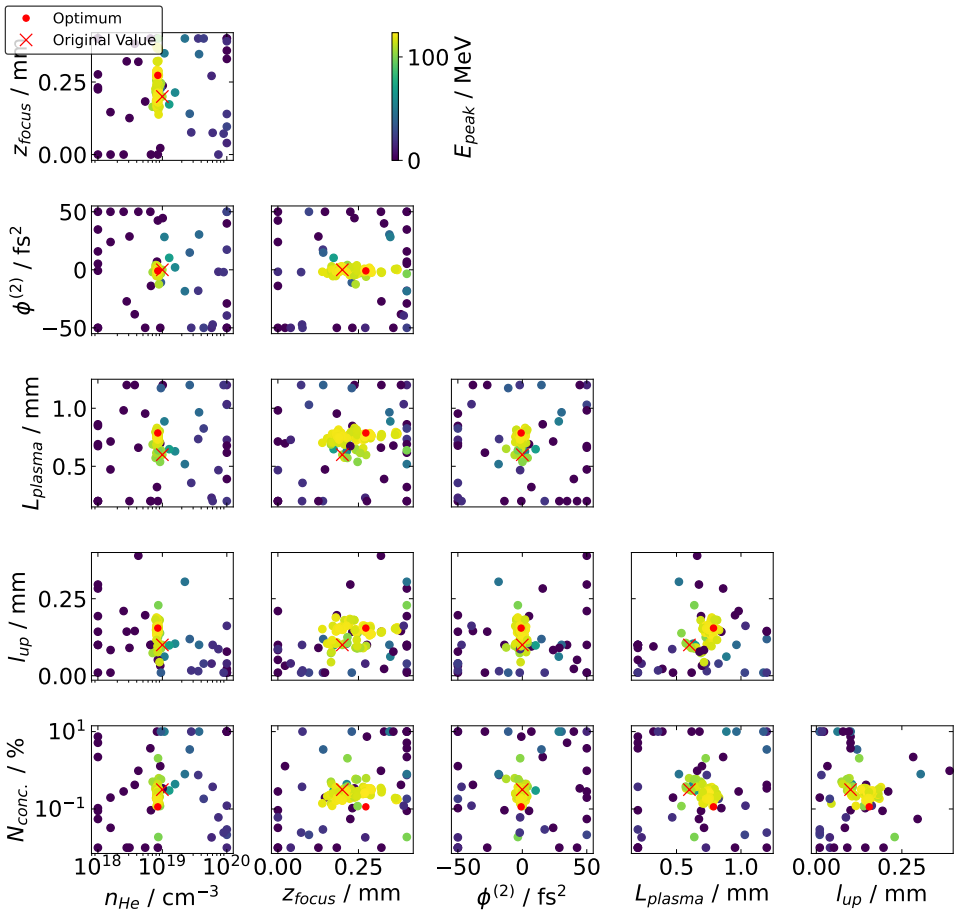


Figure 58: Scatter plots of input parameters of each simulation in the optimisation. Each scatter point is colour-coded against the peak energy of the output electron beam of its simulation.

While the optimisation only results in a 15 MeV improvement in the peak energy in this case, it is still worth understanding the electron energies that can be obtained in a parameter space like this one for SYLOS-2. In Figure 58, the input parameters of each simulation are plotted in different scatter plots and colour-coded against their output peak energy. This provides an overview of the multi-dimensional input parameter space and gives insight into the key parameters used to optimise the peak energy. Along the axes of n_{He} and $\phi^{(2)}$, the bright regions in which peak energies above 100 MeV were produced are particularly small. This implies that the peak energy is particularly sensitive to these input parameters within these regions in the parameter space. Along the axes of z_{focus} and L_{plasma} in their respective scatter plots, there is a

gradual change in colour of the points in the optimal regions. Along the axes of z_{focus}, L_{plasma} and l_{up}, the optimal bright regions are wider. Adjusting these parameters over the ranges in these plots decreases the peak energy by up to 60 MeV.

The locations of the initial and optimal simulations in the input parameter space are plotted in red in Figure 58, showing how far each the input parameter has been adjusted in the optimisation. Within the ranges in Figure 58, only small adjustments needed to be made to n_{He}, N_{conc} and $\phi^{(2)}$, to which the peak energy seems to be particularly sensitive. The largest changes from the initial to the optimal simulations in Figure 58 are along the axes of l_{up}, z_{focus} and L_{plasma}. In the optimal simulations, l_{up} has been increased, the laser pulse has been focused further into the plasma and the plasma has been made longer than in the initial simulation.

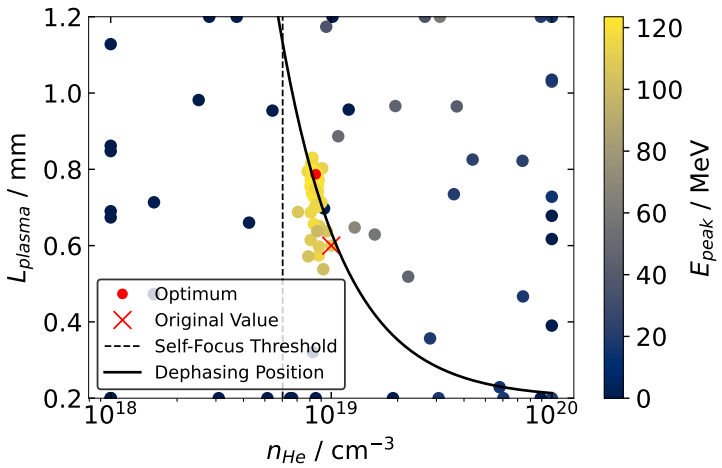


Figure 59: Scatter plot of n_{He} against L_{plasma}. Each point corresponds to a different simulation and is colour-coded against the output peak energy.

The scatter plot of n_{He} against L_{plasma} re-plotted in Figure 59 shows that electron beams are accelerated to energies above 100 MeV for n_{He} between 7×10^{18} cm^{-3} and 1×10^{19} cm^{-3}. This is the region just above the self-focusing threshold of the laser, shown as the dashed vertical line in Figure 59. Assuming that electrons start to be injected at the start of the plasma density plateau at $z \approx 0.2$ mm, the position where electrons at the front of the beam reach their dephasing limit was calculated by adding this to the dephasing length given by Equation 2.58, plotted as the black solid line. In the yellow optimal region where electron beams are accelerated to around 100 MeV, the input n_{He} and L_{plasma} roughly follow the expected dephasing position of the electrons. L_{plasma} has been adjusted such that the end of the plasma coincides with where the highest energy electrons in the beam reach their dephasing limit.

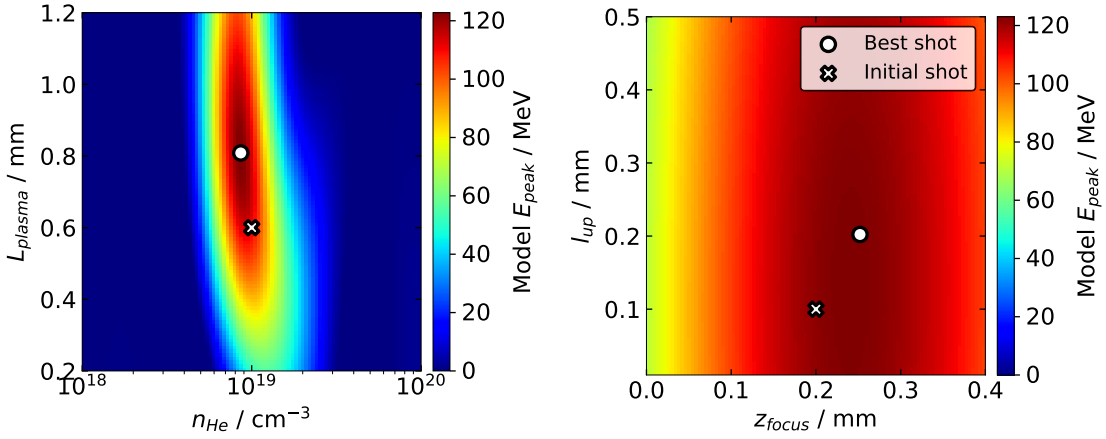


Figure 60: (Left) Model of peak electron beam energy against n_{He} and L_{plasma} produced by BO algorithm. (Right) BO model of peak energy against z_{focus} of the laser and plasma l_{up}. In both plots, all other input parameters are fixed at their values from the optimal simulation.

The reason why the optimal n_{He} does not lie closer to threshold density for self-focusing is because the laser pulse gradually loses power as it drives the wakefield, effectively increasing the self-focusing threshold. The laser diffracts and ceases to drive a wakefield before the end of the plasma. The laser pulse evolution is a complex and highly nonlinear process that is optimised more easily by the BO algorithm than could be done manually. The left plot of Figure 60 is a map of the model fitted by the BO algorithm to the n_{He}-L_{plasma} slice in the parameter space, with all other input parameters fixed at their values in the optimal simulation. This plot shows that the BO algorithm successfully models the decrease in the peak energy at lower n_{He}. As should be the case, the location of the input parameters of the optimal simulation lies at the maximum of the model.

On the right of Figure 60 is a map of the model fitted by the BO algorithm in a slice of l_{up}-z_{focus} in the parameter space. All other input parameters are fixed at their values from the optimal simulation. While the model predicts almost no change in the peak energy if l_{up} is changed, moving the z_{focus} to 0.0 mm decreases the peak energy to 60 MeV, according to the model. A scan of z_{focus} was performed by running simulations with different values of z_{focus}, while keeping all other input parameters the same as in the optimal simulation. The peak energies produced in each of these simulations are consistent with the predictions of the model in Figure 60 within 5 MeV.

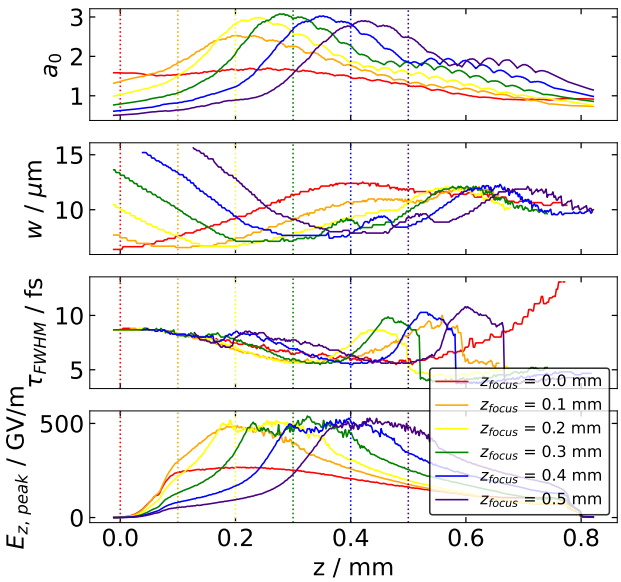


Figure 61: (Top to bottom) Normalised potential, $1/e^2$ waist, FWHM duration of the laser pulse and peak electric field in the wakefield as the laser travels through the plasma. The laser's focal position in each simulation are plotted as the vertical dashed lines. All other input parameters are at their optimal values.

In the top three panels of Figure 61, the progression of the normalised potential, $1/e^2$ waist and FWHM duration of the laser pulse are plotted for each simulation in a scan of z_{focus}. In these three panels, the progression of the laser pulse is very similar when focused between 0.2 mm and 0.5 mm, just separated by 0.1 mm distances. In the bottom panel, the peak accelerating electric field in the wakefield progresses in much the same way in all four of these simulations. For $z_{focus} = 0.0$ mm and $z_{focus} = 0.1$ mm, shown by the red and orange lines, the laser pulse reaches its focal position before the start of the plasma density plateau at 0.1 mm. In the top panel, the intensity of the laser pulse does not reach as high values as in simulations with $z_{focus} \geq 0.2$ mm. In the second and third panels, the minima in the two red lines and orange lines are at different z-positions. In these simulations, the $1/e^2$ waist of these laser pulses pass their minimum values at focus and then defocus before the laser pulse is compressed to its shortest duration in the plasma.

In the bottom panel of Figure 61, the progression of the peak accelerating electric field in the wakefield is plotted. Due to the similar evolution of the laser pulse when the laser is focused between 0.2 mm and 0.5 mm, the progression of the wakefield is also similar in these simulations, producing similar electron beams. When $z_{focus} = 0.1$ mm, the peak accelerating field does reach similar peak values as in simulations with higher z_{focus}, but the distance over which this peak electric field is sustained is about half of

the distance achieved in the other simulations. For $z_{focus} = 0.0$ mm, the peak accelerating field of the laser pulse does not reach as high values as in the simulations with a higher z_{focus}, so electrons are not accelerated to as high energies.

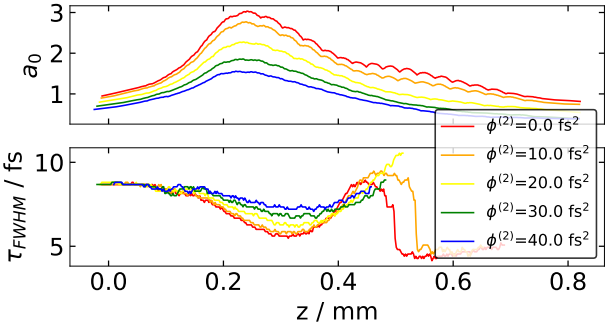


Figure 62: (Top) Normalised potential and (bottom) pulse duration of laser pulses in plasma with different second-order spectral phase coefficients.

The other input parameter that the peak electron beam energy has a strong dependence on is the second-order spectral phase coefficient of the laser. The highest electron beam energies were obtained when $\phi^{(2)} = 0$, so the duration of the input laser pulse was at its transform limit. In the bottom panel of Figure 62, the duration of the laser pulse at its focal position is shortest when $\phi^{(2)} = 0$. This is also when the intensity of this laser pulse reaches the highest values, shown in the top panel, driving the wakefield with the strongest accelerating fields. Laser pulses with larger $\phi^{(2)}$ have a lower intensity, and hence drive weaker wakefields.

Simulation with Optimal Input Parameters

A peak energy of 125 MeV was simulated after optimisation by the BO algorithm. The output electron spectrum of the optimal simulation is shown in the left panel of Figure 63 in red, which is compared with the electron spectrum of the initial simulation in blue. As shown in earlier analysis, the main improvement from 110 MeV to 125 MeV comes from the optimisation of n_{He} and also the adjustment of L_{plasma} to where the electrons dephase. In the right panels of Figure 63, the progression of the electron spectrum through the plasma is plotted for both the initial and optimal simulations. Owing to the lower plasma density in the optimal simulation, the dephasing length is longer than in the initial simulation. According to Equation 2.59, a lower plasma density means a higher electron energy at the dephasing length. That is, provided that the normalised potentials of the laser pulse are similar. Plotted in black in the right panels of Figure 63 is the progression of the normalised potential of the laser in each plasma, showing that the intensity progression and the peak intensities reached by the laser pulse in each simulation are indeed similar.

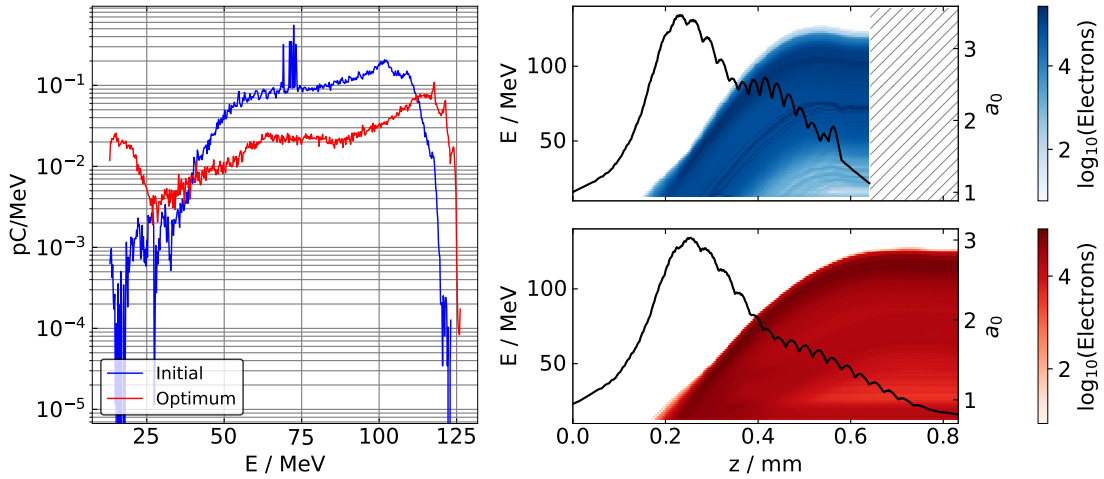


Figure 63: (Left) Output electron spectra of initial (blue) and optimal (red) simulations in peak energy optimisation. (Right, left axis) Progression of electron beam spectrum through plasma in initial (blue) and optimal (red) simulations. (Right, right axis) progression of normalised potential of the laser pulse (black line).

The electron beam in the optimal simulation was injected into the wakefield via ionisation injection. This was confirmed by running the optimal simulation with no nitrogen dopant, which produced no electron beam. The absence of an electron beam in this simulation means that virtually no electrons enter the wakefield via self-injection. In the optimum simulation, $N_{conc} = 0.2\%$, so the absence of nitrogen should not affect the plasma density significantly.

5.3.2 Optimising Total Charge

At the start of the optimisation of the total electron beam charge, the initial simulation was run with the input parameters in Table 5.3. The input parameters are largely the

Table 5.3: Starting values, upper and lower bounds of input parameters in Bayesian optimisation of total electron beam charge

Parameter	Unit	Starting Value	Lower Bound	Upper Bound
n_{He}	$\log_{10}$ [cm^{-3}]	19.6	18.0	20.0
N_{conc}	$\log_{10}$ [%]	-1	-2.0	1.0
L_{plasma}	mm	0.7	0.2	1.2
z_{focus}	mm	0.10	0.00	0.40
l_{up}	mm	0.10	0.01	0.50
l_{down}	mm	0.10	0.01	0.50
$\phi^{(2)}$	fs^2	0	-100	100
$\phi^{(3)}$	fs^3	0	-500	500
$\phi^{(4)}$	fs^4	0	-5000	5000

same as in the initial simulation in the peak energy optimisation, except for n_{He} and z_{focus}, which were adjusted to try to satisfy the conditions for self-injection and ionisation injection, given by Equations 2.48 to 2.49 and Equation 2.52. A higher n_{He} of 4×10^{19} cm^{-3} and an earlier z_{focus} of 0.1 mm were used. These parameters were chosen to maximise the growth in the intensity of the laser pulse. The laser was expected to experience the strongest self-focusing and pulse compression in the density plateau; focusing the laser at the front of the plateau minimises the depletion of the laser pulse before reaching its intended z_{focus}.

The initial simulation produced an electron beam with a total charge of 120 pC above an energy of 10 MeV. The total charge was optimised after 150 simulations to 210 pC through the adjustment of several input parameters. In Figure 64, the input parameters of each simulation are plotted in different scatter plots and colour-coded against the output total charge. Along the axes of n_{He} and N_{conc} in these plots, the red cross of the initial simulation always lies outside the brighter regions where near-optimal or optimal total charges were produced. This suggests that it was the changes in these

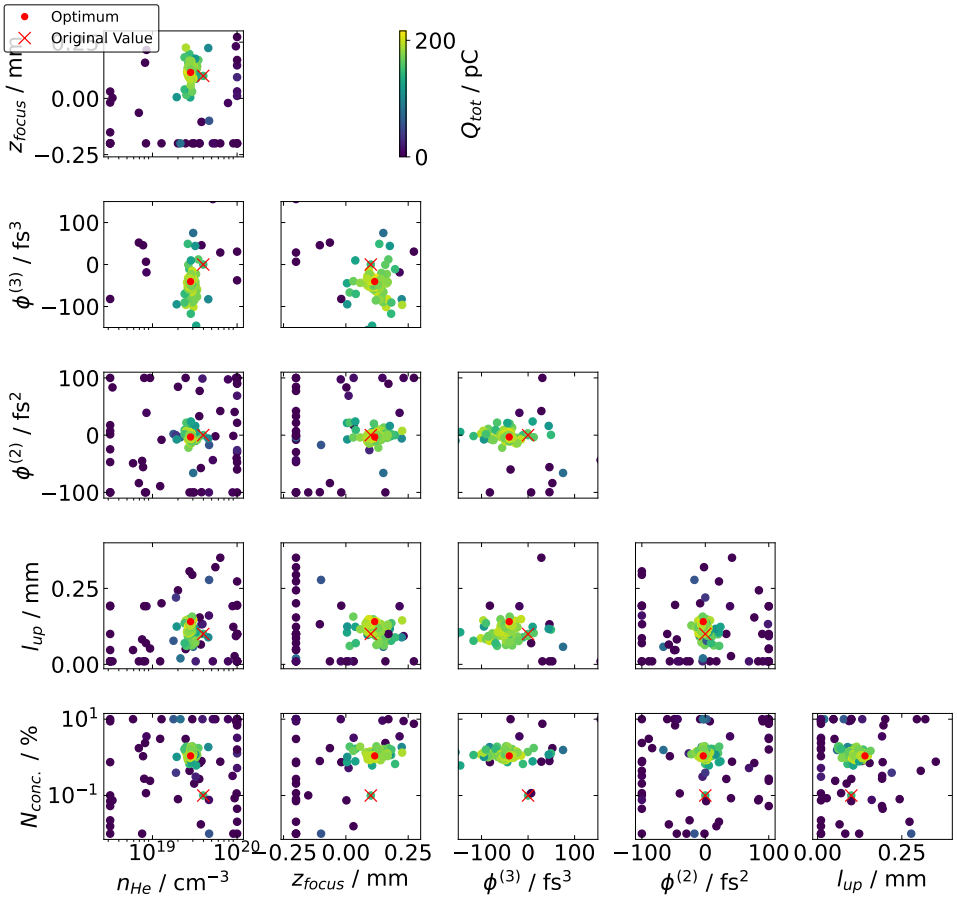


Figure 64: Scatter plots of input parameters of each simulation in the optimisation. Each scatter point is colour-coded against the total charge of the output electron beam of its simulation.

parameters that produce the largest changes in the total charge output. The bright, optimal regions in these plots are narrowest along the axes of n_{He}, N_{conc} and also $\phi^{(2)}$. The total charge falls rapidly toward zero outside of these regions, suggesting that the total charge is particularly sensitive to these parameters. Other input parameters are still important in optimising total charge, although changing their value in the plots in Figure 64 alters the output by ~ 10 pC rather than ~ 100 pC. For z_{focus}, l_{up}, N_{conc} and $\phi^{(3)}$, there is a more gradual change in the colour across the optimal regions in the scatter plots.

In simulations producing electron beams with the highest total charges, the electrons are injected via self-injection. On the left plot of Figure 65 is a map of the model of the total charge in the parameter space in the $n_{He} - N_{conc}$ plane, with all other input parameters fixed at their values from the optimal simulation. Along the axis of N_{conc}, the predicted total charge in the electron beam does not change. This was verified by running a new PIC simulation with the optimal input parameters but with no nitrogen dopant. An electron beam with the same total charge of 200 pC was produced. The BO algorithm thus adjusted the other input parameters to optimise the self-injection process. It should be noted that the BO algorithm may have found that larger total charges are produced through self-injection owing to the tendency of PIC simulations to overestimate the amount of self-injected charge [176]–[178]. However, there is still some physics in the simulated injection processes worth studying.

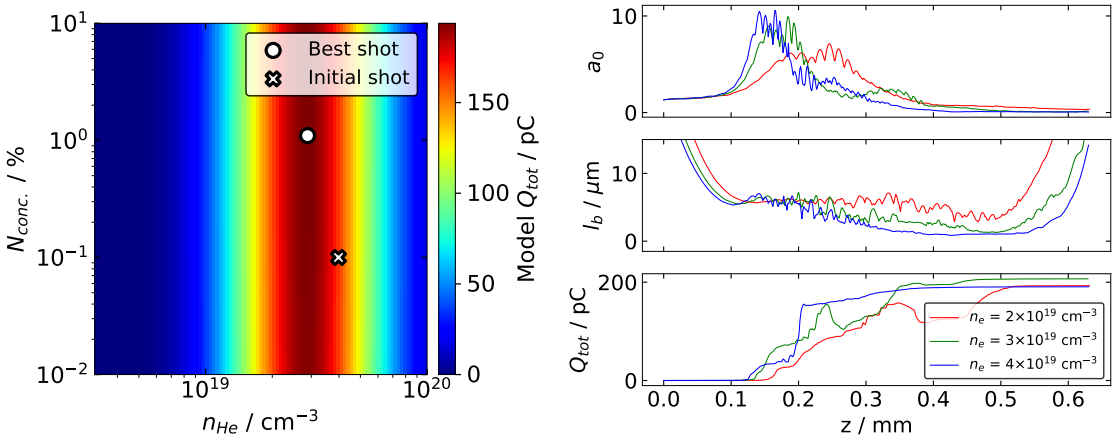


Figure 65: (Left) Model of total electron beam charge against n_{He} and L_{plasma} produced by BO algorithm. All other input parameters are at their optimal value according to the model. (Right) Progression of normalised potential of laser pulse, estimated bubble length and total electron beam charge in LWFAs with different n_{He}.

Along the axis of n_{He} in the left plot of Figure 65, the fitted model ranges from nearly zero to 200 pC in the range 10^{19} to 10^{20} cm^{-3}. The model peaks at $n_{He} = 3 \times 10^{19}$ cm^{-3}. On the right panel of Figure 65, the progression of the normalised potential of the

laser, an estimate of the bubble length using Equation 2.46 and the total electron beam charge are plotted in green for this optimal density. All other input parameters are fixed at their values in the optimal simulation. In the bottom plot, a large amount of charge is self-injected around $z = 0.2$ mm. This coincides with an increase in the bubble length in the middle plot, which is a mechanism of self injection described in Section 2.7, which is induced by the increase in the normalised potential of the laser pulse, as shown in the top plot. This intensity increase is caused by the compression and self-focusing of the laser pulse in the plasma, which is navigated more easily and precisely by the BO algorithm than could be achieved manually.

On the bottom right plot of Figure 65, the rate of charge injection in the optimal case of $n_{He} = 3 \times 10^{19}$ cm^{-3} in green is higher than in the case of $n_{He} = 2 \times 10^{19}$ cm^{-3} in red. In the case of $n_{He} = 4 \times 10^{19}$ cm^{-3} in blue, the rate of charge injection is higher but the distance over which electrons are injected is smaller than in the optimal case. The BO algorithm has found the optimal combination of these two competing factors. In the high density case, the bubble expands more rapidly, but is followed by a period of bubble compression as the laser pulse depletes faster. In the low density case, there is a long period over which the laser potential increases and the bubble expands, but the bubble expansion is slower. There is a trade-off between having a fast bubble expansion where charge is injected rapidly but over a short distance, versus having a sustained bubble expansion over which electrons are injected over a longer period of time more slowly.

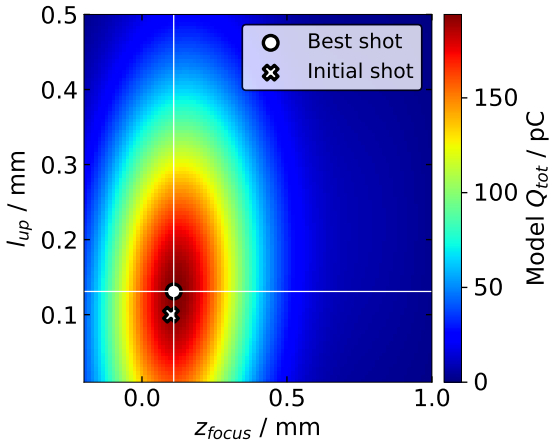


Figure 66: BO model of total charge against z_{focus} and plasma l_{up}. All other input parameters are at their predicted optimal values by the model.

In Figure 66, the predicted total charge of the model is mapped against the laser's focal position and the density up-ramp length, z_{focus} and l_{up}, with all other input parameters fixed at their values in the optimal simulation. The total charge is particularly

sensitive to z_{focus}, as the peak is thinner along this axis. The total charge falls away more slowly along the axis of l_{up}. For the optimum total charges, the laser pulse should be focused just before the start of the gas density plateau at $z_{focus} = 0.10$ mm and $l_{up} = 0.14$ mm, where the model peaks. The slight slant in the peak away from the vertical suggests some weak relation between z_{focus} and l_{up} and the total electron beam charge. As l_{up} is increased, the start of the density plateau moves further into the plasma so the laser should be focused further in, where pulse compression and self-focusing is strongest.

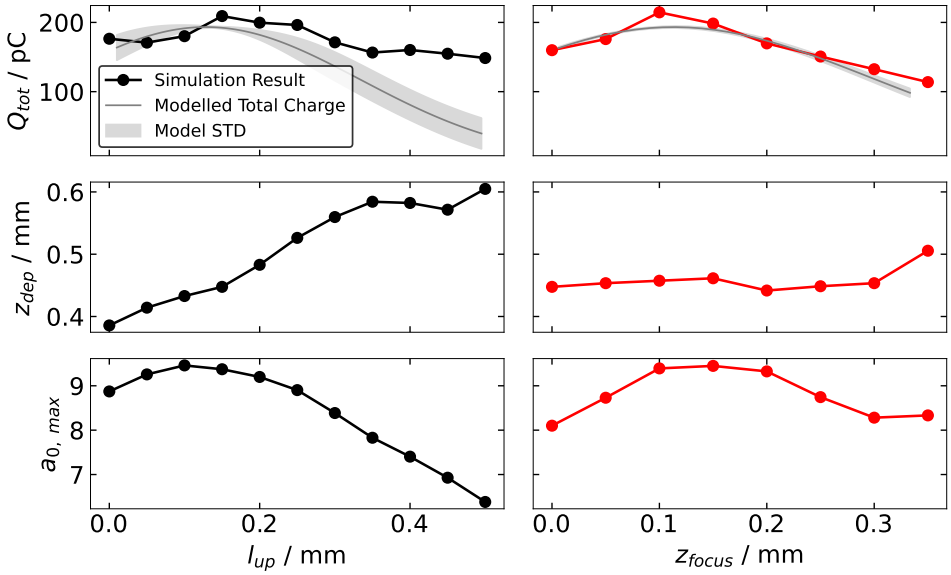


Figure 67: Scans of (left) l_{up} and (right) z_{focus}, while keeping the others at their values in the optimum simulation. (Top to bottom) Total electron beam charge, z-position where laser pulse depletes and peak normalised potential of laser pulse in simulation.

Univariate scans of l_{up} and z_{focus} have been performed by running simulations with different values of these input parameters along the white axes in Figure 66. In Figure 67, the total charge and two properties of the laser pulse in these scans are plotted. In the top panels, the total charge is plotted against each input parameter and compared with the total charge predicted by the model, plotted in grey. The simulated total charge indeed peaks around $z_{focus} = 0.10$ mm and $l_{up} = 0.14$ mm. In the top right panel, the total charge decreases similarly to the model as z_{focus} is changed. Around the peak in the model in the top left panel, the simulated total charge is similar to that of the model, but at values of l_{up} greater than 0.3 mm, the model predicts a decrease of over 50%, whereas the total charge of the simulated beams only falls by around 20%. The STD in the model, which is a measure of its error, is also larger when l_{up} is greater than 0.2 mm. This difference is probably because fewer simulations were run in that part of the parameter space, further away from the optimum.

In the left column of Figure 67, two properties of the laser pulse in the scan of l_{up} have also been plotted. In the middle panel, the z-coordinate at which the laser pulse depletes is plotted, defined as the point in the plasma where the normalised potential of the laser pulse falls below 1. The z-coordinate at which the laser pulse depletes increases with increasing l_{up}. The point of depletion changes when l_{up} is comparable to the total length of the plasma, because lengthening the density up-ramp decreases the average density that the laser propagates through. When l_{up} is increased, the depletion point is further into the plasma, as predicted by Equation 2.60 where $L_{pd} \propto \gamma_p^2 \propto 1/n_e$. The bottom plot shows that increasing l_{up} results in a decrease in the peak normalised potential reached by the laser pulse, which has been plotted as a measure of the growth in the laser intensity that causes the bubble expansion and subsequent self-injection. The highest potential reached by the laser pulse is produced at $l_{up} = 0.1$ mm, which is near the value of l_{up} producing the highest charge is produced, as shown in the top panel. This implies that a slower bubble expansion and hence a lower rate of self-injection. l_{up} has been adjusted mainly to maximise the initial bubble growth rather than sustain the bubble growth.

In the middle and bottom panels in the right column of Figure 67, the two properties of the laser pulse progression have been plotted in the scan of z_{focus}. In the middle panel, the depletion point of the laser does not change with z_{focus}. The depletion length depends on the plasma density and the duration of the laser pulse, according to Equation 2.60, so it should not change with z_{focus}. In the bottom right panel, the highest normalised potential is reached for $z_{focus} = 0.1$ mm and decreases as z_{focus} is increased after that point. This implies that the rate of charge injection is optimised at $z_{focus} = 0.1$ mm and slowly decreases at higher values of z_{focus}.

The final input parameter that was changed during the optimisation was $\phi^{(3)}$, which was zero in the initial simulation and -40 fs^3 in the optimal simulation. In Figure 68, the progression of the laser pulse and the electron beam are plotted for LWFAs driven by laser pulses with each of these values, with all other input parameters set to those of the optimal simulation. On the left panels, the electric field of the laser pulse is plotted at the start of the simulation at the top and at the point where charge starts to be injected at the bottom. The basic shapes of the two laser pulses are almost the same, with their phases slightly displaced. The progression of the laser pulse intensities are also similar, as shown in the top right plot of Figure 68. Nevertheless, in the case of $\phi^{(3)} = -40$ fs^3, charge is always injected at a higher rate, as shown in the bottom right plot, producing an electron beam with 20% more charge by the end of the plasma. Similar variations in the total charge in response to subtle changes in the

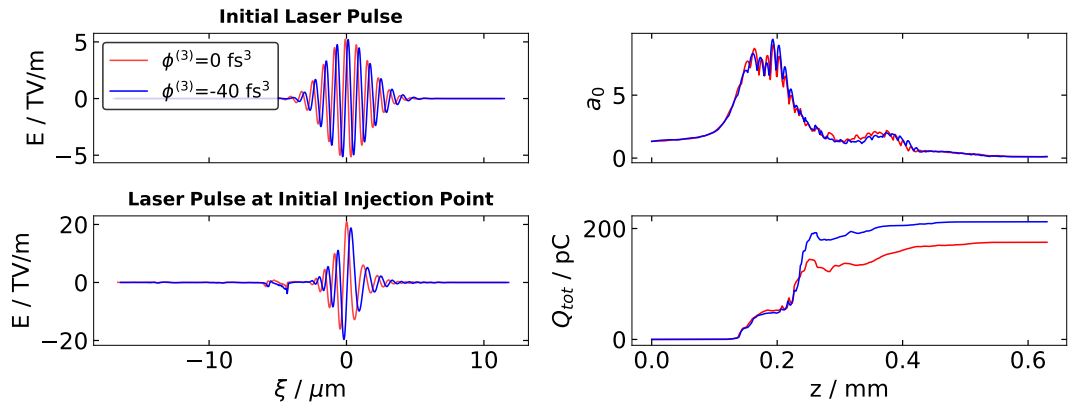


Figure 68: (Top left) Initial electric field slices of laser pulses and (bottom left) electric field slices at the start of self-injection process at $z = 0.15$ mm. (Top right) Progression of normalised potential of laser pulses in the plasma. (Bottom right) Progression of total charge in the accelerated electron beams.

laser pulse shape were found by Shalloo *et al.* in 2020 using a BO algorithm to optimise the total charge [181]. This increase in charge is difficult to predict analytically, further motivating the use of a machine learning algorithm.

Simulation with Optimal Input Parameters

In the optimal simulation, the output electron beam had a total charge of 216 pC above an energy of 10 MeV, which is a 70 pC improvement from the initial simulation run with the "best guess" input parameters. The spectra of the initial and optimal output electron beams are shown in the left panel of Figure 69. In terms of total charge, the main difference between the two spectra is that there is an increased number of electrons at energies between 0 and 30 MeV in the optimal simulation in red. The spectrum of the optimal simulation extends to 80 MeV and the spectrum of the initial simulation extends to 64 MeV, which is because the plasma density is 2×10^{19} cm^{-3} in the optimal simulation and 4×10^{19} cm^{-3} in the initial simulation. However, the electron beam in the optimal simulation does not contain significantly more total energy than in the initial simulation, suggesting that optimising the total charge as a raw parameter is simplistic. Optimising more complex parameters such as the laser-to-electron beam energy conversion efficiency or the spectral brightness of the electron beam could produce electron beams more suited to potential radiation generation applications. This will be left to future investigations.

In the top right panel in Figure 69, the progression of the normalised potential of the laser pulse is plotted. The red line shows that in the optimal simulation, the growth in the laser pulse potential is slower than in the initial simulation plotted in blue. In the optimal simulation, the normalised potential falls below 1 after a distance of 0.5 mm,

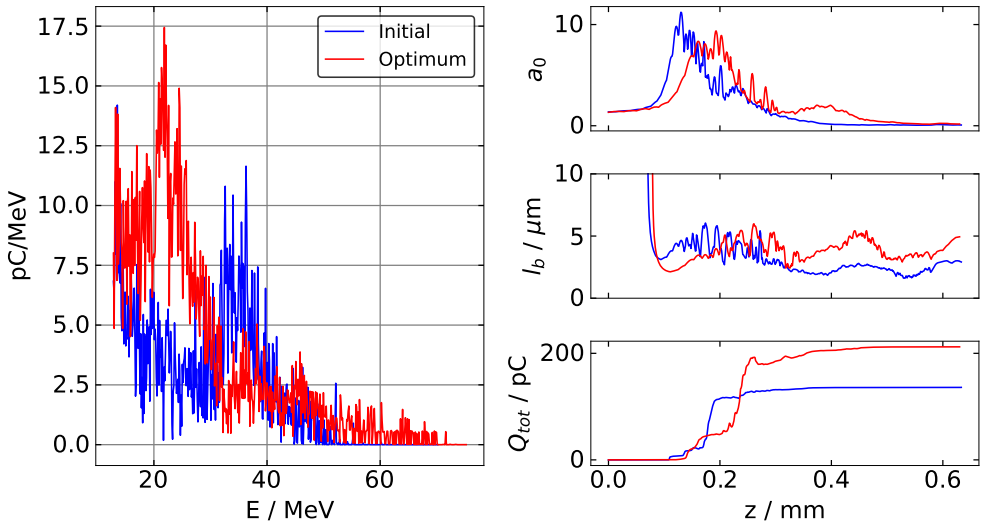


Figure 69: (Left) Electron spectra of initial and optimal simulations in total charge optimisation. (Right) (Top) Progression of normalised potential of the laser pulse, (middle) length of bubble and (bottom) total charge in electron beam.

whereas in the initial simulation, this happens after only 0.25 mm. This is primarily because of the higher n_{He} of 5×10^{19} cm^{-3} in the initial simulation. In the middle panel, the progression of the estimated bubble length is plotted, which shows that the bubble expansion in the optimal simulation starts later in the plasma than in the initial simulation. While the bubble expansion is slower in the optimal simulation, it lasts longer, up to 0.4 mm into the plasma. Charge is injected over a longer distance.

In the bottom right plot in Figure 69, the progression of the total charge in the electron beams is plotted, confirming that the injection of charge occurs over a longer distance in the optimal simulation. At $z = 0.1$ mm, the initial rate of charge injection is actually larger in the initial simulation, but in that simulation almost all electrons have been injected by 0.2 mm in the plasma. In the optimal simulation, most electrons are injected between $z = 0.1$ mm and 0.3 mm.

5.4 Summary

A BO algorithm has been built to optimise different properties of electron beams produced in PIC simulations of LWFAs. In two separate optimisations, the algorithm was used to maximise the peak energy and the total charge of electron beams accelerated in LWFAs driven by a 30 mJ, 8 fs laser pulse focused to a $1/e^2$ waist of 6.6 µm, similar to the parameters of the SYLOS-2 laser at the eSYLOS facility at ELI-ALPS.

The peak energy optimisation showed that electron beams with energies up to 125 MeV

could be produced using a laser system like SYLOS-2. This was achieved, through the adjustment of multiple parameters. n_{He} was minimised to the point where the laser pulse does not self-focus through the whole plasma and L_{plasma} was adjusted such that the end of the plasma coincides with where the electrons reach their dephasing limit. z_{focus} was also shown to change the peak energy by up to 60 MeV when varied between 0.0 and 0.2 mm. The BO algorithm adjusted this parameter such that the laser pulse had compressed to its shortest duration by its focal point, where electrons were injected into the wakefield via ionisation injection. This produced the highest laser intensity, and thereby the strongest accelerating field. The adjustment of n_{He} and z_{focus} optimised the highly nonlinear evolution of the laser pulse in the plasma, which is done more easily with the BO algorithm than with analytical scaling laws.

In the optimisation of the total charge, electron beams with a total charge of 210 pC above and energy of 10 MeV were produced. By adjusting n_{He}, l_{up} and z_{focus}, the expansion of the bubble was optimised to maximise the amount of self-injected charge in the wakefield. By adjusting these parameters, the BO algorithm was able to find the best balance between maximising the initial expansion of the bubble and sustaining the bubble expansion over a long distance. This, once again, is a highly nonlinear and complex process that a machine learning algorithm is better placed to manipulate than someone using analytical relations. In the optimal simulations, all 210 pC was self-injected over a distance of 0.2 mm in the plasma density plateau; the peak intensity of the laser pulse was not as high as in simulations with higher n_{He} and smaller l_{up}, but in those simulations charge was injected over a shorter distance of around 0.1 mm. The BO algorithm also found that 20% more charge was injected into the wakefield when $\phi^{(3)} = -40$ fs $^{-3}$ compared to $\phi^{(3)} = 0$ fs $^{-3}$.

6. Electron Beams from LWFAs Driven by the SEA Laser at eSYLOS

This chapter reports on the first experiment performed at the eSYLOS facility. At the time of the experiment, the SYLOS-2 laser was not available so its alignment laser, the SEA laser, was used instead. The SEA laser delivers laser pulses with energies of up to 44 mJ with a duration shorter than 13 fs [102]. The main difference between the SYLOS-2 and SEA lasers is that the SEA laser operates at a repetition rate of 10 Hz, rather than 1 kHz. The first half of this chapter reports on the experimental methods used to measure the laser focal spot, plasma density and electron beam spectrum. In the second half of this chapter, we report on the results of the first experimental work at the eSYLOS facility, where electron beams were produced in LWFAs driven by the SEA laser. Preliminary scans of the plasma density and laser's focal position were performed, where the peak energy and total charge were measured.

6.1 Experimental Setup and Methods

In this section, we recount the experimental methods used in the first LWFA experiment at the eSYLOS facility. An overview of the basic experimental setup of eSYLOS is given in Figure 70. The drive beam is the SEA laser, which was focused into a nitrogen-filled gas cell by an $f/9$ parabolic mirror, which drove the LWFA. The residual laser light was reflected out of the path of the accelerated electron beam with a mirror with a 3 mm diameter hole at its centre. Electrons leaving the gas cell passed through this hole, and then passed though an approximately uniform magnetic field of 1.0 T, between the poles of a dipole magnet. The magnetic field deflected electrons through different angles depending on their energy, so they reached different positions on a scintillator screen, from which a spectrum of the electrons was produced, as described in Section 6.1.4.

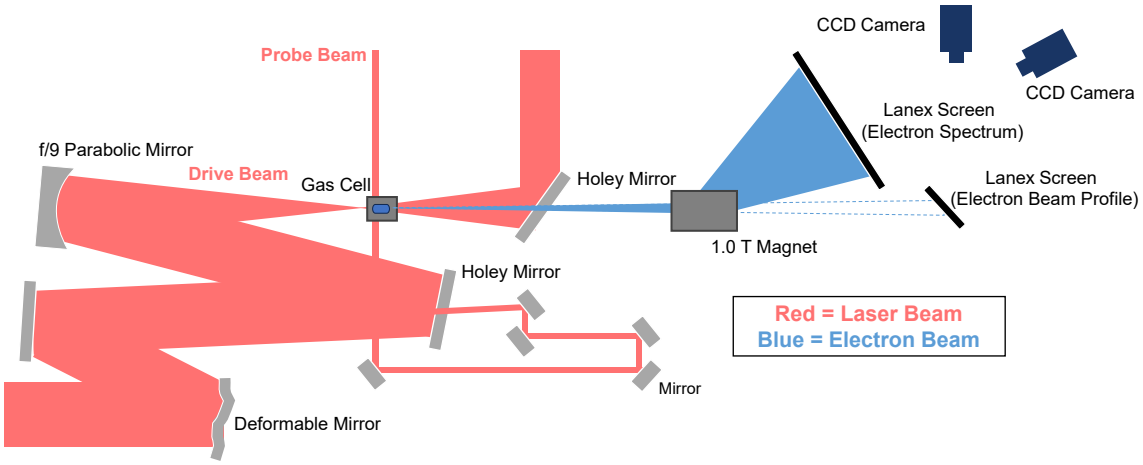


Figure 70: Schematic of basic experimental setup of eSYLOS.

Before the laser beam reached the focusing optic, it was reflected off of a mirror with a hole at its centre, which is the first “holey mirror” in Figure 70. The centre of the laser beam passed through that hole, was reflected off of a series of mirrors and passed across the gas cell perpendicular to the drive beam. This beam was used to probe the density of the plasma channel forged by the drive beam ionising the nitrogen gas in the cell. The plasma density was measured using interferometry, a technique described in Section 6.1.2.

6.1.1 Gas Target

In this experiment, the SEA laser was focused into a gas cell containing nitrogen. A drawing of the gas cell is shown in Figure 71. The laser was focused through a pinhole at the centre of a ceramic plate at the front of the cell. The pinhole had an initial aperture of 60 µm. At the back of the cell is also a ceramic plate with a pinhole

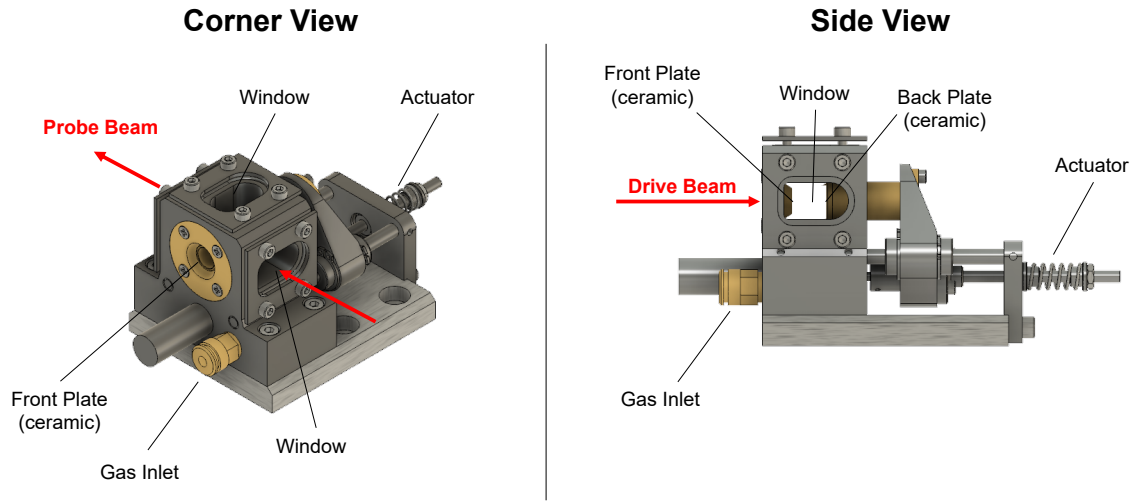


Figure 71: Drawing of gas cell used in experiment. Drawing was made by Andy Rochester and recoloured by the author for this work.

at its centre, through which the laser pulse exited the cell. The ceramic plates often needed to be replaced as the edges of the laser ablated the perimeter of the pinholes, making them larger with a diameter of up to 200 µm. Larger pinholes would allow for gas to escape the cell more quickly, reducing the achievable densities in the cell. A larger pinhole diameter also lengthens the up-ramp at the front of the gas density profile [192], which unfortunately could not be measured with interferometry as the front of the cell blocked the incoming probe beam.

The nitrogen came in through the gas inlet at the front of the cell, which was connected to a bottle of pressurised nitrogen. The gas density was adjusted by changing the backing pressure in the gas system connecting the gas bottle to the gas cell. The backing pressure was measured using a barometer with a precision of 1 bar and the plasma electron density was measured using interferometry, a technique described in Section 6.1.2. Given the few-TW power of the SEA and SYLOS-2 lasers, the electron density needed to be above a threshold of 6×10^{18} cm^{-3} to self-focus in the plasma, calculated from Equation 2.37.

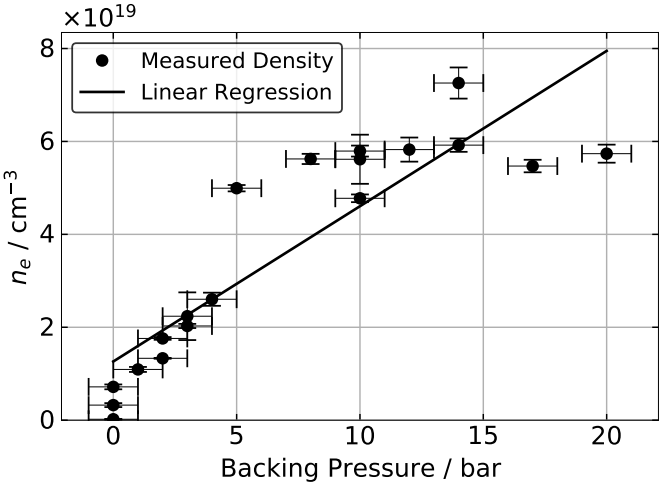


Figure 72: Backing pressure against electron density in gas cell. (Points) Mean electron density measured from multiple frames at same density with (error bars) standard deviation in the measurements. (Line) Linear regression of measured data.

In Figure 72, the measured electron density is plotted against backing pressure, showing that plasma densities on the order of 10^{19} cm^{-3} were accessible in this experiment. The error bars indicate the standard deviation in the ~ 200 measured electron density measurements at the same backing pressure. The straight line is a linear regression of the density measurements, which gives the expected plasma density if the nitrogen behaves as an ideal gas in a closed volume and is fully ionised. At the gas pressures and densities, it is suspected that there is more leakage through the windows of the gas cell, so a linear relation is only a rough prediction. If a density measurement was

not available, which is not the case in this work, then the linear regression would be used to predict the plasma density.

The gas cell also has an actuator that varies the position of the exit plate, changing the length of the gas by ~ 0.1 mm distances. At the $\sim 10^{19}$ cm^{-3} electron densities in this experiment, the dephasing and pump depletion lengths of the LWFA are both on the order of 0.1 mm. When $n_e \sim 10^{20}$ cm^{-3}, these lengths are even shorter: $L_{dph} \approx 0.02$ mm and $L_{pd} \approx 0.05$ mm. With these considerations in mind, the gas cell was initially set to a length of 0.1 mm.

6.1.2 Interferometry

An electromagnetic wave passing through a plasma experiences a phase shift, relative to an identical electromagnetic wave propagating through vacuum. This is due to the smaller refractive index of the plasma, which is typically lower than unity. Over the entire width of the plasma, the total phase shift of the wave is found by integrating the refractive index over the width of the plasma:

$$\Delta\phi(y,z) = \frac{2\pi}{\lambda_0}\int_0^{w_{plasma}} \big(\eta(x,y,z) - 1\big)\, dx, \tag{6.1}$$

where λ_0 is the central wavelength and w_{plasma} is the width of the plasma. In this equation, the wave travels in the x-direction. If the electromagnetic wave is a laser with some transverse size, then the phase shift undergone at different transverse points in the wave can be different. The spatial distribution of the phase shift provides a measure of the distribution in the refractive index of the plasma. The electron density distribution can then be inferred using Equation 2.24.

Interferometry is an experimental technique that provides a quantitative measure of the electron density profile, by determining the relative phase shift between an electromagnetic wave that has passed through a plasma and a reference wave that has passed through vacuum. In this case, the electromagnetic waves are laser beams, both of which originate from the same laser beam often referred to as the "probe beam." The phase-shifted beam interferes with the reference beam. If a detector is placed at a position where the two beams overlap, it detects the intensity of the superposing beams [193]:

$$I(y,z) \propto 1 + V(z)\cos\big(k_0 z\sin\theta + \Delta\phi(y,z)\big), \tag{6.2}$$

where θ is the angle between the wavevectors of the two beams, which is taken to be in the x-z plane. The oscillatory term means that across the cross-sections of the

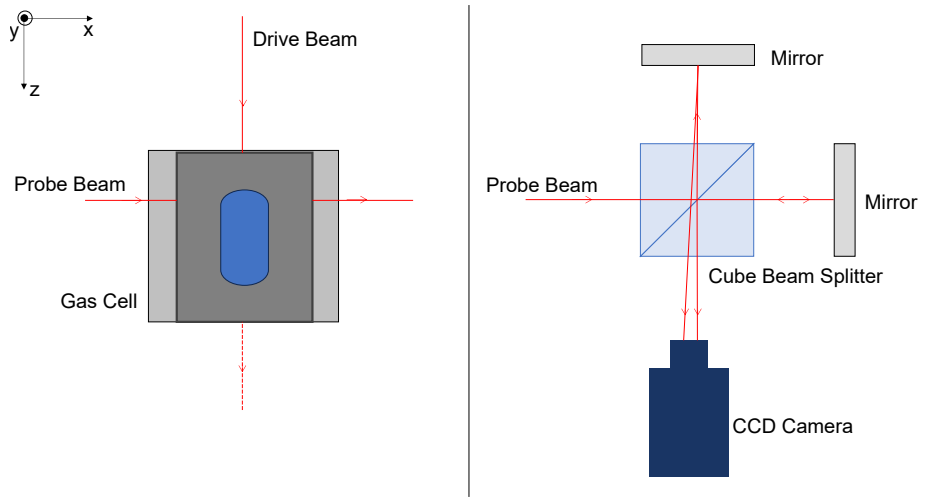


Figure 73: (Left) Layout of probe beam and drive beam in gas cell. (Right) Basic setup of a Michelson interferometer.

interfering beams, in the y-z plane, there is a series of fringes showing where the beams interfere constructively and destructively. $V(z)$ is a function that relates to the contrast of the fringes. If the phase difference between the two beams is constant, then the fringes have a constant spacing. If there are phase-shifted regions in the cross-section of the laser beam, an additional phase is introduced by a nonzero $\Delta\phi$ in the oscillatory term; the interference fringes are bent in these regions.

Experimental Setup

The density of the plasma was probed by a probe beam that traversed the width of the plasma. The probe beam propagated perpendicular to the laser beam that drove the LWFA, known as the drive beam, as shown on the left side of Figure 73. The pulses of the drive beam and the probe beam must cross the plasma at the same time. The cross-section of the probe beam contains the phase information relating to the electron density distribution in the y-z plane in the plasma. This is particularly useful because the electron density can vary along the z-axis as the intensity of the drive beam changes due to pulse compression, self-focusing and depletion. A map of the electron density of the plasma channel can be produced from the phase information contained in the cross-section of the probe beam.

In this experiment, a Michelson interferometer was used to retrieve the phase information in the probe beam. The basic setup of the interferometer is shown on the right of Figure 73, in which the incoming laser beam is split into two identical beams by a 50:50 cube beamsplitter. Each beam has half the intensity of the incoming laser beam. The two beams are reflected off of mirrors, pass through the beamsplitter and recombine at the detector, which is the CCD camera at the bottom of the schem-

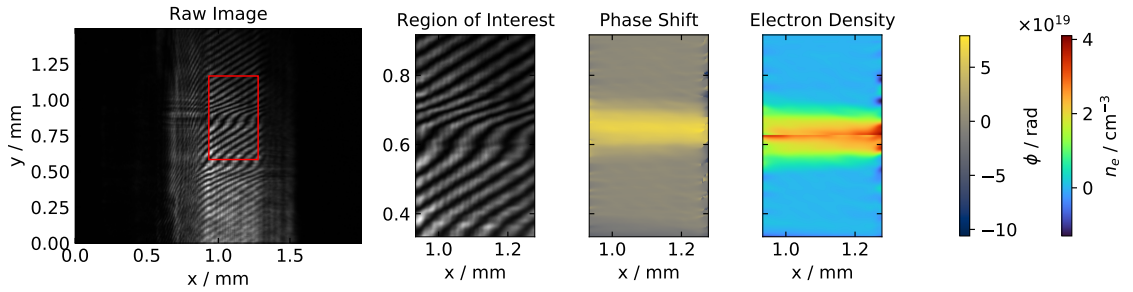


Figure 74: Overview of retrieval of electron density from the image obtained from the interferometer. This image consists of interference fringes which are bent in the region of interest in the red rectangle. The phase shift of the probe beam and then the electron density distribution are calculated in this region of interest.

atic. An image of the plasma is focused onto the CCD chip via a two lens imaging system; two convex lenses were placed between the plasma and the interferometer setup. The CCD camera observes the fringes produced by the interference of the two beams. The two beams are directed and offset such that the region of one beam whose phase has been shifted by the plasma overlaps with a region in the other beam that has not passed through the plasma. The relative direction of the beams also determines the direction in which fringes move in relation to phase delays.

An example of the signal measured by the CCD camera is shown in the left image of Figure 74. The signal consists of a series of diagonal fringes. They are diagonal because in the Michelson interferometer the direction of travel of the two beams is coupled with the position of the beam in the image. Two images of the plasma are produced in the regions where the fringes are curved, one from each beam in the interferometer. The region inside the red rectangle is the region of interest for retrieving the electron density. This region contains the bent fringes produced by the plasma, where they are not obscured by the diffraction patterns from the edges of the gas cell.

Phase and Density Retrieval

The phase shift in the probe beam and thereby the electron density distribution in the plasma are obtained from the interference patterns using a Python code written by Michael Backhouse [192]. In brief, the phase distribution in the cross-section of the probe beam is obtained by comparing the detected image with a reference image in which the probe beam passed through an empty gas cell so it has not undergone any phase shift. The phase difference of the two beams is the argument of the ratio of these two images [192]. A plot of the phase can be produced like the one shown in Figure 74, from which the refractive index of the plasma is obtained using Equation 6.1. However, this equation integrates the phase shift along an axis in a Cartesian

coordinate system, whereas the plasma channel is assumed to be more cylindrical in shape owing to the circular shape of the laser beam producing it. Applying an Abel transform to Equation 6.1 [192], [193] produces an electron density distribution along the radial and longitudinal axes in the plasma, like the example shown by the electron density on the right of Figure 74.

6.1.3 Laser Focal Spot

The focal spot of the laser was imaged using an apochromatic microscope objective lens connected to a CCD camera some distance behind it. The imaging system used in this experiment produced a magnified image of the focal spot with a resolution of 0.99 µm/pixel. The images were taken when the laser was at a low power, with an energy of 100 µJ and a duration of multiple picoseconds, to avoid damaging the components of the imaging system. The focal spot camera was used as a monitor to optimise the intensity and the propagation of the focused laser into the nitrogen gas. The shape of the focal spot was changed using the deformable mirror (DM), whose position in the optical setup was included in Figure 70. The DM comprises a reflective membrane whose shape could be adjusted with actuators behind it, changing the shape of the wavefronts in the laser beam [194].

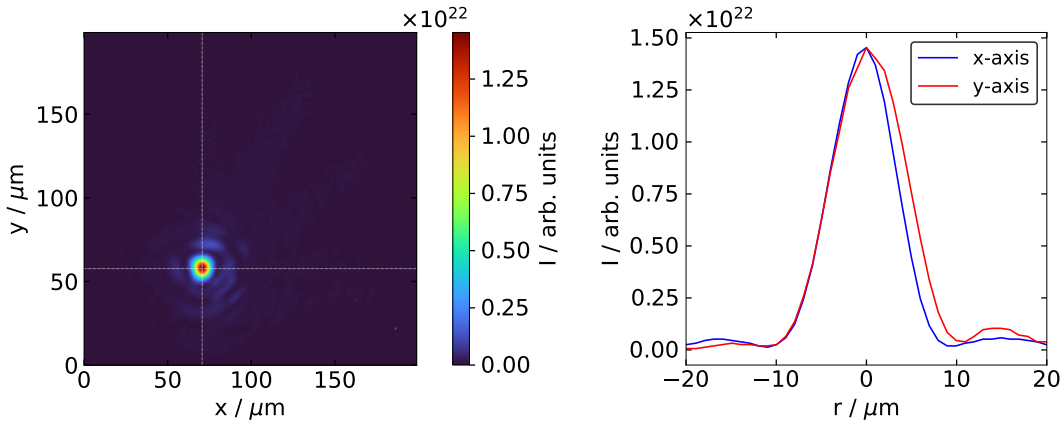


Figure 75: (Left) Typical image of focal spot intensity. (Right) Intensity profiles of focal spot along the x-axis and y-axis.

An example image of the focal spot after optimisation is shown on the left of Figure 75. At the SEA laser's maximum energy of 44 mJ, a peak intensity of 1.5×10^{18} W/cm^2 was estimated, corresponding to a peak normalised potential of 0.94. This lies at the centre of the intense central spot, which is surrounded by a series of rings. These rings are normally produced when a laser beam with a flattened-Gaussian spatial intensity profile is focused [195], like the SEA laser. On the right of Figure 75, the intensity along the central x and y axes is plotted. These intensity profiles are ap-

proximately Gaussian near the peak intensity in the focal spot, but at the edges the intensity rises again. The widths of these two profiles also vary slightly. The $1/e^2$ radius of the focal spot was estimated from the contour of I_{peak}/e^2 around the peak intensity, which was achieved by modifying a Python code written by Michael Backhouse. Because the focal spot is slightly elliptical, it is perhaps more informative to measure the radius along the major and minor axes in the ellipse. The radius of this focal spot along its major axis is 8 ± 1 µm and along its minor axis 7 ± 1 µm, where the error is due to the pixel-limited resolution of the focal spot image.

6.1.4 Electron Spectrometer

In this experiment, the electron spectrometer comprised a dipole magnet and a single scintillator screen. The dipole magnet had a gap of 10 mm between its poles, which had dimensions of 100×30 mm, as shown in the map of the electron spectrometer in Figure 76. The magnetic field between the poles of the magnet was approximately uniform, with a flux density of 1.0 T. Directed along the y-axis, this magnetic field deflects electrons. Inside the field, the electrons follow circular paths with radii dependent on their energies: $\rho = \gamma m_e c^2/(eBc)$. Electrons with different energies leave the magnetic field at different angles from the axis along which they entered. The deflected electrons were detected on the scintillator screen, which was a 200×50 mm strip of Lanex as used in previous electron spectrometers [196], [197]. The scintillator screen was imaged onto a CCD camera using a camera lens attached to its front, which had an $f/1.4$ aperture.

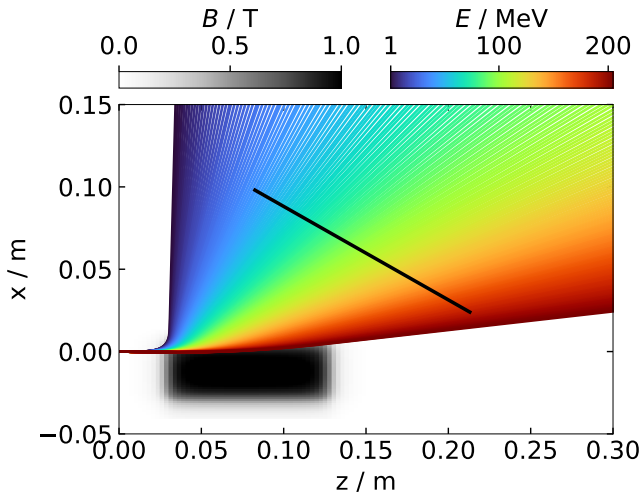


Figure 76: Layout of electron spectrometer, including a map of the magnetic field and the trajectories of electrons with different energies through the setup. The electrons' energies are colour-coded against their energy.

The layout of the electron spectrometer is plotted in Figure 76. This includes a map of

the magnetic field, which was measured using a Hall probe on two motorised translation stages. The position of the scintillator screen is represented by the thick black line in Figure 76. Its normal is at an angle of 30° from the z-axis at a distance of around 0.4 m from the magnet, which allows electrons with energies in the range of 10 MeV to 200 MeV to hit the screen. The trajectories of electrons with different energies are plotted as they pass through the magnetic field and on to the scintillator screen. Their trajectories were computed using a tracking code written by Matthew Streeter. In Figure 76, the colours of the plotted trajectories correspond to their energy.

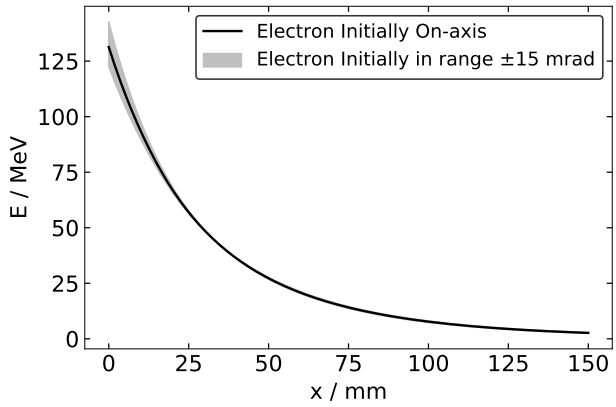


Figure 77: Plot of position of electrons on scintillator screen against energy, including a ± 15 mrad error in their initial direction of travel.

In Figure 77, the electron energy is plotted against the expected position on the scintillator screen. From an image of the fluorescing scintillator screen from the interaction with the dispersed electron beam, the electron spectrum can be extrapolated from the plotted curve. The gradient in this curve is smaller at higher energies, which means that some unit width on the screen corresponds to a larger bandwidth in the electron spectrum. The error on the electron energy, which stems from the 15 mrad uncertainty in the initial direction of travel, thus increases. This is represented by the shaded region around the curve. At angles of divergence larger than 15 mrad, electrons would not travel through the hole in the mirror between the gas cell and the magnet and would instead be scattered by the mirror.

Background Subtraction

An example image of the scintillator screen is shown on the left panel of Figure 78. This image is a cut of the original image taken by the CCD camera and has been warped to obtain effectively a front-on view of the screen, which was achieved using a Python code also written by Matthew Streeter. The image is noisy and obscured by background light produced by electrons scattered off of the holey mirror hitting the

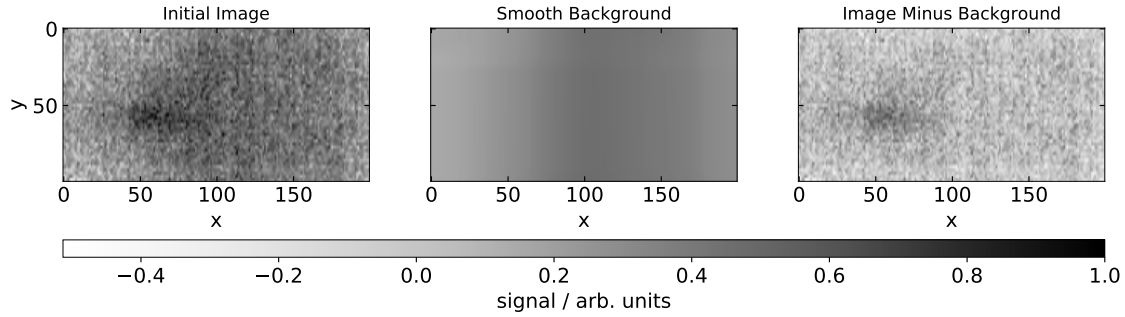


Figure 78: (Left) Initial image of scintillator screen in electron spectrometer. (Middle) Calculated background from filtering the edges of the initial image. (Right) Resultant image from subtracting the background image from the initial image.

scintillator screen and reflections of the light off of metal and glass objects in the vacuum chamber. To remove this background, the parts of the image where there is no electron beam signal were taken. The main part of the signal is the bright patch near the centre of the left-most image in Figure 78, produced by the electrons passing through the hole in the mirror. The upper and lower strips of the image were taken as a sample of the background, either side of the main patch. A median filter was applied to these edges, before performing a two-dimensional linear interpolation between the two strips to obtain a background estimate for the central strip of the image. A smooth image is produced, like in the central image of Figure 78. This is the estimated background. The background is largest at horizontal positions around where the main signal would be and towards the low energy end of the image, which is to the right. The smooth background in the middle panel of Figure 78 is subtracted from the initial image on the left, producing the background-subtracted image on the right of Figure 78. The signal in the middle of the right-most image is clearer than in the original image, but the image is still noisy.

Estimation of Electron Beam Charge

The electron beam charge on the scintillator screen was estimated from the signal on the CCD camera, the properties of the camera, the imaging system and the scintillator screen. Each count on a pixel in the CCD camera corresponds to a number of electrons released in the CCD. As a high gain was used on the camera, the number of counts needed to be calculated from the signal of the pixel; from this, the number of electrons in the pixel could be calculated:

$$N_e = \frac{S_{pixel}}{\sqrt{10^{0.1G}}} \left(\frac{dN_{counts}}{dN_e} \right)^{-1}, \tag{6.3}$$

where S_{pixel} is the signal of the pixel, G is the gain used in the camera in decibels and $\frac{dN_{counts}}{dN_e}$ is the number of counts per electron in the pixel. $\frac{dN_{counts}}{dN_e}$ is a property of the camera. In this experiment, the camera imaging the electron spectrometer was a LUCID-ATLAS-028S camera, which has a value of $\frac{dN_{counts}}{dN_e}$ of 0.15 counts/electron [198]. The total number of photons incident on the pixel is the number of electrons divided by the quantum efficiency of the camera:

$$N_{ph} = \frac{N_e}{\eta_{CCD}}. \tag{6.4}$$

The wavelength at which the scintillator screen emits light is 543 nm [197]; at this wavelength, the quantum efficiency of the camera sensor is 0.73 [199]. Assuming it to be constant with respect to angle, the number of photons emitted per solid angle was calculated by dividing the number of observed photons by the solid angle covered by the imaging system:

$$\frac{dN_{ph}}{d\Omega} = \frac{N_{ph}}{\frac{\Omega}{F}\,T^{N_{surf}}}, \tag{6.5}$$

where Ω is the solid angle covered by the camera lens, F is the F-number of the camera lens, T is the transmittance of the glass surfaces between the scintillator screen and the CCD chip and N_{surf} is the number of surfaces. At each uncoated surface, a portion of the light is reflected, which is accounted for by the $T^{N_{surf}}$ factor. The transmittance of the uncoated glass surfaces was estimated to be 0.96 [200]. There were 10 surfaces between the screen and the CCD chip; one window and four glass components inside the camera lens.

For each unit charge on the scintillator screen, the screen emits a certain number of photons. The total number of photons emitted per unit solid angle per unit charge of the scintillator is a value that can be quoted from literature values or from the manufacturer. In this case, the scintillator screen was a piece of Kodak Regular Lanex, with a literature value of 7×10^9 photons/sr/pC [197]. The total charge on the scintillator screen was calculated by dividing the estimated total photons emitted per unit solid angle by the quoted number of photons emitted per unit solid angle per unit charge on the Lanex:

$$Q = \frac{dN_{ph}}{d\Omega}\left(\frac{d^2N_{ph}}{d\Omega\,dQ}\right)^{-1}_{LANEX}. \tag{6.6}$$

When $\frac{dN_{ph}}{d\Omega}$ corresponds to the photons incident on a single pixel, then this equation produces the total charge on that pixel in the image of the scintillator. When $\frac{dN_{ph}}{d\Omega}$ corresponds to the total number of photons on the CCD chip, then this equation produces an estimate for the total charge on the scintillator screen.

6.2 Experimental Results

In this section, we report on the spectra of the electron beams produced in scans of the plasma electron density and laser focal position. We compare the cutoff energies in the spectra to scaling laws derived in Chapter 2 and with FBPIC simulations. Finally, we discuss the total charge in the detected electron beams, calculated from the signal on the scintillator screen of the electron spectrometer.

FBPIC simulations of the SEA laser in initially neutral nitrogen gas were performed to compare with the experimental results. These simulations had a spatial resolution of $\Delta z = 0.02$ µm and $\Delta r = 0.25$ µm, with 1, 2 and 4 particles per cell in the longitudinal, transverse and azimuthal directions. The input laser pulse had a total energy of 44 mJ, a 12 fs FWHM duration and a $1/e^2$ radius of 7.2 µm at focus. In every simulation, the gas density profile had a plateau length of 0.275 mm, equal to the spacing between the front and back plates in the gas cell that was set in all of the shots reported here. The density up-ramp and down-ramp were given lengths of 0.3 mm, which is based on the initial radii of the pinholes in the entrance and exit plates of the gas cell [192], [201]. However, it should be noted that the pinhole diameter was measured to be 0.1 mm after use, which is because the plates are ablated by the laser, gradually widening the holes over many shots.

6.2.1 Plasma Electron Density

A scan of the plasma electron density was first performed, from which the cutoff energy in the electron beams were determined. In each shot, the distance between the entrance and exit plates in the gas cell was 0.275 mm and the laser pulse was focused 0.5 mm into the plasma, which seemed to produce the strongest signal on the electron spectrometer at that time in the experiment; a scan of the laser's focal position in the plasma is presented and discussed in the next section. In Figure 79,

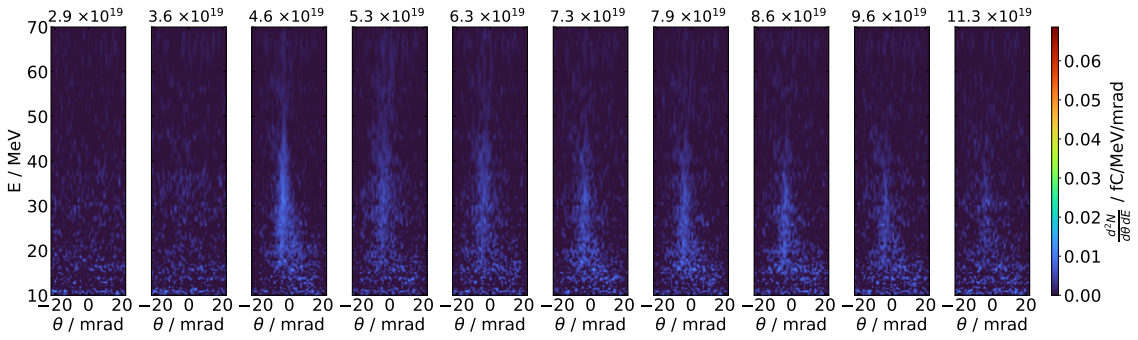


Figure 79: Average electron spectra per shot produced in scan of electron density. Electron density values at the top are in units of cm^{-3}.

the electron spectra produced in a scan of the plasma electron density are presented. Each spectrum is an average spectrum produced from an averaged image of the scintillator screen over 200 shots. Even still, the signal-to-noise ratio of the spectra is low, primarily due to the low charge of the detected electron beams. In Section 6.2.3, we estimate the total charge of the measured electron beam to be around 3 fC.

At an electron density of 4.6×10^{19} cm^{-3}, the electron spectrum stretches to the highest energy of around 50 MeV, before the electron beam signal disappears into the background noise. Above this density, both the cutoff energy and the signal strength decrease to under 35 MeV by a density of 9.8×10^{19} cm^{-3}. Below 4.6×10^{19} cm^{-3}, the signal on the electron spectrum consists mainly of noise. In Figure 80, the cutoff energy in each spectrum is plotted against the electron density. The black dots are the cutoff energies in the electron spectra above which the central slice in the electron spectrum falls below $5\sigma_n$, where σ_n is the average noise level in the spectrum. The error bars are from the noise level in the spectra around their cutoff energies. The cutoff energies are lower than the ~ 100 MeV energies reached in the simulations of LWFAs driven by the SYLOS-2 laser in Chapter 5. This is mainly put down to the imperfect nature of the focused laser pulse in contrast to in simulations, where a smooth Gaussian profile is defined. A smaller laser pulse intensity would produce weaker accelerating fields in the plasma wave.

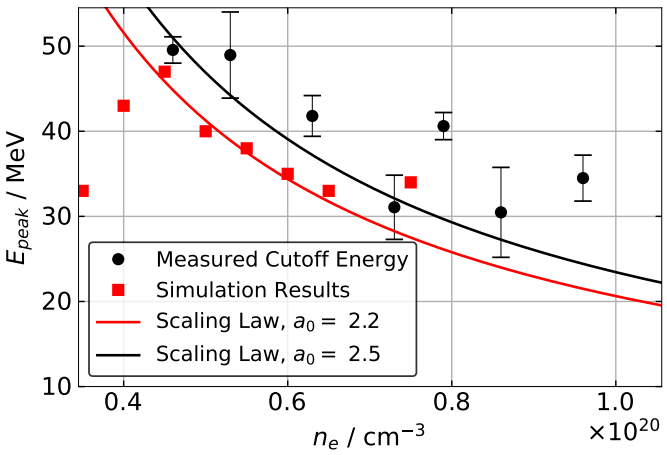


Figure 80: Cutoff energy in electron spectrum against plasma electron density in (black) experiment and (red) simulations, compared with scaling law for dephasing limit in wakefield driven by a laser with (red) $a_0 = 2.2$ and (black) $a_0 = 2.5$.

The red squares in Figure 80 are the highest electron energies in the output beams of FBPIC simulations at different electron densities. In general, the simulated cutoff energies are slightly lower than the measured cutoff energies. However, at the densities around 5×10^{19} cm^{-3}, the cutoff energies of the measured and simulated electron

beams are roughly equal. The simulated cutoff energy is highest at a plasma density of 4.5×10^{19} cm^{-3}, falling gradually at progressively higher densities. At densities immediately below 4.5×10^{19} cm^{-3}, the simulated cutoff energy falls rapidly. In these simulations, the electrons have not reached their dephasing limit by the end of the plasma. A longer plasma would be required.

At plasma densities above 7.5×10^{19} cm^{-3}, the wakefield producing the highest energy electrons is driven by the front of the electron beam rather than the laser pulse. The cutoff energies in these simulations are not plotted because the strength of a beam-driven wakefield is dependent on the amount of charge in the electron beam driving it [202], [203] and PIC simulations have a tendency to over-inject charge through self-injection [176]–[178]. Thus, the strength of the simulated wakefield driven by the electron beam is too strong. The simulated cutoff energies at these densities exceed the experimental values by at least 10 MeV and as such are not plotted.

The black and red lines in Figure 80 represent the scaling law for the cutoff energy reached by electrons at their dephasing limit in the bubble regime, given by Equation 2.59. This equation can be used if there is continual injection of electrons into the wakefield, as seen in the PIC simulations, so there will always be some electrons injected at the right place in the plasma to exit at their dephasing limit. In Equation 2.59, $E_{peak} \propto a_0/n_e$. By adjusting a_0, these lines have been fitted to the experimental and simulated cutoff energies for densities above 4.5×10^{19} cm^{-3}. For the black line fitted to the experimental data, the normalised potential was set to 2.5. For the red line, the normalised potential was set to 2.2 to best fit the line to the simulated data. These values are greater than the normalised potential vacuum of 0.9, which is due to the compression and self-focusing of the laser in the plasma increasing its intensity, as was seen in the simulations in Chapter 5.

Figure 81 gives an overview of the electron beam and laser pulse progression in the PIC simulation at an electron density of 4.5×10^{19} cm^{-3}, taken as 7 times the atomic nitrogen density in the simulation. In the top panel, the progression of the electron beam spectrum is plotted as the blue colour map, while on the right axis the expected electron density profile, is plotted in orange. The highest energy electrons leaving the plasma are accelerated at the start of the density down-ramp. The region in which they are accelerated is covered by the grey shaded region, between 0.65 mm and 0.75 mm. At the start of this region, the electron density is just starting to fall, but is still close to the plateau density of 4.5×10^{19} cm^{-3}. In the bottom panel of Figure 81, the normalised potential of the laser pulse is plotted against its longitudinal position in the plasma. In the grey acceleration region, the normalised potential falls from 2.2 to

below 1. The normalised potential falls below unity around 0.7 mm in the plasma.

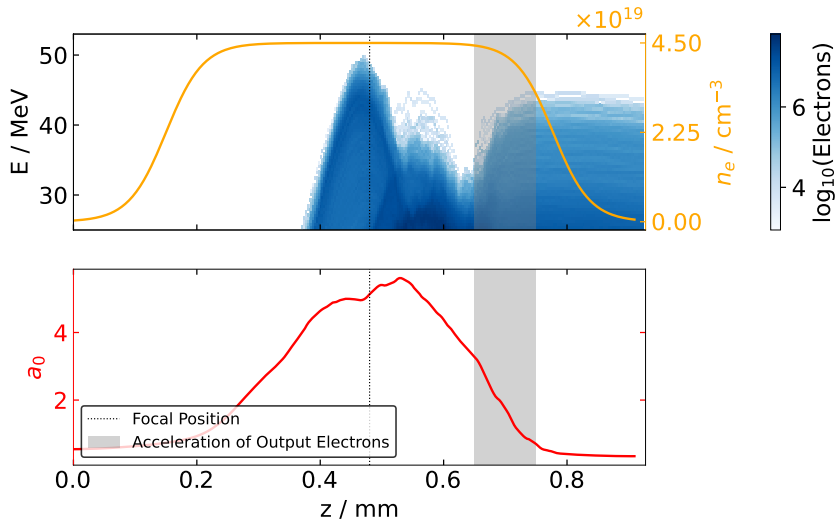


Figure 81: Simulation of LWFA driven by the SEA laser with a plasma density of 4.5×10^{19} cm^{-3}. (Top) Progression of (blue) electron spectrum in the plasma and (orange) longitudinal electron density profile of plasma. (Bottom) Progression of normalised potential of laser pulse in plasma.

The cutoff energy reached by the electrons is thus determined by a combination of the increasing phase velocity of the wakefield, the changing electric field strength and the expanding bubble, all caused by the decrease in plasma density and the laser intensity. However, the scaling laws fitted in Figure 80 assumed a constant plasma density of 4.5×10^{19} cm^{-3} for all electrons accelerated in the plasma. At the average density of 4.0×10^{19} cm^{-3} over the acceleration region that neglects the evolution of the wakefield, using Equation 2.59 for an approximate calculation, a normalised potential of 1.5 produces a dephasing limit of 48 MeV. This is around the average potential in the acceleration region, shown in the bottom panel of Figure 81. Equation 2.59 at least provides a rough understanding of the cutoff energies of the electron beams accelerated in these plasmas.

6.2.2 Focal Position of Laser

After the plasma density scan, a scan of the laser's focal position was performed at an electron density of 4.5×10^{19} cm^{-3}. This plasma density was selected because the electron beams with the highest energies and total charge were produced at this density in the previous scan. Figure 82 shows the electron spectra produced in the focal position scan. At the top of each spectrum, the distance written in millimetres is how far the laser was focused into the gas density profile, zero being the start of the density up-ramp. The spectra show that the electron beam's signal gets stronger and the cutoff energy increases when the laser pulse is focused 0.25 mm into the plasma or

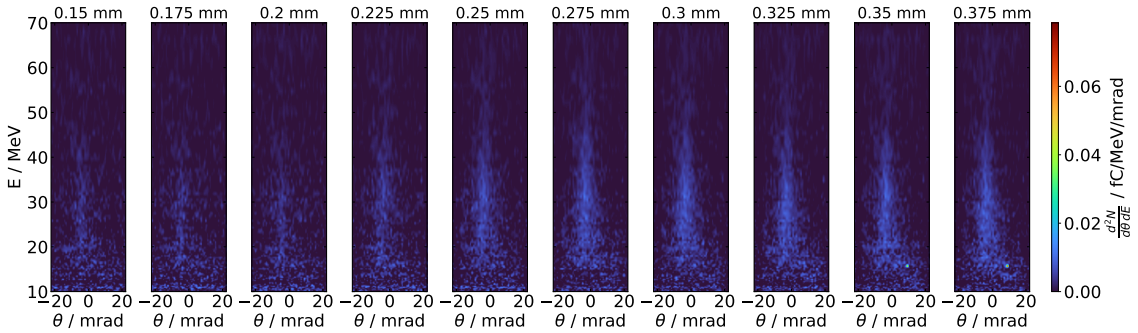


Figure 82: Average electron spectra per shot produced in scan of laser's focal position.

further, so the electron beam properties are clearly sensitive to 0.1 mm-scale changes in the focal position of the laser, as shown in the previous chapter. At focal positions further into the gas cell, neither the cutoff energy nor the total charge in the electron change significantly when inspecting their spectra by eye, similarly to the focal scan performed when analysing the peak energy in the previous chapter.

In Figure 83, the measured cutoff energy is plotted against the focal position. When the laser is focused further than 0.2 mm into the plasma, electron beams with cutoff energies between 40 and 60 MeV were measured. Comparing the measured cutoff energies with those in the output electron beams of FBPIC simulations, plotted as the red squares in Figure 83, there is a general agreement in the scale of the energies reached at focal positions higher than 0.2 mm. This should not be surprising after comparing the experimental and simulated data of the previous scan. However, the cutoff energies in the simulated electron beams do not vary in the same way as the in the measured beams. This is put down to differences in the laser pulse evolution in the plasma. In experiment, the laser does not maintain a smooth, symmetric,

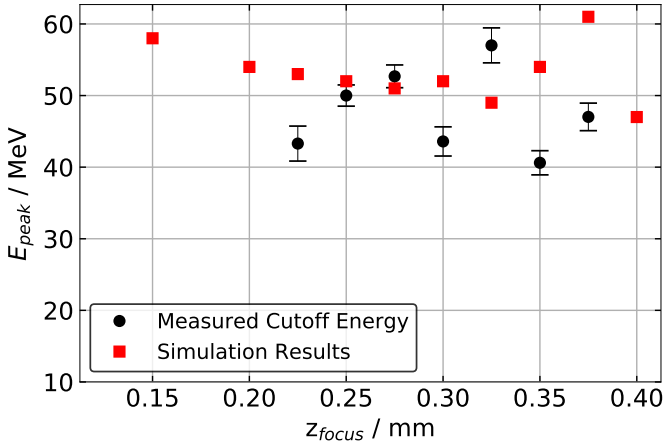


Figure 83: Cutoff energy against laser's focal position obtained (black) in experiment and (red) in simulations.

Gaussian-like intensity profile as it defocuses, as it does in simulations. This may affect the self-focusing and compression of the laser pulse away from its focal position in the plasma, and thereby the structure and strength of the wakefield that it drives.

At focal positions less than 0.2 mm, no electron beam signal could be distinguished above the spectrum's noise level. This suggests that the electron beam has a lower total charge, so fewer electrons are injected into the wakefield when the laser pulse is focused before the start of the gas density plateau. In simulations with focal positions less than 0.2 mm, electron beams with similar charge and cutoff energies are produced as compared to other simulations with larger focal positions. This discrepancy is likely due to the imperfect nature of the laser away from its focal position in experiment, as the laser does not maintain a smooth, symmetric, Gaussian-like intensity profile away from its focal position, unlike the simulated laser pulse. When the focal position is smaller than 0.2 mm, the laser pulse is focused towards the front of the density up-ramp. The plasma density around the focal position of the laser is not sufficient to cause the laser to self-focus and compress. Further into the plasma where the plasma density is high enough, the imperfect nature of the defocused laser may result in a lack of self-focusing and compression. The wakefield driven by this laser pulse would be weaker than simulated and fewer electrons may be injected.

6.2.3 Estimated Total Charge

The total charge in the electron beam was estimated from the amount of signal produced on the scintillator screen of the electron spectrometer. It is expected that this is only a portion of the electron beam, as many electrons should exit the plasma at a divergence angle larger than 10 mrad, which is the maximum divergence that they can have to pass through the hole in the mirror positioned between the gas cell and the magnet. This was confirmed in simulations, where electrons left the plasma divergences up to 100 mrad. Many electrons are thus scattered when they hit the mirror, though some still reach the scintillator screen after being scattered, adding background noise to the images. In the processing of the above electron spectra, the background signal from these scattered electrons was removed, as described in Section 6.1.4. However, a total charge calculation without a background subtraction was also performed, although a background subtraction of the room light was still made for this calculation too.

In Figure 84, the estimated total charge above an energy of 10 MeV is plotted in the scans of the plasma electron density and the laser's focal position. In the top plots, the total charge estimates were produced by integrating the electron spectra shown

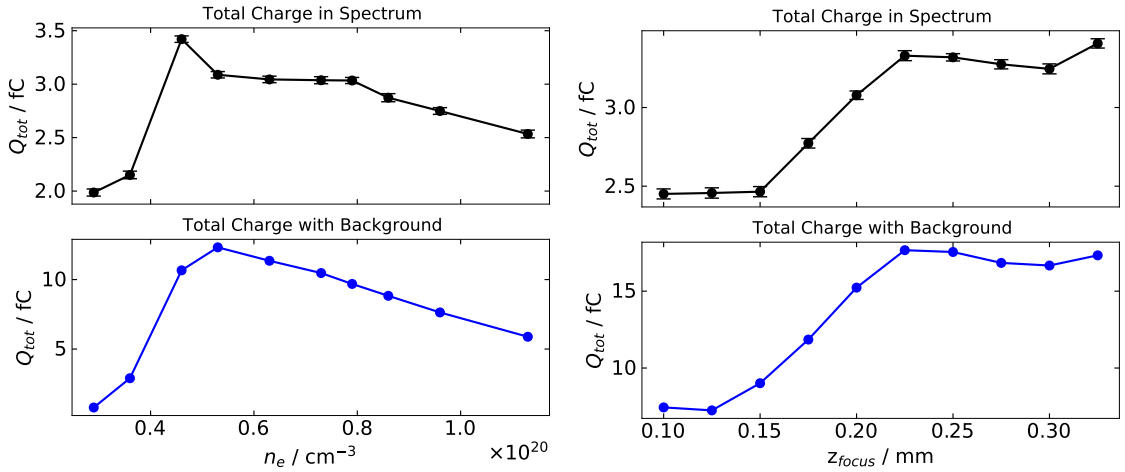


Figure 84: Predicted total charge in electron beams in scans of (left) electron density and (right) laser's focal position. The total charge was estimated from the scintillator screen signal (top) without and (bottom) with the low energy background.

in Figures 79 and 82. The top plots show that a total charge on the order of 1 fC reached the scintillator screen per shot, having passed through the electron spectrometer. In the bottom plots, the total charge has been estimated from the scintillator screen signals without the background subtraction, as described above. This does not account for the charge of the entire electron beam leaving the plasma, as many electrons would have been scattered in other directions. The bottom plots suggest that the electron beams that initially left the gas cell had a total charge of tens of femtocoulombs. This is still much smaller than the total charge of the electron beams produced in the PIC simulations, which usually had on the order of 100 pC above 10 MeV. While PIC simulations have a tendency to overestimate the amount of self-injected charge in LWFAs [176]–[178], this suggests that a more thorough exploration of the parameter space and optimisation of the total charge is needed, which is planned for future runs.

In the top left plot of Figure 84, the highest total charge estimate in the density scan is at 4.5×10^{19} cm^{-3}, which is also roughly where the electron beams with the highest energies were produced. In the top right plot, the highest charge estimates are at focal positions above 0.2 mm, again where the electron beams with the highest energies were produced. This is different to what was suggested in Chapter 5 by the BO algorithm when optimising the total charge, where the increasing the total charge in the beam was to the detriment of the energies reached in the spectrum. The coinciding of the high cutoff energy and total charge could be because of the reduced divergence of electron beams containing electrons with higher energies, so more electrons pass through the hole in the mirror and into the electron spectrometer. To validate this, a measurement of the spatial profile of the electron beam would be useful, which is planned for future runs at the eSYLOS facility. Another explanation could be that the

electron beams with higher charge produced spectra with a higher signal-to-noise ratio, so high cutoff energies could only be picked out of these spectra. Sophisticated methods of noise removal such as deep learning would likely be required to confirm this [204], as the noise in the electron spectra presented here could not be removed just by using median or Gaussian filtering [205].

6.3 Summary

In this chapter, we have reported on the first experimental work performed at the eSYLOS facility. The 44 mJ, 12 fs SEA laser was focused into a gas cell containing nitrogen to drive an LWFA. The gas cell had a variable length, position and backing pressure, which allowed the plasma length, focal position in the plasma and the plasma density to be adjusted. The plasma density was measured using interferometry and the energy spectrum and the total charge of the output electron beams were measured using an electron spectrometer.

In a scan of the plasma density, electron beams with cutoff energies of up to 50 MeV were measured. The electron beams had this cutoff energy at a plasma density of 4.5×10^{19} cm^{-3}, consistent with a PIC simulation performed with the same plasma density. Above this density, the measured and simulated cutoff energies fell approximately according to Equation 2.56. At lower plasma densities, no electron beam could be distinguished from the background noise in the electron spectrum. In a PIC simulation at a plasma density of 4.5×10^{19} cm^{-3}, the energetic electrons that left the plasma were accelerated at the start of the density down-ramp at the back end of the plasma density profile.

It was also shown that the cutoff energy and total charge of the electron beams were sensitive to the focal position of the laser in the plasma, over 0.1 mm scales. In a scan of the focal position, the electron beam energies were as high as 57 MeV, produced at a focal position of 0.325 mm in the plasma. At focal positions later than 0.225 mm, PIC simulations produced electron beams with comparable cutoff energies between 50 and 60 MeV. However, in the experimental scan, no electron beams were distinguishable from the background noise of the measured spectra when the laser was focused earlier than 0.225 mm.

The electron beam signal on the electron spectrometer was measured to be from a total charge of 2.0 to 3.5 fC. This was measured from the background-subtracted electron beam signal on the scintillator screen, from electrons that passed through the hole in the mirror between the gas cell and the magnet. Including the signal from

electrons that were scattered off of the mirror onto the scintillator screen produced values for the electron beam charge of up to 18 fC. As most electrons would not be scattered towards the scintillator screen, this implies that the electron beams leaving the plasma had a total charge on the order of 10 fC.

7. Conclusions

This thesis has focused on the generation of x-rays and electron beams from LWFAs. In this final chapter, we summarise the main conclusions of the models developed and the experimental work carried out in each chapter. Overviews of potential future work are also given.

7.1 Modelled X-ray Beams from LWFAs

In Chapters 3 and 4, we reported on two radiation computation codes (RCCs) that have been built to model the properties of x-ray beams produced by oscillating electrons in LWFAs. These RCCs have been applied to PIC simulations of six different LWFA light source experiments. The LWFAs in these experiments had lengths of up to 20 mm and lasers with powers from 30 TW to 1 PW. As far as we are aware, numerical modelling of LWFA-based x-ray beams have not been performed on these scales before. The first RCC models the temporal intensity profile of ~ 10 fs and ~ 100 fs x-ray pulses with sub-femtosecond resolution and energy density spectra containing photon energies up to 2 MeV. The second RCC models the angular energy density distribution of the x-ray beams with milliradian or sub-milliradian resolution.

In Section 4.2, a relation was derived for the on-axis temporal intensity profile of the x-ray pulse, Equation 4.2, which is proportional to the $N(t)\gamma(t)^4$ profile of the electron beam. The on-axis temporal intensity profiles produced by the RCC were plotted in Section 4.2.2 with the $N(t)\gamma(t)^4$ profiles of the electron beams at the end of the plasma, and showed good agreement. Discrepancies arise mainly from the differences in the oscillation amplitudes of different electron bunches, as Equation 4.2 was scaled to the RCC-modelled profile by adjusting the parameter r_β, the betatron oscillation amplitude of the electrons, to which Equation 4.2 is directly proportional. This also produced estimates for the source size. The temporal intensity profiles produced by the RCC and the $N(t)\gamma(t)^4$ profile revealed the multi-pulse structure of x-ray pulses from LWFAs, produced by the constituent bunches of the electron beam. The temporal profile could thus be used to help describe the energy progression of electron beam during its acceleration.

In Section 4.3, we reported on the photon fluence spectra of each x-ray beam modelled by the first RCC. The modelled spectra have a large bandwidth, stretching to photon energies of ~ 100 keV and 1 MeV, from LWFAs driven by sub-100 TW, 100 TW-order and PW-order laser powers [60], [65], [70], [72], [164]. In experiments, the x-ray beam's spectrum is detected over a small 10 keV to 50 keV bandwidth in experiments, restricted by the transmission of the materials between the LWFA and x-ray detector and the quantum efficiency of the detector. Over this narrow bandwidth, analytical circular orbit spectra are often fitted to the experimental spectra. However, the significantly larger bandwidth of the RCC-modelled spectra of the initial x-ray beam that leaves the plasma throws this fitting procedure into question.

The modelled x-ray beams had a peak spectral fluence ranging from 3×10^2 to 7×10^4 photons/s/mrad^2/0.1% BW, scaling loosely with the power of the input laser pulse. With the x-ray pulse duration and the source size obtained from the RCC and the PIC simulation, the modelled x-ray sources were calculated to have a peak brightness in the range of 2×10^{21} to 6×10^{22} photons/s/mrad^2/mm^2/0.1% BW using an assumed x-ray pulse duration and imprecise source size measurements [60], [65], [70], [72], [164]. This quantity has always been inferred in experiments. The modelled peak brightness values are generally lower than the corresponding experimental values, due mainly to the longer modelled x-ray pulse duration than assumed in the experimental calculation.

The first RCC also modelled the photon fluence spectra at off-axis observation points. This could be a useful tool as the angular variation of the radiation spectra are difficult to model analytically, owing to the variation in the spectra within their instantaneous radiation cones and the spectra emitted at each point in an electron's oscillating trajectory. Moreover, it was shown in the following section that there is an overlapping of the angular distributions of the radiation from electrons oscillating in different planes, which could also modify the angular variation of the radiation spectrum.

In Section 4.4, the angular energy density distributions of the x-ray beams produced by the second RCC were presented. The RCC-modelled angular distributions were compared with predicted angular distributions derived from mathematical relations. The first predicted angular distribution was derived by integrating the product of the time-averaged spectrum of the electron beam throughout its acceleration and Equation 4.13, describing the angular energy density distribution from a single electron following a sinusoidal trajectory. The resulting distribution had a similar divergence but a different form to the RCC-modelled angular distribution. Considering the overlap-

ping of the angular energy density distributions from electrons oscillating in different planes, an angular distribution was produced with a similar form to the RCC-modelled angular distributions, but with a much smaller divergence. Three-dimensional plots of example electron trajectories in PIC simulations showed that some electrons in the beam follow elliptical spirals, rather than performing oscillations in a single plane. These trajectories are more complicated than assumed in the derived distributions, and could be due to space charge effects in the electron beam, magnetic field effects [179] or some electrons could have an azimuthal momentum component when injected into the wakefield.

7.1.1 Future Work

The main limitation of the RCCs' computation process is that in PIC simulations, a high number, N, of electrons are represented by single macroparticles. The radiation from a single macroparticle is equivalent to the radiation of N electrons radiating coherently, which was shown to be untrue for many electron beams in LWFAs in Section 3.7. To remedy this, the amplitude of the Liénard-Wiechert field from each macroparticle was set to be proportional to $\sqrt{N}$, equal to the amplitude of N incoherently radiating particles. Without resorting to modelling more particles representing fewer electrons, which would be detrimental to the RCCs' computation time, a more realistic approach could be to use a form factor to pre-define the spatial distribution of the electrons of each macroparticle [165].

The elliptical spirals followed by many electrons is a reason for the discrepancy between the RCC-modelled angular energy density distribution and the predicted angular distributions presented in Section 4.4. The ability to reconstruct the measured or simulated angular energy density distribution from the electron spectrum could provide a new way of inferring the source size of the x-ray beams from LWFAs. Deriving analytical relations for the angular distributions produced by electrons following elliptical trajectories would be a good first step in improving the predicted angular distributions. From this, scaling laws equating the amplitudes of oscillation and the energies in the electron beam to the x-ray beam divergence could potentially be derived. The distribution of the electron trajectories' ellipticity, the distribution of their oscillation amplitudes and the overlapping and adding together of their individual angular distributions need to be carefully considered.

7.2 Bayesian Optimisation of PIC Simulations of eSYLOS

In Chapter 5, a BO algorithm was used to optimise the peak energy and the total charge in PIC simulations of a 30 mJ, 8 fs laser pulse in an LWFA. The BO algorithm was demonstrated to be a useful tool to optimise the highly nonlinear evolution of the laser pulse in the plasma, which is difficult to do using analytical scaling laws. This, in turn, optimised the accelerating electric field and the self-injection process in the plasma wave.

Section 5.3.1 reported on the optimisation of the peak energy of the electron beam. After 100 epochs, the optimised electron beams had a local maximum in their spectra at energies of 125 MeV. This was achieved by minimising the density of the helium gas to 9×10^{18} cm^{-3}, below which the laser pulse diffracts away after its power falls below the threshold for self-focusing. The length of the plasma was set to 0.7 mm, such that the end of the plasma coincides with the point where the electrons reach their dephasing limits. It was shown that in this regime, the focal position of the laser is also important in optimising the electron spectrum. Focusing the laser 0.24 mm into the gas optimised the compression of the laser in the plasma to produce the highest intensities, driving the strongest accelerating fields in the wakefield and accelerating electrons to the highest energies of 125 MeV.

The other electron beam property optimised by the BO algorithm was the total charge, reported in Section 5.3.2. The BO algorithm maximised the self-injected charge in the electron beam by maximising the bubble growth caused by the increase in intensity of the laser pulse. The BO algorithm optimised the total charge injected by balancing the rate of bubble growth and charge injection with the distance over which charge is injected, which is a difficult task to perform analytically. The main parameters adjusted in this optimisation were the helium gas density, the laser's focal position and the length of the density up-ramp. The BO algorithm also adjusted the third-order spectral phase coefficient of the laser pulse to -40 fs^3, producing a 20% increase in charge, which is difficult to predict analytically. After 150 epochs, the BO algorithm converged on a total charge of 200 pC above 10 MeV.

7.2.1 Future Work

Optimising the simulated electron beam properties was a first step in looking to optimise the radiation produced in LWFAs driven by laser systems like SYLOS-2. In future optimisations, the intensity of modelled x-ray beams could be optimised by calculating the radiation properties using one of the RCCs, then using the BO algorithm to

optimise the chosen radiation property. However, this would at least double the computation time of each epoch, making the optimisation a much longer process. A faster but more approximate approach would be to calculate and optimise a property of the electron beam that correlates with the radiation intensity, for example the integrated $N(t)\gamma_{peak}^4(t)$ profile, at different points along the plasma.

In terms of optimising the electron beam for radiation generation applications, optimising basic electron beam properties like the peak energy and total charge is perhaps too simplistic. Calculating and optimising more complex quantities such as the laser-to-electron beam conversion efficiency could be useful for such applications. Optimising the conversion efficiency, for example, would maximise the total energy in the accelerated electron beam, producing higher photon yields in the radiation generated.

7.3 Electron Beams from LWFAs Driven by the SEA Laser at eSYLOS

Chapter 6 is a report on the first experiment performed at the eSYLOS facility, where the 44 mJ, 12 fs SEA laser was focused into a nitrogen gas cell with variable density, length and position. The laser pulse was focused into the plasma with a density plateau length of 0.275 mm and an assumed up-ramp length of 0.3 mm. The measured electron spectra consisted of energies of up to 60 MeV before falling below a background noise level. The total charge in the beam above 10 MeV was measured to be on the order of 10 fC to 100 fC.

A plasma density scan was performed, which is reported in Section 6.2.1. The laser pulse was focused 0.53 mm into the plasma. Focusing the laser this far into the plasma seemed to produce the highest signal on the electron spectrometer at the time of the experiment. The highest cutoff energy of 48 MeV in the electron beam was produced at an electron density of 4.5×10^{19} cm^{-3}. The cutoff energies fell gradually at higher densities and there was good agreement between the experimental and simulated cutoff energies within a density range of 4.5×10^{19} cm^{-3} to 8.0×10^{19} cm^{-3}. In simulations, the electron beam was seen to be accelerated at the start of the down-ramp in density at the back of the LWFA.

A scan of the laser's focal position in Section 6.2.2 demonstrated the sensitivity of the acceleration to this parameter. When the laser was focused after 0.2 mm, the cutoff energy varied between 40 and 60 MeV. Similar energies were obtained in PIC simulations when focusing at these positions. When the laser pulse was focused be-

fore 0.2 mm in the plasma, the electron beam signal was not distinguishable from the noise in the electron spectrum, implying that the electron beam had less charge. At these focal positions, however, electron beams with ~ 100 pC above 10 MeV were obtained in PIC simulations. This discrepancy is put down to the imperfect nature of the intensity profile of the laser after its focal position, which becomes important when the laser is focused towards the start of the plasma density up-ramp and defocuses before the density plateau.

In Section 6.2.3, the total charge in the electron beam was estimated from the measured signal on the scintillator of the electron spectrometer. A total charge of up to 5 fC per shot was measured to have passed through the magnet of the electron spectrometer and hit the scintillator screen. The total charge was also estimated without a background subtraction, which could have been produced by scattered electrons that did not pass though the central hole in the mirror between the gas cell and the magnet. Then, a total charge of up to 15 fC was produced, implying that the electron beam leaving the plasma had a total charge on the order of 10 fC. This is significantly lower than the total charge in the simulated electron beams, which were on the order of 100 pC, suggesting scope for further exploration and optimisation.

7.3.1 Future Work

The main issue in obtaining the cutoff energies and total charges in the electron beams in the scans presented here was the low signal-to-noise ratio in the electron spectra. The most obvious way to increase the the signal-to-noise ratio is to increase the total charge incident on the scintillator screen through a more thorough optimisation. The most simple suggestion would be to use a more sensitive scintillator screen in the electron spectrometer, as more sensitive Lanex screens can produce up to three times the photons per unit charge than the type of Lanex that was used in this experiment [197].

In any case, a good first step would be to do a more thorough exploration of the parameter space of the focal position, plasma density and plasma length. An exploration could also be done to decrease the divergence of the electron beam so that more electrons pass through the hole in the mirror between the gas cell and the electron spectrometer and also decrease the noise due to scattering of electrons with a high divergence. This would primarily involve increasing the average energy of the electron beam. For monitoring the electron beam divergence, a measurement of the spatial profile of the electron beam would be useful, which is planned for future runs at the eSYLOS facility.

Producing the first electron beams at the eSYLOS facility is a first step in producing radiation beams. Measurements of any radiation beams are yet to be made, but intermediate steps should include a more thorough optimisation of the peak energy and charge in the output electron beam, perhaps using a machine learning algorithm like the one described in Chapter 5. Other electron beam properties such as the spectral brightness and conversion efficiency could also be optimised for radiation generation applications. For the purposes of radiation generation, it would be advantageous to use the SYLOS-3 laser, which has a higher energy and a shorter pulse duration than the SEA laser of 100 mJ and 8 fs [107]. This laser system would produce electron beams with higher energies and thereby x-rays beams with higher intensity than are accessible to the SYLOS-2 and SEA lasers. The SYLOS-3 laser will be available in future experimental runs.

Bibliography

[1] J. D. Cockcroft and E. T. S. Walton, «Experiments with high velocity positive ions», *Proceedings of the Royal Society of London. Series A, Containing Papers of a Mathematical and Physical Character*, vol. 129, no. 811, pp. 477–489, 1930. DOI: 10.1098/rspa.1930.0169. eprint: https://royalsocietypublishing.org/doi/pdf/10.1098/rspa.1930.0169. [Online]. Available: https://royalsocietypublishing.org/doi/abs/10.1098/rspa.1930.0169.

[2] H. Wiedemann, *Particle Accelerator Physics*, 4th ed. Springer, 2015.

[3] B. R. Wheaton, «Bremsstrahlung», in *Compendium of Quantum Physics*, D. Greenberger, K. Hentschel and F. Weinert, Eds. Berlin, Heidelberg: Springer Berlin Heidelberg, 2009, pp. 78–81, ISBN: 978-3-540-70626-7. DOI: 10.1007/978-3-540-70626-7_23. [Online]. Available: https://doi.org/10.1007/978-3-540-70626-7_23.

[4] P. Willmott, *An Introduction to Synchrotron Radiation Techniques and Applications*, eng. Hoboken: Wiley, 2011, ISBN: 1-283-17772-2.

[5] R. Bhandari and M. K. Dey, «Applications of accelerator technology and its relevance to nuclear technology», *Energy Procedia*, vol. 7, pp. 577–588, 2011, Asian Nuclear Prospects 2010, ISSN: 1876-6102. DOI: https://doi.org/10.1016/j.egypro.2011.06.078. [Online]. Available: https://www.sciencedirect.com/science/article/pii/S1876610211015876.

[6] M. G. Ronga, M. Cavallone, A. Patriarca *et al.*, «Back to the future: Very high-energy electrons (vhees) and their potential application in radiation therapy», *Cancers*, vol. 13, no. 19, 2021, ISSN: 2072-6694. DOI: 10.3390/cancers13194942. [Online]. Available: https://www.mdpi.com/2072-6694/13/19/4942.

[7] L. Whitmore, R. I. Mackay, M. van Herk, J. K. Jones and R. M. Jones, «Focused vhee (very high energy electron) beams and dose delivery for radiotherapy applications», *Scientific Reports*, vol. 11, no. 1, p. 14 013, Jul. 2021, ISSN: 2045-2322. DOI: 10.1038/s41598-021-93276-8. [Online]. Available: https://doi.org/10.1038/s41598-021-93276-8.

[8] K. Kokurewicz, E. Brunetti, A. Curcio *et al.*, «An experimental study of focused very high energy electron beams for radiotherapy», *Communications Physics*, vol. 4, no. 1, p. 33, Feb. 2021, ISSN: 2399-3650. DOI: 10.1038/s42005-021-00536-0. [Online]. Available: https://doi.org/10.1038/s42005-021-00536-0.

[9] B. Lin, F. Gao, Y. Yang *et al.*, «Flash radiotherapy: History and future», *Frontiers in Oncology*, vol. 11, 2021, ISSN: 2234-943X. DOI: 10.3389/fonc.2021.644400. [Online]. Available: https://www.frontiersin.org/journals/oncology/articles/10.3389/fonc.2021.644400.

[10] J. C. L. Chow and H. E. Ruda, «Flash radiotherapy: Innovative cancer treatment», *Encyclopedia*, vol. 3, no. 3, pp. 808–823, 2023, ISSN: 2673-8392. DOI: 10.3390/encyclopedia3030058. [Online]. Available: https://www.mdpi.com/2673-8392/3/3/58.

[11] N. Matuszak, W. M. Suchorska, P. Milecki *et al.*, «FLASH radiotherapy: An emerging approach in radiation therapy», en, *Rep. Pract. Oncol. Radiother.*, vol. 27, no. 2, pp. 344–351, May 2022.

[12] A. A. Friedl, K. M. Prise, K. T. Butterworth, P. Montay-Gruel and V. Favaudon, «Radiobiology of the flash effect», *Medical Physics*, vol. 49, no. 3, pp. 1993–2013, 2022. DOI: https://doi.org/10.1002/mp.15184. eprint: https://aapm.onlinelibrary.wiley.com/doi/pdf/10.1002/mp.15184. [Online]. Available: https://aapm.onlinelibrary.wiley.com/doi/abs/10.1002/mp.15184.

[13] L. Faillace, D. Alesini, G. Bisogni *et al.*, «Perspectives in linear accelerator for flash vhee: Study of a compact c-band system», *Physica Medica*, vol. 104, pp. 149–159, 2022, ISSN: 1120-1797. DOI: https://doi.org/10.1016/j.ejmp.2022.10.018. [Online]. Available: https://www.sciencedirect.com/science/article/pii/S1120179722020798.

[14] P. Korysko, J. Bateman, R. Corsini *et al.*, «Methods for VHEE/FLASH Radiotherapy Studies and High Dose Rate Dosimetry at the CLEAR User Facility», in *Proc. LINAC'22*, (Liverpool, UK), ser. International Linear Accelerator Conference, JACoW Publishing, Geneva, Switzerland, Sep. 2022, THPOPA06, pp. 758–761, ISBN: 978-3-95450-215-8. DOI: 10.18429/JACoW-LINAC2022-THPOPA06. [Online]. Available: https://jacow.org/linac2022/papers/thpopa06.pdf.

[15] P. G. Maxim, S. G. Tantawi and B. W. Loo, «Phaser: A platform for clinical translation of flash cancer radiotherapy», *Radiotherapy and Oncology*, vol. 139, pp. 28–33, 2019, FLASH radiotherapy International Workshop, ISSN: 0167-

8140. DOI: https://doi.org/10.1016/j.radonc.2019.05.005. [Online]. Available: https://www.sciencedirect.com/science/article/pii/S0167814019304049.

[16] J.-E. Rubensson, *Synchrotron Radiation* (2053-2571). Morgan and Claypool Publishers, 2016, ISBN: 978-1-6817-4115-4. DOI: 10.1088/978-1-6817-4115-4. [Online]. Available: http://dx.doi.org/10.1088/978-1-6817-4115-4.

[17] A. L. Robinson, «History of synchrotron radiation», *Synchrotron Radiation News*, vol. 28, no. 4, pp. 4–9, 2015. DOI: 10.1080/08940886.2015.1059228. eprint: https://doi.org/10.1080/08940886.2015.1059228. [Online]. Available: https://doi.org/10.1080/08940886.2015.1059228.

[18] J. R. Helliwell, «Synchrotron radiation facilities», *Nature Structural Biology*, vol. 5, no. 8, pp. 614–617, Aug. 1998, ISSN: 1545-9985. DOI: 10.1038/1307. [Online]. Available: https://doi.org/10.1038/1307.

[19] D. H. Bilderback, P. Elleaume and E. Weckert, «Review of third and next generation synchrotron light sources», *Journal of Physics B: Atomic, Molecular and Optical Physics*, vol. 38, no. 9, S773–S797, Apr. 2005. DOI: 10.1088/0953-4075/38/9/022. [Online]. Available: https://doi.org/10.1088%2F0953-4075%2F38%2F9%2F022.

[20] S. Doniach, K. Hodgson, I. Lindau, P. Pianetta and H. Winick, «Early work with synchrotron radiation at stanford», *Journal of synchrotron radiation*, vol. 4, pp. 380–95, Dec. 1997. DOI: 10.1107/S0909049597012235.

[21] W. Eberhardt, «Synchrotron radiation: A continuing revolution in x-ray science — diffraction limited storage rings and beyond», *Journal of Electron Spectroscopy and Related Phenomena*, vol. 200, pp. 31–39, 2015, Special Anniversary Issue: Volume 200, ISSN: 0368-2048. DOI: https://doi.org/10.1016/j.elspec.2015.06.009. [Online]. Available: https://www.sciencedirect.com/science/article/pii/S0368204815001383.

[22] M. Berndt, W. Brunk, R. Cronin *et al.*, «Initial operation of ssrl wiggler in spear», *IEEE Transactions on Nuclear Science*, vol. 26, no. 3, pp. 3812–3815, 1979. DOI: 10.1109/TNS.1979.4330617.

[23] K. Halbach, J. Chin, E. Hoyer *et al.*, «A permanent magnet undulator for spear», *IEEE Transactions on Nuclear Science*, vol. 28, no. 3, pp. 3136–3138, 1981. DOI: 10.1109/tns.1981.4332031.

[24] J. Chavanne and P. Elleaume, «Insertion devices at the ESRF», *Review of Scientific Instruments*, vol. 66, no. 2, pp. 1868–1871, Feb. 1995, ISSN: 0034-6748. DOI: 10.1063/1.1145809. eprint: https://pubs.aip.org/aip/rsi/article-pdf/66/2/1868/7369112/1868_1_online.pdf. [Online]. Available: https://doi.org/10.1063/1.1145809.

[25] A. Hofmann, *The physics of synchrotron radiation* (Cambridge monographs on particle physics, nuclear physics, and cosmology ; 20), eng. Cambridge: Cambridge University Press, 2004, ISBN: 1-107-14141-9.

[26] A. S. Schlachter, «Third-generation synchrotron light sources», in *New Directions in Research with Third-Generation Soft X-Ray Synchrotron Radiation Sources*, A. S. Schlachter and F. J. Wuilleumier, Eds. Dordrecht: Springer Netherlands, 1994, pp. 1–22, ISBN: 978-94-011-0868-3. DOI: 10.1007/978-94-011-0868-3_1. [Online]. Available: https://doi.org/10.1007/978-94-011-0868-3_1.

[27] S. Varro, *Free Electron Lasers*, eng. Rijeka, Croatia: IntechOpen, 2012, ISBN: 953-51-4975-X.

[28] P. O'Shea and H. Freund, «Free electron lasers: Status and applications», *Science*, vol. 292, pp. 1853–1858, 2001. DOI: 10.1126/science.1055718.

[29] Z. Huang and K.-J. Kim, «Review of x-ray free-electron laser theory», *Phys. Rev. ST Accel. Beams*, vol. 10, p. 034801, 3 Mar. 2007. DOI: 10.1103/PhysRevSTAB.10.034801. [Online]. Available: https://link.aps.org/doi/10.1103/PhysRevSTAB.10.034801.

[30] P. Schmüser, M. Dohlus and J. Rossbach, *Ultraviolet and Soft X-Ray Free-Electron Lasers*. Jan. 2009, vol. 229, ISBN: 978-3-540-79571-1. DOI: 10.1007/978-3-540-79572-8.

[31] A. Wolski, *Cern accelerator school: Introduction to free electron lasers*, Sep. 2014.

[32] P. Emma, R. Akre, J. Arthur *et al.*, «First lasing and operation of an ångstrom-wavelength free-electron laser», *Nature Photonics*, vol. 4, no. 9, pp. 641–647, Sep. 2010, ISSN: 1749-4893. DOI: 10.1038/nphoton.2010.176. [Online]. Available: https://doi.org/10.1038/nphoton.2010.176.

[33] I. Nam, C.-K. Min, B. Oh *et al.*, «High-brightness self-seeded x-ray free-electron laser covering the 3.5 kev to 14.6 kev range», *Nature Photonics*, vol. 15, no. 6, pp. 435–441, Jun. 2021, ISSN: 1749-4893. DOI: 10.1038/s41566-021-00777-z. [Online]. Available: https://doi.org/10.1038/s41566-021-00777-z.

[34] N. Huang, H. Deng, B. Liu, D. Wang and Z. Zhao, «Features and futures of x-ray free-electron lasers», *The Innovation*, vol. 2, no. 2, p. 100 097, 2021, ISSN: 2666-6758. DOI: https://doi.org/10.1016/j.xinn.2021.100097. [Online]. Available: https://www.sciencedirect.com/science/article/pii/S2666675821000229.

[35] R. N. Coffee, J. P. Cryan, J. Duris, W. Helml, S. Li and A. Marinelli, «Development of ultrafast capabilities for x-ray free-electron lasers at the linac coherent light source», *Philosophical Transactions of the Royal Society A: Mathematical, Physical and Engineering Sciences*, vol. 377, no. 2145, p. 20 180 386, 2019. DOI: 10.1098/rsta.2018.0386. eprint: https://royalsocietypublishing.org/doi/pdf/10.1098/rsta.2018.0386. [Online]. Available: https://royalsocietypublishing.org/doi/abs/10.1098/rsta.2018.0386.

[36] T. Tajima and J. M. Dawson, «Laser electron accelerator», *Phys. Rev. Lett.*, vol. 43, pp. 267–270, 4 Jul. 1979. DOI: 10.1103/PhysRevLett.43.267. [Online]. Available: https://link.aps.org/doi/10.1103/PhysRevLett.43.267.

[37] S. M. Hooker, «Developments in laser-driven plasma accelerators», *Nature Photonics*, vol. 7, no. 10, pp. 775–782, 2013. DOI: 10.1038/nphoton.2013.234.

[38] C. M. Tang, P. Sprangle and R. N. Sudan, «Excitation of the plasma waves in the laser beat wave accelerator», *Applied Physics Letters*, vol. 45, no. 4, pp. 375–377, Aug. 1984, ISSN: 0003-6951. DOI: 10.1063/1.95225. eprint: https://pubs.aip.org/aip/apl/article-pdf/45/4/375/7754723/375_1_online.pdf. [Online]. Available: https://doi.org/10.1063/1.95225.

[39] C. E. Clayton, C. Joshi, C. Darrow and D. Umstadter, «Relativistic plasma-wave excitation by collinear optical mixing», *Phys. Rev. Lett.*, vol. 54, pp. 2343–2346, 21 May 1985. DOI: 10.1103/PhysRevLett.54.2343. [Online]. Available: https://link.aps.org/doi/10.1103/PhysRevLett.54.2343.

[40] C. E. Clayton, K. A. Marsh, A. Dyson *et al.*, «Ultrahigh-gradient acceleration of injected electrons by laser-excited relativistic electron plasma waves», *Phys. Rev. Lett.*, vol. 70, pp. 37–40, 1 Jan. 1993. DOI: 10.1103/PhysRevLett.70.37. [Online]. Available: https://link.aps.org/doi/10.1103/PhysRevLett.70.37.

[41] M. N. Rosenbluth and C. S. Liu, «Excitation of plasma waves by two laser beams», *Phys. Rev. Lett.*, vol. 29, pp. 701–705, 11 Sep. 1972. DOI: 10.1103/PhysRevLett.29.701. [Online]. Available: https://link.aps.org/doi/10.1103/PhysRevLett.29.701.

[42] N. E. Andreev, L. M. Gorbunov, V. I. Kirsanov, A. A. Pogosova and R. R. Ramazashvili, «Resonant excitation of wakefields by a laser pulse in a plasma», *Soviet Journal of Experimental and Theoretical Physics Letters*, vol. 55, p. 571, May 1992.

[43] J. Krall, A. Ting, E. Esarey and P. Sprangle, «Enhanced acceleration in a self-modulated-laser wake-field accelerator», *Phys. Rev. E*, vol. 48, pp. 2157–2161, 3 Sep. 1993. DOI: 10.1103/PhysRevE.48.2157. [Online]. Available: https://link.aps.org/doi/10.1103/PhysRevE.48.2157.

[44] K. Nakajima, D. Fisher, T. Kawakubo *et al.*, «Observation of ultrahigh gradient electron acceleration by a self-modulated intense short laser pulse», *Phys. Rev. Lett.*, vol. 74, pp. 4428–4431, 22 May 1995. DOI: 10.1103/PhysRevLett.74.4428. [Online]. Available: https://link.aps.org/doi/10.1103/PhysRevLett.74.4428.

[45] Z. Modena A.and Najmudin, A. E. Dangor, C. E. Clayton *et al.*, «Electron acceleration from the breaking of relativistic plasma waves», *Nature*, vol. 377, no. 6550, pp. 606–608, Oct. 1995, ISSN: 1476-4687. DOI: 10.1038/377606a0. [Online]. Available: https://doi.org/10.1038/377606a0.

[46] R. Wagner, S. Chen, A. Maksimchuk and D. Umstadter, «Electron acceleration by a laser wake field in a relativistically selfguided channel», *Phys. Rev. Lett.*, vol. 78, pp. 3125–3128, 1997. DOI: 10.1103/PhysRevLett.78.3125.

[47] C. I. Moore, A. Ting, K. Krushelnick *et al.*, «Electron trapping in self-modulated laser wakefields by raman backscatter», *Phys. Rev. Lett.*, vol. 79, pp. 3909–3912, 20 Sep. 1997. DOI: 10.1103/PhysRevLett.79.3909. [Online]. Available: https://link.aps.org/doi/10.1103/PhysRevLett.79.3909.

[48] D. Gordon, K. C. Tzeng, C. E. Clayton *et al.*, «Observation of electron energies beyond the linear dephasing limit from a laser-excited relativistic plasma wave», *Phys. Rev. Lett.*, vol. 80, pp. 2133–2136, 10 Mar. 1998. DOI: 10.1103/PhysRevLett.80.2133. [Online]. Available: https://link.aps.org/doi/10.1103/PhysRevLett.80.2133.

[49] V. Malka, J. Faure, J. R. Marquès *et al.*, «Characterization of electron beams produced by ultrashort (30 fs) laser pulses», *Physics of Plasmas*, vol. 8, no. 6, pp. 2605–2608, Jun. 2001, ISSN: 1070-664X. DOI: 10.1063/1.1374584. eprint: https://pubs.aip.org/aip/pop/article-pdf/8/6/2605/12730410/2605_1_online.pdf. [Online]. Available: https://doi.org/10.1063/1.1374584.

[50] D. Umstadter, «Review of physics and applications of relativistic plasmas driven by ultra-intense lasers», *Physics of Plasmas*, vol. 8, no. 5, pp. 1774–1785, 2001. DOI: 10.1063/1.1364515. eprint: https://doi.org/10.1063/1.1364515. [Online]. Available: https://doi.org/10.1063/1.1364515.

[51] D. Strickland and G. Mourou, «Compression of amplified chirped optical pulses», *Optics Communications*, vol. 55, no. 6, pp. 447–449, 1985, ISSN: 0030-4018. DOI: https://doi.org/10.1016/0030-4018(85)90151-8. [Online]. Available: http://www.sciencedirect.com/science/article/pii/0030401885901518.

[52] M. D. Perry and G. Mourou, «Terawatt to petawatt subpicosecond lasers», *Science*, vol. 264, no. 5161, pp. 917–924, 1994. DOI: 10.1126/science.264.5161.917. eprint: https://www.science.org/doi/pdf/10.1126/science.264.5161.917. [Online]. Available: https://www.science.org/doi/abs/10.1126/science.264.5161.917.

[53] M. D. Perry, D. Pennington, B. C. Stuart *et al.*, «Petawatt laser pulses», *Opt. Lett.*, vol. 24, no. 3, pp. 160–162, Feb. 1999. DOI: 10.1364/OL.24.000160. [Online]. Available: http://ol.osa.org/abstract.cfm?URI=ol-24-3-160.

[54] S. P. D. Mangles, C. D. Murphy, Z. Najmudin *et al.*, «Monoenergetic beams of relativistic electrons from intense laser–plasma interactions», *Nature*, vol. 431, no. 7008, pp. 535–538, Sep. 2004, ISSN: 1476-4687. DOI: 10.1038/nature02939. [Online]. Available: https://doi.org/10.1038/nature02939.

[55] J. Faure, Y. Glinec, A. Pukhov *et al.*, «A laser–plasma accelerator producing monoenergetic electron beams», *Nature*, vol. 431, no. 7008, pp. 541–544, Sep. 2004, ISSN: 1476-4687. DOI: 10.1038/nature02963. [Online]. Available: https://doi.org/10.1038/nature02963.

[56] C. G. R. Geddes, C. Toth, J. van Tilborg *et al.*, «High-quality electron beams from a laser wakefield accelerator using plasma-channel guiding», *Nature*, vol. 431, no. 7008, pp. 538–541, Sep. 2004, ISSN: 1476-4687. DOI: 10.1038/nature02900. [Online]. Available: https://doi.org/10.1038/nature02900.

[57] P. Mora and T. M. Antonsen, «Electron cavitation and acceleration in the wake of an ultraintense, self-focused laser pulse», *Phys. Rev. E*, vol. 53, R2068–R2071, 3 Mar. 1996. DOI: 10.1103/PhysRevE.53.R2068. [Online]. Available: https://link.aps.org/doi/10.1103/PhysRevE.53.R2068.

[58] A. Pukhov and J. Meyer-ter-Vehn, «Laser wake field acceleration: The highly non-linear broken-wave regime», *Applied Physics B*, vol. 74, no. 4, pp. 355–361, Apr. 2002, ISSN: 1432-0649. DOI: 10.1007/s003400200795. [Online]. Available: https://doi.org/10.1007/s003400200795.

[59] F. Albert and A. G. R. Thomas, «Applications of laser wakefield accelerator-based light sources», *Plasma Physics and Controlled Fusion*, vol. 58, no. 10, p. 103 001, 2016. DOI: 10.1088/0741-3335/58/10/103001.

[60] A. Rousse, K. T. Phuoc, R. Shah *et al.*, «Production of a kev x-ray beam from synchrotron radiation in relativistic laser-plasma interaction», *Physical Review Letters*, vol. 93, no. 13, 2004. DOI: 10.1103/physrevlett.93.135005.

[61] A. G. R. Thomas, «Scalings for radiation from plasma bubblesa)», *Physics of Plasmas*, vol. 17, no. 5, p. 056 708, Apr. 2010, ISSN: 1070-664X. DOI: 10.1063/1.3368678. eprint: https://pubs.aip.org/aip/pop/article-pdf/doi/10.1063/1.3368678/14921119/056708_1_online.pdf. [Online]. Available: https://doi.org/10.1063/1.3368678.

[62] S. Kneip, Z. Najmudin and A. G. Thomas, «A plasma wiggler beamline for 100 tw to 10 pw lasers», *High Energy Density Physics*, vol. 8, no. 2, pp. 133–140, 2012, ISSN: 1574-1818. DOI: https://doi.org/10.1016/j.hedp.2011.12.001. [Online]. Available: https://www.sciencedirect.com/science/article/pii/S157418181100111X.

[63] K. Ta Phuoc, R. Fitour, A. Tafzi *et al.*, «Demonstration of the ultrafast nature of laser produced betatron radiation», *Physics of Plasmas*, vol. 14, no. 8, p. 080 701, Aug. 2007, ISSN: 1070-664X. DOI: 10.1063/1.2754624. eprint: https://pubs.aip.org/aip/pop/article-pdf/doi/10.1063/1.2754624/16134945/080701_1_online.pdf. [Online]. Available: https://doi.org/10.1063/1.2754624.

[64] S. Cipiccia, M. R. Islam, B. Ersfeld *et al.*, «Gamma-rays from harmonically resonant betatron oscillations in a plasma wake», *Nature Physics*, vol. 7, no. 11, pp. 867–871, Nov. 2011, ISSN: 1745-2481. DOI: 10.1038/nphys2090. [Online]. Available: https://doi.org/10.1038/nphys2090.

[65] S. Kneip, C. McGuffey, J. L. Martins *et al.*, «Bright spatially coherent synchrotron X-rays from a table-top source», *Nature Physics*, vol. 6, no. 12, pp. 980–983, 2010, ISSN: 17452481. DOI: 10.1038/nphys1789.

[66] S. Kneip, C. McGuffey, J. L. Martins *et al.*, «Characterization of transverse beam emittance of electrons from a laser-plasma wakefield accelerator in the bubble regime using betatron x-ray radiation», *Phys. Rev. ST Accel. Beams*, vol. 15, p. 021 302, 2 Feb. 2012. DOI: 10.1103/PhysRevSTAB.15.021302. [Online]. Available: https://link.aps.org/doi/10.1103/PhysRevSTAB.15.021302.

[67] S. Kneip, C. McGuffey, F. Dollar *et al.*, «X-ray phase contrast imaging of biological specimens with femtosecond pulses of betatron radiation from a compact laser plasma wakefield accelerator», *Applied Physics Letters*, vol. 99, no. 9, p. 093 701, 2011. DOI: 10.1063/1.3627216. eprint: https://doi.org/10.1063/1.3627216. [Online]. Available: https://doi.org/10.1063/1.3627216.

[68] S. Fourmaux, S. Corde, K. T. Phuoc *et al.*, «Single shot phase contrast imaging using laser-produced betatron x-ray beams», *Opt. Lett.*, vol. 36, no. 13, pp. 2426–2428, Jul. 2011. DOI: 10.1364/OL.36.002426. [Online]. Available: https://opg.optica.org/ol/abstract.cfm?URI=ol-36-13-2426.

[69] S. P. D. Mangles, M. S. Bloom, J. Bryant *et al.*, «Producing bright x-rays for imaging applications using a laser wakefield accelerator», in *2014 Conference on Lasers and Electro-Optics (CLEO) - Laser Science to Photonic Applications*, 2014, pp. 1–3. DOI: 10.1364/CLEO_AT.2014.JTh3L.4.

[70] J. Wenz, S. Schleede, K. Khrennikov *et al.*, «Quantitative X-ray phase-contrast microtomography from a compact laser-driven betatron source», *Nature Communications*, vol. 6, no. May, pp. 1–6, 2015, ISSN: 20411723. DOI: 10.1038/ncomms8568.

[71] J. M. Cole, D. R. Symes, N. C. Lopes *et al.*, «High-resolution μCT of a mouse embryo using a compact laser-driven X-ray betatron source», *Proceedings of the National Academy of Sciences*, vol. 115, no. 25, pp. 6335–6340, 2018, ISSN: 0027-8424. DOI: 10.1073/pnas.1802314115.

[72] J. C. Wood, D. J. Chapman, K. Poder *et al.*, «Ultrafast imaging of laser driven shock waves using betatron x-rays from a laser wakefield accelerator», *Nature*, vol. 8, no. 11010, 2018. DOI: https://doi.org/10.1038/s41598-018-29347-0.

[73] M. Z. Mo, Z. Chen, S. Fourmaux *et al.*, «Laser wakefield generated X-ray probe for femtosecond time-resolved measurements of ionization states of warm dense aluminum», *Review of Scientific Instruments*, vol. 84, no. 12, p. 123 106, Dec. 2013, ISSN: 0034-6748. DOI: 10.1063/1.4842237. eprint: https://pubs.aip.org/aip/rsi/article-pdf/doi/10.1063/1.4842237/15728531/123106_1_online.pdf. [Online]. Available: https://doi.org/10.1063/1.4842237.

[74] B. Kettle, E. Gerstmayr, M. J. V. Streeter *et al.*, «Single-shot multi-kev x-ray absorption spectroscopy using an ultrashort laser-wakefield accelerator source», *Phys. Rev. Lett.*, vol. 123, p. 254 801, 25 Dec. 2019. DOI: 10.1103/PhysRevLett.

123.254801. [Online]. Available: https://link.aps.org/doi/10.1103/PhysRevLett.123.254801.

[75] Diamond Light Source, 2022. [Online]. Available: https://www.diamond.ac.uk/Home/About/FAQs/General.html#:~:text=As%20we%20enhanced%20the%20facility,growing%20number%20of%20experimental%20stations.

[76] C. Danson, D. Hillier, N. Hopps and D. Neely, «Petawatt class lasers worldwide», *High Power Laser Science and Engineering*, vol. 3, e3, 2015. DOI: 10.1017/hpl.2014.52.

[77] W. P. Leemans, R. Duarte, E. Esarey *et al.*, «The BErkeley Lab Laser Accelerator (BELLA): A 10 GeV Laser Plasma Accelerator», *AIP Conference Proceedings*, vol. 1299, no. 1, pp. 3–11, Nov. 2010, ISSN: 0094-243X. DOI: 10.1063/1.3520352. eprint: https://pubs.aip.org/aip/acp/article-pdf/1299/1/3/11927656/3_1_online.pdf. [Online]. Available: https://doi.org/10.1063/1.3520352.

[78] J. Faure, D. Gustas, D. Guénot *et al.*, «A review of recent progress on laser-plasma acceleration at khz repetition rate», *Plasma Physics and Controlled Fusion*, vol. 61, no. 1, p. 014 012, Sep. 2018. DOI: 10.1088/1361-6587/aae047. [Online]. Available: https://dx.doi.org/10.1088/1361-6587/aae047.

[79] F. Albert, M. E. Couprie, A. Debus *et al.*, «2020 roadmap on plasma accelerators», *New Journal of Physics*, vol. 23, no. 3, p. 031 101, Mar. 2021. DOI: 10.1088/1367-2630/abcc62. [Online]. Available: https://dx.doi.org/10.1088/1367-2630/abcc62.

[80] Z.-H. He, A. G. R. Thomas, B. Beaurepaire *et al.*, «Electron diffraction using ultrafast electron bunches from a laser-wakefield accelerator at kHz repetition rate», *Applied Physics Letters*, vol. 102, no. 6, p. 064 104, Feb. 2013, ISSN: 0003-6951. DOI: 10.1063/1.4792057. eprint: https://pubs.aip.org/aip/apl/article-pdf/doi/10.1063/1.4792057/14280466/064104_1_online.pdf. [Online]. Available: https://doi.org/10.1063/1.4792057.

[81] Z.-H. He, B. Beaurepaire, J. A. Nees *et al.*, «Capturing structural dynamics in crystalline silicon using chirped electrons from a laser wakefield accelerator», *Scientific Reports*, vol. 6, no. 1, p. 36 224, Sep. 2016, ISSN: 2045-2322. DOI: 10.1038/srep36224. [Online]. Available: https://doi.org/10.1038/srep36224.

[82] J. Faure, B. van der Geer, B. Beaurepaire, G. Gallé, A. Vernier and A. Lifschitz, «Concept of a laser-plasma-based electron source for sub-10-fs electron diffraction», *Phys. Rev. Accel. Beams*, vol. 19, p. 021 302, 2 Feb. 2016. DOI: 10.1103/PhysRevAccelBeams.19.021302. [Online]. Available: https://link.aps.org/doi/10.1103/PhysRevAccelBeams.19.021302.

[83] F. Salehi, A. J. Goers, G. A. Hine *et al.*, «Mev electron acceleration at 1 khz with <10 mj laser pulses», *Opt. Lett.*, vol. 42, no. 2, pp. 215–218, Jan. 2017. DOI: 10.1364/OL.42.000215. [Online]. Available: https://opg.optica.org/ol/abstract.cfm?URI=ol-42-2-215.

[84] L. Rovige, J. Huijts, I. Andriyash *et al.*, «Demonstration of stable long-term operation of a kilohertz laser-plasma accelerator», *Phys. Rev. Accel. Beams*, vol. 23, p. 093 401, 9 Sep. 2020. DOI: 10.1103/PhysRevAccelBeams.23.093401.

[85] L. Rovige, J. Huijts, I. A. Andriyash *et al.*, «Optimization and stabilization of a kilohertz laser-plasma accelerator», *Physics of Plasmas*, vol. 28, no. 3, p. 033 105, Mar. 2021, ISSN: 1070-664X. DOI: 10.1063/5.0040926. eprint: https://pubs.aip.org/aip/pop/article-pdf/doi/10.1063/5.0040926/13823876/033105_1_online.pdf. [Online]. Available: https://doi.org/10.1063/5.0040926.

[86] F. Salehi, M. Le, L. Railing, M. Kolesik and H. M. Milchberg, «Laser-accelerated, low-divergence 15-mev quasimonoenergetic electron bunches at 1 khz», *Phys. Rev. X*, vol. 11, p. 021 055, 2 Jun. 2021. DOI: 10.1103/PhysRevX.11.021055. [Online]. Available: https://link.aps.org/doi/10.1103/PhysRevX.11.021055.

[87] C. P. Hauri, P. Schlup, G. Arisholm, J. Biegert and U. Keller, «Phase-preserving chirped-pulse optical parametric amplification to 17.3 fs directly from a ti:sapphire oscillator», *Opt. Lett.*, vol. 29, no. 12, pp. 1369–1371, Jun. 2004. DOI: 10.1364/OL.29.001369. [Online]. Available: https://opg.optica.org/ol/abstract.cfm?URI=ol-29-12-1369.

[88] S. Witte, R. T. Zinkstok, A. L. Wolf, W. Hogervorst, W. Ubachs and K. S. E. Eikema, «A source of 2 terawatt, 2.7 cycle laser pulses based on noncollinear optical parametric chirped pulse amplification», *Opt. Express*, vol. 14, no. 18, pp. 8168–8177, Sep. 2006. DOI: 10.1364/OE.14.008168. [Online]. Available: https://opg.optica.org/oe/abstract.cfm?URI=oe-14-18-8168.

[89] F. Tavella, Y. Nomura, L. Veisz, V. Pervak, A. Marcinkevičius and F. Krausz, «Dispersion management for a sub-10-fs, 10 tw optical parametric chirped-pulse amplifier», *Opt. Lett.*, vol. 32, no. 15, pp. 2227–2229, Aug. 2007. DOI:

10.1364/OL.32.002227. [Online]. Available: https://opg.optica.org/ol/abstract.cfm?URI=ol-32-15-2227.

[90] D. Herrmann, L. Veisz, R. Tautz *et al.*, «Generation of sub-three-cycle, 16 tw light pulses by using noncollinear optical parametric chirped-pulse amplification», *Opt. Lett.*, vol. 34, no. 16, pp. 2459–2461, Aug. 2009. DOI: 10.1364/OL.34.002459. [Online]. Available: https://opg.optica.org/ol/abstract.cfm?URI=ol-34-16-2459.

[91] D. E. Rivas, A. Borot, D. E. Cardenas *et al.*, «Next generation driver for attosecond and laser-plasma physics», *Scientific Reports*, vol. 7, no. 1, p. 5224, Jul. 2017, ISSN: 2045-2322. DOI: 10.1038/s41598-017-05082-w. [Online]. Available: https://doi.org/10.1038/s41598-017-05082-w.

[92] A. Kessel, V. E. Leshchenko, O. Jahn *et al.*, «Relativistic few-cycle pulses with high contrast from picosecond-pumped opcpa», *Optica*, vol. 5, no. 4, pp. 434–442, Aug. 2018. DOI: 10.1364/OPTICA.5.000434. [Online]. Available: https://opg.optica.org/optica/abstract.cfm?URI=optica-5-4-434.

[93] K. Schmid, «Supersonic micro-jets and their application to few-cycle laser-driven electron acceleration», Jul. 2009. [Online]. Available: http://nbn-resolving.de/urn:nbn:de:bvb:19-104632.

[94] J. Xu, A. Buck, S.-W. Chou *et al.*, «Dynamics of electron injection in a laser-wakefield accelerator», *Physics of Plasmas*, vol. 24, no. 8, p. 083 106, Aug. 2017, ISSN: 1070-664X. DOI: 10.1063/1.4996906. eprint: https://pubs.aip.org/aip/pop/article-pdf/doi/10.1063/1.4996906/15649735/083106_1_online.pdf. [Online]. Available: https://doi.org/10.1063/1.4996906.

[95] S. Bohman, A. Suda, T. Kanai, S. Yamaguchi and K. Midorikawa, «Generation of 5.0fs, 5.0mj pulses at 1khz using hollow-fiber pulse compression», *Opt. Lett.*, vol. 35, no. 11, pp. 1887–1889, Jun. 2010. DOI: 10.1364/OL.35.001887. [Online]. Available: https://opg.optica.org/ol/abstract.cfm?URI=ol-35-11-1887.

[96] X. Chen, A. Malvache, A. Ricci, A. Jullien and R. Lopez-Martens, «Efficient hollow fiber compression scheme for generating multi-mj, carrier-envelope phase stable, sub-5 fs pulses», *Laser Physics*, vol. 21, no. 1, pp. 198–201, Jan. 2011, ISSN: 1555-6611. DOI: 10.1134/S1054660X11010063. [Online]. Available: https://doi.org/10.1134/S1054660X11010063.

[97] S. Prinz, M. Schnitzenbaumer, D. Potamianos *et al.*, «Thin-disk pumped optical parametric chirped pulse amplifier delivering cep-stable multi-mj few-cycle pulses at 6 khz», *Opt. Express*, vol. 26, no. 2, pp. 1108–1124, Jan. 2018. DOI: 10.1364/OE.26.001108. [Online]. Available: https://opg.optica.org/oe/abstract.cfm?URI=oe-26-2-1108.

[98] F. J. A. Furch, T. Witting, M. Osolodkov, F. Schell, C. P. Schulz and M. J. J. Vrakking, «High-repetition rate optical parametric chirped pulse amplification system for attosecond science experiments», in *Short-pulse High-energy Lasers and Ultrafast Optical Technologies*, P. Bakule and C. L. Haefner, Eds., International Society for Optics and Photonics, vol. 11034, SPIE, 2019, p. 110340I. DOI: 10.1117/12.2523891. [Online]. Available: https://doi.org/10.1117/12.2523891.

[99] B. Beaurepaire, A. Lifschitz and J. Faure, «Electron acceleration in sub-relativistic wakefields driven by few-cycle laser pulses», *New Journal of Physics*, vol. 16, no. 2, p. 023 023, Feb. 2014. DOI: 10.1088/1367-2630/16/2/023023. [Online]. Available: https://dx.doi.org/10.1088/1367-2630/16/2/023023.

[100] M. Ouillé, A. Vernier, F. Böhle *et al.*, «Relativistic-intensity near-single-cycle light waveforms at khz repetition rate», *Light: Science & Applications*, vol. 9, no. 1, p. 47, Mar. 2020, ISSN: 2047-7538. DOI: 10.1038/s41377-020-0280-5. [Online]. Available: https://doi.org/10.1038/s41377-020-0280-5.

[101] D. Guénot, D. Gustas, A. Vernier *et al.*, «Relativistic electron beams driven by khz single-cycle light pulses», *Nature Photonics*, vol. 11, no. 5, pp. 293–296, May 2017, ISSN: 1749-4893. DOI: 10.1038/nphoton.2017.46. [Online]. Available: https://doi.org/10.1038/nphoton.2017.46.

[102] S. Toth, T. Stanislauskas, I. Balciunas *et al.*, «Sylos lasers – the frontier of few-cycle, multi-tw, khz lasers for ultrafast applications at extreme light infrastructure attosecond light pulse source», *Journal of Physics: Photonics*, vol. 2, no. 4, p. 045 003, Jul. 2020. DOI: 10.1088/2515-7647/ab9fe1. [Online]. Available: https://dx.doi.org/10.1088/2515-7647/ab9fe1.

[103] C. M. Lazzarini, G. M. Grittani, P. Valenta *et al.*, *50 mev electron beams accelerated by a terawatt scalable khz laser*, 2023. arXiv: 2302.11415.

[104] X.-L. Zhu, W.-Y. Liu, M. Chen *et al.*, «Generation of 100-mev attosecond electron bunches with terawatt few-cycle laser pulses», *Phys. Rev. Appl.*, vol. 15, p. 044 039, 4 Apr. 2021. DOI: 10.1103/PhysRevApplied.15.044039. [Online]. Available: https://link.aps.org/doi/10.1103/PhysRevApplied.15.044039.

[105] D. Papp, Z. Lécz, C. Kamperidis and N. A. M. Hafz, «Highly efficient few-cycle laser wakefield electron accelerator», *Plasma Physics and Controlled Fusion*, vol. 63, no. 6, p. 065 019, May 2021. DOI: 10.1088/1361-6587/abf80d. [Online]. Available: https://dx.doi.org/10.1088/1361-6587/abf80d.

[106] M. J. V. Streeter, Y. Ma, B. Kettle *et al.*, «Characterization of laser wakefield acceleration efficiency with octave spanning near-ir spectrum measurements», *Phys. Rev. Accel. Beams*, vol. 25, p. 101 302, 10 Oct. 2022. DOI: 10.1103/PhysRevAccelBeams.25.101302. [Online]. Available: https://link.aps.org/doi/10.1103/PhysRevAccelBeams.25.101302.

[107] G. Hicks, R. Shalloo, R. Yembadi *et al.*, «Esylos- technical design report», John Adams Institute, Imperial College London, Tech. Rep., 2021.

[108] J. Csontos, *Sylos 3 laser system*. [Online]. Available: https://up.eli-laser.eu/laser/sylos-3-680165396.

[109] J. Götzfried, A. Döpp, M. F. Gilljohann *et al.*, «Physics of high-charge electron beams in laser-plasma wakefields», *Phys. Rev. X*, vol. 10, p. 041 015, 4 Oct. 2020. DOI: 10.1103/PhysRevX.10.041015. [Online]. Available: https://link.aps.org/doi/10.1103/PhysRevX.10.041015.

[110] J. P. Couperus, R. Pausch, A. Köhler *et al.*, «Demonstration of a beam loaded nanocoulomb-class laser wakefield accelerator», *Nature Communications*, vol. 8, no. 1, p. 487, Sep. 2017, ISSN: 2041-1723. DOI: 10.1038/s41467-017-00592-7. [Online]. Available: https://doi.org/10.1038/s41467-017-00592-7.

[111] Extreme Light Infrastructure, «Whitebook», Extreme Light Infrastructure, Tech. Rep., 2011.

[112] T. Pak, M. Rezaei-Pandari, S. B. Kim *et al.*, «Multi-millijoule terahertz emission from laser-wakefield-accelerated electrons», *Light: Science & Applications*, vol. 12, no. 1, p. 37, Feb. 2023, ISSN: 2047-7538. DOI: 10.1038/s41377-022-01068-0. [Online]. Available: https://doi.org/10.1038/s41377-022-01068-0.

[113] E. Beyreuther, W. Enghardt, M. Kaluza *et al.*, «Establishment of technical prerequisites for cell irradiation experiments with laser-accelerated electrons», en, *Med. Phys.*, vol. 37, no. 4, pp. 1392–1400, Apr. 2010.

[114] R. Polanek, N. A. Hafz, Z. Lécz *et al.*, «1 khz laser accelerated electron beam feasible for radiotherapy uses: A pic–monte carlo based study», *Nuclear Instruments and Methods in Physics Research Section A: Accelerators, Spectrometers, Detectors and Associated Equipment*, vol. 987, p. 164 841, 2021, ISSN: 0168-9002. DOI: https://doi.org/10.1016/j.nima.2020.164841.

[Online]. Available: https://www.sciencedirect.com/science/article/pii/S0168900220312389.

[115] C. Joshi, S. Corde and W. B. Mori, «Perspectives on the generation of electron beams from plasma-based accelerators and their near and long term applications», *Physics of Plasmas*, vol. 27, no. 7, p. 070 602, Jul. 2020, ISSN: 1070-664X. DOI: 10.1063/5.0004039. eprint: https://pubs.aip.org/aip/pop/article-pdf/doi/10.1063/5.0004039/13872177/070602_1_online.pdf. [Online]. Available: https://doi.org/10.1063/5.0004039.

[116] H. Goldstein, C. P. Poole and J. L. Safko, *Classical Mechanics*, eng, 3rd ed. Boston, MA: Addison Wesley, 2002, OCLC: 248389949, ISBN: 978-8131758915.

[117] E. Esarey, P. Sprangle, J. Krall and A. Ting, «Self-focusing and guiding of short laser pulses in ionizing gases and plasmas», *IEEE Journal of Quantum Electronics*, vol. 33, no. 11, pp. 1879–1914, 1997. DOI: 10.1109/3.641305.

[118] R. Fitzpatrick, *Solution of Inhomogeneous Helmholtz Equation*, 2014. [Online]. Available: https://farside.ph.utexas.edu/teaching/jk1/lectures/node126.html.

[119] R. Brown, Dec. 2007. [Online]. Available: http://webhome.phy.duke.edu/~rgb/Class/phy319/phy319/node74.html.

[120] J. M. Dawson, «Nonlinear Electron Oscillations in a Cold Plasma», *Nucl. Phys.*, vol. 13, no. 1, pp. 104–116, 1959, ISSN: 0029-5582.

[121] V. I. Berezhiani and I. G. Murusidze, «Interaction of highly relativistic short laser pulses with plasmas and nonlinear wake-field generation», *Physica Scripta*, vol. 45, no. 2, p. 87, Feb. 1992. DOI: 10.1088/0031-8949/45/2/007. [Online]. Available: https://dx.doi.org/10.1088/0031-8949/45/2/007.

[122] E. Esarey, A. Ting, P. Sprangle, D. Umstadter and X. Liu, «Nonlinear analysis of relativistic harmonic generation by intense lasers in plasmas», *IEEE Transactions on Plasma Science*, vol. 21, no. 1, pp. 95–104, 1993, ISSN: 0093-3813. DOI: 10.1109/27.221107. [Online]. Available: https://dx.doi.org/10.1109/27.221107.

[123] D. Teychenné, G. Bonnaud and J. Bobin, «Wave-breaking limit to the wake-field effect in an underdense plasma», *Physical review. E, Statistical physics, plasmas, fluids, and related interdisciplinary topics*, vol. 48, R3248–R3251, Dec. 1993. DOI: 10.1103/PhysRevE.48.R3248.

[124] J. Vieira, R. A. Fonseca and L. O. Silva, «Multidimensional plasma wake excitation in the non-linear blowout regime», 2016. [Online]. Available: https://api.semanticscholar.org/CorpusID:92986774.

[125] V. Berezhiani and I. Murusidze, «Relativistic wake-field generation by an intense laser pulse in a plasma», *Physics Letters A*, vol. 148, no. 6, pp. 338–340, 1990, ISSN: 0375-9601. DOI: https://doi.org/10.1016/0375-9601(90)90813-4. [Online]. Available: https://www.sciencedirect.com/science/article/pii/0375960190908134.

[126] P. Sprangle, E. Esarey and A. Ting, «Nonlinear interaction of intense laser pulses in plasmas», *Phys. Rev. A*, vol. 41, pp. 4463–4469, 8 Apr. 1990. DOI: 10.1103/PhysRevA.41.4463. [Online]. Available: https://link.aps.org/doi/10.1103/PhysRevA.41.4463.

[127] W. Lu, C. Huang, M. Zhou *et al.*, «A nonlinear theory for multidimensional relativistic plasma wave wakefields», *Physics of Plasmas*, vol. 13, no. 5, p. 056 709, 2006. DOI: 10.1063/1.2203364. eprint: https://doi.org/10.1063/1.2203364. [Online]. Available: https://doi.org/10.1063/1.2203364.

[128] W. Lu, C. Huang, M. Zhou, W. B. Mori and T. Katsouleas, «Nonlinear theory for relativistic plasma wakefields in the blowout regime», *Phys. Rev. Lett.*, vol. 96, p. 165 002, 16 Apr. 2006. DOI: 10.1103/PhysRevLett.96.165002. [Online]. Available: https://link.aps.org/doi/10.1103/PhysRevLett.96.165002.

[129] W. Lu, M. Tzoufras, C. Joshi *et al.*, «Generating multi-gev electron bunches using single stage laser wakefield acceleration in a 3d nonlinear regime», *Phys. Rev. ST Accel. Beams*, vol. 10, p. 061 301, 6 Jun. 2007. DOI: 10.1103/PhysRevSTAB.10.061301. [Online]. Available: https://link.aps.org/doi/10.1103/PhysRevSTAB.10.061301.

[130] I. Kostyukov, A. Pukhov and S. Kiselev, «Phenomenological theory of laser-plasma interaction in "bubble" regime», *Physics of Plasmas*, vol. 11, no. 11, pp. 5256–5264, 2004. DOI: 10.1063/1.1799371. eprint: https://doi.org/10.1063/1.1799371. [Online]. Available: https://doi.org/10.1063/1.1799371.

[131] I. Kostyukov, E. Nerush, A. Pukhov and V. Seredov, «Electron self-injection in multidimensional relativistic-plasma wake fields», *Phys. Rev. Lett.*, vol. 103, p. 175 003, 17 Oct. 2009. DOI: 10.1103/PhysRevLett.103.175003. [Online]. Available: https://link.aps.org/doi/10.1103/PhysRevLett.103.175003.

[132] S. P. D. Mangles, G. Genoud, M. S. Bloom *et al.*, «Self-injection threshold in self-guided laser wakefield accelerators», *Phys. Rev. ST Accel. Beams*, vol. 15, p. 011 302, 1 Jan. 2012. DOI: 10.1103/PhysRevSTAB.15.011302. [Online]. Available: https://link.aps.org/doi/10.1103/PhysRevSTAB.15.011302.

[133] S. Kalmykov, S. A. Yi, V. Khudik and G. Shvets, «Electron self-injection and trapping into an evolving plasma bubble», *Phys. Rev. Lett.*, vol. 103, p. 135 004, 13 Sep. 2009. DOI: 10.1103/PhysRevLett.103.135004. [Online]. Available: https://link.aps.org/doi/10.1103/PhysRevLett.103.135004.

[134] S. Bulanov, N. Naumova, F. Pegoraro and J. Sakai, «Particle injection into the wave acceleration phase due to nonlinear wake wave breaking», *Phys. Rev. E*, vol. 58, R5257–R5260, 5 Nov. 1998. DOI: 10.1103/PhysRevE.58.R5257. [Online]. Available: https://link.aps.org/doi/10.1103/PhysRevE.58.R5257.

[135] P. Tomassini, M. Galimberti, A. Giulietti *et al.*, «Production of high-quality electron beams in numerical experiments of laser wakefield acceleration with longitudinal wave breaking», *Phys. Rev. ST Accel. Beams*, vol. 6, p. 121 301, 12 Dec. 2003. DOI: 10.1103/PhysRevSTAB.6.121301. [Online]. Available: https://link.aps.org/doi/10.1103/PhysRevSTAB.6.121301.

[136] H. Ekerfelt, M. Hansson, I. Gallardo González, X. Davoine and O. Lundh, «A tunable electron beam source using trapping of electrons in a density down-ramp in laser wakefield acceleration», *Scientific Reports*, vol. 7, no. 1, p. 12 229, Sep. 2017, ISSN: 2045-2322. DOI: 10.1038/s41598-017-12560-8. [Online]. Available: https://doi.org/10.1038/s41598-017-12560-8.

[137] S. A. Yi, V. Khudik, S. Y. Kalmykov and G. Shvets, «Hamiltonian analysis of electron self-injection and acceleration into an evolving plasma bubble», *Plasma Physics and Controlled Fusion*, vol. 53, no. 1, p. 014 012, Dec. 2010. DOI: 10.1088/0741-3335/53/1/014012. [Online]. Available: https://dx.doi.org/10.1088/0741-3335/53/1/014012.

[138] S. Y. Kalmykov, S. A. Yi, A. Beck *et al.*, «Dark-current-free petawatt laser-driven wakefield accelerator based on electron self-injection into an expanding plasma bubble», *Plasma Physics and Controlled Fusion*, vol. 53, no. 1, p. 014 006, Dec. 2010. DOI: 10.1088/0741-3335/53/1/014006. [Online]. Available: https://dx.doi.org/10.1088/0741-3335/53/1/014006.

[139] A. Pak, K. A. Marsh, S. F. Martins, W. Lu, W. B. Mori and C. Joshi, «Injection and trapping of tunnel-ionized electrons into laser-produced wakes», *Phys. Rev. Lett.*, vol. 104, p. 025 003, 2 Jan. 2010. DOI: 10.1103/PhysRevLett.104.025003. [Online]. Available: https://link.aps.org/doi/10.1103/PhysRevLett.104.025003.

[140] C. McGuffey, A. G. R. Thomas, W. Schumaker *et al.*, «Ionization induced trapping in a laser wakefield accelerator», *Phys. Rev. Lett.*, vol. 104, p. 025 004,

2 Jan. 2010. DOI: 10.1103/PhysRevLett.104.025004. [Online]. Available: https://link.aps.org/doi/10.1103/PhysRevLett.104.025004.

[141] M. Mirzaie, S. Li, M. Zeng *et al.*, «Demonstration of self-truncated ionization injection for gev electron beams», *Scientific Reports*, vol. 5, no. 1, p. 14 659, Oct. 2015, ISSN: 2045-2322. DOI: 10.1038/srep14659. [Online]. Available: https://doi.org/10.1038/srep14659.

[142] Q. Zhao, S. M. Weng, Z. M. Sheng *et al.*, «Ionization injection in a laser wakefield accelerator subject to a transverse magnetic field», *New Journal of Physics*, vol. 20, no. 6, p. 063 031, Jun. 2018. DOI: 10.1088/1367-2630/aac926. [Online]. Available: https://dx.doi.org/10.1088/1367-2630/aac926.

[143] P. Lee, T. Audet, R. Lehe, J.-L. Vay, G. Maynard and B. Cros, «Investigation of the dynamics of ionization induced injected electrons under the influence of beam loading effects», *Nuclear Instruments and Methods in Physics Research Section A: Accelerators, Spectrometers, Detectors and Associated Equipment*, vol. 909, pp. 428–432, 2018, 3rd European Advanced Accelerator Concepts workshop (EAAC2017), ISSN: 0168-9002. DOI: https://doi.org/10.1016/j.nima.2018.02.004. [Online]. Available: https://www.sciencedirect.com/science/article/pii/S0168900218301542.

[144] M. Chen, E. Esarey, C. B. Schroeder, C. G. R. Geddes and W. P. Leemans, «Theory of ionization-induced trapping in laser-plasma accelerators», *Physics of Plasmas*, vol. 19, no. 3, p. 033 101, Mar. 2012, ISSN: 1070-664X. DOI: 10.1063/1.3689922. eprint: https://pubs.aip.org/aip/pop/article-pdf/doi/10.1063/1.3689922/15651230/033101_1_online.pdf. [Online]. Available: https://doi.org/10.1063/1.3689922.

[145] P. Gibbon, *Short pulse laser interactions with matter : an introduction*, eng. London: Imperial College Press, 2005, ISBN: 9781860941351.

[146] A. Kramida, Yu. Ralchenko, J. Reader and and NIST ASD Team, NIST Atomic Spectra Database (ver. 5.10), Oct. 2023. [Online]. Available: https://physics.nist.gov/asd.

[147] A. M. Perelomov, V. S. Popov and M. V. Terent'ev, «Ionization of Atoms in an Alternating Electric Field», *Soviet Journal of Experimental and Theoretical Physics*, vol. 23, p. 924, Nov. 1966.

[148] M. V. Ammosov, N. B. Delone and V. P. Krainov, «Tunnel Ionization Of Complex Atoms And Atomic Ions In Electromagnetic Field», in *High Intensity Laser Processes*, J. A. Alcock, Ed., International Society for Optics and Photonics, vol. 0664, SPIE, 1986, pp. 138–141. DOI: 10.1117/12.938695. [Online]. Available: https://doi.org/10.1117/12.938695.

[149] C. D. Decker, W. B. Mori, K.-C. Tzeng and T. Katsouleas, «The evolution of ultra-intense, short-pulse lasers in underdense plasmas», *Physics of Plasmas*, vol. 3, no. 5, pp. 2047–2056, 1996. DOI: 10.1063/1.872001. eprint: https://doi.org/10.1063/1.872001. [Online]. Available: https://doi.org/10.1063/1.872001.

[150] L. Alfred-Marie, «Champ électrique et magnétique produit par une charge concentrée en un point et animée d'un mouvement quelconque», *L'éclairage électrique*, vol. 16, pp. 5–14, Jul. 1898.

[151] E. Wiechert, «Elektrodynamische elementargesetze», *Annalen der Physik*, vol. 309, no. 4, pp. 667–689, 1901. DOI: https://doi.org/10.1002/andp.19013090403. eprint: https://onlinelibrary.wiley.com/doi/pdf/10.1002/andp.19013090403. [Online]. Available: https://onlinelibrary.wiley.com/doi/abs/10.1002/andp.19013090403.

[152] G. Materlik, T. Rayment and D. I. Stuart, «Diamond light source: Status and perspectives», *Philosophical Transactions of the Royal Society A: Mathematical, Physical and Engineering Sciences*, vol. 373, no. 2036, p. 20 130 161, 2015. DOI: 10.1098/rsta.2013.0161. eprint: https://royalsocietypublishing.org/doi/pdf/10.1098/rsta.2013.0161. [Online]. Available: https://royalsocietypublishing.org/doi/abs/10.1098/rsta.2013.0161.

[153] N. Marks, J. Clarke and D. Holder, «Magnetic design of the dipole magnets for the diamond synchrotron source», 2002. [Online]. Available: https://api.semanticscholar.org/CorpusID:110792486.

[154] E. Esarey, B. A. Shadwick, P. Catravas and W. P. Leemans, «Synchrotron radiation from electron beams in plasma-focusing channels», *Phys. Rev. E*, vol. 65, p. 056 505, 2002. DOI: 10.1103/PhysRevE.65.056505. [Online]. Available: https://link.aps.org/doi/10.1103/PhysRevE.65.056505.

[155] Diamond Light Source, *Diamond II Conceptual Design Report*. 2019.

[156] P. Elleaume, «Insertion devices for the new generation of synchrotron sources: A review (invited)», *Review of Scientific Instruments*, vol. 63, no. 1, pp. 321–326, Jan. 1992, ISSN: 0034-6748. DOI: 10.1063/1.1142744. eprint: https://pubs.aip.org/aip/rsi/article-pdf/63/1/321/7442299/321_1_online.pdf. [Online]. Available: https://doi.org/10.1063/1.1142744.

[157] E. Levichev and N. Vinokurov, «Undulators and other insertion devices», *Reviews of Accelerator Science and Technology*, vol. 03, no. 01, pp. 203–220, 2010. DOI: 10.1142/S1793626810000403. eprint: https://doi.org/10.1142/S1793626810000403. [Online]. Available: https://doi.org/10.1142/S1793626810000403.

[158] R. Ferguson, *Australian Senior Mathematics Journal*, vol. 32, no. 2, pp. 16–22, 2018. [Online]. Available: https://search.informit.org/doi/10.3316/informit.210409216264181.

[159] J. Derouillat, A. Beck, F. Pérez *et al.*, «Smilei : A collaborative, open-source, multi-purpose particle-in-cell code for plasma simulation», *Computer Physics Communications*, vol. 222, pp. 351–373, 2018, ISSN: 0010-4655. DOI: https://doi.org/10.1016/j.cpc.2017.09.024. [Online]. Available: http://www.sciencedirect.com/science/article/pii/S0010465517303314.

[160] A. Lifschitz, X. Davoine, E. Lefebvre, J. Faure, C. Rechatin and V. Malka, «Particle-in-cell modelling of laser–plasma interaction using fourier decomposition», *Journal of Computational Physics*, vol. 228, no. 5, pp. 1803–1814, 2009, ISSN: 0021-9991. DOI: https://doi.org/10.1016/j.jcp.2008.11.017. [Online]. Available: https://www.sciencedirect.com/science/article/pii/S0021999108005950.

[161] B. B. Godfrey and J.-L. Vay, «Numerical stability of relativistic beam multidimensional pic simulations employing the esirkepov algorithm», *Journal of Computational Physics*, vol. 248, pp. 33–46, 2013, ISSN: 0021-9991. DOI: https://doi.org/10.1016/j.jcp.2013.04.006. [Online]. Available: https://www.sciencedirect.com/science/article/pii/S0021999113002556.

[162] R. Lehe, A. Lifschitz, C. Thaury, V. Malka and X. Davoine, «Numerical growth of emittance in simulations of laser-wakefield acceleration», *Phys. Rev. ST Accel. Beams*, vol. 16, p. 021 301, 2 Feb. 2013. DOI: 10.1103/PhysRevSTAB.16.021301. [Online]. Available: https://link.aps.org/doi/10.1103/PhysRevSTAB.16.021301.

[163] J. D. Jackson, *Classical Electrodynamics*, 3rd ed. New York: Wiley, 1999, ISBN: 978-0-471-30932-1.

[164] M. S. Bloom, M. J. V. Streeter, S. Kneip *et al.*, «Bright x-ray radiation from plasma bubbles in an evolving laser wakefield accelerator», *Phys. Rev. Accel. Beams*, vol. 23, p. 061 301, 6 Jun. 2020. DOI: 10.1103/PhysRevAccelBeams.23.061301. [Online]. Available: https://link.aps.org/doi/10.1103/PhysRevAccelBeams.23.061301.

[165] R. Pausch, A. Debus, A. Huebl *et al.*, «Quantitatively consistent computation of coherent and incoherent radiation in particle-in-cell codes—a general form factor formalism for macro-particles», *Nuclear Instruments and Methods in Physics Research Section A: Accelerators, Spectrometers, Detectors and Associated Equipment*, vol. 909, pp. 419–422, 2018, 3rd European Advanced Accelerator Concepts workshop (EAAC2017), ISSN: 0168-9002. DOI: https:

//doi.org/10.1016/j.nima.2018.02.020. [Online]. Available: https://www.sciencedirect.com/science/article/pii/S0168900218301748.

[166] Central Laser Facility, Rutherford Appleton Laboratory, *Introducing the extreme photonics applications centre*, 2023. [Online]. Available: https://www.clf.stfc.ac.uk/Pages/EPAC-introduction-page.aspx.

[167] A. M. Wojtusiak, J. Phillips, J. Smith *et al.*, «Extreme photonics applications centre: high energy DPSSL pump for a 10 Hz PW-level laser», in *High-power, High-energy Lasers and Ultrafast Optical Technologies*, P. Bakule, C. L. Haefner, J. Hein and T. J. Butcher, Eds., International Society for Optics and Photonics, vol. 12577, SPIE, 2023, p. 1 257 707. DOI: 10.1117/12.2665736. [Online]. Available: https://doi.org/10.1117/12.2665736.

[168] V. Horný, J. Nejdl, M. Kozlová *et al.*, «Temporal profile of betatron radiation from laser-driven electron accelerators», *Physics of Plasmas*, vol. 24, no. 6, p. 063 107, 2017. DOI: 10.1063/1.4985687. eprint: https://doi.org/10.1063/1.4985687. [Online]. Available: https://doi.org/10.1063/1.4985687.

[169] J. L. Martins, S. F. Martins, R. A. Fonseca and L. O. Silva, «Radiation post-processing in pic codes», in *Harnessing Relativistic Plasma Waves as Novel Radiation Sources from Terahertz to X-Rays and Beyond*, D. A. Jaroszynski and A. Rousse, Eds., International Society for Optics and Photonics, vol. 7359, SPIE, 2009, p. 73590V. DOI: 10.1117/12.820736. [Online]. Available: https://doi.org/10.1117/12.820736.

[170] A. G. R. Thomas, «Algorithm for calculating spectral intensity due to charged particles in arbitrary motion», *Phys. Rev. ST Accel. Beams*, vol. 13, p. 020 702, 2 Feb. 2010. DOI: 10.1103/PhysRevSTAB.13.020702. [Online]. Available: https://link.aps.org/doi/10.1103/PhysRevSTAB.13.020702.

[171] M. Chen, E. Esarey, C. G. R. Geddes *et al.*, «Modeling classical and quantum radiation from laser-plasma accelerators», *Phys. Rev. ST Accel. Beams*, vol. 16, p. 030 701, 3 Mar. 2013. DOI: 10.1103/PhysRevSTAB.16.030701. [Online]. Available: https://link.aps.org/doi/10.1103/PhysRevSTAB.16.030701.

[172] May 1996. [Online]. Available: https://physics.nist.gov/PhysRefData/XrayMassCoef/chap2.html.

[173] May 1996. [Online]. Available: https://www.nist.gov/pml/x-ray-mass-attenuation-coefficients.

[174] S. Fourmaux, S. Corde, K. T. Phuoc *et al.*, «Demonstration of the synchrotron-type spectrum of laser-produced betatron radiation», *New Journal of Physics*, vol. 13, no. 3, p. 033 017, Mar. 2011. DOI: 10.1088/1367-2630/13/3/033017. [Online]. Available: https://dx.doi.org/10.1088/1367-2630/13/3/033017.

[175] K. Snelgrove, *Epac installation update june 2023*, Jun. 2023. [Online]. Available: https://www.clf.stfc.ac.uk/Pages/EPAC-Installation-update-June-2023.aspx.

[176] D. H. Froula, C. E. Clayton, T. Döppner *et al.*, «Measurements of the critical power for self-injection of electrons in a laser wakefield accelerator», *Phys. Rev. Lett.*, vol. 103, p. 215 006, 21 Nov. 2009. DOI: 10.1103/PhysRevLett.103.215006. [Online]. Available: https://link.aps.org/doi/10.1103/PhysRevLett.103.215006.

[177] S. P. D. Mangles, A. G. R. Thomas, C. Bellei *et al.*, «Self-guided wakefield experiments driven by petawatt-class ultrashort laser pulses», *IEEE Transactions on Plasma Science*, vol. 36, no. 4, pp. 1715–1721, 2008. DOI: 10.1109/TPS.2008.2000961.

[178] S. Banerjee, S. Y. Kalmykov, N. D. Powers *et al.*, «Stable, tunable, quasi-monoenergetic electron beams produced in a laser wakefield near the threshold for self-injection», *Phys. Rev. ST Accel. Beams*, vol. 16, p. 031 302, 3 Mar. 2013. DOI: 10.1103/PhysRevSTAB.16.031302. [Online]. Available: https://link.aps.org/doi/10.1103/PhysRevSTAB.16.031302.

[179] M. C. Kaluza, H.-P. Schlenvoigt, S. P. D. Mangles *et al.*, «Measurement of magnetic-field structures in a laser-wakefield accelerator», *Phys. Rev. Lett.*, vol. 105, p. 115 002, 11 Sep. 2010. DOI: 10.1103/PhysRevLett.105.115002. [Online]. Available: https://link.aps.org/doi/10.1103/PhysRevLett.105.115002.

[180] K. T. Phuoc, S. Corde, R. Shah *et al.*, «Imaging electron trajectories in a laser-wakefield cavity using betatron x-ray radiation», *Phys. Rev. Lett.*, vol. 97, p. 225 002, 22 Nov. 2006. DOI: 10.1103/PhysRevLett.97.225002. [Online]. Available: https://link.aps.org/doi/10.1103/PhysRevLett.97.225002.

[181] R. J. Shalloo, S. J. D. Dann, J.-N. Gruse *et al.*, «Automation and control of laser wakefield accelerators using bayesian optimization», *Nature Communications*, vol. 11, no. 1, p. 6355, Dec. 2020, ISSN: 2041-1723. DOI: 10.1038/s41467-020-20245-6. [Online]. Available: https://doi.org/10.1038/s41467-020-20245-6.

[182] S. J. D. Dann, C. D. Baird, N. Bourgeois *et al.*, «Laser wakefield acceleration with active feedback at 5 hz», *Phys. Rev. Accel. Beams*, vol. 22, p. 041 303, 4 Apr. 2019. DOI: 10.1103/PhysRevAccelBeams.22.041303. [Online]. Available: https://link.aps.org/doi/10.1103/PhysRevAccelBeams.22.041303.

[183] A. Döpp, C. Eberle, S. Howard, F. Irshad, J. Lin and M. Streeter, «Data-driven science and machine learning methods in laser–plasma physics», *High Power Laser Science and Engineering*, vol. 11, e55, 2023. DOI: 10.1017/hpl.2023.47.

[184] M. J. V. Streeter, C. Colgan, C. C. Cobo *et al.*, «Laser wakefield accelerator modelling with variational neural networks», *High Power Laser Science and Engineering*, vol. 11, e9, 2023. DOI: 10.1017/hpl.2022.47.

[185] R. Lehe, M. Kirchen, I. A. Andriyash, B. B. Godfrey and J.-L. Vay, «A spectral, quasi-cylindrical and dispersion-free particle-in-cell algorithm», *Computer Physics Communications*, vol. 203, pp. 66–82, 2016, ISSN: 0010-4655. DOI: https://doi.org/10.1016/j.cpc.2016.02.007. [Online]. Available: https://www.sciencedirect.com/science/article/pii/S0010465516300224.

[186] J.-C. Diels and W. Rudolph, *Ultrashort Laser Pulse Phenomena*, 2nd ed. Amsterdam: Elsevier Amsterdam, 2006.

[187] C. E. Rasmussen and C. K. I. Williams, *Gaussian Processes for Machine Learning*. The MIT Press, Nov. 2005, ISBN: 9780262256834. DOI: 10.7551/mitpress/3206.001.0001. [Online]. Available: https://doi.org/10.7551/mitpress/3206.001.0001.

[188] Scikit-Learn Developers, *Gaussian processes*, 2023. [Online]. Available: https://scikit-learn.org/stable/modules/gaussian_process.html (visited on 27/06/2023).

[189] A. Irman, J. P. Couperus, A. Debus *et al.*, «Improved performance of laser wakefield acceleration by tailored self-truncated ionization injection», *Plasma Physics and Controlled Fusion*, vol. 60, no. 4, p. 044 015, Mar. 2018. DOI: 10.1088/1361-6587/aaaef1. [Online]. Available: https://dx.doi.org/10.1088/1361-6587/aaaef1.

[190] M.-W. Lin, C.-Y. Hsieh, D. K. Tran and S.-H. Chen, «Simulation study of ionization-induced injection in sub-terawatt laser wakefield acceleration», *Physics of Plasmas*, vol. 27, no. 1, p. 013 102, Jan. 2020, ISSN: 1070-664X. DOI: 10.1063/1.5129483. eprint: https://pubs.aip.org/aip/pop/article-pdf/doi/10.1063/1.5129483/16025011/013102_1_online.pdf. [Online]. Available: https://doi.org/10.1063/1.5129483.

[191] S. Bohlen, J. C. Wood, T. Brümmer *et al.*, «Stability of ionization-injection-based laser-plasma accelerators», *Phys. Rev. Accel. Beams*, vol. 25, p. 031 301, 3 Mar. 2022. DOI: 10.1103/PhysRevAccelBeams.25.031301. [Online]. Available: https://link.aps.org/doi/10.1103/PhysRevAccelBeams.25.031301.

[192] M. Backhouse, «Measurement and optimisation of beam quality from laser wakefield accelerators», Available at https://spiral.imperial.ac.uk/handle/10044/1/105539, PhD thesis, Imperial College London, London, UK, Dec. 2022.

[193] J. Cole, «Diagnosis and application of laser wakefield accelerators», Available at https://spiral.imperial.ac.uk/handle/10044/1/42222, PhD thesis, Imperial College London, London, UK, Apr. 2016.

[194] P. S. Salter and M. J. Booth, «Adaptive optics in laser processing», *Light: Science & Applications*, vol. 8, no. 1, p. 110, Nov. 2019, ISSN: 2047-7538. DOI: 10.1038/s41377-019-0215-1. [Online]. Available: https://doi.org/10.1038/s41377-019-0215-1.

[195] R. B. M. Santarsiero D. Aiello and S. Vicalvi, «Focusing of axially symmetric flattened gaussian beams», *Journal of Modern Optics*, vol. 44, no. 3, pp. 633–650, 1997. DOI: 10.1080/09500349708232927. eprint: https://doi.org/10.1080/09500349708232927. [Online]. Available: https://doi.org/10.1080/09500349708232927.

[196] Y. Glinec, J. Faure, A. Guemnie-Tafo *et al.*, «Absolute calibration for a broad range single shot electron spectrometer», *Review of Scientific Instruments*, vol. 77, no. 10, p. 103 301, Oct. 2006, ISSN: 0034-6748. DOI: 10.1063/1.2360988. eprint: https://pubs.aip.org/aip/rsi/article-pdf/doi/10.1063/1.2360988/11169366/103301_1_online.pdf. [Online]. Available: https://doi.org/10.1063/1.2360988.

[197] A. Buck, K. Zeil, A. Popp *et al.*, «Absolute charge calibration of scintillating screens for relativistic electron detection», *Review of Scientific Instruments*, vol. 81, no. 3, p. 033 301, Mar. 2010, ISSN: 0034-6748. DOI: 10.1063/1.3310275. eprint: https://pubs.aip.org/aip/rsi/article-pdf/doi/10.1063/1.3310275/15782664/033301_1_online.pdf. [Online]. Available: https://doi.org/10.1063/1.3310275.

[198] Nov. 2023. [Online]. Available: https://thinklucid.com/product/atlas-2-8-mp-imx421/.

[199] Feb. 2020. [Online]. Available: https://thinklucid.com/tech-briefs/camera-sensor-review/.

[200] J. Dziedzic and M. Inglot, «Ultrathin glass for the photovoltaic applications», *Acta Physica Polonica A*, vol. 132, pp. 176–178, Jul. 2017. DOI: 10.12693/APhysPolA.132.176.

[201] O. Kononenko, N. Lopes, J. Cole *et al.*, «2d hydrodynamic simulations of a variable length gas target for density down-ramp injection of electrons into a laser wakefield accelerator», *Nuclear Instruments and Methods in Physics Research Section A: Accelerators, Spectrometers, Detectors and Associated Equipment*, vol. 829, pp. 125–129, 2016, 2nd European Advanced Accelerator Concepts Workshop - EAAC 2015, ISSN: 0168-9002. DOI: https://doi.org/10.1016/j.nima.2016.03.104. [Online]. Available: https://www.sciencedirect.com/science/article/pii/S0168900216301498.

[202] N. Barov, J. B. Rosenzweig, M. E. Conde, W. Gai and J. G. Power, «Observation of plasma wakefield acceleration in the underdense regime», *Phys. Rev. ST Accel. Beams*, vol. 3, p. 011 301, 1 Jan. 2000. DOI: 10.1103/PhysRevSTAB.3.011301. [Online]. Available: https://link.aps.org/doi/10.1103/PhysRevSTAB.3.011301.

[203] P. Muggli and M. J. Hogan, «Review of high-energy plasma wakefield experiments», *Comptes Rendus Physique*, vol. 10, no. 2, pp. 116–129, 2009, Laser acceleration of particles in plasma, ISSN: 1631-0705. DOI: https://doi.org/10.1016/j.crhy.2009.03.004. [Online]. Available: https://www.sciencedirect.com/science/article/pii/S1631070509000383.

[204] T. Miyatake, K. Shiokawa, H. Sakaki *et al.*, «Denoising application for electron spectrometer in laser-driven ion acceleration using a simulation-supervised learning based cdae», *Nuclear Instruments and Methods in Physics Research Section A: Accelerators, Spectrometers, Detectors and Associated Equipment*, vol. 999, p. 165 227, 2021, ISSN: 0168-9002. DOI: https://doi.org/10.1016/j.nima.2021.165227. [Online]. Available: https://www.sciencedirect.com/science/article/pii/S0168900221002114.

[205] A. Kumar and S. S. Sodhi, «Comparative analysis of gaussian filter, median filter and denoise autoenocoder», in *2020 7th International Conference on Computing for Sustainable Global Development (INDIACom)*, 2020, pp. 45–51. DOI: 10.23919/INDIACom49435.2020.9083712.

[206] D. S. Simon, *A Guided Tour of Light Beams* (2053-2571). Morgan and Claypool Publishers, 2016, ISBN: 978-1-6817-4437-7. DOI: 10.1088/978-1-6817-4437-7. [Online]. Available: https://dx.doi.org/10.1088/978-1-6817-4437-7.

A. General Definitions and Equations

A.1 Normalised Parameters

The interaction of a laser pulse with a plasma and the motion of charged particles in plasma are often described in terms of normalised parameters. These quantities are defined in Table A.1. They are normalised by constants such as the particle's mass, m, the particle's charge, q, and the speed of light in vacuum, c.

Table A.1: Normalised Parameters used in Laser-Plasma Calculations

Original Quantity	Normalised Quantity	Definition
Electromagnetic Vector Potential ($\mathbf{A}$)	$\mathbf{a}$	$\mathbf{a} = \frac{q\mathbf{A}}{mc}$
Electromagnetic Scalar Potential (ϕ)	Φ	$\Phi = \frac{q\phi}{mc^2}$
Particle Velocity ($\mathbf{v}$)	$\boldsymbol{\beta}$	$\boldsymbol{\beta} = \frac{\mathbf{v}}{c}$
Particle Kinetic Momentum ($\mathbf{p}$)	$\mathbf{P}$	$\mathbf{P} = \frac{\mathbf{p}}{mc}$

A.2 Maxwell's Equations

Maxwell's equations form the basis of the theory of electromagnetism. They describe the spatial structure and time evolution of electric and magnetic fields due to charges, currents and nonzero rates of change in the fields in the considered system [163].

Gauss' Law

Gauss' law relates the electric field originating from an object to its charge density. In its differential form, Gauss' law states that at a given position near the object the flux density of the electric field, denoted by its divergence, is directly proportional to its charge density [163]:

$$\nabla \cdot \mathbf{E} = \frac{\rho}{\epsilon_0}, \tag{A.1}$$

where $\mathbf{E}$ is the electric field, ρ is the charge density distribution in the object and ϵ_0 is the permittivity of free space.

Faraday's Law

Faraday's law relates the electric field induced by a change of a magnetic field over time. In differential form, the curl of the electric field is equal to the negative rate of change of the magnetic field [163]:

$$\nabla \times \mathbf{E} = -\frac{\partial \mathbf{B}}{\partial t}, \tag{A.2}$$

where $\mathbf{B}$ is the magnetic field.

Ampère's Law

Ampère's law describes the magnetic field induced by a current density or a change in electric field over time. Ampère's law in differential form relates the curl of the magnetic field to the rate of change of the electric field and the current density [163]:

$$\nabla \times \mathbf{B} = \mu_0 \mathbf{j} + \frac{1}{c^2}\frac{\partial \mathbf{E}}{\partial t}, \tag{A.3}$$

where $\mathbf{j}$ is the current density.

A.3 Electromagnetic Potentials

In the theory of electromagnetism, the potentials of an electromagnetic field are defined such that they are related to their fields by the following relations [163]:

$$\mathbf{E} = -\nabla\phi - \frac{\partial \mathbf{A}}{\partial t}, \tag{A.4}$$

$$\mathbf{B} = \nabla \times \mathbf{A}, \tag{A.5}$$

where ϕ is the scalar potential and $\mathbf{A}$ is the vector potential.

A.4 Poisson's Equation

A gauge invariance may exist for some electromagnetic fields, where different electromagnetic potentials produce the same electromagnetic field solutions. An example of this is for a monochromatic electromagnetic plane wave in vacuum. The potential of an electromagnetic wave can be written in the Coulomb gauge [163]: $\nabla \cdot \mathbf{A} = 0$. In the

Coulomb gauge, Gauss' law can be written in terms of the electromagnetic potential:

$$\nabla \cdot \mathbf{E} = \frac{\rho}{\epsilon_0} = \nabla \cdot \left(-\nabla\phi + \frac{d\mathbf{A}}{dt} \right) \tag{A.6}$$

$$= -\nabla^2\phi + \frac{d}{dt}\cancelto{0}{(\nabla \cdot \mathbf{A})}, \tag{A.7}$$

This expression for Gauss's law is known as Poisson's equation:

$$\nabla^2\phi = -\frac{\rho}{\epsilon_0}. \tag{A.8}$$

A.5 Continuity Equation

Ampère's law can be used to derive the continuity equation relating the flow of charge in or out of a system to the gradient in the current density. Taking the divergence of Ampère's law, given by Equation A.3,

$$\nabla \cdot (\nabla \times \mathbf{B}) = \nabla \cdot (\mu_0 \mathbf{j}) + \nabla \cdot \left(\frac{1}{c^2} \frac{\partial \mathbf{E}}{\partial t} \right). \tag{A.9}$$

As the divergence of the curl of any vector field is equal to zero,

$$0 = \mu_0 \big(\nabla \cdot \mathbf{j} \big) + \frac{1}{c^2} \frac{\partial}{\partial t} \big(\nabla \cdot \mathbf{E} \big). \tag{A.10}$$

Recalling Gauss' law, given by Equation A.1, the divergence of the electric field is equal to the enclosed charge density divided by the permittivity of free space. Equation A.1 is substituted into Equation A.10:

$$0 = \mu_0 \big(\nabla \cdot \mathbf{j} \big) + \frac{1}{\epsilon_0 c^2} \frac{\partial \rho}{\partial t}. \tag{A.11}$$

The equation for the speed of light, $c = \frac{1}{\sqrt{\epsilon_0 \mu_0}}$, where μ_0 is the permeability of free space, can be used to further simplify this expression:

$$0 = \cancel{\mu_0} \left(\nabla \cdot \mathbf{j} + \frac{\partial \rho}{\partial t} \right). \tag{A.12}$$

This produces the continuity equation for any electromagnetic system, given by Equation A.13 [163]:

$$\nabla \cdot \mathbf{j} + \frac{\partial \rho}{\partial t} = 0. \tag{A.13}$$

This equation expresses the conservation of charge locally in a system. A gradient in the current flowing in or out of a point in the system corresponds to an increase or decrease in the charge density at that point, respectively.

B. Single Charged Particle Interactions with Electromagnetic Waves

B.1 Lagrangian of a Relativistic Charged Particle in an Electromagnetic Potential

The Lagrangian for a relativistic charged particle in an electromagnetic potential can be derived by considering the Lorentz force on the particle. If there are no other external forces acing on the particle, then the net force on the particle is given by the Lorentz force. According to Newton's second law of motion, the net force on a particle is equal to the rate of change of its kinetic momentum:

$$\mathbf{F} = \frac{d\mathbf{p}}{dt} = q(\mathbf{E} + \mathbf{v} \times \mathbf{B}), \tag{B.1}$$

where F is the net force on the particle, $\mathbf{p}$ is its kinetic momentum and $\mathbf{v}$ is its velocity in the electromagnetic field. Equations A.4 and A.5 expressing the electromagnetic fields in terms of their vector and scalar potentials are substituted into Equation B.1:

$$\frac{d\mathbf{p}}{dt} = q\bigg(-\nabla\phi - \frac{\partial \mathbf{A}}{\partial t} + \mathbf{v} \times \nabla \times \mathbf{A}\bigg). \tag{B.2}$$

The triple vector product in this expression can be expressed using the following identity: $\mathbf{v} \times \nabla \times \mathbf{A} = \nabla(\mathbf{v} \cdot \mathbf{A}) - \mathbf{A}(\mathbf{v} \cdot \nabla)$. This is then substituted to Equation B.2:

$$\frac{d\mathbf{p}}{dt} = q\bigg(-\nabla\phi - \frac{\partial \mathbf{A}}{\partial t} + \nabla(\mathbf{v} \cdot \mathbf{A}) - \mathbf{A}(\mathbf{v} \cdot \nabla)\bigg). \tag{B.3}$$

The partial time derivative of the vector potential is now expressed in terms of its full time derivative. Because the vector potential is a function of position and time,

$$\frac{d\mathbf{A}}{dt} = \frac{\partial \mathbf{A}}{\partial \mathbf{r}}\frac{\partial \mathbf{r}}{\partial t} + \frac{\partial \mathbf{A}}{\partial t}. \tag{B.4}$$

Writing $\nabla = \frac{\partial}{\partial \mathbf{r}}$ and $\mathbf{v} = \frac{\partial \mathbf{r}}{\partial t}$, the full time derivative of the vector potential is thus expressed in terms of the differential operator and the particle velocity:

$$\frac{d\mathbf{A}}{dt} = (\mathbf{v} \cdot \nabla)\mathbf{A} + \frac{\partial \mathbf{A}}{\partial t}. \tag{B.5}$$

Rearranging Equation B.5, the partial time derivative of the vector potential is substituted into Equation B.3, producing a simplified expression for the Lorentz force in terms of the electromagnetic potentials:

$$\frac{d\mathbf{p}}{dt} = q\bigg(-\nabla\phi - \frac{d\mathbf{A}}{dt} + \cancel{(\mathbf{v} \cdot \nabla)\mathbf{A}} + \nabla(\mathbf{v} \cdot \mathbf{A}) - \cancel{(\mathbf{v} \cdot \nabla)\mathbf{A}} \bigg). \tag{B.6}$$

An equation of motion is produced that is of the form of the Euler-Lagrange equation:

$$\frac{d}{dt}(\mathbf{p} + q\mathbf{A}) = q\nabla(-\phi + \mathbf{v} \cdot \mathbf{A}). \tag{B.7}$$

The general expression for the Euler-Lagrange equation is given by Equation 2.1. The quantity in the time derivative on the left-hand side of Equation B.7 is the canonical momentum of the particle:

$$\frac{\partial L}{\partial \mathbf{v}} = \mathbf{p} + q\mathbf{A}. \tag{B.8}$$

The relativistic kinetic momentum of the particle is expressed in terms of its velocity: $\mathbf{p} = \gamma m \mathbf{v}$, where $\gamma = 1/\sqrt{1 - v^2/c^2}$ is the relativistic gamma-factor of the particle. Substituting this definition into the canonical momentum,

$$\frac{\partial L}{\partial \mathbf{v}} = \frac{m\mathbf{v}}{\sqrt{1 - \frac{v^2}{c^2}}} + q\mathbf{A}. \tag{B.9}$$

Comparing the right-hand side of Equation B.7 to the Euler-Lagrange equation, given by Equation 2.1,

$$\frac{\partial L}{\partial \mathbf{r}} = q\nabla(-\phi + \mathbf{v} \cdot \mathbf{A}). \tag{B.10}$$

Integrating Equations B.9 and B.10 with respect to the velocity and position vectors of the particle, respectively, produces two expressions for the Lagrangian of the system:

$$L_1 = \int \frac{\partial L}{\partial \mathbf{v}} d\mathbf{v} = -mc^2\sqrt{1 - \frac{v^2}{c^2}} + q(\mathbf{v} \cdot \mathbf{A}) + C_1(\mathbf{r}), \tag{B.11}$$

$$L_2 = \int \frac{\partial L}{\partial \mathbf{r}} d\mathbf{r} = -q\phi + q\mathbf{v} \cdot \mathbf{A} + C_2(\mathbf{v}). \tag{B.12}$$

To satisfy the Euler-Lagrange equation, $L = L_1 = L_2$. The constants of integration can be inferred by inspection to be $C_1(\mathbf{r}) = -q\phi$ and $C_2(\mathbf{v}) = -mc^2\sqrt{1 - v^2/c^2}$. This produces the expression for the Lagrangian of the relativistic (or subrelativistic)

charged particle in an electromagnetic potential:

$$L = -mc^2\sqrt{1 - \frac{v^2}{c^2}} + q(\mathbf{v} \cdot \mathbf{A}) - q\phi. \tag{B.13}$$

B.2 Ponderomotive Force

In section 2.2.2, the equation of motion for an electron in a plasma interacting with a laser pulse was derived from the Lagrangian for a charged particle in an electromagnetic potential. This equation was then expressed in terms of normalised units, as given in Appendix A.1:

$$\frac{d}{dt}(\mathbf{P} + \mathbf{a}) = c\nabla(-\Phi + \boldsymbol{\beta} \cdot \mathbf{a}). \tag{B.14}$$

Terms containing the scalar potential can be neglected by assuming that the duration of the laser pulse is much greater than its period: $\tau \gg T$, where τ is the FWHM duration of the laser pulse and T is its period of oscillation. Typically in an LWFA, $\tau \sim 10$ fs and $T \sim 1$ fs. The laser pulse can be approximated as a plane wave, whose potential can be written using the Coulomb gauge: $\nabla \cdot \mathbf{a} = 0$. As shown in Appendix A.4, Gauss' law can then be rewritten as Poisson's equation, which is given by Equation A.8. As there is zero charge density in the system, the plane wave has a scalar potential of $\Phi = 0$. This simplifies the equation of motion:

$$\frac{d}{dt}(\mathbf{P} + \mathbf{a}) = c\nabla(\boldsymbol{\beta} \cdot \mathbf{a}). \tag{B.15}$$

The time-averaged rate of change of canonical momentum of the electron interacting with the laser pulse is described by averaging this equation of motion over one period in the laser pulse:

$$\frac{1}{T}\int_{t_{start}}^{t_{start}+T} \frac{d\mathbf{u}}{dt}\, dt' = \frac{1}{T}\int_{t_{start}}^{t_{start}+T} \left(-\frac{c}{\gamma}\nabla\frac{\mathbf{a}^2}{2} + \frac{c}{\gamma}\mathbf{u} \cdot \nabla\mathbf{a} \right) dt', \tag{B.16}$$

where t' is the time in the laser pulse's oscillation. Equation B.16 describes the time-averaged rate of change of canonical momentum of the system. Evaluating the integrals in Equation B.16,

$$\left\langle \frac{d\mathbf{u}}{dt} \right\rangle = -\left\langle \frac{c}{\gamma}\nabla\frac{\mathbf{a}^2}{2} \right\rangle + \left[\frac{c}{\gamma}\nabla\langle\mathbf{a}\rangle \cdot \mathbf{u} \right]_{t_{start}}^{t_{start}+T} - \nabla\langle\mathbf{a}\rangle \cdot \int_{t_{start}}^{t_{start}+T} \frac{c}{\gamma}\frac{\partial\mathbf{u}}{\partial t}\, dt', \tag{B.17}$$

where time-averaged quantities are expressed in triangular brackets. When $\tau \gg T$, the time-average of the normalised potential over one period is zero: $\langle\mathbf{a}\rangle \approx 0$. The final two terms in Equation B.17 hence average to zero. The time-averaged rate of change of canonical momentum yields an expression for the time-averaged rate of

change of canonical momentum:

$$\left\langle \frac{d\mathbf{u}}{dt} \right\rangle = -\left\langle \frac{c}{\gamma} \nabla \frac{\mathbf{a}^2}{2} \right\rangle. \tag{B.18}$$

As $\mathbf{u} = \mathbf{P} + \mathbf{a}$,

$$\left\langle \frac{d\mathbf{u}}{dt} \right\rangle = \left\langle \frac{d\mathbf{P}}{dt} + \frac{d\mathbf{a}}{dt} \right\rangle \tag{B.19}$$

$$= \left\langle \frac{d\mathbf{P}}{dt} \right\rangle + \cancelto{0}{\left\langle \frac{d\mathbf{a}}{dt} \right\rangle} \tag{B.20}$$

$$= \left\langle \frac{d\mathbf{P}}{dt} \right\rangle \tag{B.21}$$

The time-averaged rate of change of canonical momentum therefore describes the net force on the electron. Equation B.22 is the ponderomotive force of the laser pulse acting on the electron:

$$\mathbf{F_p} = -\left\langle \frac{c}{\gamma} \nabla \frac{\mathbf{a}^2}{2} \right\rangle. \tag{B.22}$$

B.3 Charged Particle in an Electromagnetic Plane Wave

The equation of motion for a charged particle in an electromagnetic plane wave can be derived from the Lagrangian for a relativistic charged particle in an electromagnetic potential. This Lagrangian, given by Equation 2.6, is written in terms of the normalised parameters defined in Appendix A.1:

$$L = -\sqrt{1 - \boldsymbol{\beta}^2} + (\boldsymbol{\beta} \cdot \mathbf{a}) - \Phi. \tag{B.23}$$

The potential of an electromagnetic plane wave can be written in the Coulomb gauge, as shown in Appendix A.4. In the Coulomb gauge, Gauss' law can be written in terms of the scalar potential as Poisson's equation, given by Equation A.8. The plane wave is considered to propagate through vacuum. As there is no charge density in the system, Poisson's equation dictates that the scalar potential is zero: $\Phi = 0$. The Lagrangian is thus simplified:

$$L = -\sqrt{1 - \boldsymbol{\beta}^2} + (\boldsymbol{\beta} \cdot \mathbf{a}). \tag{B.24}$$

From this Lagrangian, equations of motion in terms of the vector potential of the plane wave are derived by relating the longitudinal and transverse momenta of the charged particle to its total energy and then the vector potential during the interaction. For a wave propagating in the z-direction, the transverse axes are the x-axis and y-axis.

Transverse Momentum

The directions of the electromagnetic vector potential of the wave is transverse to the direction of propagation. The transverse components of the canonical momentum of the particle are calculated from the Lagrangian:

$$u_{x,y} = \frac{\partial L}{\partial \beta_{x,y}} \tag{B.25}$$

$$= \frac{\beta_{x,y}}{\sqrt{1-\boldsymbol{\beta}^2}} + a_{x,y} \tag{B.26}$$

$$= \gamma\beta_{x,y} + a_{x,y} \tag{B.27}$$

$$= P_{x,y} + a_{x,y}. \tag{B.28}$$

This canonical momentum is conserved because the generalised force in the Euler-Lagrange equations equals zero:

$$\frac{du_x}{dt} = \frac{\partial L}{\partial x} = 0, \tag{B.29}$$

$$\frac{du_y}{dt} = \frac{\partial L}{\partial y} = 0, \tag{B.30}$$

This means that the canonical momentum of the particle interacting with the electromagnetic potential is zero throughout the interaction. Consequently,

$$P_{x,y} = -a_{x,y}. \tag{B.31}$$

This is a useful relation that is used at multiple stages in the derivation of the equations of motion for this system.

From its definition given by Equation B.32, the Hamiltonian is then expressed:

$$H = \frac{\partial L}{\partial \boldsymbol{\beta}} \cdot \boldsymbol{\beta} - L \tag{B.32}$$

$$= \boldsymbol{\beta} \cdot \mathbf{P} + \cancel{\boldsymbol{\beta} \cdot \mathbf{a}} + \sqrt{1-\beta^2} - \cancel{\boldsymbol{\beta} \cdot \mathbf{a}} \tag{B.33}$$

$$= \boldsymbol{\beta} \cdot \mathbf{P} + \gamma^{-1}. \tag{B.34}$$

Using the identities $\gamma = 1/\sqrt{1-\beta^2}$ and $\mathbf{P} = \gamma\boldsymbol{\beta}$ for the normalised quantities,

$$H = \beta^2\gamma + \gamma^{-1} \tag{B.35}$$

$$= \gamma(\beta^2 + \gamma^{-2}) \tag{B.36}$$

$$= \gamma(\cancel{\beta^2} + 1 - \cancel{\beta^2}) \tag{B.37}$$

$$H = \gamma. \tag{B.38}$$

This is result that will be used later to relate the rate of change of the Lagrangian to the rate of change of the relativistic γ-factor.

Hamiltonian of the Interaction

It has been shown from the Euler-Lagrange equations that the canonical momentum is constant and equal to zero. The rate of change of the Hamiltonian is then equal to the negative rate of change of the Lagrangian:

$$\frac{dH}{dt} = \frac{d}{dt}\left(\frac{\partial L}{\partial \boldsymbol{\beta}} \cdot \boldsymbol{\beta} - L\right) \tag{B.39}$$

$$= \boldsymbol{\beta} \cdot \cancelto{0}{\frac{d}{dt}\left(\frac{\partial L}{\partial \boldsymbol{\beta}}\right)} + \cancelto{0}{\frac{\partial L}{\partial \boldsymbol{\beta}} \cdot \frac{d\boldsymbol{\beta}}{dt}} - \frac{\partial L}{\partial t} \tag{B.40}$$

$$\frac{dH}{dt} = -\frac{\partial L}{\partial t}. \tag{B.41}$$

The time derivative of the Lagrangian is expressed in terms of a comoving coordinate:

$$\frac{\partial L}{\partial t} = \frac{\partial L}{\partial \xi}\frac{\partial \xi}{\partial t}, \tag{B.42}$$

where ξ is the comoving coordinate defined as $\xi = ct - z$. The comoving coordinate denotes the difference in the longitudinal coordinates of a considered phase point in the wave and the particle at some point in time. Normalising the comoving coordinate by the wavelength of the plane wave such that $\xi = \lambda^{-1}(ct - z)$, where λ is the wavelength, then

$$\frac{\partial \xi}{\partial t} = \frac{c}{\lambda} = f, \tag{B.43}$$

where f is the frequency of the wave. Substituting this expression into Equation B.42 and then Equation B.41,

$$\frac{dH}{dt} = -\frac{\partial L}{\partial t} = -f\frac{\partial L}{\partial \xi}. \tag{B.44}$$

Recalling Equation B.38, $\frac{dH}{dt} = \frac{d\gamma}{dt}$, which can be substituted into Equation B.41:

$$-f\frac{\partial L}{\partial \xi} = \frac{d\gamma}{dt}. \tag{B.45}$$

This is a relation that will later be used to relate the rate of change of the relativistic γ-factor to the kinetic momentum of the particle.

Longitudinal Momentum

The motion of the particle in the longitudinal direction is now considered. The relations of the longitudinal and transverse momenta of the particle to its relativistic γ-factor

are used to derive the equations of motion in both directions. The Euler-Lagrange equation is first written in terms of normalised units by multiplying by c:

$$\frac{d}{dt}\left(\frac{\partial L}{\partial \beta_z}\right) - c\frac{\partial L}{\partial z} = 0. \tag{B.46}$$

Then, the spatial derivative of the Lagrangian is changed to be with respect to the normalised comoving coordinate, as in the previous part of the derivation:

$$\frac{\partial L}{\partial z} = \frac{\partial L}{\partial \xi}\frac{\partial \xi}{\partial z} \tag{B.47}$$

$$= \frac{\partial L}{\partial \xi}\frac{\partial}{\partial z}\left(\lambda^{-1}(ct - z)\right) \tag{B.48}$$

$$= -\lambda^{-1}\frac{\partial L}{\partial \xi}. \tag{B.49}$$

Substituting this into the normalised Euler-Lagrange equation, with $f = c/\lambda$,

$$\frac{d}{dt}\left(\frac{\partial L}{\partial \beta_z}\right) + f\frac{\partial L}{\partial \xi} = 0. \tag{B.50}$$

The longitudinal canonical momentum is first evaluated, remembering that longitudinal component of the electromagnetic potential is zero:

$$\frac{\partial L}{\partial \beta_z} = \frac{\beta_z}{\sqrt{1 - \boldsymbol{\beta}^2}} + \cancelto{0}{a_z} \tag{B.51}$$

$$= \gamma\beta_z \tag{B.52}$$

$$= P_z. \tag{B.53}$$

Applying this to the normalised Euler-Lagrange equation,

$$-f\frac{\partial L}{\partial \xi} = \frac{dP_z}{dt}. \tag{B.54}$$

The term on the left-hand side of this equation is the generalised force in the longitudinal direction on the particle, which is the same quantity that is described in Equation B.45. Subtracting Equation B.54 from Equation B.45,

$$\frac{d}{dt}(\gamma - P_z) = 0. \tag{B.55}$$

Throughout the interaction, the difference in the relativistic γ-factor and the longitudinal kinetic momentum of the particle is equal to its initial value. As the particle was initially stationary, the starting values of the parameters are $P_z = 0$ and $\gamma = 1$. This

value is constant during the interaction:

$$\gamma - P_z = 1. \tag{B.56}$$

Relating the Longitudinal and Transverse Momenta

The longitudinal and transverse momenta of the particle can then be related by taking the square of Equation B.55:

$$\gamma^2 = (1 + P_z)^2 \tag{B.57}$$

$$= 1 + 2P_z + P_z^2. \tag{B.58}$$

When the total energy and total momentum of the particle are normalised by the rest mass energy, $\gamma^2 = 1+P^2$, where P is the total momentum. This quantity is expressed in terms of the particle's momentum components:

$$\gamma^2 = 1 + P_x^2 + P_y^2 + P_z^2. \tag{B.59}$$

Equations B.58 and B.59 can be treated as a pair of simultaneous equations. Their subtraction from one another produces a relation for the momentum components: $P_z = \frac{P_x^2+P_y^2}{2}$. Because the transverse momenta are equal to their respective electromagnetic potential components, as given in Equation B.31, the components of the momentum and electromagnetic potential can be related:

$$P_z = \frac{a_x^2 + a_y^2}{2} \tag{B.60}$$

As $a^2 = a_x^2 + a_y^2$,

$$P_z = \frac{a^2}{2}. \tag{B.61}$$

Similarly, for the transverse momentum,

$$P_r = \sqrt{P_x^2 + P_y^2} \tag{B.62}$$

$$= \sqrt{a_x^2 + a_y^2} \tag{B.63}$$

$$P_r = a. \tag{B.64}$$

For electromagnetic waves with weak potentials, $a < 1$, the momentum of the electron is directed more closely in the transverse direction. For waves with stronger potentials, $a > 1$, the longitudinal momentum component dominates. This is confirmed by the solutions to the equations of motion of the electron, which are derived in Section 2.2.1.

Equations of Motion

The longitudinal and transverse equations of motion for the interaction are derived by equating the momenta expressed in Equations B.61 and B.64 as first order derivatives of time. These derivatives are transformed to become derivatives of the non-normalised comoving coordinate, $\xi = ct - z$. To perform this procedure, the following identity is needed, which is derived using Equation B.56:

$$\frac{\gamma}{c}\frac{d\xi}{dt} = \frac{\gamma}{c}\frac{d}{dt}(ct - z) \tag{B.65}$$

$$= \frac{\gamma}{c}(c - v_z) \tag{B.66}$$

$$= \gamma - \gamma\beta_z \tag{B.67}$$

$$= \gamma - p_z = 1. \tag{B.68}$$

Following the procedure for both the longitudinal and transverse momenta,

$$P_z = \gamma\beta_z = \frac{\gamma}{c}\frac{dz}{dt} \tag{B.69}$$

$$= \frac{\gamma}{c}\frac{dz}{d\xi}\frac{d\xi}{dt} \tag{B.70}$$

$$= \frac{dz}{d\xi}. \tag{B.71}$$

$$P_r = \gamma\beta_r = \frac{\gamma}{c}\frac{dr}{dt} \tag{B.72}$$

$$= \frac{\gamma}{c}\frac{d\xi}{dt}\frac{dr}{d\xi} \tag{B.73}$$

$$= \frac{dr}{d\xi}, \tag{B.74}$$

Using Equations B.61 and B.64, the equations of motion of the electron are then related to the potential:

$$\frac{dz}{d\xi} = \frac{a^2}{2}, \tag{B.75}$$

$$\frac{dr}{d\xi} = a. \tag{B.76}$$

These are the equations of motion describing a charged particle in the potential of an electromagnetic plane wave.

C. Laser-Plasma Interactions

C.1 Electromagnetic Wave Equation in Plasma

The wave equation for an electromagnetic wave in plasma is derived from Faraday's law and Ampère's law, which are introduced in Appendix A.2. Taking the curl of Faraday's law,

$$\nabla \times (\nabla \times \mathbf{E}) = -\frac{\partial}{\partial t}(\nabla \times \mathbf{B}). \tag{C.1}$$

Using the vector identity $\nabla \times (\nabla \times \mathbf{E}) = \nabla^2\mathbf{E} - \nabla(\nabla \cdot \mathbf{E})$, Equation C.1 can be simplified. The second term on the right-hand side of this identity contains the divergence of the electric field, which can be calculated using Gauss' law. Although the electromagnetic wave displaces electrons in the plasma, there is zero net charge in the plasma. Thus, the term for the divergence of the electric field is equal to zero:

$$\nabla^2\mathbf{E} - \cancelto{0}{\nabla(\nabla \cdot \mathbf{E})} = \frac{\partial}{\partial t}(\nabla \times \mathbf{B}). \tag{C.2}$$

The term on the right-hand side of Equation C.2 is the partial time derivative of the curl of the magnetic field. This quantity can also be expressed by taking the partial time derivative of Ampère's law:

$$\frac{\partial}{\partial t}(\nabla \times \mathbf{B}) = \mu_0 \frac{\partial \mathbf{j}}{\partial t} + \frac{1}{c^2}\frac{\partial^2 \mathbf{E}}{\partial t^2}. \tag{C.3}$$

Equating Equations C.2 and C.3 produces the wave equation for an electromagnetic wave in plasma:

$$\nabla^2\mathbf{E} = \mu_0 \frac{\partial \mathbf{j}}{\partial t} + \frac{1}{c^2}\frac{\partial^2 \mathbf{E}}{\partial t^2}. \tag{C.4}$$

C.2 Dispersion Relation for an Electromagnetic Wave in Plasma

The dispersion relation is derived by considering an electromagnetic plane wave in plasma: $E_x = E_0 e^{i(kz-\omega t)}$, where E_0 is the amplitude of the electric field of the wave,

k is its wavenumber and ω is its angular frequency. In this case, the wave propagates along the z-axis and is polarised in the x-axis. An electron in the plasma is accelerated in the direction of the electric field vector of the wave. Using Newton's second law of motion to express the force exerted by the electric field on the electron, an expression for its acceleration is obtained in the sub-relativistic limit:

$$\frac{\partial v_x}{\partial t} = -\frac{eE_x}{m_e}, \tag{C.5}$$

where v_x is the speed of the electron in the x-direction. The motion of the electron produces a current in the plasma in the same direction as the electric field and can be expressed as $j_x = -n_e e v_x$, where n_e is the number density of electrons in the plasma. Taking the partial time derivative of the current density allows the acceleration of the electron to be related to the current density:

$$\frac{\partial j_x}{\partial t} = -n_e e \frac{\partial v_x}{\partial t}. \tag{C.6}$$

Equation C.5 is then substituted into Equation C.6, expressing the plasma response term in the wave equation:

$$\frac{\partial j_x}{\partial t} = \frac{n_e e^2}{m_e} E_x. \tag{C.7}$$

Substituting this into the wave equation, given by Equation C.4,

$$\nabla^2 E_x = \mu_0 \frac{n_e e^2}{m_e} E_x + \frac{1}{c^2} \frac{\partial^2 E_x}{\partial t^2}. \tag{C.8}$$

This expression can be re-written in terms of the plasma frequency, which is the natural frequency at which electrons oscillate in the plasma. The equation defining the plasma frequency is derived in Appendix C.3 and given by Equation C.18. Also using the relation $c = \frac{1}{\sqrt{\epsilon_0 \mu_0}}$, the resulting wave equation is expressed in Equation C.8:

$$\nabla^2 E_x = \frac{1}{c^2} \omega_p^2 E_x + \frac{1}{c^2} \frac{\partial^2 E_x}{\partial t^2}. \tag{C.9}$$

Substituting the equation for the electric field of the electromagnetic plane wave into this wave equation and performing the differentiations of the electric field produces the dispersion relation for an electromagnetic wave in plasma:

$$c^2 k^2 = \omega^2 - \omega_p^2. \tag{C.10}$$

C.3 Plasma Frequency

When an electron is displaced by a small distance in a plasma, the ions remain stationary owing to their greater mass. The charge separation leaves behind a charge density of $\rho = en_e$. The electrostatic potential produced by this charge density is given by Poisson's equation:

$$\nabla^2\phi = -\frac{\rho}{\epsilon_0}, \tag{C.11}$$

$$= -\frac{n_e e}{\epsilon_0}, \tag{C.12}$$

where ϕ is the scalar potential of the electric field. Solving this equation for the electric scalar potential,

$$\phi = -\frac{en_e}{2\epsilon_0}x^2, \tag{C.13}$$

assuming that the electron has been displaced in the x-direction. The equation of motion for the electron can then be derived from the Lagrangian for a relativistic electron in an electric potential. From Equation 2.6,

$$L = -m_e c^2\sqrt{1-\frac{v^2}{c^2}} - e\phi, \tag{C.14}$$

where v is the speed of the particle. Substituting this Lagrangian into the Euler-Lagrange equation, given by Equation 2.1,

$$\frac{d}{dt}\left(\frac{m_e v}{\sqrt{1-\frac{v^2}{c^2}}}\right) = -\frac{e^2 n_e}{\epsilon_0}x. \tag{C.15}$$

As the relativistic gamma-factor of the electron is given by $\gamma = 1/\sqrt{1-v^2/c^2}$,

$$\frac{d(\gamma v)}{dt} = -\frac{n_e e^2}{m_e\epsilon_0}x. \tag{C.16}$$

In the subrelativistic limit where $\gamma \approx 1$, this equation simplifies. Then, as $\frac{dv}{dt} = \frac{d^2x}{dt^2}$, this equation becomes a simple harmonic equation of motion:

$$\frac{d^2x}{dt^2} = -\frac{n_e e^2}{m_e\epsilon_0}x. \tag{C.17}$$

An electron is thus expected to oscillate about its equilibrium position from which it was displaced. The characteristic frequency of oscillation is the plasma frequency:

$$\omega_p = \sqrt{\frac{n_e e^2}{m_e\epsilon_0}}. \tag{C.18}$$

C.4 Nonlinear Refractive Index of a Plasma

When electrons in the plasma are moving at relativistic speeds, the refractive index of the plasma is expressed in terms of the relativistic plasma frequency:

$$\eta = \sqrt{1 - \frac{\omega_p^2}{\gamma\omega^2}}. \tag{C.19}$$

An approximate expression for the refractive index can be obtained by performing the Taylor series expansion of Equation C.19 with respect to the plasma frequency:

$$\eta \approx 1 - \frac{\omega_p^2}{2\gamma\omega^2}. \tag{C.20}$$

Equation B.56, derived in Appendix B.3, expresses the relativistic γ-factor of an electron in an electromagnetic plane wave in terms of its longitudinal momentum component. Using Equation B.61, also derived in Appendix B.3, the relativistic γ-factor is expressed in terms of the normalised potential of the electromagnetic wave:

$$\gamma = 1 + \frac{1}{2}a^2. \tag{C.21}$$

As this electromagnetic potential describes an electromagnetic plane wave, the time-average of the squared potential is just equal to half of the square of the potential's amplitude: $\langle a^2 \rangle = \frac{1}{2}a_0^2$. The time-averaged relativistic γ-factor is expressed in terms of the normalised potential amplitude:

$$\langle\gamma\rangle = 1 + \frac{a_0^2}{4}. \tag{C.22}$$

This expression can be substituted into Equation C.20:

$$\eta = 1 - \frac{1}{2}\frac{\omega_p^2}{\omega^2\left(1 + \frac{a_0^2}{4}\right)}. \tag{C.23}$$

This expression can be expanded as a Taylor series around $a_0 = 0$. Expanded up to the second-order term in the Taylor series, this produces the following expression for the refractive index of the plasma:

$$\eta = 1 - \frac{1}{2}\frac{\omega_p^2}{\omega^2}\left(1 - \frac{a_0^2}{4}\right). \tag{C.24}$$

The refractive index of the plasma depends not only on the plasma frequency and the frequency of the electromagnetic wave, but also the amplitude of the normalised potential of the wave.

C.4.1 Perturbations to the Refractive Index

Small variations in the refractive index of the plasma are also caused by small perturbations in the plasma frequency and the electromagnetic wave frequency. A perturbation in the plasma frequency from its initial value is produced by a perturbation in the electron density in the plasma:

$$n_e = n_{e,0}\left(1 + \frac{\delta n_e}{n_{e,0}}\right), \tag{C.25}$$

where $n_{e,0}$ is the initial plasma density and δn_e is the perturbation. This expression can be used if it assumed that $\frac{\delta n_e}{n_{e,0}} \ll 1$. Similarly, for a perturbation in the electromagnetic wave frequency,

$$\omega = \omega_0\left(1 + \frac{\delta\omega}{\omega_0}\right), \tag{C.26}$$

where ω_0 is the initial wave frequency and the $\delta\omega$ is the perturbation. Again, this expression is used assuming that $\frac{\delta\omega}{\omega_0} \ll 1$. Substituting these perturbative expressions into Equation 2.24 produces an expression for the perturbed refractive index:

$$\eta \approx 1 - \frac{1}{2}\frac{\omega_{p,0}^2}{\omega_0^2\left(1+\frac{\delta\omega}{\omega_0}\right)^2}\left(1 - \frac{a_0^2}{4}\right)\left(1 + \frac{\delta n_e}{n_{e,0}}\right). \tag{C.27}$$

This expression can be simplified by performing a Taylor series expansion of the perturbation of the electromagnetic wave frequency. Assuming that $\frac{\delta\omega}{\omega_0} \ll 1$, the expansion is performed around $\frac{\delta\omega}{\omega_0} \approx 0$, just up to the first order term:

$$\eta \approx 1 - \frac{1}{2}\frac{\omega_{p,0}^2}{\omega_0^2}\left(1 - \frac{a_0^2}{4}\right)\left(1 + \frac{\delta n_e}{n_{e,0}}\right)\left(1 - 2\frac{\delta\omega}{\omega_0}\right). \tag{C.28}$$

After expanding the brackets in this expression, it is assumed that the terms that consist of the product of one or more small perturbations terms are negligible. This leaves an expression with only the first-order terms in the perturbations and the normalised potential of the electromagnetic wave:

$$\eta \approx 1 - \frac{1}{2}\frac{\omega_{p,0}^2}{\omega_0^2}\left(1 + \frac{\delta n_e}{n_{e,0}} - 2\frac{\delta\omega}{\omega_0} - \frac{a_0^2}{4}\right). \tag{C.29}$$

C.5 Photon Acceleration

A longitudinal gradient in refractive index that is comoving with a laser pulse in plasma produces a gradient in its phase velocity. The distance between two consecutive wavefronts travelling with different phase velocities in a laser pulse after propagating

for a short time interval in plasma is given by Equation 2.30, which is also written here:

$$z_2' - z_1' = \lambda_0 + (v_{ph,\,2} - v_{ph,\,1})\Delta t, \tag{C.30}$$

where z_2' and z_1' are the longitudinal positions of each of the wavefronts after the time interval, Δt, $v_{ph,\,2}$ and $v_{ph,\,1}$ are their phase velocities and λ_0 is the wavelength of the laser at $t = 0$. The wavelength is simply the distance between the two consecutive wavefronts. Assuming a small difference between the phase velocities of the wavefronts, the longitudinal gradient in the phase velocity between these points is approximately constant. The distance between their new longitudinal coordinates can then be expressed in terms of the gradient in phase velocity across the pulse:

$$z_2' - z_1' \approx \lambda_0 + \frac{\partial v_{ph}}{\partial z}\lambda_0 \Delta t. \tag{C.31}$$

The rate of change of the wavelength between the two wavefronts can be determined in the limit that $\Delta t \to 0$. From first principles of the time derivative,

$$\frac{\partial \lambda}{\partial t} = \lim_{\Delta t \to 0}\left(\frac{(z_2' - z_1') - (z_2 - z_1)}{\Delta t}\right), \tag{C.32}$$

$$= \lim_{\Delta t \to 0}\left(\frac{(z_2' - z_2) - (z_1 - z_1')}{\Delta t}\right), \tag{C.33}$$

$$= v_{ph,2} - v_{ph,1}. \tag{C.34}$$

Comparing this result with Equations C.30 and C.31, the rate of change of the wavelength is related to the gradient in phase velocity:

$$v_{ph,\,2} - v_{ph,\,1} = \frac{\partial \lambda}{\partial t} = \frac{\partial v_{ph}}{\partial z}\lambda_0. \tag{C.35}$$

Because the refractive index gradient is comoving with the laser pulse, the gradient in phase velocity is written in terms of the comoving coordinate at any point in time:

$$\frac{\partial v_{ph}}{\partial z} = \frac{\partial v_{ph}}{\partial \xi}\frac{\partial \xi}{\partial z}, \tag{C.36}$$

$$= \frac{\partial v_{ph}}{\partial \xi}\frac{\partial}{\partial z}(ct - z), \tag{C.37}$$

$$= -\frac{\partial v_{ph}}{\partial \xi}. \tag{C.38}$$

Using $v_{ph} = \frac{c}{\eta}$, Equation C.35 describing the rate of change of wavelength can then be written in terms of the comoving gradient in the refractive index:

$$\frac{\partial \lambda}{\partial t} = \lambda_0 \frac{c}{\eta^2}\frac{\partial \eta}{\partial \xi}. \tag{C.39}$$

It is often useful to find the rate of change of frequency in the laser pulse, rather than for the wavelength, where $\omega = 2\pi c/\lambda$. The result of this conversion is given by Equation C.40:

$$\frac{1}{\omega}\frac{\partial \omega}{\partial t} = -\frac{c}{\eta^2}\frac{\partial \eta}{\partial \xi}. \tag{C.40}$$

C.6 Self-Focusing of a Laser Pulse in Plasma

A gradient in refractive index that is transverse to the laser's direction of propagation causes the wavefronts to bend. The angle between the centre and the edge of the laser pulse bends at a rate given by Equation 2.33, which is included here:

$$\frac{\partial \theta}{\partial t} = \frac{\partial v_{ph}}{\partial r}, \tag{C.41}$$

where θ is the bending angle, v_{ph} is the phase velocity at an arbitrary transverse coordinate, r, in the laser pulse. The rate of change of the pulse width is expressed in terms of the group velocity and the angle of the wavefront:

$$\frac{\partial w}{\partial t} = -v_g \sin\theta, \tag{C.42}$$

where w is the width of the laser pulse, v_g is the group velocity at an arbitrary transverse coordinate in the laser pulse. Using the small angle approximation,

$$\frac{\partial w}{\partial t} \approx -v_g\theta \approx -c\theta. \tag{C.43}$$

This expression is differentiated with respect to time to produce the second time derivative the laser pulse width:

$$\frac{\partial^2 w}{\partial t^2} = -c\frac{\partial \theta}{\partial t}. \tag{C.44}$$

The transverse gradient in the phase velocity of the laser pulse from Equation C.41 is then substituted into Equation C.44:

$$\frac{\partial^2 w}{\partial t^2} = -c\frac{\partial v_{ph}}{\partial r}. \tag{C.45}$$

As $v_{ph} = \frac{c}{\eta}$,

$$\frac{\partial v_{ph}}{\partial r} = \frac{\partial}{\partial r}\left(\frac{c}{\eta}\right) = c\frac{\partial}{\partial r}\left(\frac{1}{\eta}\right), \tag{C.46}$$

$$= c\frac{\partial}{\partial \eta}\left(\frac{1}{\eta}\right)\frac{\partial \eta}{\partial r}, \tag{C.47}$$

$$= -\frac{c}{\eta^2}\frac{\partial \eta}{\partial r}. \tag{C.48}$$

Equation C.45 can thus be expressed in terms of the refractive index gradient:

$$\frac{\partial^2 w}{\partial t^2} = \frac{c^2}{\eta^2}\frac{\partial \eta}{\partial r}. \tag{C.49}$$

C.6.1 Self-Focusing Threshold for a Gaussian Laser Pulse

The condition for the self-focusing of a laser pulse in plasma to overcome the pulse's diffraction after reaching its focal position is found by equating the acceleration of the laser widths due to self-focusing and diffraction:

$$\left.\frac{\partial^2 w}{\partial t^2}\right|_{diffraction} + \left.\frac{\partial^2 w}{\partial t^2}\right|_{self-focusing} = 0, \tag{C.50}$$

where w is the width of the laser pulse.

The pulse width acceleration due to diffraction is now determined analytically for a laser pulse with a Gaussian intensity profile. The width of a Gaussian laser pulse is quantified by the beam waist, which is the transverse distance from its centre where the intensity falls to a factor of $1/e^2$ of the intensity at the centre. The pulse width as a function of the longitudinal coordinate is given by Equation C.51 [206]:

$$w(z) = w_0\sqrt{1 + \frac{z^2}{z_R^2}}, \tag{C.51}$$

where w_0 is the beam waist at focus, z is the longitudinal coordinate of the laser pulse and $z_R = \frac{\pi w_0^2}{\lambda}$ is the Rayleigh range. The Rayleigh range is the longitudinal distance that the laser pulse travels from its focal position for its pulse width to double [206]. When the laser pulse is near its focal point, $z \ll z_R$ so $w \approx w_0$. The expression for the pulse width can be expanded as a Taylor series around $z = 0$:

$$w(z) \approx \frac{1}{2}\frac{z^2}{z_R^2}w_0. \tag{C.52}$$

The rate of change of the pulse width is then calculated by taking the time derivative of this expression. The only quantity in the expression that varies with time is the longitudinal coordinate, which is differentiated with respect to time:

$$\frac{dw(z)}{dt} = \frac{z}{z_R^2} w_0 \frac{dz}{dt}. \tag{C.53}$$

As the laser travels at approximately the speed of light through the plasma, $\frac{dz}{dt} \approx c$. This is used in the calculation of the time derivative:

$$\frac{dw(z)}{dt} = \frac{z}{z_R^2} w_0 c. \tag{C.54}$$

Taking the second time derivative and applying the same procedure,

$$\frac{\partial^2 w}{\partial t^2} = \frac{c^2}{z_R^2} w_0. \tag{C.55}$$

Substituting the expression for the Rayleigh range,

$$\frac{\partial^2 w}{\partial t^2} = \frac{4c^4}{w_0^3 \omega^2}. \tag{C.56}$$

This expression describes the pulse width acceleration of the Gaussian pulse due to its diffraction past its focal position.

Given by Equations 2.35 and C.55, the pulse width accelerations due to self-focusing and diffraction are substituted into the self-focusing condition given by Equation C.50:

$$\frac{c^2 \omega_p^2}{8\omega^2} \frac{\partial a^2}{\partial r} + \frac{4c^4}{w_0^3 \omega^2} = 0. \tag{C.57}$$

The spatial derivative of the square of the normalised potential of the laser pulse must now be evaluated. The potential of the Gaussian laser pulse is defined as $a(r,z) = a_0(z) e^{-\frac{r^2}{2w(z)^2}}$ [206]. Near the focal point of the laser pulse where $z \approx 0$, $w(z) \approx w_0$. The square of the normalised potential is calculated and then differentiated with respect to the transverse coordinate:

$$\frac{\partial a^2}{\partial r} = -a_0^2 \left(\frac{2r}{w_0^2} \right) e^{-\frac{r^2}{w_0^2}}. \tag{C.58}$$

Evaluating this result at $r = w_0$, where the intensity of the laser pulse has reduced by over half from its peak,

$$\frac{\partial a^2}{\partial r} = -a_0^2 \left(\frac{2r}{w_0^2} \right) e^{-1} \approx -\frac{a_0^2}{w_0}. \tag{C.59}$$

Substituting this result into Equation C.57, the condition for the laser pulse to self-focus can then be rearranged and simplified:

$$a_0^2 w_0^2 = \frac{32c^2}{\omega_p^2}. \tag{C.60}$$

When this condition is met, the diffraction of the laser pulse after its focal position is balanced by its self-focusing in the plasma.

C.7 Linear Plasma Waves

The wave equation for a plasma wave driven by a laser pulse is derived using the fluid momentum equation, the continuity equation, and Gauss' law.

Fluid Momentum Equation

The collective motion of electrons displaced by the ponderomotive force of a laser pulse in a plasma is described by the fluid momentum equation. The Lorentz force on a small fluid element in the plasma is given by the fluid momentum equation:

$$m_e\left(\frac{d\mathbf{v}}{dt} + (\mathbf{v}\cdot\nabla)\mathbf{v}\right) = -e(\mathbf{E} + \mathbf{v}\times\mathbf{B}). \tag{C.61}$$

As the electrons in an LWFA are displaced by a laser pulse, the electromagnetic fields in Equation C.61 are those of the laser pulse. Expressing the magnetic field and the electron quiver velocity in terms of the electromagnetic vector potential of the laser pulse, $\mathbf{B} = \nabla\times\mathbf{A}$ and $\mathbf{v} = \frac{e\mathbf{A}}{m_e}$, the fluid momentum equation is re-expressed:

$$m_e\frac{\partial\mathbf{v}}{\partial t} = -e\mathbf{E} - \frac{e^2}{m_e}\big((\mathbf{A}\cdot\nabla)\mathbf{A} + \mathbf{A}\times(\nabla\times\mathbf{A})\big). \tag{C.62}$$

Using the following identity, $((\mathbf{A}\cdot\nabla)\mathbf{A}) + \mathbf{A}\times(\nabla\times\mathbf{A}) = \frac{1}{2}\nabla A^2$, Equation C.62 can be simplified:

$$m_e\frac{\partial\mathbf{v}}{\partial t} = -e\mathbf{E} - \frac{e^2}{2m_e}\nabla A^2 \tag{C.63}$$

Using the normalisation given in Appendix A.1, Equation C.63 is written in terms of the normalised potential of the laser pulse:

$$m_e\frac{\partial\mathbf{v}}{\partial t} = -e\mathbf{E} - \frac{1}{2}m_e c^2\nabla a^2. \tag{C.64}$$

This is the fluid momentum equation for an electron in a plasma interacting with the electromagnetic potential of the laser pulse.

Continuity Equation

The continuity equation, derived in Appendix A.5, expresses the local conservation of charge in the plasma:

$$\frac{\partial \rho}{\partial t} + \nabla \cdot \mathbf{j} = 0. \tag{C.65}$$

The charge density due to their separation is given by $\rho = -e(n_e - n_i)$, where n_i is the number density of ions in the plasma. There is also a current density due to the velocity of the displaced electrons: $\mathbf{j} = -en_e\mathbf{v}$. These expressions are substituted into Equation C.65:

$$-e\frac{\partial}{\partial t}(n_e - n_i) - en_e\big(\nabla \cdot \mathbf{v}\big) = 0. \tag{C.66}$$

This is the continuity equation for displaced electrons in a plasma.

Gauss' Law

Gauss' law is used to determine the electric field produced by the charge separation as electrons are displaced by the laser pulse:

$$\nabla \cdot \mathbf{E} = -\frac{e(n_e - n_i)}{\epsilon_0}. \tag{C.67}$$

In the derivation of the wave equation for a plasma wave, the divergence of the electric field is required rather than the electric field vector itself. This form of Gauss' law is later substituted into the derivation.

Perturbations to Variables

A perturbative approach is used to derive the wave equation for linear plasma waves. The electron density in the plasma, the electron velocity, and the electric field due to the charge separation are perturbed by small amounts from their original values when the electrons are at their equilibrium positions:

$$\mathbf{v} = \mathbf{v_0} + \mathbf{v_1}, \tag{C.68}$$

$$n = n_0 + n_1, \tag{C.69}$$

$$\mathbf{E} = \mathbf{E_0} + \mathbf{E_1}. \tag{C.70}$$

The equilibrium values of these quantities are constants of the motion. In the case of the electric field, $\mathbf{E_0} = 0$. These quantities are substituted into Equations C.64, C.66, and C.67. Respectively,

$$m_e\frac{\partial \mathbf{v_1}}{\partial t} = -e\mathbf{E_1} - \frac{1}{2}m_e c^2 \nabla \mathbf{a}^2, \tag{C.71}$$

$$\frac{\partial n_1}{\partial t} + n_0\big(\nabla \cdot \mathbf{v_1}\big) = 0, \tag{C.72}$$

$$\nabla \cdot \mathbf{E_1} = -\frac{e n_1}{\epsilon_0}. \tag{C.73}$$

The divergence operator is then applied to the linearised fluid momentum equation, given by Equation C.71, and the time derivative is applied to the continuity equation, given by Equation C.72:

$$m_e \frac{\partial}{\partial t}(\nabla \cdot \mathbf{v_1}) = -e(\nabla \cdot \mathbf{E_1}) - \frac{1}{2} m_e c^2 \nabla^2 a^2, \tag{C.74}$$

$$\frac{\partial^2 n_1}{\partial t^2} + n_0 \frac{\partial}{\partial t}(\nabla \cdot \mathbf{v_1}) = 0, \tag{C.75}$$

$$\nabla \cdot \mathbf{E_1} = -\frac{e n_1}{\epsilon_0}. \tag{C.76}$$

The linearised continuity equation and Gauss' law are then substituted into the fluid momentum equation, given by Equation C.74, producing an equation for a linear plasma wave driven by a laser pulse:

$$\left(\frac{\partial^2}{\partial t^2} + \omega_p^2\right)\left(\frac{n_1}{n_0}\right) = \frac{1}{2} c^2 \nabla^2 a^2. \tag{C.77}$$

This is the wave equation for a linear plasma wave in terms of electron density. The wave equation can be written in terms of the scalar potential of the plasma wave using Poisson's equation, in terms of the normalised units in Appendix A.1:

$$\nabla^2 \Phi = \frac{e^2 n_1}{m_e c^2 \epsilon_0}. \tag{C.78}$$

As $n_0 = \omega_p^2 m_e \epsilon_0 / e^2$,

$$\frac{n_1}{n_0} = \frac{c^2}{\omega_p^2} \nabla^2 \Phi. \tag{C.79}$$

Substituting this into the wave equation in Equation C.77 and integrating the expression produces the wave equation in terms of the scalar potential of the plasma wave:

$$\left(\frac{\partial^2}{\partial t^2} + \omega_p^2\right)\Phi = \frac{\omega_p^2}{2} a^2. \tag{C.80}$$

Defining a comoving coordinate with the laser pulse as $\xi = z - v_g t$, where v_g is the group velocity of the laser pulse in the plasma, the wave equation can be expressed in the spatial domain:

$$\left(\frac{\partial^2}{\partial \xi^2} + k_p^2\right)\Phi = \frac{k_p^2}{2} a^2, \tag{C.81}$$

where k_p is the wavenumber of the plasma wave.

C.8 Electron Density in a Plasma Wave

The motion of electrons in a plasma wave is described by the continuity equation, given by Equation A.13. Expressed in terms of the electron density and speed in a plasma wave in one dimension,

$$\frac{\partial n}{\partial t} + \frac{\partial}{\partial z}(nv_z) = 0, \tag{C.82}$$

where n is the density and v_z is the velocity of electrons at some position in the plasma wave. The density of the plasma is perturbed by some amount from its original value, given by $n = n_0 + n_1$, where n_0 is the original electron density and n_1 is the perturbation. Substituting this into the continuity equation,

$$\frac{\partial n_1}{\partial t} + \frac{\partial}{\partial z}\big((n_0 + n_1)v_z\big) = 0. \tag{C.83}$$

Defining a comoving coordinate with the laser pulse as $\xi = z - ct$, where it has been assumed that $v_g \approx c$ in the plasma, both derivatives can be re-expressed in terms of the comoving coordinate:

$$\frac{\partial}{\partial t} = -c\frac{\partial}{\partial \xi}, \tag{C.84}$$

$$\frac{\partial}{\partial z} = \frac{\partial}{\partial \xi}. \tag{C.85}$$

Substituting these identities into the continuity equation produces an expression that contains the same spatial derivative:

$$-c\frac{\partial n_1}{\partial \xi} + \frac{\partial}{\partial \xi}\big((n_0 + n_1)v_z\big) = 0. \tag{C.86}$$

This expression can be integrated, producing a relation between the density and the velocity of electrons in the plasma:

$$-cn_1 + (n_0 + n_1)v_z + const. = 0. \tag{C.87}$$

The constant is found to be zero by applying the condition $v_z = 0$ when $n_1 = 0$. Then, the equation is rearranged to make the density perturbation the subject:

$$n_1 = \frac{n_0 v_z}{c - v_z}. \tag{C.88}$$

D. Electron-Wakefield Interactions

D.1 Electron Acceleration in the Bubble Regime

The energy change of the electron is calculated from the work done by the longitudinal electric field component in the bubble. Assuming a uniform charge density inside the bubble, $\rho = en_e$, the longitudinal electric field component along the z-axis inside the bubble can be derived using Gauss' law:

$$\frac{dE_\xi}{d\xi} = \frac{en_e}{\epsilon_0}, \tag{D.1}$$

where $\xi = v_g t - z$ is the comoving coordinate for the electron in the wakefield moving with a phase velocity equal to the group velocity of the laser pulse in the plasma. Integrating Equation D.1 with respect to the comoving coordinate,

$$E_\xi = \frac{en_e}{\epsilon_0}\xi \tag{D.2}$$

The force exerted on an electron by this electric field is given by $F_\xi = -eE_\xi$, which can be rewritten as $F_\xi = -m_e\omega_p^2\xi$. As the comoving coordinate points in the opposite direction to the z-axis, the force with respect to the z-coordinate is given by $F_z = -F_\xi$. To simplify the algebra involved in this derivation, the comoving coordinate is set such that at $t = 0$, $\xi = r_b$; it can then be written as $\xi = (v_g - c)t + r_b$. The force on an electron along the z-axis can then be written:

$$F_z = m_e\omega_p^2((v_g - c)t + r_b). \tag{D.3}$$

The energy gain of the electron due to the work done by this force can then be derived:

$$W(z) = \int F_z dz, \tag{D.4}$$

$$= m_e\omega_p^2 \int ((v_g - c)t + r_b)\, dz. \tag{D.5}$$

$$\tag{D.6}$$

As $\xi = v_g t - z = -(v_g - c)t + r_b$, $z = -r_b + ct$ and so $\frac{dz}{dt} = c$. This can be applied to the expression for the work done by the force on the electron, to produce an expression for the energy gained by the electron against time:

$$W(t) = m_e \omega_p^2 c \int ((v_g - c)t + r_b)\, dt, \tag{D.7}$$

$$= m_e \omega_p^2 c \left(\frac{1}{2}(v_g - c)t^2 + r_b t \right), \tag{D.8}$$

where the constant of integration is found to be zero as the work done is zero at $t = 0$. Equation D.5 can be simplified if it is written in terms of the Lorentz factor corresponding to the phase velocity of the wakefield:

$$W(t) = m_e \omega_p^2 c^2 \left(-\frac{1}{4\gamma_p^2} t^2 + \frac{r_b}{c} t \right), \tag{D.9}$$

where $(1 - v_g/c)$ approximates to half of the inverse square of the Lorentz factor:

$$\left(1 - \frac{v_g}{c}\right) = (1 - \beta_g) \tag{D.10}$$

$$, = \frac{1 + \beta_g}{1 + \beta_g}(1 - \beta_g), \tag{D.11}$$

$$= \frac{1 - \beta_g^2}{1 + \beta_g}, \tag{D.12}$$

$$= \frac{1}{\gamma_p^2 (1 + \beta_g)}, \tag{D.13}$$

$$\approx \frac{1}{2\gamma_p^2}. \tag{D.14}$$

The time-progression of the total energy of the electron is simply the initial energy of the electron at injection added to the work done: $E = E_0 + W$. If it assumed that the initial energy of the electron is high enough such that its speed is equal to the phase velocity of the wakefield,

$$E(t) = \gamma_p m_e c^2 + m_e \omega_p^2 c^2 \left(-\frac{1}{4\gamma_p^2} t^2 + \frac{r_b}{c} t \right). \tag{D.15}$$

Substituting $\xi \approx -t/2\gamma_p^2 + r_b$ into Equation D.9, it can also be expressed in terms of the comoving coordinate:

$$W(\xi) = \frac{1}{2} m_e \omega_p^2 \gamma_p^2 (r_b^2 - \xi^2), \tag{D.16}$$

which matches the equation derived by Thomas in 2010 [61].

D.2 Transverse Scalar Potential in the Bubble Regime

If the electromagnetic potential in the bubble does not evolve over time, then its electric field is equal to the negative gradient in the scalar potential:

$$\mathbf{E} = -\boldsymbol{\nabla}\phi + \frac{\partial \mathbf{A}}{\partial t}^{0}, \tag{D.17}$$

$$= -\boldsymbol{\nabla}\phi. \tag{D.18}$$

Gauss' law then equates to the second spatial derivative of the scalar potential, producing Poisson's equation. The charge density enclosed in the bubble is estimated as $\rho = en_e$. The scalar potential can then be calculated from Poisson's equation in cylindrical coordinates:

$$\nabla^2\phi = \frac{1}{r}\frac{\partial}{\partial r}\left(r\frac{\partial\phi}{\partial r}\right) = \frac{en_e}{\epsilon_0}. \tag{D.19}$$

The scalar potential of the bubble is produced by solving Poisson's equation:

$$\phi = \frac{en_e}{4\epsilon_0}r^2. \tag{D.20}$$

D.3 Betatron Oscillations at Constant Energy

The equation of motion for an electron with constant energy is derived inside a cylindrically symmetric, non-evolving bubble in plasma. Using Equation 2.6 for the Lagrangian of a relativistic charged particle in an electromagnetic potential, the Lagrangian for the transverse motion of an off-axis relativistic electron in the bubble regime can be written:

$$L = -m_e c^2\sqrt{1-\beta_r^2} - e(v_r A_r) + e\phi. \tag{D.21}$$

The transverse equation of motion for the electron is then derived from the Euler-Lagrange equation:

$$\frac{d}{dt}\left(\gamma m_e v_r - eA_r\right) = -e\frac{\partial\phi}{\partial r}. \tag{D.22}$$

If the field structure in the bubble is non-evolving, then $\frac{d\mathbf{A}}{dt} = 0$, or $\frac{dA_r}{dt} = 0$. The scalar potential in the non-evolving bubble is expressed in terms of the electron density in the plasma in Equation D.20, derived in Appendix D.2. The result of the Euler-Lagrange equation is then simplified and re-written:

$$\frac{d}{dt}\left(\gamma m_e v_r\right) = -\frac{e^2 n_e}{2\epsilon_0}r. \tag{D.23}$$

For an electron with constant energy, the Lorentz factor is a constant of the motion. Rewriting the rate of change of the radial velocity as the second time derivative of the radial coordinate of the electron, the equation of motion describes the simple harmonic oscillation about the central axis of the bubble:

$$\frac{d^2r}{dt^2} = -\frac{e^2 n_e}{2\gamma m_e \epsilon_0} r. \tag{D.24}$$

Recalling Equation 2.20, this simple harmonic equation of motion can be expressed in terms of the plasma frequency:

$$\frac{d^2r}{dt^2} = -\frac{\omega_p^2}{2\gamma} r. \tag{D.25}$$

D.4 Electron Trajectories in the Bubble Regime

In the bubble regime, an injected electron experiences both a longitudinal force accelerating it and a transverse focusing force towards the central longitudinal axis of the bubble. The transverse motion of the electron in the bubble is considered. The Lagrangian describing the transverse motion of the electron initially off-axis in the bubble can be written:

$$L = -m_e c^2 \sqrt{1 - \beta_r^2} - e(v_r A_r) + e\phi. \tag{D.26}$$

The transverse equation of motion for the electron produced from the Euler-Lagrange equation. The scalar potential as a function of the transverse coordinate is derived in Appendix D.2 and given by Equation D.20. It is also noted that if the field structure in the bubble is non-evolving, then $\frac{d\mathbf{A}}{dt} = 0$, or $\frac{dA_r}{dt} = 0$. These equations are substituted into the equation of motion:

$$c\beta_r \frac{d\gamma}{dt} + c\gamma \frac{d\beta_r}{dt} = -\frac{e^2 n_e}{2\epsilon_0} r. \tag{D.27}$$

Recalling Equation 2.20 defining the plasma frequency,

$$c\beta_r \frac{d\gamma}{dt} + c\gamma \frac{d\beta_r}{dt} = -\frac{1}{2}\omega_p^2 r. \tag{D.28}$$

This is different to the result for an electron in the bubble with constant energy because the Lorentz factor is not a constant of the motion in this case. However, if $\beta_r \frac{d\gamma}{dt} \ll \gamma \frac{d\beta_r}{dt}$, then the first term in Equation D.28 can be neglected. It is shown that this is valid in Section 2.10.2. Rewriting the rate of change of the transverse velocity as the second time derivative of the transverse coordinate then produces a simple

harmonic equation of motion:

$$\frac{d^2r}{dt^2} = -\frac{\omega_p^2}{2\gamma}r, \tag{D.29}$$

where the Lorentz factor is a parameter that varies slowly in time.

D.4.1 Solution for the Electron Trajectory

The equation of motion is in the form of a differential equation describing an electron performing simple harmonic motion; however, the frequency factor on the right-hand side is also a function of time. The electron is expected to oscillate about the central longitudinal axis of the bubble with a slowly varying frequency: $\Omega_\beta(t) = \frac{\omega_p}{\sqrt{2\gamma(t)}}$, where the Lorentz factor is a function of time. An initial guess of the solution to the equation of motion could be of the form of a trigonometric function of time:

$$r(t) \propto \sin\left[\int_{t_0}^{t} \Omega_\beta(t)\, dt\right], \tag{D.30}$$

$$\propto \frac{i}{2}\big(e^{i\int_{t_0}^{t}\Omega_\beta(t)\,dt} - e^{-i\int_{t_0}^{t}\Omega_\beta(t)\,dt}\big). \tag{D.31}$$

The validity of this trial solution can be checked by substituting this expression into the equation of motion:

$$i\frac{d\Omega_\beta(t)}{dt}\big(\big(e^{i\int_{t_0}^{t}\Omega_\beta(t)dt} + e^{-i\int_{t_0}^{t}\Omega_\beta(t)dt}\big) - \cancel{\Omega_\beta(t)^2 r(t)} + \cancel{\Omega_\beta(t)^2 r(t)} = 0. \tag{D.32}$$

The trial solution only satisfies the equation of motion when the rate of change of the frequency is zero. However, the solution approximately satisfies the equation of motion when $\frac{d\Omega_\beta(t)}{dt} \ll \Omega_\beta(t)^2$, when the frequency of oscillation is slowly varying. The WKB approximation is applied to derive solution, as was performed by Kostyukov *et al.* in 2004 [130]. The trigonometric function in Equation D.31 is used as a zeroth order approximation for the solution:

$$r(t) = R\,\frac{i}{2}\big(e^{iu(t)} - e^{-iu(t)}\big), \tag{D.33}$$

$$= R\,\frac{i}{2}\big(\psi_1(t) + \psi_2(t)\big), \tag{D.34}$$

where $u(t)$ is an arbitrary function of time and R is the amplitude of oscillation , which will be determined later in the derivation. $\psi_1(t) = e^{iu(t)}$ and $\psi_2(t) = e^{-iu(t)}$ both satisfy the equation of motion of the electron, which will be shown. Because the equation of motion is a homogeneous, linear differential equation, $\psi_1(t) + \psi_2(t)$ is also a solution.

Substituting $\psi_1(t)$ into the equation of motion,

$$i\frac{d^2u(t)}{dt^2}\cancel{e^{iu(t)}} - \left(\frac{du(t)}{dt}\right)^2\cancel{e^{iu(t)}} + \Omega_\beta(t)^2\cancel{e^{iu(t)}} = 0. \tag{D.35}$$

$$i\frac{d^2u(t)}{dt^2} - \left(\frac{du(t)}{dt}\right)^2 + \Omega_\beta(t)^2 = 0. \tag{D.36}$$

If $\frac{d^2u(t)}{dt^2} = \frac{d\Omega_\beta}{dt} \approx 0$, valid as $\Omega_\beta(t)$ is slowly varying, it follows that an initial zeroth order approximation for the unknown function can be made:

$$u_0(t) = \pm\int_{t_0}^{t}\Omega_\beta(t)dt. \tag{D.37}$$

This function produces a solution that has a constant amplitude, which perhaps neglects any change in amplitude due to the evolution of the transverse momentum of the electrons as it is accelerated. Rearranging Equation D.36 with $u(t) = u_0(t)$, a first order approximation for the unknown function can be made:

$$u_1(t) = \int_{t_0}^{t}\sqrt{\Omega_\beta(t)^2 + i\frac{d^2u_0(t)}{dt^2}}\;dt. \tag{D.38}$$

Expanding the integrand in this expression as a Taylor series around $\frac{d\Omega_\beta}{dt} = 0$,

$$u_1(t) = \int_{t_0}^{t}\Omega_\beta(t)\sqrt{1 \pm \frac{i}{\Omega_\beta(t)^2}\frac{d^2u_0(t)}{dt^2}}\;dt, \tag{D.39}$$

$$\approx \int_{t_0}^{t}\left(\Omega_\beta(t) \pm \frac{i}{2\Omega_\beta(t)}\frac{d\Omega_\beta(t)}{dt}\right)dt, \tag{D.40}$$

$$= \int_{t_0}^{t}\Omega_\beta(t)\,dt \pm \frac{i}{2}\int_{t_0}^{t}\frac{d\Omega_\beta}{\Omega_\beta}, \tag{D.41}$$

$$= \int_{t_0}^{t}\Omega_\beta(t)\,dt \pm \frac{i}{2}\ln\left(\Omega_\beta(t)\right). \tag{D.42}$$

This result for $u(t)$ is substituted into $\psi_1(t)$:

$$\psi_1(t) = \sqrt{\Omega_\beta(t)}e^{i\int_{t_0}^{t}\Omega_\beta(t)\,dt}. \tag{D.43}$$

Following the same procedure for $\psi_2(t)$ produces a result in a similar form:

$$\psi_2(t) = \sqrt{\Omega_\beta(t)}e^{-i\int_{t_0}^{t}\Omega_\beta(t)\,dt}. \tag{D.44}$$

Equations D.43 and D.44 can then be substituted into the initial approximation for the solution, given by Equation D.34. Defining a temporary constant, R', such that

$R = \sqrt{\Omega_\beta(t)}\, R'$,

$$r(t) = R'\sqrt{\Omega_\beta(t)}\frac{i}{2}\left(e^{i\int_{t_0}^{t}\Omega_\beta(t)dt} + e^{-i\int_{t_0}^{t}\Omega_\beta(t)dt}\right), \tag{D.45}$$

$$= R'\sqrt{\Omega_\beta(t)}\,\sin\left[\int_{t_0}^{t}\Omega_\beta(t)\,dt\right]. \tag{D.46}$$

The time progression of the transverse momentum of the oscillating electron is now derived. This not only provides a more comprehensive description of the dynamics of the electron's motion, but also allows the amplitude of oscillation to be expressed in terms of the initial properties of the electron at the point of injection. The transverse velocity component of the electron is first calculated by differentiating Equation D.46 with respect to time:

$$\begin{aligned} v_r(t) = \frac{dr(t)}{dt} =& \frac{1}{2}R'\frac{d\Omega_\beta(t)}{dt}\Omega_\beta(t)^{-\frac{1}{2}}\sin\left[\int\Omega_\beta(t)\,dt\right] + \\ & R'\Omega_\beta(t)^{\frac{3}{2}}\cos\left[\int\Omega_\beta(t)\,dt\right]. \end{aligned} \tag{D.47}$$

To compare the two terms, the second term is written in the same form as the first:

$$\begin{aligned} v_r(t) = \frac{dr(t)}{dt} =& \frac{1}{2}R'\frac{d\Omega_\beta(t)}{dt}\Omega_\beta(t)^{-\frac{1}{2}}\sin\left[\int\Omega_\beta(t)\,dt\right] + \\ & R'\Omega_\beta(t)^2\Omega_\beta(t)^{-\frac{1}{2}}\cos\left[\int\Omega_\beta(t)\,dt\right]. \end{aligned} \tag{D.48}$$

The WKB approximation requires that $\frac{d\Omega_\beta(t)}{dt} \gg \Omega_\beta(t)^2$, which is valid for the case of an ultrarelativistic electron in the bubble regime, as explained in Section 2.10.2. The first term in Equation D.48 is thus neglected:

$$v_r(t) \approx R'\Omega_\beta(t)^{\frac{3}{2}}\cos\left[\int\Omega_\beta(t)\,dt\right]. \tag{D.49}$$

The transverse momentum of the electron is then calculated by $p_r(t) = \gamma(t)m_e v_r(t)$. In the expression, the time-varying frequency of oscillation is expressed in terms of the Lorentz factor, $\Omega_\beta(t) = \omega_p/\sqrt{2\gamma(t)}$, producing the following expression for the transverse momentum against time:

$$p_r(t) = \frac{m_e\omega_p^{\frac{3}{2}}R'}{2^{\frac{3}{4}}}\gamma(t)^{\frac{1}{4}}\cos\left[\int\Omega_\beta(t)\,dt\right]. \tag{D.50}$$

At $t = 0$, the initial transverse momentum of the electron is determined by its initial

Lorentz factor:

$$p_{r0} = \frac{m_e \omega_p^{\frac{3}{2}} R'}{2^{\frac{3}{4}}} \gamma_0^{\frac{1}{4}}, \tag{D.51}$$

where the zero subscript denotes the initial values at injection. From this expression, the temporary constant can be expressed in terms of these initial parameters:

$$R' = \frac{2^{\frac{3}{4}} p_{r0}}{m_e \omega_p^{\frac{3}{2}}} \gamma_0^{-\frac{1}{4}}. \tag{D.52}$$

Substituting Equation D.52 into Equation D.50 produces the equation for the time progression of the transverse momentum of the electron:

$$p_r(t) = p_{r0} \left(\frac{\gamma(t)}{\gamma_0} \right)^{\frac{1}{4}} \cos \left[\int \Omega_\beta(t)\, dt \right]. \tag{D.53}$$

Substituting Equation D.52 into Equation D.46 produces the equation for the progression of the transverse coordinate of the electron:

$$r(t) = \frac{p_{r0}}{m_e \omega_p} \sqrt{\frac{2}{\gamma_0}} \left(\frac{\gamma_0}{\gamma(t)} \right)^{\frac{1}{4}} \sin \left[\int \Omega_\beta(t)\, dt \right]. \tag{D.54}$$

Equations D.53 and D.54 are solutions for the transverse momentum and coordinate of the oscillating electron in the bubble regime, written in terms of its initial transverse momentum and Lorentz factor.

E. Synchrotron Radiation Properties

E.1 Angular Intensity Distribution of Radiated Synchrotron Radiation

The Poynting vector describes the energy flux of the radiation and can be calculated from the far-field terms of the electromagnetic fields:

$$\mathbf{S} = \frac{1}{\mu_0}\mathbf{E} \times \mathbf{B} = \frac{E^2}{c\mu_0}\mathbf{n}, \tag{E.1}$$

where $\mathbf{E}$ and $\mathbf{B}$ are the electic and magnetic fields of the radiation, and $\mathbf{n}$ is the unit vector in the direction of the observer from the electron's position. It is taken that $\mathbf{n} \cdot \mathbf{E} = 0$ for the far-field. The Liénard-Wiechert fields are the electromagnetic fields of the synchrotron radiation produced by an accelerating charged particle. In this work, the charged particle being considered is an electron. The far-field term in the Liénard-Wiechert field, given in Equation 2.76, can be substituted into the above Poynting vector expression:

$$\mathbf{S} = \frac{e^2}{(4\pi)^2\epsilon_0 c}\left|\frac{\mathbf{n} \times ((\mathbf{n} - \boldsymbol{\beta}) \times \dot{\boldsymbol{\beta}})}{r(1 - \mathbf{n} \cdot \boldsymbol{\beta})^3}\right|^2_{ret}\mathbf{n}. \tag{E.2}$$

This Poynting vector describes the energy flux of the observed radiation. To describe the energy flux of the emitted radiation, in terms of the retarded time, the difference between corresponding time intervals in the retarded and observed needs to be accounted for. This difference arises from the motion of the electron and its distance from the observer, as described in Section 2.11.1. Using Equation 2.74, the Poynting vector of the emitted radiation can be expressed:

$$\mathbf{S_{ret}} = \frac{d\mathbf{S}'}{dt_{ret}} = \frac{d\mathbf{S}'}{dt_{obs}}\frac{dt_{obs}}{dt_{ret}}, \tag{E.3}$$

$$= \mathbf{S}\,\frac{dt_{obs}}{dt_{ret}}, \tag{E.4}$$

$$= \mathbf{S}\,(1 - \mathbf{n} \cdot \boldsymbol{\beta}), \tag{E.5}$$

where $\mathrm{S}' = \int \mathrm{S}\, dt_{obs} = \int \mathrm{S}\, dt_{ret}$, which describes the direction along which the energy density is radiated. At any point along an electron's trajectory, the total power emitted by the electron is calculated by integrating the Poynting vector over the entire surface area enclosing all of the emitted radiation:

$$P = \int_{\Omega} \mathbf{S_{ret}} \cdot \mathbf{n}\, r^2\, d\Omega, \tag{E.6}$$

where Ω is the solid angle covered by the radiation, $\mathbf{n}$ is the unit vector in the direction of the observer from the electron's position and r is the distance of the electron to the observer. The angular distribution of emitted power can thus be expressed:

$$\frac{dP}{d\Omega} = (\mathbf{S_{ret}} \cdot \mathbf{n})\, r^2. \tag{E.7}$$

The expression for the Poynting vector, given by Equation E.2, is substituted into Equation E.7 and the result is simplified:

$$\frac{dP}{d\Omega} = \frac{e^2}{(4\pi)^2 \epsilon_0 c} \frac{\left(\mathbf{n} \times ((\mathbf{n} - \boldsymbol{\beta}) \times \dot{\boldsymbol{\beta}})\right)^2}{(1 - \mathbf{n} \cdot \boldsymbol{\beta})^5}. \tag{E.8}$$

E.1.1 Total Radiated Power

The total power radiated by an accelerating electron is derived by integrating the entire angular power distribution over the solid angle that it covers. To simplify the integration, the triple vector product is re-expressed in terms of scalar products using the identity $\mathbf{a} \times \mathbf{b} \times \mathbf{c} = (\mathbf{a} \cdot \mathbf{c})\mathbf{b} - (\mathbf{b} \cdot \mathbf{c})\mathbf{a}$. Then, expanding the square of the triple vector product,

$$\begin{aligned} P = \frac{e^2}{(4\pi)^2 \epsilon_0 c} \int_{-2\pi}^{2\pi} \Bigg(& -(1 - \boldsymbol{\beta}^2)(\mathbf{n} \cdot \dot{\boldsymbol{\beta}})^2 + (1 - \mathbf{n} \cdot \boldsymbol{\beta})^2 \dot{\boldsymbol{\beta}}^2 + \\ & 2(1 - \mathbf{n} \cdot \boldsymbol{\beta})(\boldsymbol{\beta} \cdot \dot{\boldsymbol{\beta}})(\mathbf{n} \cdot \dot{\boldsymbol{\beta}}) \Bigg) \frac{d\Omega}{(1 - \mathbf{n} \cdot \boldsymbol{\beta})^5}. \end{aligned} \tag{E.9}$$

The angle between the electron velocity and the electron observer displacement is defined as $\cos\theta = \mathbf{n} \cdot \boldsymbol{\beta}$. The angle between the velocity and acceleration is defined as $\cos\phi = \boldsymbol{\beta} \cdot \frac{\dot{\boldsymbol{\beta}}}{|\dot{\boldsymbol{\beta}}|}$. The angle between the acceleration vector and the electron-observer displacement is simply the difference in these angles. Expressing the scalar products in Equation E.9 in terms of these angles,

$$P = \frac{e^2}{(4\pi)^2\epsilon_0 c}\int_{-2\pi}^{2\pi}\dot{\beta}^2\Bigg((1-2\beta^2\cos^2\theta+\beta^2)\cos(\theta-\phi)- \\ 2(\cos^2(\theta-\phi)-\beta\cos\phi\cos(\theta-\phi))(1-\beta\cos\theta)+ \\ 1-2\beta\cos\theta+\beta^2\cos^2\theta)\Bigg)\frac{d\Omega}{(1-\beta\cos\theta)^5}. \tag{E.10}$$

Using the trigonometric identity, $\cos(\theta-\phi)=\cos\theta\cos\phi-\sin\theta\sin\phi$, this expression can be simplified:

$$P = \frac{e^2}{(4\pi)^2\epsilon_0 c}\int_{-2\pi}^{2\pi}\dot{\beta}^2\Bigg((\beta^2-1)(\cos^2\theta\cos^2\phi+\frac{1}{2}(1-\cos^2\theta)\sin^2\theta) \\ 2\cos^2\phi\cos\theta\beta(1-\beta\cos\theta)+ \\ (1-2\beta\cos\theta+\beta^2\cos^2\theta)\Bigg)\frac{d\Omega}{(1-\beta\cos\theta)^5}. \tag{E.11}$$

The infinitesimal solid angle element can be written as $d\Omega = 2\pi\, d(\cos\theta)$. Defining $u=\cos\theta$, then $du = d(\cos\theta)$ and $d\Omega = 2\pi\, du$. Thus, the integral can be rewritten:

$$P = \frac{e^2\dot{\beta}^2}{8\pi\epsilon_0 c}\int_{-1}^{1}\Bigg((\beta^2-1)(u^2\cos^2\phi+\frac{1}{2}(1-u^2)\sin^2\phi)+ \\ 2\cos^2\phi\, u\beta(1-\beta u)+1-2\beta u+\beta^2u^2\Bigg)\frac{du}{(1-\beta u)^5}. \tag{E.12}$$

Expanding the integrand,

$$P = \frac{e^2\dot{\beta}^2}{8\pi\epsilon_0 c}\int_{-1}^{1}\Bigg((1-u^2)+ \\ \sin^2\phi\Bigg(\Bigg(\frac{3}{2}+\frac{1}{2}\beta^2\Bigg)u^2-2\beta u-\frac{1}{2}(1-\beta^2)\Bigg)\Bigg)\frac{du}{(1-\beta u)^5}. \tag{E.13}$$

The integration can be performed by introducing the variable $v = 1-\beta u$, and thus $dv = -\beta\, du$. Substituting these variables into Equation E.13,

$$P = \frac{e^2\dot{\beta}^2}{8\pi\epsilon_0 c\beta^3}\int_{1-\beta}^{1+\beta}\Bigg((\beta^2-1+2v-v^2)+ \\ \sin^2\phi\Bigg(\frac{1}{2}(3-4\beta^2+\beta^4)+(\beta^2-2)v+\frac{1}{2}(3+\beta^2)v^2\Bigg)\Bigg)\frac{dv}{v^5}. \tag{E.14}$$

The integral is now in a form that can be evaluated analytically:

$$P = \frac{e^2\dot{\beta}^2}{4\pi\epsilon_0 c\beta^3}\left[\left(\frac{\beta^2-1}{4v^4}+\frac{2}{3v^3}-\frac{1}{2v^2}\right)+ \right. \tag{E.15}$$

$$\left. \sin^2\phi\left(\frac{(3-\beta^2)(1-\beta^2)}{8v^4}+\frac{\beta^2-3}{3v^3}+\frac{3+\beta^2}{4v^2}\right)\right]_{1-\beta}^{1+\beta}, \tag{E.16}$$

After some tedious algabraic manipulation, this result produces an expression for the total power radiated by the accelerating electron:

$$P = \frac{e^2\dot{\beta}^2}{8\pi\epsilon_0 c\beta^3}\gamma^6\left(\frac{2}{3}\beta^3-\frac{2}{3}\beta^5\sin^2\phi\right), \tag{E.17}$$

$$= \frac{e^2}{6\pi\epsilon_0 c}\gamma^6(\dot{\beta}^2-\dot{\beta}^2\beta^2\sin^2\phi). \tag{E.18}$$

The second term in this expression is the square of the vector product of the velocity and acceleration vectors of the electron. The total radiated power can be written in terms of the velocity and acceleration vectors of the electron:

$$P = \frac{e^2}{6\pi\epsilon_0 c}\gamma^6\left(\dot{\boldsymbol{\beta}}^2-(\dot{\boldsymbol{\beta}}\times\boldsymbol{\beta})^2\right). \tag{E.19}$$

E.1.2 Angular Intensity Distribution Radiated by an Electron Following a Circular Trajectory

The spatial distribution of the power emitted by an electron undergoing some sort of acceleration was derived earlier in the appendix and is given by Equation E.20:

$$\frac{dP}{d\Omega} = \frac{e^2}{(4\pi)^2\epsilon_0 c}\frac{\left(\mathbf{n}\times((\mathbf{n}-\boldsymbol{\beta})\times\dot{\boldsymbol{\beta}})\right)^2}{(1-\mathbf{n}\cdot\boldsymbol{\beta})^5}. \tag{E.20}$$

The angular power distribution depends on the angle between the vectors in this equation. It is more convenient to express the angular power distribution in a spherical coordinate system, while the vectors are often expressed as Cartesian vectors. The Cartesian unit vectors ($\boldsymbol{\epsilon_1}$, $\boldsymbol{\epsilon_2}$, $\boldsymbol{\epsilon_3}$) are related to the angular unit vectors ($\mathbf{n}$, $\hat{\boldsymbol{\theta}}$, $\hat{\boldsymbol{\phi}}$) by the rotation matrix:

$$\begin{pmatrix}\boldsymbol{\epsilon_1}\\ \boldsymbol{\epsilon_2}\\ \boldsymbol{\epsilon_3}\end{pmatrix} = \begin{pmatrix}\sin\theta\cos\phi & \cos\theta\cos\phi & -\sin\phi\\ \sin\theta\sin\phi & \cos\theta\sin\phi & \cos\phi\\ \cos\theta & -\sin\theta & 0\end{pmatrix}\begin{pmatrix}\mathbf{n}\\ \hat{\boldsymbol{\theta}}\\ \hat{\boldsymbol{\phi}}\end{pmatrix}. \tag{E.21}$$

The angle between the electron velocity and the electron observer displacement is defined as $\cos\theta = \mathbf{n}\cdot\boldsymbol{\beta}$. The angle between the velocity and acceleration is defined

as $\cos\phi = \boldsymbol{\beta}\cdot\frac{\dot{\boldsymbol{\beta}}}{|\dot{\boldsymbol{\beta}}|}$. For an electron following a circular trajectory, the coordinate system is set up such that $\boldsymbol{\beta} = \beta\boldsymbol{\epsilon_1}$ and $\dot{\boldsymbol{\beta}} = \dot{\beta}\boldsymbol{\epsilon_3}$. The first vector product in Equation E.20 can thus be expressed in terms of the angular unit vectors:

$$
\begin{aligned}
(\mathbf{n}-\boldsymbol{\beta})\times\dot{\boldsymbol{\beta}} &= \mathbf{n}\times\dot{\boldsymbol{\beta}} - \boldsymbol{\beta}\times\dot{\boldsymbol{\beta}}, && \text{(E.22)}\\
&= \dot{\beta}(\mathbf{n}\times\boldsymbol{\epsilon_1}) - \beta\dot{\beta}(\boldsymbol{\epsilon_1}\times\boldsymbol{\epsilon_3}), && \text{(E.23)}\\
&= \dot{\beta}(0\boldsymbol{\epsilon_1} + n\cos\phi\boldsymbol{\epsilon_2} + n\sin\phi\boldsymbol{\epsilon_3}) - \beta\dot{\beta}\boldsymbol{\epsilon_2}, && \text{(E.24)}\\
&= \dot{\beta}(0\boldsymbol{\epsilon_1} + \cos\phi\boldsymbol{\epsilon_2} + \sin\phi\boldsymbol{\epsilon_3}) - \beta\dot{\beta}\boldsymbol{\epsilon_2}, && \text{(E.25)}\\
&= \dot{\beta}(\cos\theta\cos\phi\hat{\boldsymbol{\phi}} + \sin\phi\hat{\boldsymbol{\theta}}) - \\
&\qquad \beta\dot{\beta}(\sin\theta\sin\phi\mathbf{n} + \cos\theta\sin\phi\hat{\boldsymbol{\theta}} - \sin\theta\hat{\boldsymbol{\phi}}) && \text{(E.26)}\\
&= \dot{\beta}\big((\beta\sin\theta\sin\phi)\mathbf{n} + (\sin\phi - \beta\cos\theta\sin\phi)\hat{\boldsymbol{\theta}} + \\
&\qquad (\cos\theta\cos\phi - \beta\cos\phi)\hat{\boldsymbol{\phi}}\big). && \text{(E.27)}
\end{aligned}
$$

Then, calculating the second vector product in Equation E.20,

$$
\begin{aligned}
\mathbf{n}\times\big((\mathbf{n}-\boldsymbol{\beta})\times\dot{\boldsymbol{\beta}}\big) &= (\mathbf{n} + 0\hat{\boldsymbol{\theta}} + 0\hat{\boldsymbol{\phi}})\times \\
&\qquad \dot{\beta}\big((\beta\sin\theta\sin\phi)\mathbf{n} + \\
&\qquad (\sin\phi - \beta\cos\theta\sin\phi)\hat{\boldsymbol{\theta}} + (\cos\theta\cos\phi - \beta\cos\phi)\hat{\boldsymbol{\phi}}\big), && \text{(E.28)}\\
&= \dot{\beta}\big(0\mathbf{n} + (\beta\cos\phi - \cos\theta\cos\phi)\hat{\boldsymbol{\theta}} + \\
&\qquad (\sin\phi - \beta\cos\theta\sin\phi)\hat{\boldsymbol{\phi}}\big). && \text{(E.29)}
\end{aligned}
$$

The square of this vector product is then calculated:

$$
\begin{aligned}
\big(\mathbf{n}\times\big((\mathbf{n}-\boldsymbol{\beta})\times\dot{\boldsymbol{\beta}}\big)\big)^2 &= \dot{\beta}^2\big(\cos^2\phi(\beta-\cos\theta)^2 + \sin^2\phi(1-\beta\cos\theta)^2\big), && \text{(E.30)}\\
&= \dot{\beta}^2\big(\cos^2\phi\sin^2\theta(1-\beta^2) + (1-\beta\cos\theta)^2\big). && \text{(E.31)}
\end{aligned}
$$

This result can then be substituted into Equation E.20:

$$
\frac{dP}{d\Omega} = \frac{e^2}{(4\pi)^2\epsilon_0 c}\dot{\beta}^2\left(\frac{\cos^2\phi\sin^2\theta(1-\beta^2) + (1-\beta\cos\theta)^2}{(1-\mathbf{n}\cdot\boldsymbol{\beta})^5}\right). \qquad \text{(E.32)}
$$

The denominator of Equation E.20 can also be written in terms of the angle between the vectors: $(1-\mathbf{n}\cdot\boldsymbol{\beta})^5 = (1-\beta\cos\theta)^5$. Also, $(1-\beta^2) = \gamma^{-2}$. The angular power distribution of the radiation can then be expressed solely in terms of the magnitude of the vectors describing the motion of the electron and the angular coordinates relative to the electron's position:

$$
\frac{dP}{d\Omega} = \frac{e^2}{(4\pi)^2\epsilon_0 c}\frac{\dot{\beta}^2}{(1-\beta\cos\theta)^3}\left(1 - \frac{\cos^2\phi\sin^2\theta}{\gamma^2(1-\beta\cos\theta)^2}\right). \qquad \text{(E.33)}
$$

E.2 Angular Energy Density Distribution in an LWFA

A two-dimensional and a three-dimensional model for the angular energy density distribution of the radiation beam are derived for an electron following a sinusoidal trajectory with $K \gg 1$. The two-dimensional model produces an distribution of the energy radiated per unit angle; the three-dimensional model produces an expression for the energy radiated per unit solid angle.

E.2.1 Two-Dimensional Model

The total energy radiated by an electron can be obtained by integrating the angular intensity distribution over the whole angular range covered in its trajectory:

$$W = \int U(\theta_e)\, d\theta_e, \tag{E.34}$$

where $U(\theta) = \frac{dW}{d\theta_e}$ is the energy radiated per unit angle and θ_e is the angle between the electron's direction of travel and the z-axis. This is the direction that the electron emits its radiation cone. The quantity $\frac{dW}{d\theta_e}$ can be re-expressed using the chain rule:

$$\frac{dW}{d\theta_e} = \frac{dW}{dt_{ret}} \frac{dt_{ret}}{d\theta_e}, \tag{E.35}$$

where t_{ret} is the time at which the electron emits the radiation. The first derivative is the rate at which the electron emits energy, which is the power emitted by the electron:

$$\frac{dW}{d\theta_e} = P(t_{ret}) \frac{dt_{ret}}{d\theta_e}. \tag{E.36}$$

The second derivative is the rate of change if time with respect to the direction of travel of the electron; this accounts for the amount of time spent by the electron travelling in each direction. If the power emitted in a specific direction is considered, so the power is written in terms of the angle rather than time, then:

$$\frac{dW}{d\theta_e} = P(\theta_e) \frac{dt_{ret}}{d\theta_e}. \tag{E.37}$$

Both of these derivatives will be evaluated and expressed in terms of the angle of divergence in the electron's trajectory, θ_e.

Power Emitted by Electron

The power emitted by the electron is given by the Liénard formula. For an electron following a sinusoidal trajectory, the transverse acceleration dominates the power emit-

ted. Only this contribution to the emitted power is considered, which is given by Equation 2.84. The transverse momentum of the electron can is given by $p_r = \gamma m_e \beta_r c$, where β_r is the transverse component of the velocity factor of the electron. An expression for this quantity was derived in Section 2.10 for an electron following a sinusoidal trajectory, moving with constant energy. The expression is given by Equation 2.64, which is repeated here:

$$\beta_r(t_{ret}) = -k_\beta r_\beta \sin \omega_\beta t_{ret}, \tag{E.38}$$

where k_β is the wavenumber, r_β is the amplitude and ω_β is the frequency of oscillation of the electron. Substituting this into $p_r = \gamma m_e \beta_r c$ and differentiating this with respect to time produces an expression for the rate of change of angular momentum:

$$\frac{dp_r}{dt_{ret}} = m_e \omega_\beta^2 r_\beta \cos(\omega_\beta t_{ret}). \tag{E.39}$$

Substituting this into the expression for the transverse contribution to the emitted power, given by Equation 2.84, then produces an expression for the power emitted by the electron as a function of time:

$$P(t_{ret}) = \frac{e^2}{6\pi\epsilon_0 c^3} \gamma^4 \omega_\beta^4 r_\beta^2 \cos^2(\omega_\beta t_{ret}). \tag{E.40}$$

This equation can be written in terms of the angle between the electron's trajectory and the z-axis. It was shown in Section 2.12.1 that, when much smaller than unity, the angle of divergence of an ultrarelativistic electron's trajectory can be expressed as a function of the retarded time:

$$\theta_e(t_{ret}) = -\frac{K}{\gamma} \sin(\omega_\beta t_{ret}) \tag{E.41}$$

where ω_β is the frequency of the betatron oscillations and K is the dimensionless K-parameter of the electron. Expressing the square of this angle,

$$\big(\theta_e(t_{ret})\big)^2 = \frac{K^2}{\gamma^2} \sin^2(\omega_\beta t_{ret}), \tag{E.42}$$

$$= \frac{K^2}{\gamma^2} \big(1 - \cos^2(\omega_\beta t_{ret})\big). \tag{E.43}$$

By substituting Equation E.43 into Equation E.40 for the emitted power,

$$P(t_{ret}) = \frac{e^2}{6\pi\epsilon_0 c}\omega_\beta^2 K^2\gamma^2(1-\sin^2(\omega t_{ret})), \tag{E.44}$$

$$= \frac{e^2}{6\pi\epsilon_0 c}\omega_\beta^2\gamma^4\left(\frac{K^2}{\gamma^2} - \frac{K^2}{\gamma^2}\sin^2(\omega t_{ret})\right), \tag{E.45}$$

$$= \frac{e^2}{6\pi\epsilon_0 c}\omega_\beta^2\gamma^4\left(\frac{K^2}{\gamma^2} - \theta_e(t_{ret})^2\right). \tag{E.46}$$

Hence,

$$P(\theta_e) = \frac{e^2}{6\pi\epsilon_0 c}\omega_\beta^2\gamma^4\left(\frac{K^2}{\gamma^2} - \theta_e^2\right). \tag{E.47}$$

Rate of Change of Time with respect to Angle

To evaluate the derivative $\frac{dt_{ret}}{d\theta}$ in Equation E.37, Equation E.43 is first rearranged:

$$t_{ret} = \frac{1}{\omega_\beta}\arcsin\left(-\frac{\gamma}{K}\theta_e\right). \tag{E.48}$$

Then, differentiating this expression,

$$\frac{dt_{ret}}{d\theta_e} = \frac{1}{\omega_\beta}\frac{\frac{-\gamma}{K}}{\sqrt{1-\frac{\gamma^2}{K^2}\theta_e^2}}, \tag{E.49}$$

$$= \frac{-1}{\omega_\beta\sqrt{\frac{K^2}{\gamma^2}-\theta_e^2}}. \tag{E.50}$$

However, a negative gradient in time does not make any real physical sense. The negative sign is due to the decrease in the angle over time. It is the magnitude of this derivative that is of interest, as it quantifies the amount of time spent by the electron radiating in any chosen direction. Equation E.37 could be written to account for this:

$$\frac{dW}{d\theta_e} = P(\theta_e)\left|\frac{dt_{ret}}{d\theta_e}\right|. \tag{E.51}$$

Energy Radiated per unit Angle

Substituting Equations E.46 and E.50 into Equation E.51, an expression for the angular energy density distribution is produced:

$$\frac{dW}{d\theta_e} = \frac{e^2}{6\pi\epsilon_0 c}\gamma^4\omega_\beta\sqrt{\frac{K^2}{\gamma^2}-\theta_e^2}. \tag{E.52}$$

E.2.2 Three-Dimensional Model

The main difference between the two-dimensional and the three-dimensional model derived here is that in this derivation the intensity distribution of the radiation cone is considered, rather than assuming that all of the radiation power is emitted in the plane of oscillation of the electron. The total power radiated by the electron can be found by integrating the angular intensity distribution of the radiation cone over all solid angles, which would produce a function of time for the total radiated power. The total energy radiated by the electron during its trajectory is found by integrating this function with respect to time:

$$W = \iiint \frac{dP}{d\Omega}\, d\theta_y\, d\theta_x\, dt_{ret}, \tag{E.53}$$

where $\frac{dP}{d\Omega}$ is the power radiated per unit solid angle in the radiation cone and θ_x and θ_y are the angles of divergence along the x-axis and y-axis. If this expression is differentiated with respect to θ_y,

$$\frac{dW}{d\theta_y} = \iint \frac{dP}{d\Omega}\, d\theta_x\, dt_{ret}. \tag{E.54}$$

Similarly to the derivation of the two-dimensional model, this expression can be written in terms of the direction of travel of the electron by applying the chain rule:

$$\frac{dW}{d\theta_y} = \iint \frac{dP}{d\Omega}\, d\theta_y\, d\theta_x \frac{dt_{ret}}{d\theta_e}\, d\theta_e, \tag{E.55}$$

Rearranging,

$$\frac{d^2W}{d\theta_y\, d\theta_e} = \int \frac{dP}{d\Omega}\, d\theta_x\, \frac{dt_{ret}}{d\theta_e}. \tag{E.56}$$

The derivative $\frac{dt_{ret}}{d\theta_e}$ can be interpreted as the amount of time taken for the electron to pass through each angle covered by it trajectory. This is the key quantity in determining the divergence of the angular energy density distribution produced by the electron over its entire trajectory.

Integrating the Intensity Distribution of the Radiation Cone

While a sinusoidal electron trajectory is being considered here, it has been shown that most of the radiation power is emitted around the turning points of the trajectory. It is shown in Section 2.12.2 that a circular arc can be used to approximate the trajectory around its turning points. For an ultrarelativistic electron following an approximately circular trajectory, the angular intensity distribution of the radiation cone is approximated by Equation 2.86, which is repeated here:

$$\frac{dP}{d\Omega} = \frac{e^2}{2\pi^2\epsilon_0 c}\frac{\gamma^6\dot{\beta}^2}{(1+\gamma^2\theta^2)^3}\left(1-\frac{4\gamma^2\theta^2\cos^2\phi}{(1+\gamma^2\theta^2)^2}\right), \tag{E.57}$$

where $\dot{\beta}$ is the rate of change of the speed factor of the electron and θ is the polar angle in the angular intensity distribution of the radiation cone. It is important to note that $\theta \neq \theta_e$; θ_e is the direction of travel of the electron, whereas θ refers only to the angular distribution of the radiation cone at a specific point in time.

The angular intensity distribution of the radiation cone is written in a spherical polar coordinate system. However, it is easier to understand the intensity of the radiation while the electron oscillates in a Cartesian coordinate system. The angles in the spherical coordinate system are transformed to angles of divergence along the x-axis and y-axis:

$$\theta_x = \theta\cos\phi, \tag{E.58}$$

$$\theta_y = \theta\sin\phi. \tag{E.59}$$

The angular intensity of the radiation cone can ten be written in terms of these angles:

$$\frac{dP}{d\Omega} = \frac{e^2}{2\pi^2\epsilon_0 c}\frac{\gamma^6\dot{\beta}^2}{(1+\gamma^2\theta_x^2+\gamma^2\theta_y^2)^3}\left(1-\frac{4\gamma^2\theta_x^2}{(1+\gamma^2\theta_x^2+\gamma^2\theta_y^2)^2}\right), \tag{E.60}$$

where the electron oscillates in the x-z plane. To derive the angular energy density distribution in Equation E.56, the angular distribution of the radiation cone needs to be integrated with respect to θ_x:

$$\int_{-\pi}^{\pi}\frac{dP}{d\Omega}\,d\theta_x = \frac{e^2}{2\pi^2\epsilon_0 c}\gamma^6\dot{\beta}^2\int_{-\pi}^{\pi}\frac{1}{(1+\gamma^2\theta_x^2+\gamma^2\theta_y^2)^3}\left(1-\frac{4\gamma^2\theta_x^2}{(1+\gamma^2\theta_x^2+\gamma^2\theta_y^2)^2}\right)d\theta_x, \tag{E.61}$$

$$= \frac{e^2}{2\pi^2\epsilon_0 c}\gamma^6\dot{\beta}^2\left(\frac{3\pi}{8\gamma(1+\theta_y^2)^{\frac{5}{2}}}-\frac{5\pi}{32\gamma(1+\gamma^2\theta_y^2)^{\frac{7}{2}}}\right) \tag{E.62}$$

For an electron following a sinusoidal trajectory, the acceleration of the electron can be written in terms of the K-parameter and the direction of travel of the electron:

$$\dot{\beta} = \frac{d\beta_r}{dt_{ret}} = \frac{d}{dt_{ret}}(-k_\beta r_\beta\sin(\omega_\beta t_{ret})), \tag{E.63}$$

$$= -\frac{\omega_\beta^2}{c}r_\beta\cos(\omega_\beta t_{ret}), \tag{E.64}$$

$$= -\frac{\omega_\beta^2}{c}r_\beta\sqrt{1-\frac{\gamma^2\theta_e^2}{K^2}}. \tag{E.65}$$

Substituting this into Equation E.62,

$$\int_{-\pi}^{\pi} \frac{dP}{d\Omega}\, d\theta_x = \frac{e^2}{16\pi\epsilon_0 c^3}\gamma^5\omega_\beta^4 r_\beta^2 \left(1 - \frac{\gamma^2\theta_e^2}{K^2}\right) F(\theta_y), \tag{E.66}$$

where $F(\theta_y)$ is a function of the divergence angle in the direction perpendicular to the plane of oscillation:

$$F(\theta_y) = \frac{1}{(1+\gamma^2\theta_y^2)^{\frac{5}{2}}}\left(3 - \frac{5}{4(1+\gamma^2\theta_y^2)}\right). \tag{E.67}$$

Rate of Change of Time with respect to Angle

The quantity $\frac{dt_{ret}}{d\theta_e}$ was already derived in the two-dimensional case, and is briefly recapped here. Equation E.43 expresses the direction of travel of the electron as a function of time. This equation is first rearranged:

$$t_{ret} = \frac{1}{\omega_\beta}\arcsin\left(-\frac{\gamma}{K}\theta_e\right). \tag{E.68}$$

Then, differentiating this expression,

$$\frac{dt_{ret}}{d\theta_e} = \frac{-\frac{\gamma}{K}}{\omega_\beta\sqrt{1-\frac{\gamma^2\theta_e^2}{K^2}}}. \tag{E.69}$$

Energy Density Distribution

Substituting Equations E.66 and E.50 into Equation E.56 , an expression is produced for the angular energy density distribution of the radiation produced by an electron over its entire sinusoidal trajectory:

$$\frac{d^2W}{d\theta_y\, d\theta_e} = \int \frac{dP}{d\Omega}\, d\theta_x \frac{dt_{ret}}{d\theta_e}, \tag{E.70}$$

$$= \frac{e^2}{16\pi\epsilon_0 c^3}\gamma^3\omega_\beta^4 r_\beta^2\, F(\theta_y)\left(1 - \frac{\gamma^2\theta_e^2}{K^2}\right)\frac{-\frac{\gamma}{K}}{\omega_\beta\sqrt{1-\frac{\gamma^2\theta_e^2}{K^2}}}, \tag{E.71}$$

$$= \frac{e^2}{16\pi\epsilon_0 c^3}\frac{\gamma^6}{K}\omega_\beta^3 r_\beta^2\, F(\theta_y)\sqrt{1-\frac{\gamma^2\theta_e^2}{K^2}}, \tag{E.72}$$

$$= \frac{e^2}{16\pi\epsilon_0 c}\gamma^5\omega_\beta\, F(\theta_y)\sqrt{\frac{K^2}{\gamma^2} - \theta_e^2}. \tag{E.73}$$

Written in full,

$$\frac{d^2W}{d\theta_y\, d\theta_e} = \frac{e^2}{16\pi\epsilon_0 c}\gamma^5\omega_\beta\sqrt{\frac{K^2}{\gamma^2} - \theta_e^2}\left[\frac{1}{(1+\gamma^2\theta_y^2)^{\frac{5}{2}}}\left(3 - \frac{5}{4(1+\gamma^2\theta_y^2)}\right)\right]. \tag{E.74}$$

E.3 Inverse Doppler Shifting Factor

A time interval in the retarded time corresponds to a time interval in the time of observation according to Equation 2.75:

$$dt_{obs} = dt_{ret}\,(1 - \mathbf{n} \cdot \boldsymbol{\beta}). \tag{E.75}$$

When the speed of an electron is close to the speed of light, so $\beta \approx 1$, the factor can be approximated when the electron is travelling in the direction towards the observer:

$$\begin{aligned}(1 - \mathbf{n} \cdot \boldsymbol{\beta}) &\approx (1 - \beta) && \text{(E.76)}\\ &= (1 - \beta) \cdot \frac{1 + \beta}{1 + \beta} && \text{(E.77)}\\ &= \frac{1 - \beta^2}{1 + \beta} && \text{(E.78)}\\ &\approx \frac{1}{2\gamma^2}. && \text{(E.79)}\end{aligned}$$

E.4 Duration of a Synchrotron Radiation Flash

An electron performing instantaneous circular motion produces synchrotron radiation in a cone with an opening angle given by Equation 2.87: $\theta_{cone} = \frac{2}{\gamma}$. As the electron moves around its trajectory, the radiation is seen as a flash by a stationary observer, whose duration depends on the amount of time that the radiation cones spends sweeping across the observer's position. The front of the observed radiation flash is emitted when one edge of the cone points in the direction of the observer, as can be seen in Figure 19. The back of the observed radiation flash is emitted when the other edge of the cone points in the direction of the observer. The duration of the observed radiation flash is the difference in time between the first photon passing through the ending position of the electron and when the last photon is emitted at that ending position:

$$\Delta t_{flash} = t_{end} - t_{start}. \tag{E.80}$$

The arc made by the electron trajectory producing the radiation flash has an angle equal to the angle of the radiation cone, as shown in Figure 19. Its length is also determined by the radius of curvature of the electron's trajectory. The time taken for the radiation to travel in a straight line from the starting point of the electron to the ending point can be written:

$$t_{start} = \frac{2\rho \sin \frac{1}{\gamma}}{c}, \tag{E.81}$$

where ρ is the radius of curvature. The electron emits the final photon in the flash after travelling the length of the arc: $s = \rho\theta_{cone} = 2\rho/\gamma$. The time taken for the electron to travel this length depends on the speed of the electron:

$$t_{end} = \frac{2\rho}{\beta c\gamma}. \tag{E.82}$$

Substituting Equations E.81 and E.82 into the definition for the duration of the radiation flash, given by Equation E.80,

$$\Delta t_{flash} = \frac{2\rho}{\beta c\gamma} - \frac{2\rho \sin\frac{1}{\gamma}}{c}. \tag{E.83}$$

Considering an ultrarelativistic electron in instantaneous circular motion, the reciprocal of the Lorentz factor is close to zero. The trigonometric function is expanded as a Taylor series up to its third order term:

$$\sin\frac{1}{\gamma} = \frac{1}{\gamma} - \frac{1}{6\gamma^3}. \tag{E.84}$$

This expansion is then substituted into Equation E.83:

$$\Delta t_{flash} = \frac{2\rho}{\beta c\gamma} - \frac{2\rho}{c}\left(\frac{1}{\gamma} - \frac{1}{6\gamma^3}\right) \tag{E.85}$$

$$= \frac{2\rho}{\beta c\gamma}\left(1 - \beta\left(1 - \frac{1}{6\gamma^2}\right)\right), \tag{E.86}$$

$$= \frac{2\rho}{6\beta c\gamma}\left(6 - 6\beta + \frac{1}{\gamma^2}\right). \tag{E.87}$$

Using the identity $\gamma^{-2} = 1 - \beta^2$ derived in Appendix E.3,

$$\left(6 - 6\beta + \frac{1}{\gamma^2}\right) = 6(1-\beta) + \frac{1}{\gamma^2}, \tag{E.88}$$

$$= 6(1-\beta)\frac{1+\beta}{1+\beta} + \frac{1}{\gamma^2}, \tag{E.89}$$

$$= 6\frac{1-\beta^2}{1+\beta} + \frac{1}{\gamma^2}, \tag{E.90}$$

$$= \frac{6}{\gamma^2(1+\beta)} + \frac{1}{\gamma^2}, \tag{E.91}$$

$$= \frac{1}{\gamma^2}\left(\frac{6}{1+\beta} + 1\right), \tag{E.92}$$

The factor in Equation E.87 can be simplified when considering an ultrarelativistic electron, as $\beta \approx 1$:

$$\left(6 - 6\beta + \frac{1}{\gamma^2}\right) = \frac{1}{\gamma^2}\frac{6 + (1+\beta)}{1+\beta}, \tag{E.93}$$

$$\approx 4\gamma^{-2}. \tag{E.94}$$

Substituting this factor into Equation E.87 produces the expression for the duration of the synchrotron radiation flash:

$$\Delta t_{flash} = \frac{4\rho}{3c\gamma^3}. \tag{E.95}$$